UNIVERSIDADE DE SANTIAGO DE COMPOSTELA

FACULTADE DE FÍSICA

Departamento de Física de Partículas

Prototype of a new calorimeter for the studies of nuclear reactions with relativistic radioactive beams

UNIVERSIDADE DE SANTIAGO DE COMPOSTELA
Departamento de Física de Partículas
GENP (Grupo Experimental de Núcleos y Partículas)

El Prof. Ignacio Durán Escribano, y el Prof. Héctor Álvarez Pol, del Departamento de Física Atómica, Molecular y Nuclear de la Universidad de Santiago de Compostela

CERTIFICAN:

que la memoria titulada **Prototype of a new calorimeter for the studies of nuclear reactions with relativistic radioactive beams** ha sido realizada por **D. Martín Gascón Vázquez** bajo su dirección y constituye su **Tesis Doctoral** que presenta para optar al grado de **Doctor en Ciencias Físicas**.

Santiago de Compostela, Septiembre de 2010

Ignacio Durán Escribano   Héctor Álvarez Pol

Acknowledgments

First, I would like to thank my supervisor Prof. Ignacio Durán for his invaluable help. He taught me not only Physics but also the way to face many problems we have to deal with in our daily life. I also want to thank my co-supervisor Prof. Héctor Álvarez because part of this work could not be achieved without his excellent job in CALIFA simulations. Special thanks to Prof. Dolores Cortina (the R3B Calorimeter Coordinator) who was pushing me to get the best results and for her valuable help to this work. I would like to mention the work performed by Paloma Díaz with the Prototype and crystal light transmission simulations because her work and Hector's were the base of the simulations performed in this thesis.

Thanks to Prof. José Benlliure, because he gave me the opportunity to make this PhD and to participate in several experiments from which I learnt so many things and allowed me to meet a lot of excellent people. Thanks to Noelia, because she "fought against" the preamplifiers that made possible the development of this Prototype. A lot of special thanks to David González who came with me to all the experiments and took over all the experimental work in the Lab.

Finally, I can not forget to mention all the people I was working with: Saúl Beceiro, Dusan Dragosavac, Yassid Ayyad (who spent his time in the CMAM experiment), Jossitt Vargas, Carlos Paradela, Manuel Caamaño (for his helpful discussions and advices but not for his inopportune questions), Magdalena Mostazo, Juan Alcántara, Marisol Robles, Raquel Sorribas, Juan Llerena, Juan Ramón Pereira, Carme Rodríguez, Diego Tarrío.

I have grateful acknowledgments to David Pérez, because thank to his wonderful patience, incredible memory and better willingness this work is better. Thanks to David, I finally won the war against ROOT. We also had the chance to learn more about the Physics of Billiards. Thanks to Bea and Charo, for their support.

Finalmente me gustaría agradecer especialmente a mi familia y amigos que de

Contents

Introduction

OUR knowledge of the matter and how the universe evolved relies on the progress of nuclear science. This field of study experienced tremendous advances during the mid-20th century, then slowed to near paralysis during the last quarter of the century, leaving many questions unresolved. Currently, the search for new properties of hadronic matter has revived interest in Nuclear Physics. The most sophisticated experiments are being performed in huge facilities built around accelerators, which require tremendous, joint investments of capital. The many countries that contribute financially and intellectually to the development of innovative set-ups make it possible to go deeper into the secrets of matter. Collaborative, international research produces new information for nuclear physics and other fields such as astronomy, condensed matter and technology. The methods used in these facilities often become relevant for interdisciplinary fields like nanotechnology, medicine or microelectronics. Among the new facilities, one of the most ambitious is FAIR (Facility for Antiproton and Ion Research) [1] a sixteen-country endeavor that is expected to serve more than 2000 international users.

Hadronic matter (e.g. neutrons and protons) is composed of quarks, which are bound by the strong force, one of the three fundamental forces in nature (strong, electroweak, and gravitational forces). The strong force acts between the quarks that constitute nucleons, generating a short-range attractive force between the nucleons, which keeps them bound to form the nucleus in spite of the proton Coulomb repulsion. Quantum Chromodynamics (QCD), the framework used to describe strong force interactions, does not provide a precise analytical form of the interaction at a length scale relevant to the nucleon-nucleon interaction. Moreover, the nucleon-nucleon force within the nucleus is different from that between two free nucleons because it depends on the neutron and proton densities of the surrounding nuclear medium. One of the main aims of nuclear physics is to determine this effective force by investigating nuclei in extreme conditions, which could lead to a better understanding of the behavior of nuclear matter.

The stability of nuclear matter is determined by the potential energy resulting from the residual strong force and the repulsive Coulomb force between protons, together with the strong magnetic couplings of nucleons. This leads to stable heavy nuclei with an excess of neutrons compared to protons. In a nuclear chart,

neutron and proton driplines represent the limits beyond which any more neutrons or protons added to the nucleus would be spontaneously rejected. About 3000 elements have up to now been created and observed in laboratories, but theoretical models predicts that more than 6000 different bound nuclei are expected to exist between the neutron and proton driplines, which are defined as the limits of existence. While neutron and proton driplines for light nuclei are well known, we are far from reaching the neutron dripline for medium- and heavy-mass nuclei. By discovering how many protons and neutrons can be bound in a nucleus, we become acquainted with the limits of nuclear existence, an area that remains largely unexplored.

Most of the information about nuclei comes from the study of reactions in which an exchange of nuclear matter is produced. In the past, both beam and target nuclei had to be stable and this limited access to some regions in the nuclear chart. With the advent of beams made from what are known as exotic nuclei[1], inverse kinematics[2] can be used, resulting in reactions that involve nuclei far from the stability line. This makes it possible to study the nuclear structure of weakly bound nuclei in great detail.

Recent research in the area of unstable neutron-rich isotopes pointed to the existence of nuclei with "halos"[3] and "skins"[4]. The structure and dynamics of such nuclei are very different from those of stable nuclei. Further study of exotic nuclei is also expected to reveal new shell structures, new collective modes, new isospin phases, regions of the nuclear chart where deformed nuclei have special symmetries and possibly new decay modes (e.g., two-proton emission).

In the field of nuclear astrophysics, understanding the formation, evolution and ultimate fate of stars requires simulations of possible thermodynamical equilibrium scenarios (in terms of temperature, density, pressure) as well as their chemical composition, including the mass and half-lives of nuclei that are created and destroyed during the complex steps of nucleosynthesis. Experiments in the new generation exotic beam facilities will allow us to understand the behavior (half-lives and reaction rates) of short-lived nuclei and to explain the relative abundance of elements in our solar system, in our galaxy and in the entire universe.

---

[1] Nuclei with neutron (N) to proton (Z) number ratio far from those of nuclei found in nature.

[2] For experimental reasons, it is sometimes easier to measure the inverse reaction, in which the roles of the target and the projectile are exchanged. This technique, known as inverse kinematics, provides complete information about a direct reaction.

[3] In nuclear physics, an atomic nucleus is called a halo nucleus or is said to have a nuclear halo if its radius is appreciably larger than that predicted by the liquid drop model, wherein the nucleus is assumed to be a sphere of constant density.

[4] For neutron-rich isotopes near drip line, the loosely bound neutrons in the neutron distributions form a neutron skin. In the skin, the proton distribution is small compared with that of neutron. The same explanation can be applied to proton-rich nuclei, but in this case, the neutron distribution in the skin is small compared with that of protons.

There are two different approaches to producing exotic nuclear beams: the in-flight method, which involves high-energy, heavy-ion fragmentation of stable nuclei, and the Isotope Separation On-Line (ISOL) technique, where fragments stopped in the targets are post-accelerated. While the in-flight method provides a clean separation of the chemical elements, the ISOL technique is thought to provide better beam intensity. However, the beam quality can be improved for the in-flight method by cooling the beam in ion storage rings. First-generation in-flight nuclear-beam facilities operate at various laboratories in Europe, the USA, and Japan. Of these, GSI (Helmholtzzentrum für Schwerionenforschung, Darmstadt, Germany) is the only facility in the world where beams of all elements up to Uranium can be produced, with energies up to about 1 GeV/u. The future FAIR facility will upgrade the existing facility, offering improved beam intensity, separation efficiency and beam quality; which will make it possible to investigate secondary beam species very far from stability. The new facility will have a Super-conducting FRagment Separator (Super-FRS) that will accept a much larger phase space than the present FRS.

The R^{3}B setup (Reactions with Relativistic Radioactive Beams [4]) will be located at the focal plane of the high-energy branch of the Super-FRS. It is a sophisticated experimental setup for the study of nuclear reactions with high-energy radioactive beams. The experimental configuration is based on a concept similar to the existing ALADIN-LAND reaction setup, but with substantial improvements in resolution and an extended detection scheme comprised of a high-resolution fragment spectrometer together with an additional detection of light recoil particles.

One of the more challenging requirements of the R^{3}B experiment is to design and construct a calorimeter for detecting in-flight emitted gammas and light charged particles. This calorimeter, named CALIFA, will surround the R^{3}B target and will be used in most of the physical cases presented in the R^{3}B technical collaboration proposal. It must have a high total absorption capability and remarkable resolution in order to identify gamma cascades and light charged particles.

This dissertation presents the results of an experimental study to define the crystals for the R^{3}B Calorimeter. Chapter 1 provides a brief description of FAIR, the R^{3}B setup and the physics involved in these experiments. It also describes the conceptual design, geometry and requirements of the R^{3}B Calorimeter. Chapter 2 explains the calorimeter simulations, including the implementation of the Lorentz boost correction and the observables obtained from the GEANT4 code. It also describes in detail the simulation carried out using CsI(Tl) prototype crystals under gamma and proton beam irradiation. Chapter 3 provides a careful description of how the CsI(Tl) crystals and photosensors were characterized and of the parameters that can be improved to optimize crystal performance. Finally, Chapter 4 gives details regarding the construction of the CsI(Tl) prototype, the results obtained from three different test beams and the conclusions extracted from the data analysis.

Chapter 1

Motivation

1.1. FAIR and the physics of the R^{3}B experiment

1.1.1. FAIR highlights

FAIR (Facility for Antiproton and Ion Research) [1] is a new international accelerator facility (Figure 1.1) to be built at the Helmholtzzentrum für Schwerionenforschung (GSI) site in Darmstadt, Germany. FAIR will substantially expand both the research fields and the technical possibilities of the current GSI accelerator system [2]. The goal of this multi-nation project is to provide the European and international scientific community with a unique and technically innovative accelerator system, for carrying out cutting-edge research in fields related to the basic structure of matter. This facility will make an extensive range of particle beams available, from proton or antiproton beams, to ion beams for all chemical elements up to Uranium. The intensities achieved for many of these nuclei will be the highest ever reached.

The proposed facility will have a new 100/200 T·m double-ring synchrotron (SIS 100/200), 1.1 km circumference, with superconducting magnets and a system of associated storage rings for beam collection, cooling, phase-space optimization and experimentation. The current linear accelerator (UNILAC) and Synchrotron SIS18 ring accelerator will be used as injectors. Ion beam intensity will be increased by a factor of 10^2 to 10^3, and the secondary radioactive beam intensity by up to 10^5 over the present GSI capabilities.

A key feature of FAIR will be the generation of intense, high-quality secondary beams. These include beams with short-lived radioactive nuclei (often referred to as exotic or rare isotope beams) and antiprotons beams. Precision will be achieved through sophisticated beam handling methods, such as stochastic and electron cooling of the ion beams. Finally, the new facility will provide a substantial increase in beam energy, at least fifteen times greater for beams as heavy as uranium [3].

FAIR is expected to serve about 2000 international users from all around the world, and about twice the number of users currently involved in research at GSI.
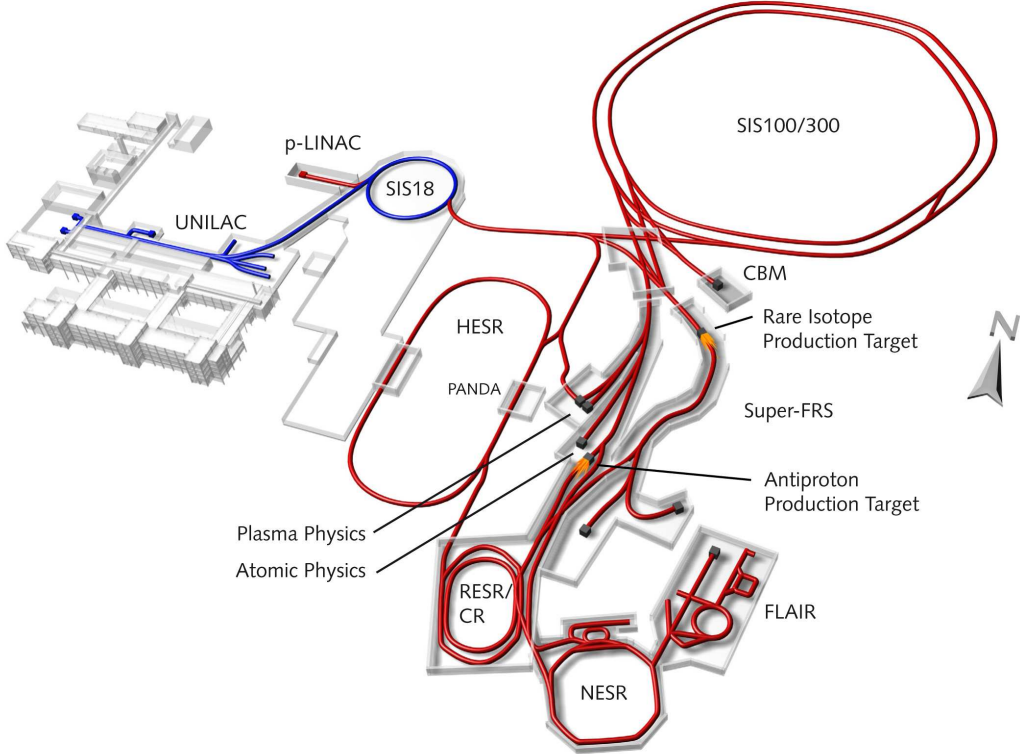
Figure 1.1: The existing GSI facility (blue) and the planned new facility (red).

1.1.2.   Reactions with Relativistic and Radioactive Beams

One of the specific programs that will be pursued at the future facility is research with short-lived radioactive nuclei beams, in order to address important questions concerning nuclei far from stability, areas of astrophysics, nucleosynthesis in supernovae and other stellar processes. The program will be carried out using the R^{3}B [4] (Reactions with Relativistic Radioactive Beams) experimental setup. This versatile set-up provides high efficiency, acceptance, and resolution, for obtaining kinematically complete measurements of reactions induced by high-energy radioactive beams.

The R^{3}B setup will be located at the focal plane of the high-energy branch of the Super-FRS (see Figure 1.1). The experimental configuration is based on a concept similar to the existing ALADIN-LAND reaction setup at GSI, with substantial improvements in resolution and an extended detection scheme that includes an additional detection of light (target-like) recoil particles and a new high-resolution fragment spectrometer (see Figure 1.2). The setup is adaptable to the highest beam energies (corresponding to 20 T·m magnetic rigidity) provided by the Super-FRS, in order to achieve the highest possible transmission of secondary beams [5]).
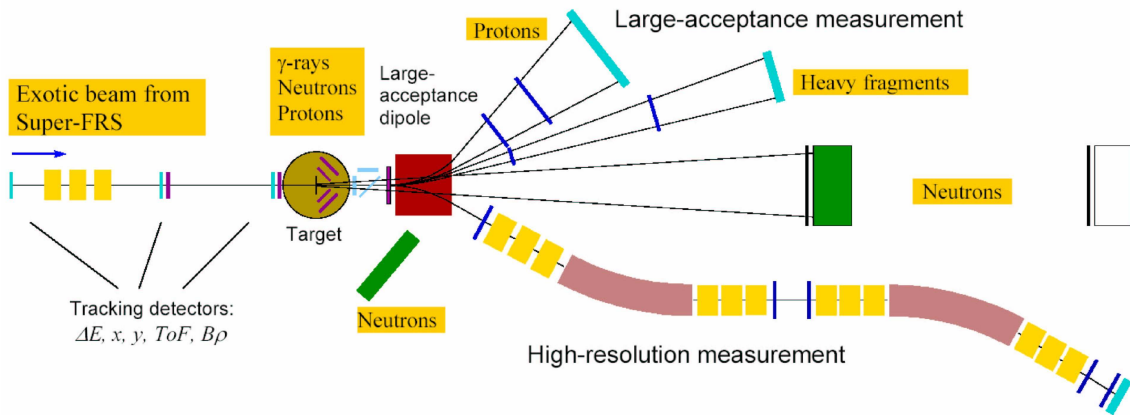
Figure 1.2: Schematic picture of the R³B experimental setup. From left to right, we can see the secondary target that will be surrounded by the CALIFA calorimeter, the large acceptance superconducting dipole magnet, position detectors for tracking, the neutron detector (LAND), and a ToF wall for charged-particle identification. The high resolution magnetic spectrometer is shown at the bottom of the picture.

1.1.3. The physics of the R³B experiment

The experimental setup is suitable for a wide variety of scattering experiments, such as heavy-ion induced electromagnetic excitation, knockout and breakup reactions or light-ion elastic/inelastic and quasi-free scattering in inverse kinematics, thus facilitating a broad physics program with rare-isotope beams.

The different reaction types and associated physics goals are detailed in the following list:

Total-absorption measurements. Nuclear *matter radii* may be inferred from total interaction cross sections, which are derived from the total-absorption measurements of radioactive ions in thick targets. These data, together with isotope shift measurements, could provide the first experimental manifestation of *neutron skins* [6].

Elastic-proton scattering. The radial distribution of *nuclear density* of exotic nuclei can be extracted from high energy proton elastic scattering. Previous experiments have demonstrated the power of this method for detecting *halos* and *skins* in nuclei far from stability [7].

Break-up and knockout reactions. Break-up reactions induced by high-energy radioactive beams make it possible to explore *ground-state* configurations and excited states. Knockout reactions have been used to map the halo nucleon wave function in the momentum space. A Fourier transformation is then used to calculate their spatial distribution [8].

Quasi-free scattering. The R³B experimental setup is intended to develop and apply the technique of quasi-free scattering using radioactive beams in inverse kinematics. Reactions of this type make it possible to extract information about *single-particle shell-structure, nucleon-nucleon correlations* and *cluster knockout reactions* [9].

Electromagnetic excitation. The electromagnetic processes in heavy ion interactions at energies far above the Coulomb barrier constitute an excellent source of information on exotic nuclei structure. Some examples are *surface vibrations* and *giant resonances* [10].

Charge exchange reactions. Studies of the Gamow Teller (GT) strength are of particular astrophysical interest, apart from their importance in the area of nuclear structure. For example, the (p,n) charge exchange reaction can be used to excite GT and spin dipole resonances. The electron-capture reactions leading to stellar collapse and supernova formation are mediated by GT transitions [11].

Fission. Since fission corresponds to a typical large-scale motion process, it is considered one of the most promising tools for deducing information on *nuclear viscosity, shell effects* and *collective excitations at extreme deformation* [12].

Spallation reactions. Spallation reactions are important in various fields of research such as *astrophysics, neutron sources* and *production of radioactive beams* [13].

Projectile fragmentation and multifragmentation. Heavy ion collisions offer the possibility of probing nuclear matter under extreme density and temperature conditions. In addition, isotopic effects in multifragmentation reflect the strength of the symmetry term in the *equation of state*. Projectile fragmentation of secondary beams in conjunction with γ-ray spectroscopy is a powerful method for exploring *excited states in exotic nuclei* [14].

1.2. CALIFA: The R³B Calorimeter

1.2.1. Definition

CALIFA (CALorimeter for In-Flight emitted gAmmas) is a calorimeter that has been proposed as part of the R³B detection system for gamma-rays and light charged particles originated in nuclear reactions from relativistic exotic beams. It will surround the target of the R³B experimental setup and will be used in most of the physical cases presented in the R³B technical proposal [15]. This calorimeter will be composed of thousands of inorganic scintillating crystals that, when operating in coincidence with the Target Recoil Detector (TRD), serve to

distinguish charged particles from target residues.

1.2.2.   Requirements

The CALIFA main requirements are summarized in Table 1.1.

The most challenging aspect of CALIFA is to ensure its wide dynamic range, from low energy gammas to 300 MeV protons. Requirements differ significantly from one experiment to another. A typical R^{3}B experiment will investigate inverse kinematics reactions induced by projectiles with energies up to 1 AGeV. This energy introduces a considerable Lorentz boost to both gammas and protons emitted in-flight by the reaction remnants. In some cases, accurate γ-ray sum energy is required, while in others the detector must provide γ-ray multiplicities and individual γ-ray energies ($\Delta E/E < 5\%$ FWHM for 1 MeV gammas) for spectroscopic purposes.

To overcome the Doppler effect, the angular polar granularity in CALIFA must be kept below $\sim$1.2 degrees in some areas, which limits crystal thickness (see Ref. [16]). The detector must also act as a total absorption calorimeter, subtending the angular region from 7 to 130 degrees, to get about 80% efficiency. To accomplish this, the device will be composed of a huge number of individual crystals ($\approx$ 5000) with different shapes and angular apertures for the different polar angle regions.

The Target Recoil Detector (TRD) is a silicon detector (described in Ref. [5]) that will be placed between the target and the calorimeter. High-energy light charged particles not stopped by the silicon detector must be measured by CALIFA with good energy resolution ($\Delta E/E < 1\%$ FWHM).

Total absorption efficiency	80% (up to E= 15 MeV Lab system)
γ-sum energy	$\sigma(E_{sum})/<E_{sum}> < 10\%$
γ multiplicity	$\sigma(N_\gamma)/<N_\gamma> < 10\%$
Energy resolution	$< 5\% \Delta E/E$ (for 1 MeV gammas)
High-energy light charged particles	Up to 300 MeV in Lab system
Light charged particles energy resolution	$< 1\% \Delta E_p/E_p$

Table 1.1: Summary of the CALIFA main requirements.

The kinematics of the reactions to be studied will impose particular constraints on the calorimeter geometry. As we will see in Section 1.2.4 the Lorentz transformation makes to peak the gamma distribution in the forward direction (smaller polar angles) with greater energy-boost. On the other hand, the crystal length can be reduced at backward angles where the Doppler effect reduces the energy of the

emitted gammas.

Gamma-ray intensity drops drastically at polar angles larger than 100 degrees, which suggests that, it is not necessary to cover the full solid angle in order to reach the specification in terms of total-absorption efficiency. This calorimeter will be constituted by only an Endcap for the forward polar angles, where the highest gamma-ray energies are expected, and a Barrel to cover just up to 130 degrees for the backward polar angles.

Several kinds of scintillating crystals are still being considered for the use in different areas of the calorimeter, but several convincing factors influenced the decision to use CsI(Tl) as scintillating material in the Barrel. CsI(Tl) was chosen for its good energy resolution, high probability for γ interactions (high Z and density), ease of handling, and relatively low price. This will be discussed in more detail in Chapter 3. However, two options for the Forward Endcap are being considered. The first is based on $LaBr_3(Ce) + LaCl_3(Ce)$ in phoswich mode, due to their excellent energy resolution. The main disadvantage of these materials is that they are very hygroscopic and would need to be encapsulated. The second option would be to use long ($\geq$ 200 mm) CsI(Tl) detectors, which could be a cheaper solution but would provide worse resolution.

1.2.3. Detector shape and granularity

General considerations

Several aspects should be taken into account during the initial stages of the detector design,

- the optimal polar angle granularity should be determined in order to guarantee the required energy resolution, which will be discussed later.

- minimum set of different crystal shapes should be used to simplify construction and reduce costs;

- the azimuthal angle granularity should remain low to reduce the number of channels required.

- the longitudinal length of the crystals is determined by the total absorption criterion, leading to different crystal lengths for different polar angles.

- the distance between the beam and the inner surface of the detector should be kept small to reduce the total crystal mass needed for the detector, but a minimum distance is required in the construction of the target area and the target recoil silicon detectors.

- on the other hand, a larger distance is desirable in order to accommodate larger crystal volumes within the same polar angle granularity, which improves the

probability of having the full shower/cascade on a single crystal or only a few crystals in the primary γ-ray direction.

■ the dead volume (empty space and material as wrapping and support structures) must be minimized.

■ gammas passing through the spaces between crystals should be reduced by slightly tilting the crystal axis with respect to the radial direction, primarily in the azimuthal direction.

■ simplicity in shape, number of elements, general design, etc. should be kept in mind.

The geometrical description presented here is based on Ref. [16] and on R³B Calorimeter Working Group internal notes [17–20]. The required energy resolution and the particular kinematics of energetic γ-rays emitted by sources moving with relativistic velocities impose constraints on the polar angle resolution, which will be introduced here and fully treated in Chapter 2.

Two sub-detector parts will be defined to conceptually and constructively simplify the understanding of the different processes involved: a Barrel that surrounds the target and covers backward angles, and a Forward Endcap for the forward polar angles. The geometrical design will include the overall description of the sizes and geometries of these sub-detector parts and the keep-in volume for each crystal. The keep-in volume includes the crystal bulk, wrapping, mechanical support (alveolar thin walls) and any light collection system.

The Barrel and the Endcap are each divided into a number of sectors. Mechanical supports and the sub-detector assembly containers are not considered here. The preliminary designs described here are intended as models for studying the optimum geometry of the R³B calorimeter, with its particular kinematics. In particular, the dimensions of the inner crystal faces will be discussed in detail. Final dimensions should be discussed and established after more extensive simulations, a survey of crystal availability from the crystal providers, prototype testing and other viability studies.

Energy resolution vs. angular granularity

Gammas being emitted by sources moving with relativistic energies and observed within the Laboratory Reference Frame (LRF) are seen to suffer the relativistic Doppler effect. In our case, the moving sources are the residual nuclei produced in the reactions under study. Calculation of their energy in the Source Reference Frame (SRF) requires accurate measurement of both the LRF energy and the emission polar angle. This means that, even if their energy were perfectly determined, a limited polar angle resolution would contribute to the uncertainty

of the gamma energy, when calculated within the SRF. The calorimeter design is thus constrained by the relevant contributions of both the choice of the scintillating material and its angular granularity.

The laboratory energy (E^L) of a γ-ray emitted by a fast residual fragment is boosted by the Lorentz transformation to

$$E^L = E^S \frac{1}{\gamma(1 - \beta \cos\theta)} \tag{1.1}$$

where E^S is the energy of the γ-ray in the SRF, θ the emission polar angle, β the projectile velocity divided by the speed of light and $\gamma = 1/\sqrt{1 - \beta^2}$.

From this formula, we can define the Doppler Factor (DF) as the relation between the γ-ray energies in the LRF and the γ-ray energies in the SRF

$$DF = \frac{E^L}{E^S} = \frac{1}{\gamma(1 - \beta \cos\theta)} \tag{1.2}$$
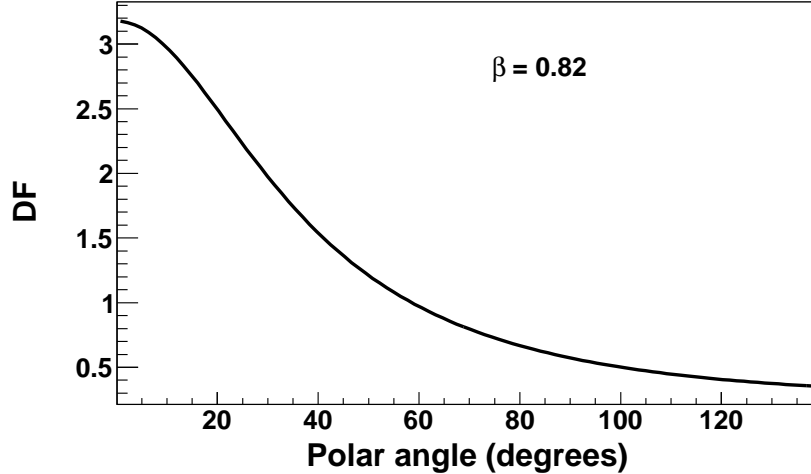
Figure 1.3: Doppler factor as a function of the polar angle.

Figure 1.3 represents the Doppler Factor as a function of the polar angle for β=0.82, a relativistic velocity that approximately corresponds to the incoming fragments at 700 AMeV. At polar angles below 10 degrees (gammas emitted in the very forward region), we can see that the laboratory energy can be up to 3 times higher than the energy in the SRF. In contrast, for angles greater than 60 degrees the energy measured in the LRF becomes lower than the energy in the SRF, dropping to below half of the value for an angle above 100 degrees. This occurs for gammas arriving at the highest polar angles in the backward region of the Barrel. Since the Doppler shift is a function of θ, the uncertainty in the determination of θ introduces a broadening of the spectroscopic peaks of the measured gammas.

Let us assume that we know the polar angle θ of the emitted gamma with an uncertainty $\Delta\theta$ derived from the 'angular aperture', which is determined by the size of the crystals. With this, the uncertainty in energy ΔE^S due exclusively to the limited angular resolution can be approximately deduced (See Appendix A), resulting in an energy resolution given by

$$\frac{\Delta E^S}{E^S} = \frac{\beta \sin\theta}{1 - \beta \cos\theta}\Delta\theta \tag{1.3}$$
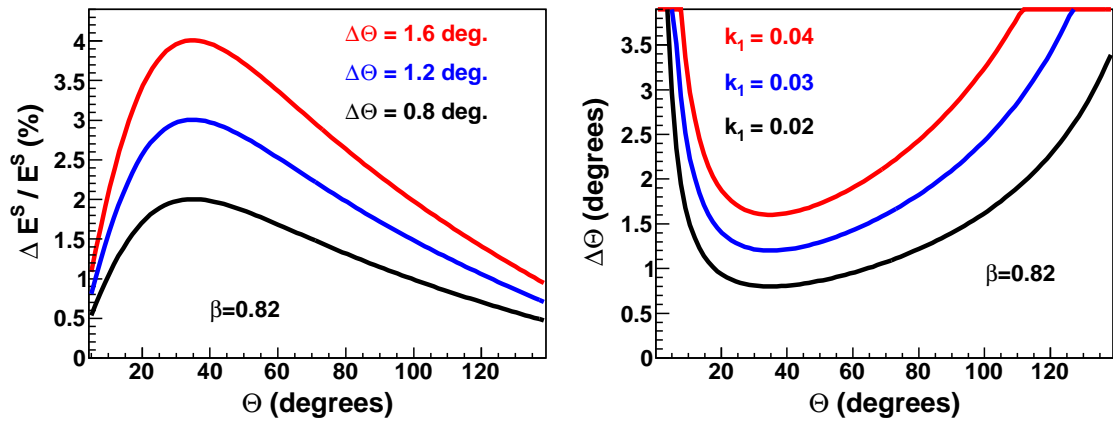
Figure 1.4: Left: Contribution to the energy resolution in the SRF for different polar angle uncertainties. See text for further explanations. Right: The polar angular uncertainty required to make constant the equation 1.3 as a function of the polar angle. The colored lines correspond to k_1 values as defined for equation 1.4.

The dependence of this ratio on the polar angle is shown in Figure 1.4 (left). The three different curves correspond to three different polar angle uncertainties. We can observe the sensitivity of the energy resolution in the SRF on $\Delta\theta$, with the maximum contribution at around 35° for this projectile energy (β=0.82).

Every fixed angular aperture of each crystal gives a different contribution to the relative energy uncertainty of the gammas emitted in-flight by the reaction remnants. If this contribution to the energy resolution for the reconstruction of the γ-ray energy in the SRF must be constant and independent from the polar angle, the 'aperture' assigned to each crystal should depend on its position in the calorimeter. We can express the angular resolution as a function of the polar angle for a given energy resolution in the SRF. If we replace $\Delta E^S/E^S = k_1$ in Equation 1.3, keeping k_1 constant we obtain the expression

$$\Delta\theta = k_1 \frac{1 - \beta \cos\theta}{\beta \sin\theta} \tag{1.4}$$

which can be used to determine the angle that should be covered by each crystal in order to contribute equally to the reconstructed energy resolution in the SRF.

The dependence of $\Delta\theta$ on the polar angle is shown in Figure 1.4 (right). Three different curves are included, corresponding to k_1 values of 2%, 3% and 4%, respectively. From this plot, it is easier to understand the crucial role of the polar angle resolution required at different sectors of the detector in order to obtain a given energy resolution.

To deal with real crystals, a finite value of their energy resolution, scaling with $1/\sqrt{E^L}$ in the LRF, must be introduced (As explained in the Appendix A). Now, the final energy resolution in the SRF becomes

$$\left(\frac{\Delta E^S}{E^S}\right)^2 = \left[\frac{A}{\sqrt{E^L}} + B\right]^2 + \left[\frac{\beta\sin\theta}{1 - \beta\cos\theta}\Delta\theta\right]^2 \tag{1.5}$$

where A is the energy resolution at 1 MeV and B is its asymptotic value, which includes the intrinsic energy resolution of the crystals and the contribution of the whole electronic chain.
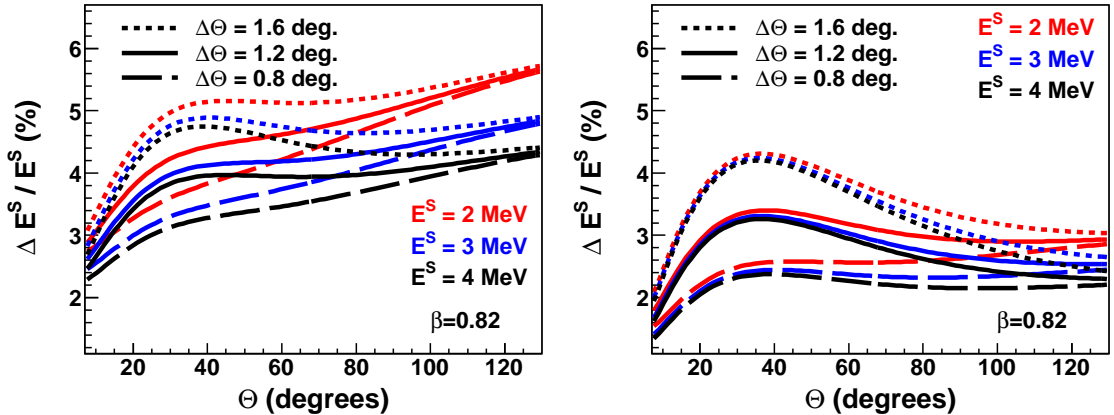
Figure 1.5: Energy resolution in the SRF for three different energies and for $\Delta\theta$ values from 0.8 to 1.6 degrees. In the left panel, parameters A and B (as defined in the text) are 0.04 and 0.01 and in the right panel they are 0.02 and 0.005, respectively.

Using Equation 1.1, the Equation 1.5 becomes

$$\left(\frac{\Delta E^S}{E^S}\right)^2 = \left[\frac{A\cdot\sqrt{\gamma(1 - \beta\cos\theta)}}{\sqrt{E^S}} + B\right]^2 + \left[\frac{\beta\sin\theta}{1 - \beta\cos\theta}\Delta\theta\right]^2 \tag{1.6}$$

This formula can be used when the energy resolution in the SRF depends not only on the uncertainty in θ but also on the uncertainty of the gamma energy measured by the crystals. This is given by the first term on the right side of Equations 1.5 and 1.6. Now we can assign values to the constants A and B and thus obtain the energy resolution in the SRF. Figure 1.5 shows the behavior of the energy resolution as a function of the polar angle, for three different gamma energies in the SRF (2, 3

and 4 MeV) and for three $\Delta\theta$ values (0.8, 1.2 and 1.6 degrees). Two different values of the crystal resolution were considered: in the left panel parameters A and B are 0.04 and 0.01 (corresponding to typical CsI(Tl) crystals) and in the right panel the values are 0.02 and 0.005 (corresponding to typical LaBr crystals), respectively.

We can see that the energy resolution deteriorates as the energy of the emitted gamma decreases. This is more evident for polar angles above 60 degrees due to the influence of the limited energy resolution of the scintillating crystals in the LRF. As a rule of thumb, we can say that the value of $\Delta\theta$ dominates in the polar angle range from 20 to 60 degrees. However, from 90 to 130 degrees, the energy resolution strongly depends on the energy at the source, due to the limited resolution of the scintillating crystals.

In this section an analysis with close-to-real crystals was performed in order to show the complexity of the calorimeter design. The required energy resolution in the SRF depends not only on the 'angular aperture' but also on the energy of the gammas emitted by moving sources.

1.2.4. CALIFA Geometry: A preliminary version

Even though a huge amount of work has already been done in relation to the CALIFA design, there is not yet a final version when writting this work. All that is said here about the guiding idea behind the CALIFA design is based on preliminary simulations of γ emission from excited projectile remnants that are detected by scintillating crystals distributed according to the sketch shown at the top of Figure 1.6. In this sketch, we can distinguish different regions:

- The Forward Endcap covers the region from 7 to 40 degrees. Around 50% of the total γ-rays emitted by the fast remnants are concentrated there. Such a high concentration makes the region extremely complex, especially between 20 and 40 degrees, where the Doppler shift boosts the energy to 1.5-2.5 times its value in the SRF.

- The Barrel encompasses polar angles between 40 and 130 degrees, and more than 40% of the γ-rays are emitted in this polar range. The region covering polar angles above 130 degrees is expected to receive only about 5% of the emitted gammas and therefore will be not covered by scintillation crystals. The region below 7 degrees must be kept clear in order to allow the reaction products to pass through the calorimeter for analysis by the GLAD magnet and the detectors in the last part of the R³B experimental setup.

The azimuthal symmetry of the design makes it possible to use of same crystal size throughout the whole azimuthal range. Unfortunately, different polar angles require different crystal designs to cope with the CALIFA requirements. The crystal
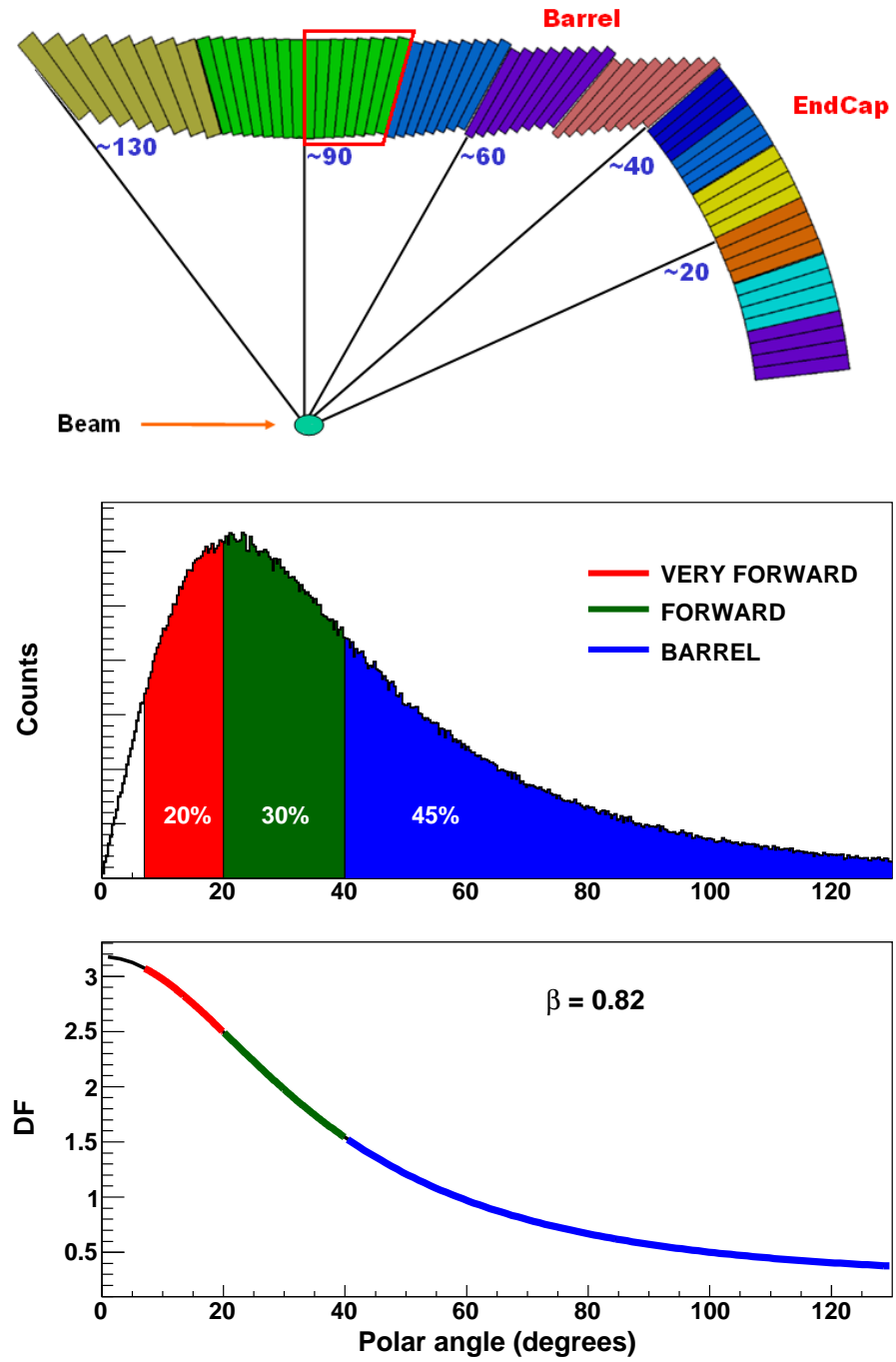
Figure 1.6: Schematic drawing of the CALIFA profile (top). Angular distribution of gammas in the LRF (middle) and their corresponding Doppler shift, assuming isotropic distribution in SRF (bottom).

sizing can be roughly estimated from Figures 1.4 and 1.5 but a more precise design requires extensive simulation work, which will be described in the next Chapter.

Nevertheless, more accurate information on the crystal behavior was required to do conscious calculations. The tests performed to get such information are the main subject of this thesis.

Both high-energy gammas and protons must be identified with good geometrical efficiency, which is an important factor for establishing the angular dependence of the scintillating crystals granularity. Degradation of the gamma energy resolution and the maximum acceptable proton energy loss during their scattering along the detector material will determine the selection of the maximum crystal size in function of both polar and azimuthal angles.
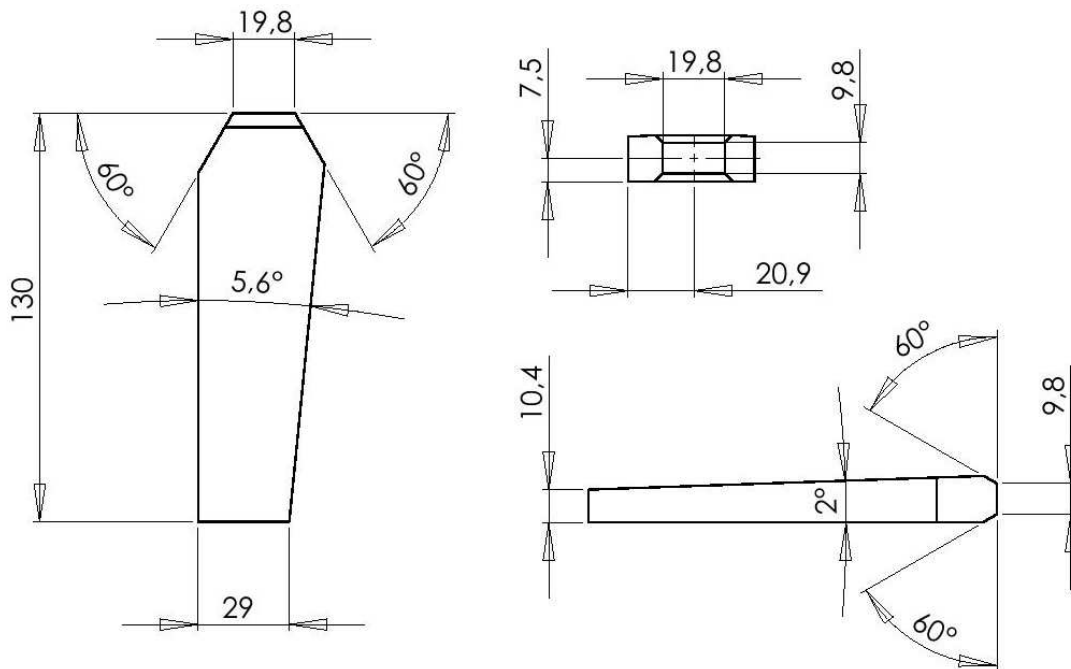
Figure 1.7: Design of bi-frustum-shaped crystals. All dimensions are in mm. The crystals correspond to Barrel with a 30 cm-long inner radius.

Furthermore, the crystal length along the γ-ray direction depends on the crystal bulk material and should be selected according to the detection efficiency required at different polar angles: shorter crystals are required for the larger polar angles, where the Lorentz boost reduces the energy of the gammas and protons. Conversely, longer crystals are required for the forward polar angles.

At this stage, the CALIFA Barrel will supposedly be constituted of CsI(Tl) crystals that are arranged in a cylindrical pattern around the beam line, covering polar angles between $\sim40^o$ and $\sim130^o$. The longer axis of the crystals points approximately towards the target and so they must be tilted along the Barrel, making necessary to use specifically tapered forms. The most forward polar angles

are covered by an Endcap region, which is still in the design phase.

This work will focus on the study of crystals with a geometry very close to that of those required for the section located at the 90° polar angle (inside the box in Figure 1.6).

The proposed design for this region uses crystals in the shape of two truncated pyramids (bi-frustum-shaped crystals), with the following approximate dimensions: a frontal area of 30x10 mm^2, a readout area of 10x20 mm^2, and lengths between 100 and 160 mm (technical drawing of one crystal is shown in Figure 1.7).

An artistic rendering of the preliminary design for the large angle Barrel section is shown in Figure 1.8.

Chapter conclusions

This chapter gave a brief description of the future FAIR facility and the physics involved in the R^{3}B experiment. A detailed outline of the proposed R^{3}B CALIFA Calorimeter was also provided, including its requirements and the specific constraints on the calorimeter geometry imposed by the particular kinematics of the reactions to be studied in the R^{3}B program. The relation between the polar sector covered by each crystal and the polar angle resolution that will be obtained with the detector has been discussed.
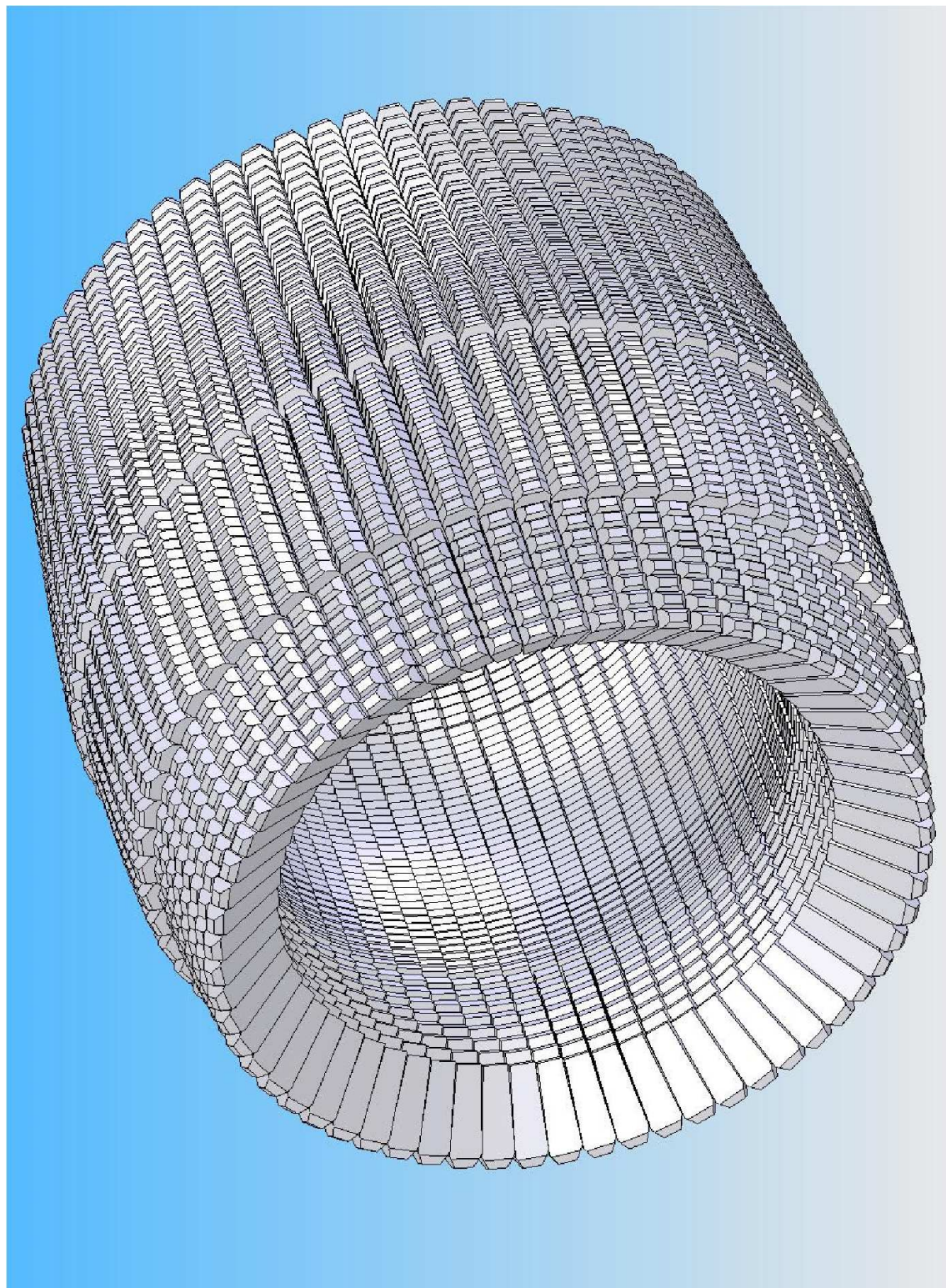
Figure 1.8: Artistic view of the CALIFA calorimeter. The inner radius of the Barrel is approximately 30 cm long.

Chapter 2

Calorimeter and Prototype simulations

T HE first part of this chapter summarizes the simulations of a proposed calorimeter geometry, including the CALIFA crystals, a silicon tracker and a target. The results of the Doppler shift and the broadening of the reconstructed energy resolution were studied for different energies in the Source Reference Frame (SRF). The observables resulting from the simulation (energy resolution, efficiency, multiplicity, etc.) were analyzed for different crystal energy resolution values, as well as for a 'perfect' crystal, in order to evaluate the geometrical effects on the energy resolution.

The second part of the chapter deals with the simulations of a small-scale prototype known as ProtoZero, which incorporates a reduced set of CALIFA crystals. The aim was to get an idea of the real calorimeter response under different beam conditions. Two different prototype configurations were studied: in the first one, fifteen crystals were used, irradiated with gammas at 1, 2, 4, 7 and 10 MeV and in the second one, four crystals were used, irradiated with protons at 90, 120, 180 and 220 MeV, to match the experimental setup used for each case.

2.1. Calorimeter implementation

The R^3B Calorimeter design is based on the physics of the reactions under study, and is addressed in [20]. The kinematics of the reaction, given the high velocity of the incident ions and the resulting large Lorentz boost in the emitted gammas, imposes particular constraints on the calorimeter geometry. The energy of the emitted gammas is increased when measured at lower polar angles due to the Lorentz boost. The Lorentz transformation also peaks the angular gamma distribution in the forward direction. Finally, the reconstruction of the energy in the SRF requires a good polar angle resolution, which is different for different angles.

As was mentioned in the previous chapter, the calorimeter design is based on long (finger-like) crystals, each of which points to the target covering a polar

angle region compatible with the polar angle resolution imposed by the reaction kinematics. The crystal lengths are dependent on the polar angle and were chosen so that most of the energy of the emitted gammas and protons might be deposited inside their crystal bulk.

The intent of this simulation was to determine the effects of the Doppler shift on the broadening of the energy reconstruction for our particular geometry. There is no considered 'background gamma source' to obscure the Doppler effects and complicate the comparison between different alternative solutions. More complex simulations are needed to determine the effects of background sources, to study the reconstruction algorithms, the reconstruction capabilities for high multiplicity events, etc.

2.1.1. R3BSim description

The CALIFA simulation was performed using the R3BSim [21] package, which has been developed to describe the experimental devices that will be used in the R^3B experiment. This program is based on GEANT4 [22] and ROOT [23]. The program is written in C++ code and the ROOT libraries are included, allowing a fully integrated simulation and data analysis framework.

The program contains a gamma generator that includes a realistic interaction vertex (beam emittance + target interaction) and the Lorentz transformation for boosting gamma energies. It also features a Gaussian-like beam profile that follows an isotropic pattern along the target length.

R3BSim includes a multihit data structure for event-loop analysis. Its modular geometry allows the integration of new detectors and the selection of different target structures and parameters (paraffin, LiH, etc). Different materials can be used to describe the active crystals and other elements in the setup.

The energy deposited in each crystal is actually measured with a certain resolution, which was implemented in our simulation, for each event, with an energy-dependent Gaussian smearing in the detected energy.

2.1.2. R3BSim calorimeter features

The R3BSim package contains the calorimeter geometry. Each crystal is individually defined with a the separation between crystals of 1 mm (half a mm reserved for wrapping).

A paraffin target (110 μm thick, 1 cm radius) was implemented, with the silicon tracker detector and a layer (200 μm thick) of carbon fibre constituting the interposed materials. Figure 2.1 shows a drawing of the inner part of the calorimeter, where the circular target and the two hexagonal silicon trackers can
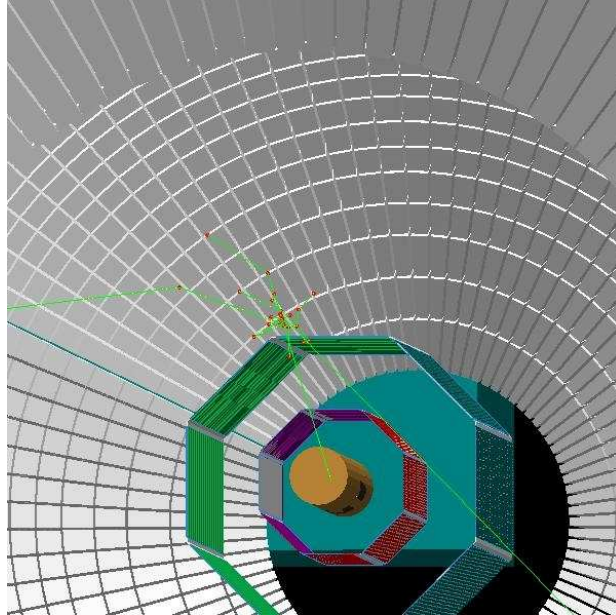
Figure 2.1: Paraffin target and silicon tracker as represented in the graphical visualization of the simulation code.

be seen. The green lines represent the neutral particle trajectories (gammas in this case) and the red dots correspond to the positions were the gammas experienced some kind of interaction.

In order to discuss about the finite energy resolution effect, smearing factors of 3%, 4% and 5% at 1 MeV (FWHM) scaling as $1/\sqrt{E}$ (equivalent to 3.7%, 4.9% and 6.1% (FWHM) at 662 keV usually taken as reference) were used, in addition to no smearing at all (that in the following is labeled as 'perfect' resolution).

Gammas of selected energies in the range of interest (0.5, 1, 2, 5 and 10 MeV, in SRF) were used as input for a beam energy of 700 AMeV, corresponding to a relativistic velocity of $\beta \sim 0.82$. The selected gamma energies were Lorentz boosted according to the velocity of the incident particle. The FWHM of the Gaussian beam profile was 10 mm.

The results presented here were obtained using CsI(Tl) as the scintillator material and, at this preliminary step, neither wrapping tape nor any support structure were considered. Figure 2.2 shows three different views of the CALIFA Calorimeter. This calorimeter version (v4.0b) was produced in cooperation with IPN[1]. It features a Barrel covering the large polar angles and an Endcap for the forward polar angles where the largest gamma energies are expected. Table 2.1 shows the main parameters of this calorimeter design.

---

[1]Institut de Physique Nucleaire d'Orsay.
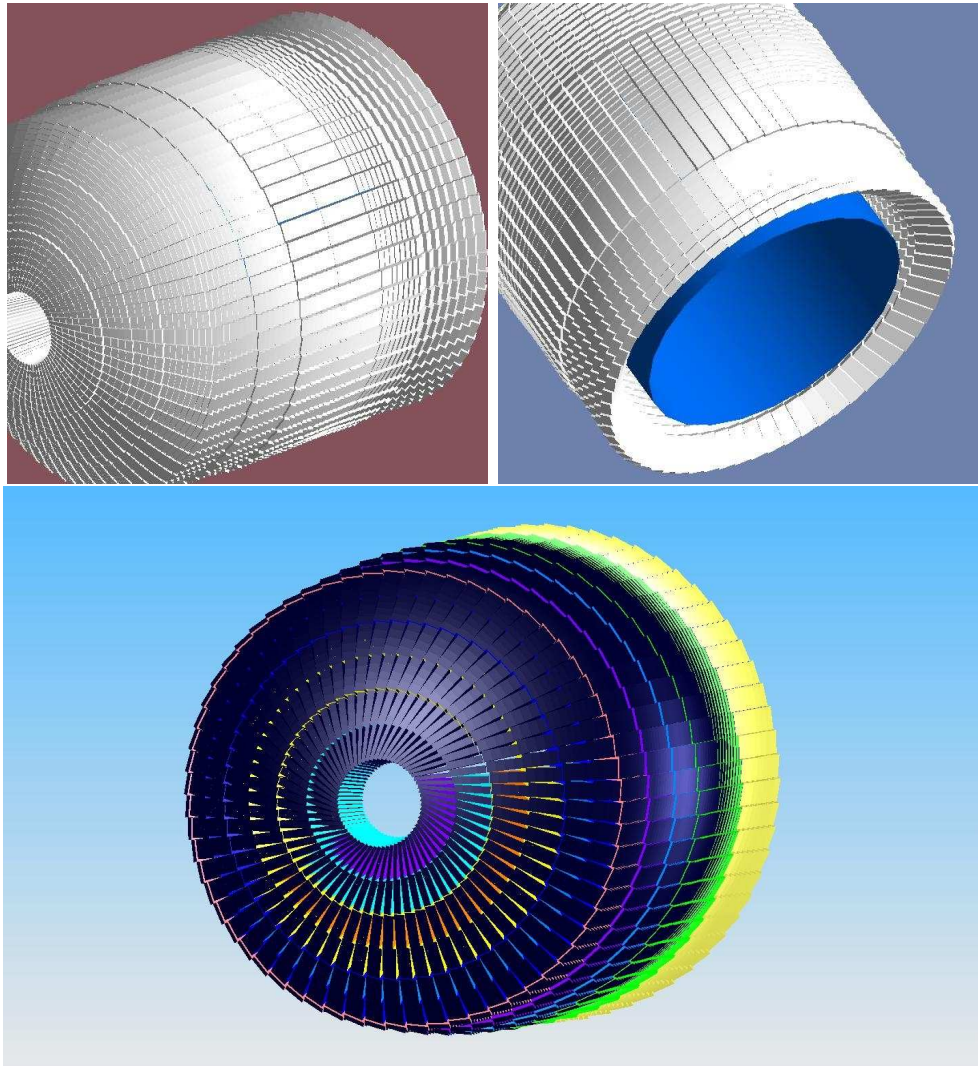
Figure 2.2: Three different views of the CALIFA Calorimeter

	Barrel	Endcap	Total
Number of crystals	3584	1536	5120
Crystal types	5	24	29
Covered polar angle (deg)	40 - 130	7-40	7-130

Table 2.1: Main design parameters of this calorimeter version.

In order to check the effect of crystal length on efficiency and resolution, three different crystal sets, labeled with *short*, *medium* and *long* crystals, were evaluated in the simulation. They have the same geometry, but different crystal lengths in

each position covering approximately 60%, 70% and 80%, of the full-energy peak efficiency for 5 MeV gammas in the SRF. The *short* types included crystals 9 to 12 cm long in the Barrel region, increasing in length as the polar angle decreases. The *medium* types are 3 cm longer than the *short* ones (11-15 cm), and the *long* types are 3 cm longer than the *medium* ones (14-18 cm).

Such crystal combinations were carefully evaluated in the simulation. The volumes and weights of the crystal bulk for the different 'calorimeter sizes' were reported in [18–20] and are shown in Table 2.2.

Quantity - Type	Short	Medium	Long
Volume BARREL (l)	277.1	352.5	435.5
Weight BARREL (Kg)	1249.9	1589.7	1964.3
Volume ENDCAP (l)	115.4	145.0	174.8
Weight ENDCAP (Kg)	520.2	654.1	787.9
Total volume (l)	392.5	497.5	610.3
Total weight (Kg)	1770.1	2243.8	2752.2

Table 2.2: Volumes and weights of the crystal bulk in the different "calorimeter sizes" (Data taken from [19]).

2.1.3.   Analysis algorithms

The simulation program allow us to choose from among several algorithms in order to determine the polar angle of the incident gammas and calculate the energies in the SRF. An add-back treatment of the signal coming from all or some of the crystals was implemented for calculating the energy deposited in the entire detector.

The results presented in this work are based on one of the simplest possible algorithm, in which the polar angle of the impinging gamma (or proton) is determined by the crystal with largest deposited energy and the energy is calculated from the sum of the energy depositions in all crystals.

More complex algorithms are required to reconstruct the polar angle from a weighted average of the energy deposited in the crystals around the crystal with maximum deposited energy. The total energy is then calculated either from the sum of the energy depositions in all crystals or from the sum of the neighboring crystals.

These algorithms have proven to be useful for studying the energy distribution in the crystals for this particular geometry.

RF γ-ray energy	0.5 MeV	1 MeV	2 MeV	5 MeV	10 MeV
Detection efficiency	90.0%	88.9%	87.7%	87.1%	87.8%
Total absorption eff.	83.1%	80.5%	76.8%	72.3%	65.2%
Crystals multiplicity	2.1	2.7	3.5	5.8	9.3

Table 2.3: Geometry-dependent (algorithm-independent) observables: detection efficiency, total absorption efficiency and crystals multiplicity for the different energies considered in this study.

2.2. Simulation results

Different observables were reconstructed as an outcome of the simulation work. These include the number of crystals with some energy deposited in them, the (laboratory) energy deposited in the calorimeter crystals, the incident polar angle of the emitted gamma, the gamma energy in the SRF, etc.

For any given crystal material characterized by a density and an atomic content, there are a few observables that depend solely on the geometrical properties of the calorimeter design, regardless of the reconstruction algorithm and the crystal resolution:

- the detection efficiency (also known as geometrical efficiency), or the percentage of events depositing part or all their energy in the total crystal volume.

- the total absorption efficiency or full-energy peak efficiency, comprising those gammas depositing their full-energy in the crystals.

- the crystal multiplicity defined as the number of crystals with signals over an energy threshold.

All these observables depend on the gamma energy and provide physical information about the incident gamma interactions. For example, the detection efficiency tells us whether these gammas had at least one interaction or passed through the crystals or in a region not covered by the calorimeter without being detected, while the full-energy peak efficiency indicates if these gammas left their total energy in the crystals. The crystal multiplicity indicates the mean number of crystals fired by the incoming gammas, affecting the add-back algorithms.

The values obtained for these observables are shown in Table 2.3 for the different energies considered in this study.

The detection efficiency is basically defined by the calorimeter geometry. Note that the numerical values for this observable are obtained using an isotropic gamma distribution in the SRF. The values for each energy differ because of the different

polar angle distribution after the Lorentz boost. The losses are due in part to the spacing between crystals, which were not optimized in this preliminary design version.

The ratio of gammas detected with full-energy deposition (that is, the total absorption efficiency or full-energy peak efficiency) also depends on the material selected. For materials with either higher density or higher effective Z, a larger full-energy peak efficiency is expected.

2.2.1. Geometrical efficiency

The geometrical efficiency, defined as the fraction of gammas depositing part or all their energy in active volume of the calorimeter, was higher than 85% for the *long* crystals, higher than 82% for *medium* crystals and higher than 77% for *short* crystals, for all the energies in the SRF. A more detailed discussion will be provided in Section 2.3.2. The Barrel accounts for more than 30% and the Endcap for around 47% of the geometrical efficiency (Figure 2.3). The simulation values obtained for the geometrical efficiency meet the CALIFA specifications.
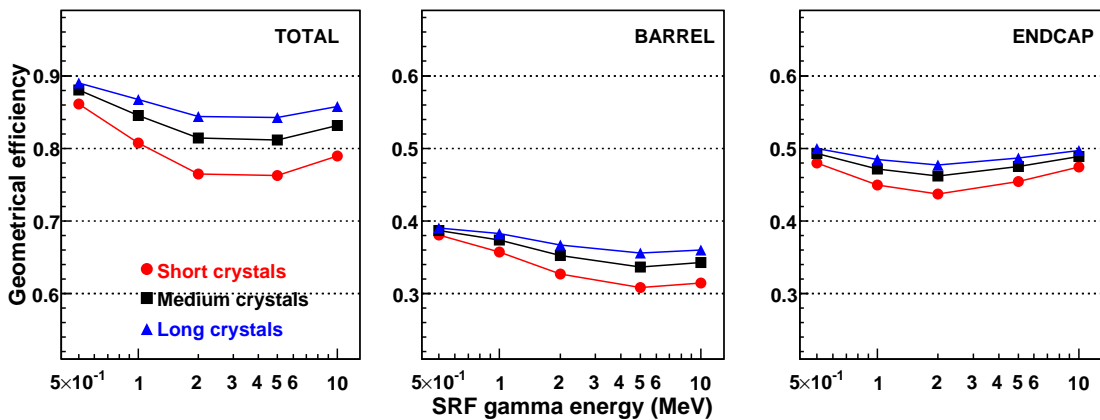
Figure 2.3: Geometrical efficiency vs. energy for a) the whole calorimeter b) Barrel c) Endcap

Note that the efficiency plotted in Figure 2.3 is not normalized to the gammas emitted in the polar angle covered by the Barrel and the Endcap, but for the total (4π) gammas emitted. The polar region covered by each section are, respectively, 41% for the Barrel and 54% for the Endcap. Therefore, to normalize the data to the gammas emitted in the polar region covered by each section, the geometrical and full-energy peak efficiencies must be multiplied by the factors 2.46 (Barrel) and 1.85 (Endcap). With this correction, the geometrical efficiency would reach values of 80-90% for each part.

2.2.2.   Full-energy peak efficiency

The full-energy peak efficiency used in the reconstruction depends on the energy, on the algorithm and to a lesser extent on the crystal length. This observable is calculated by counting events within 3 sigmas of a Gaussian fit around the peak centroid (99.7% of the events) and dividing them by the total number of emitted gammas. The Gaussian fit around the peak centroid is shown in Figure 2.4 for reconstructed 2 MeV gammas (in the SRF).
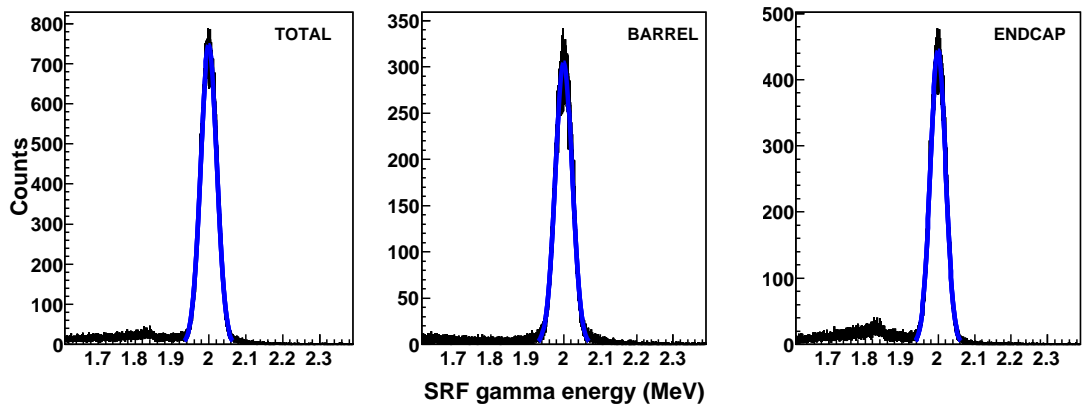
Figure 2.4: Energy spectra for reconstructed 2 MeV gammas (in the SRF) detected by the whole setup (left), the Barrel (middle) and the Endcap (right). In blue is the Gaussian fit, which is used to calculate the full-energy peak efficiency as described in the text.
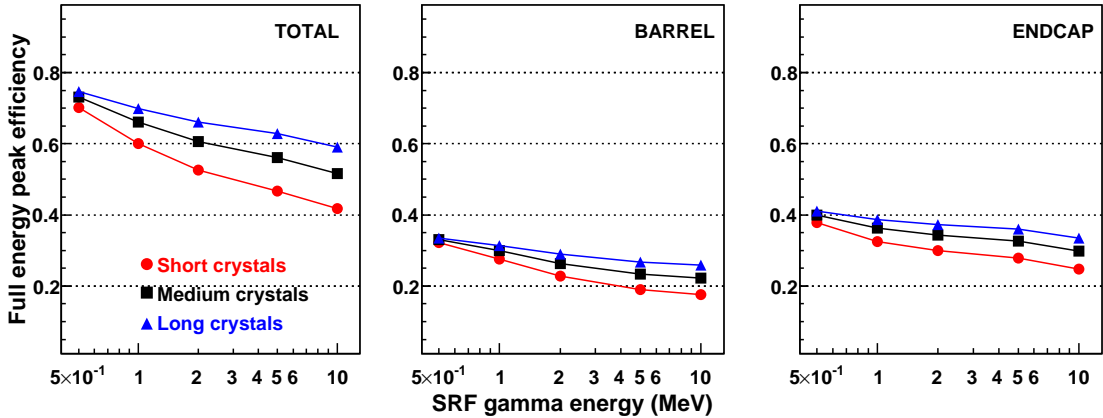
Figure 2.5: Full-energy peak efficiency vs. energy for short, medium and long crystals.

For the simplest algorithm using *medium* crystals, the full-energy peak efficiency

decreased from 70% at low energies to around 50% at high energies (see Figure 2.5). At high energies, the length introduces a variation of ∼14% between *long* (higher full-energy peak eff.) and *short* (lower full-energy peak eff.) crystals. However, this variation disappears at low energies, which is expected due to the limited range of the electromagnetic shower.

2.2.3.   Crystal multiplicity

The crystal multiplicity (mean number of crystals with energy deposition over a threshold) increases with the γ-ray energy, from almost two at 0.5 MeV up to eight crystals at 10 MeV for the Forward Endcap (see Figure 2.6). The multiplicities in the Barrel region are limited to a maximum of four fired crystals (mean values in all cases), since the gammas arriving at the Barrel section have less energy due to the Lorentz boost.
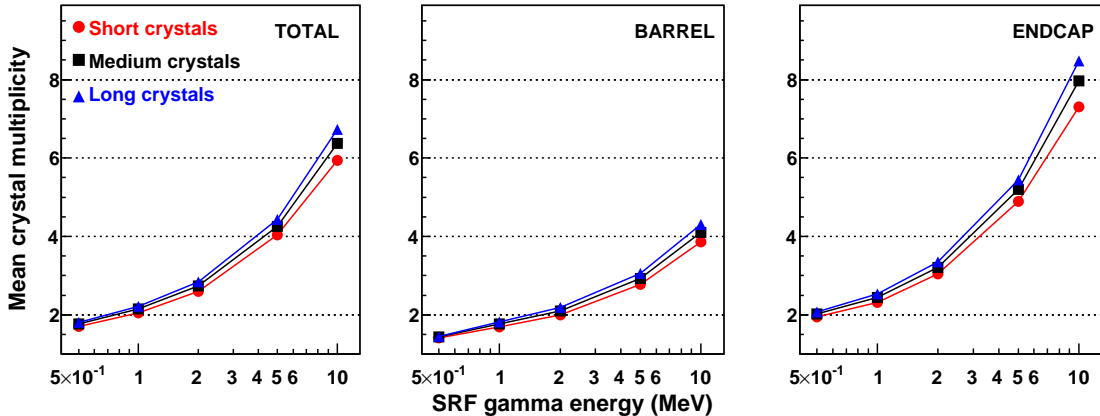
Figure 2.6: Mean crystal multiplicity vs. energy for short, medium and long crystals.

The crystal length has a small influence on the crystal multiplicity as can be seen in the results shown in Figure 2.6.

2.2.4.   Energy resolution

The energy resolution can be calculated from the histogram of the reconstructed energy in the SRF, which is obtained after add-back and Doppler shift correction, according to the procedures described in each algorithm.

As a general trend, the simplest algorithm provided the best overall results for the simulated energies. In this algorithm the gamma energy is obtained from all the crystals in the calorimeter (full add-back), prior to the Lorentz transformation. For a real detector, such an approach is actually difficult to use mainly because of the background and other noise sources, and because the gamma multiplicity could

be larger than the unity in many events.

The energy resolution was found to be quite independent from the analysis algorithm at low energy, but at high energies (above 5 MeV in the SRF of the projectile) only those algorithms that performs an efficient add-back offer a reasonable energy resolution.

The dependence of the $\Delta E^S/E^S$ of the reconstructed energy in SRF on the initial gamma energy using the simplest algorithm is shown in Figure 2.7, for a 5% crystal resolution (squares) and an ideal detection system (circles), made of scintillators with 0% energy resolution ('perfect crystal').
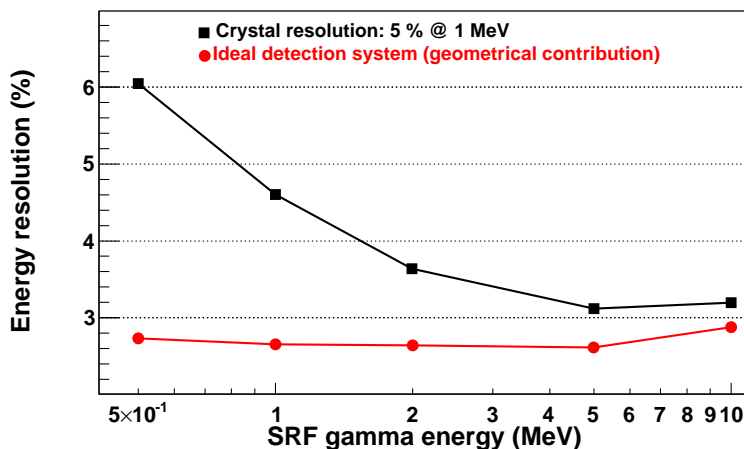
Figure 2.7: Dependence of the reconstructed energy resolution for medium crystals on the energy in the SRF.

The energy resolution obtained by assuming an exact energy determination in each crystal, that is, the contribution to the energy resolution due only to the polar angle uncertainty, was found to be below 3% for all tested energies. For real crystals, energy resolution degradation was observed at low energies, due to the limited energy resolution of individual crystals, and raised again at high energies, where the electromagnetic shower spreads over several crystals.

These findings can be also applied to Figure 2.8, which shows the energy resolution as a function of the crystal length for different crystal energy resolutions (3%, 4%, 5% and perfect resolution). For perfect resolution crystals, the energy resolution is only due to geometrical effects and was below 3% for all tested energies and all crystal types.

The small differences in energy resolution within the crystal length groupings are due to the differences in the way the energy is spread in the crystals. Other effects that could depend on the crystal length (for instance, the possible decrease of the energy resolution with increased crystal length due to optical processes) were
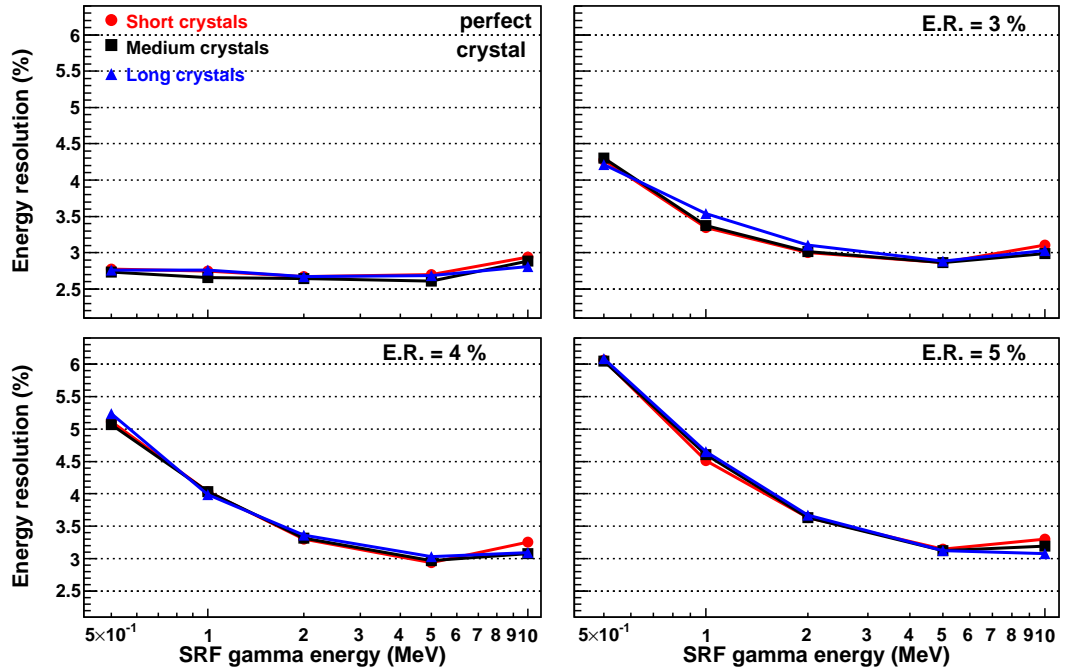
Figure 2.8: Energy resolution for medium, short and long crystals as a function of the energy for 3%, 4%, 5% and perfect resolution.

not included in these simulations.
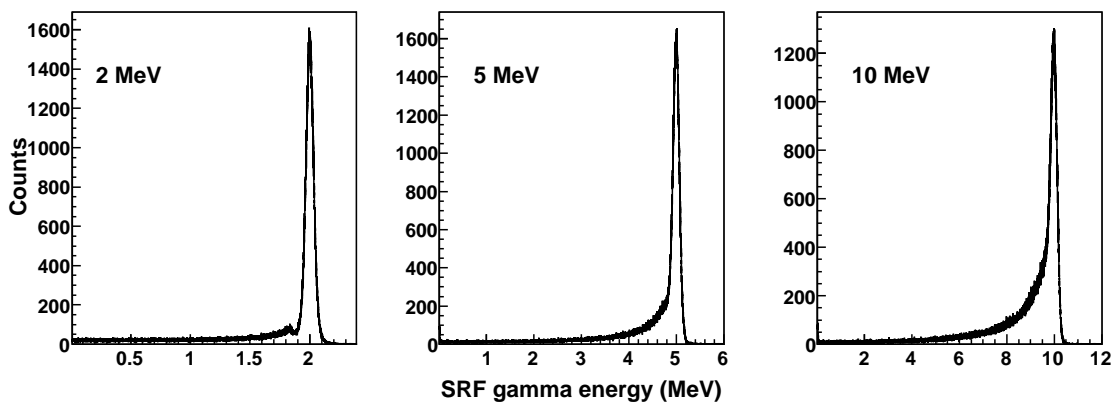
Figure 2.9: Energy corrected by Lorentz boost for 2, 5 and 10 MeV gammas

In Figure 2.9 three different spectra for 2, 5 and 10 MeV gamma energies that were corrected by Lorentz boost are shown as an example.

2.3.   ProtoZero simulation

Besides the CALIFA simulations described in the previous section, other additional simulations were carried out for the ProtoZero prototype, which consists of bi-frustum-shaped crystals (see technical drawins in Section 1.2.3). The aim of this was three-fold: to compare the simulation results with the prototype results, to establish the validity of the simulation and to understand the effects observed in the experiment. The first step involved a simulation of the complete prototype response after irradiating it with proton and gamma beams.

A simulation was performed for a gamma beam, using a configuration consisting of 15 *medium* size CALIFA crystals assembled in a 3x5 array and belonging to the 90° polar angle region. Another simulation using a 4 crystal configuration was carried out for proton beams. Both configurations are shown in Figure 2.10.
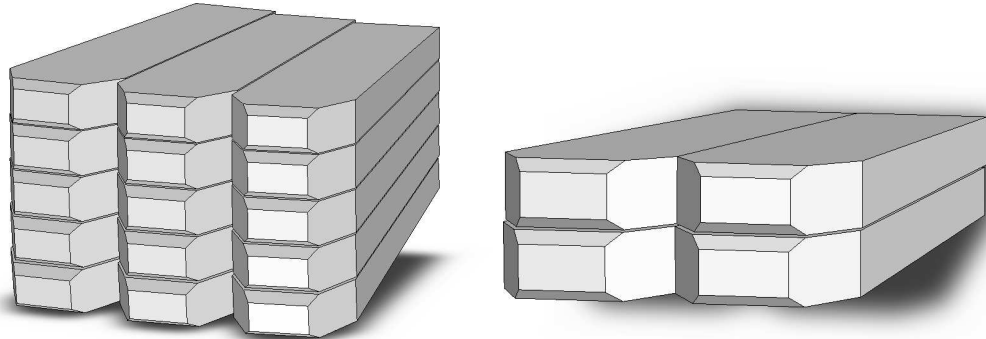
Figure 2.10: Artistic rendering of the ProtoZero simulation setup; in the left side, the configuration used for the high-energy gamma tests and in the right that used for protons.

2.3.1.   Simulation features

The simulation program was adapted to these particular configurations and introduced several changes. For example, the small crystal chamfers, performed in the readout face to fit the APD active area, were eliminated in order to simplify the geometry as can be seen in Figure 2.11. This minor modification influences the way the light is collected (which is not part of this simulation) but not the energy deposition in the crystals.

ProtoZero simulations were performed using CsI crystals with a density of 4.51 g/cm^3 and vacuum as the surrounding medium. The dopant concentration has no influence on the energy deposition and therefore was not taken into account.
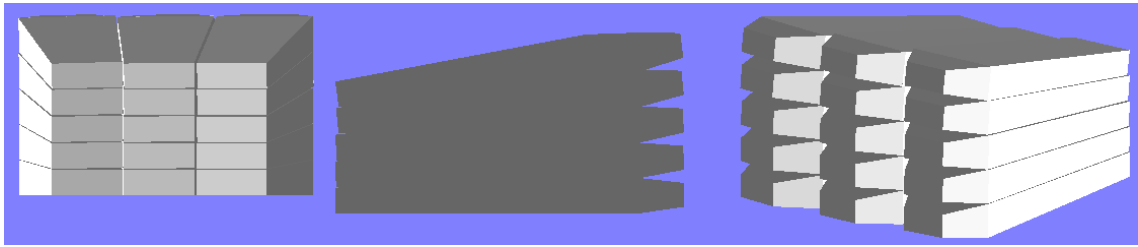
Figure 2.11: Different views of the ProtoZero configuration with 15 crystals as seen in the R3BSim simulation program.

The gamma energies considered in this simulation were 1, 2, 4, 7 and 10 MeV and the proton energies were 90, 120, 180, 220, 260 and 300 MeV, to include some of the energies achieved in each experiment. Simulations for other gamma beam energies achieved at TUD Darmstadt facility were also performed. The results of these are listed in Chapter 4, where they are compared with the experimental results.

The gamma and proton sources were placed 25 cm away from the ProtoZero. The emission was isotropic inside a 1 mm diameter source and directed parallel to the central crystal of the array. Gamma and proton statistics up to 10^6 and $5 \cdot 10^4$ incident particles were considered, respectively.

Several additional materials were included in the proton beam simulation, in order to make it as accurate as possible:

- a 300 μm layer for simulating the crystal wrapping, made by Enhanced Specular Reflector [24] (ESR);

- a 2 *mm* thick silicon sheet for simulating the Double Sided Silicon Strip Detectors (DSSSDs) [25];

- a 5 *mm* thick aluminum box for simulating the ProtoZero Box (see details of the experimental setup in Section 4.3.5).

The silicon and aluminum layers were placed between the proton source and the crystals. The crystal wrapping, silicon sheet and aluminum box were not considered for gammas because the gamma energy losses in these material thicknesses are negligible.

2.3.2. Results for gamma beams

A systematic study of the energy resolution for different gamma energies was performed. We proceeded analogously as in the CALIFA simulation. We also reconstructed some observables in order to compare them with the calorimeter simulations and, as in prior section, the simplest algorithm was used to reconstruct

the incident gamma energies.

Geometrical observables and energy resolution
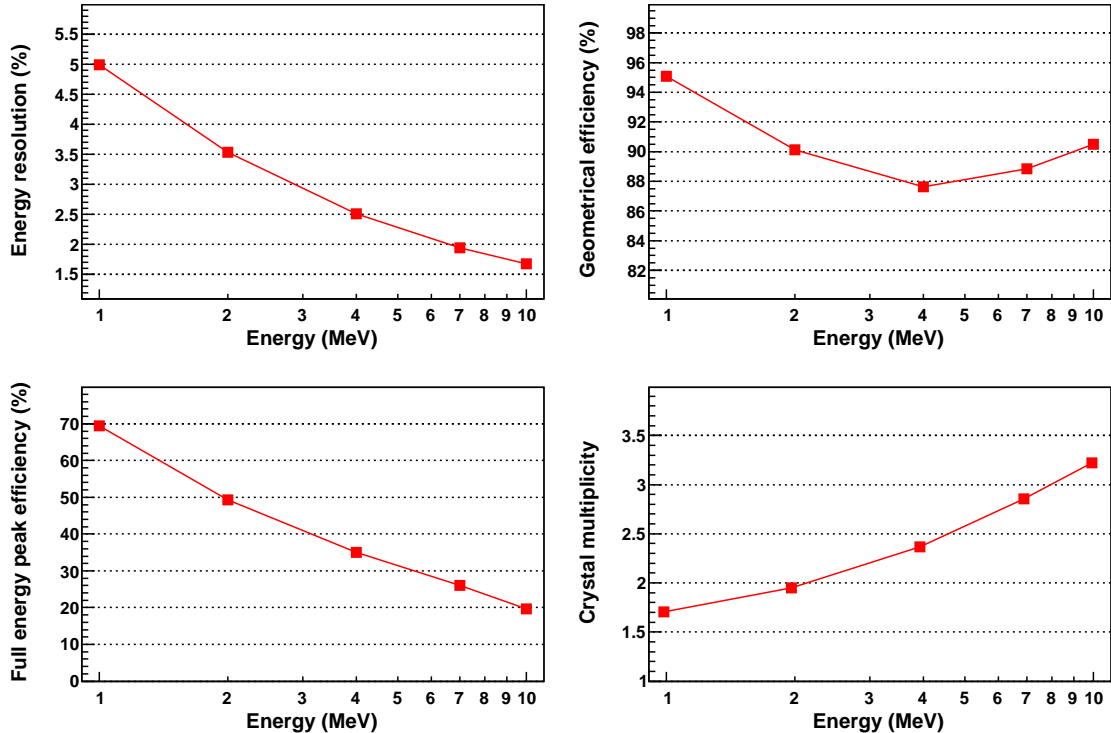
Figure 2.12: Simulation observables vs. incident-gamma energy for the ProtoZero prototype crystals: energy resolution (top-left), geometrical efficiency (top-right), full-energy peak efficiency (bottom-left), crystal multiplicity (bottom-right)

Figure 2.12 shows the efficiencies, energy resolution and multiplicity for several incident gamma energies. The energy resolution decreases proportionally to the square root of the energy, and that is how it was implemented in the simulation. With a 5% resolution at 1 MeV, a resolution below 2% can be obtained for 10 MeV gammas.

A close look at the geometrical efficiency shows a decreasing trend up to 4 MeV and the opposite for higher values. This effect is correlated with the total inter-action cross-section that has a minimum around the same value (see [27], pp. 51-53).

As the energy of the incident gammas increases, the full-energy peak efficiency decreases due to a rise in the number of secondary interactions (Compton scattering and pair production). A higher number of secondary interactions increase the probability of no collecting the total energy of the incident gammas. The counts

that are not under the main peak are not taken into account when calculating this observable. The values obtained for high energies should be higher for a prototype with more crystals and proper add-back method, since the escape probability of the scattered gammas would decrease and the 511 keV photons produced in the pair production would not escape from the ProtoZero.

The multiplicity is higher for high energies due to an increase of both the chance of multiple Compton scattering and the pair production cross section with the energy. This means that more scattered gammas (or 511 keV photons) reach more neighbor crystals, which increases the crystal multiplicity.

Figure 2.13 shows the reconstructed energy spectra for gammas at several energies, taking a 5% energy resolution ($\Delta E^L / E^L$) at 1 MeV as reference. In the spectra observed for gammas with energies above 4 MeV (that is, well above the threshold for the pair production), two additional peaks appear below the reconstructed peak. They correspond to single and double escape peaks of pair production and their intensities are higher for high gamma energies due to an increase in the pair production cross-section.

Energy and multiplicity vs. incident-gamma energy

Our simulation allow us to see in detail where the energy depositions (or hits) have occurred. The top-left panel of Figure 2.14 shows a frontal view of the prototype with the mean energy deposition in keV. The same observable is seen in the top-right panel in percentage values. The bottom panels show the number of hits (left) and the multiplicity (right) for each crystal of this configuration.

These values were obtained using a 1 MeV gamma beam with 10^6 emitted gammas.

As we can see, 74.2% of the incident-gamma energy was deposited in the central crystal, while another 19.8% was collected by the nearest-neighbor crystals, the so-called 'first onion-layer'. The rest of the energy (6.0%) was detected in the six next-to-nearest-neighbor crystals, or the 'second onion-layer'.

These numbers are slightly different for the crystal multiplicity distribution. The central crystal has multiplicity equal to 1, which means that this crystal is hit 100% of the time (all the emitted gammas are entering the prototype through this crystal). The first onion-layer was hit 55% of the time and the second onion-layer is hit only 15% of the time.

These observables vary with the initial gamma energy as can be seen in Tables 2.4 and 2.5.

We can conclude that the higher the gamma energy, the greater the percentage of energy deposited in the central crystal. As for the multiplicity distribution, the central crystal is hit 100% of the time and the percentage of hits in the first and
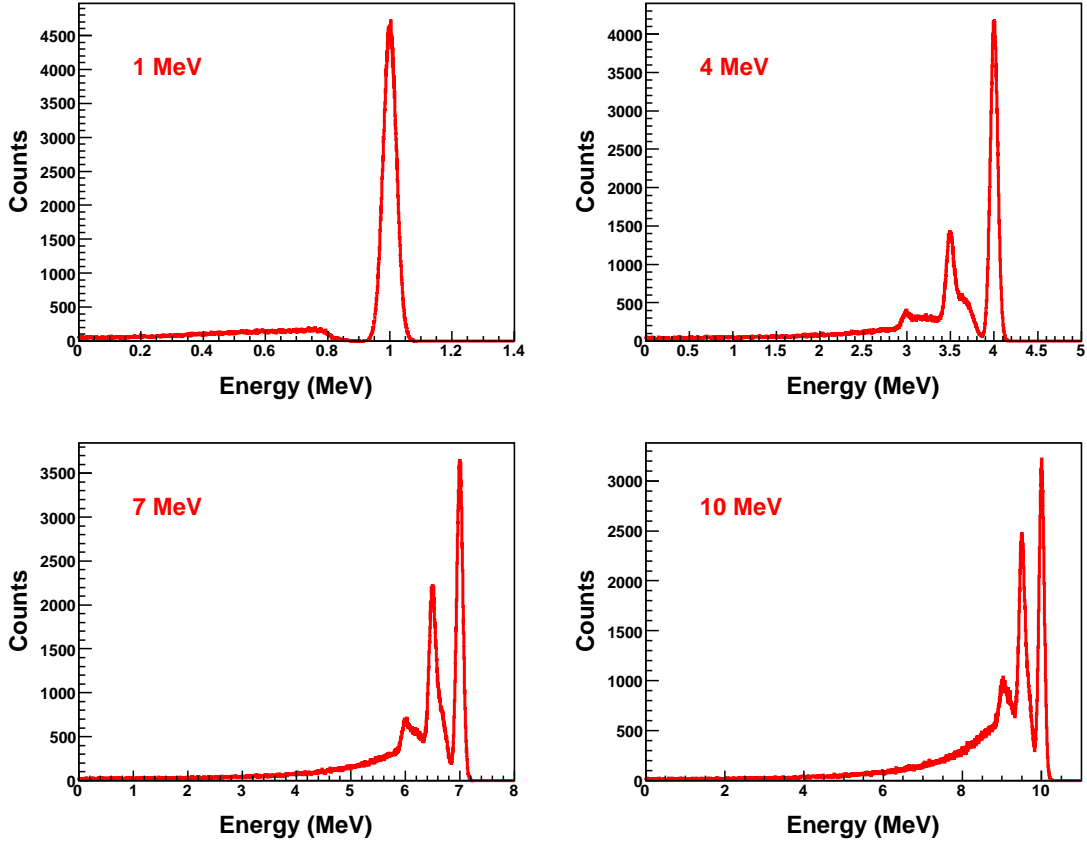
Figure 2.13: ProtoZero reconstructed energy spectra for gammas emitted at different energies using 5% resolution at 1 MeV.

γ-ray energy	1 MeV	2 MeV	4 MeV	7 MeV	10 MeV
Central Crystal	74.2%	77.6%	82.6%	86.4%	87.6%
1st. layer	19.8%	17.1%	13.4%	10.6%	9.8%
2nd. layer	6.0%	5.3%	4.0%	3.0%	2.6%

Table 2.4: Energy deposition distribution in percentage for several incident gamma energies

second onion-layers increases as the energy increases.

This effect produces an increase in the total crystal multiplicity and can be explained by the higher cross section of the Compton process for gammas with high energies. The 10 MeV gammas are an exception: the total multiplicity decreases because the EM (electro-magnetic) shower is developed at the end of the crystals, giving scattered gammas the possibility of escaping from the ProtoZero before
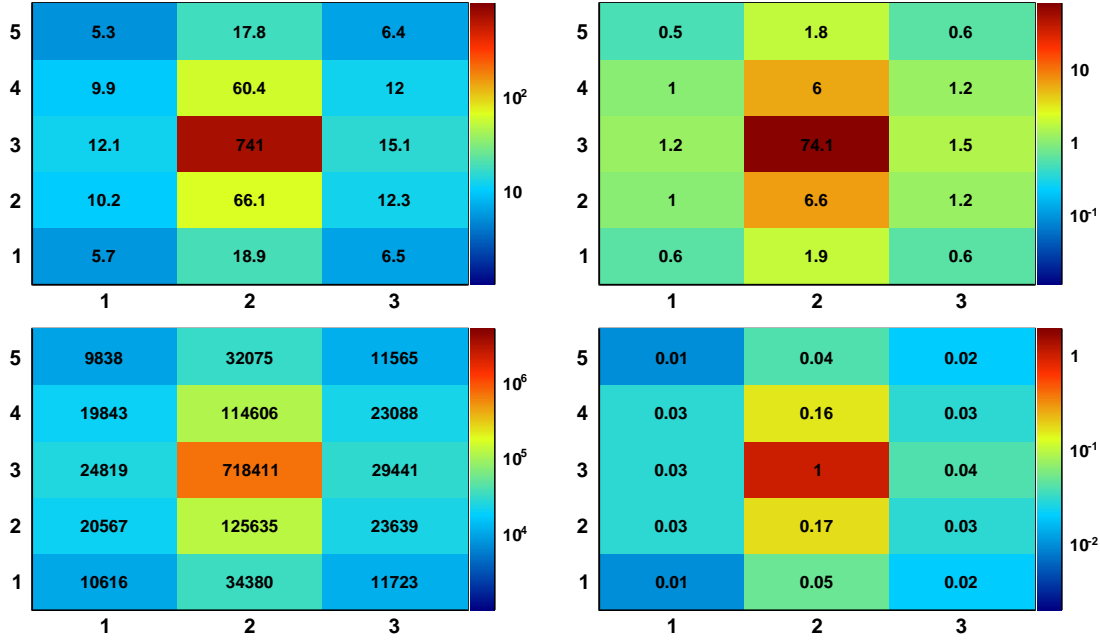
Figure 2.14: The mean energy deposition in keV (top-left) and in percentage values (top-right), number of hits (bottom-left) and multiplicity (bottom-right) for each crystal of this configuration, using 1 MeV gammas.

γ-ray energy	1 MeV	2 MeV	4 MeV	7 MeV	10 MeV
Central crystal	1.00	1.00	1.00	1.00	1.00
1st. onion-layer	0.53	0.71	1.03	1.40	1.69
2nd. onion-layer	0.15	0.22	0.32	0.43	0.53
Total	1.68	1.93	2.34	3.96	3.22

Table 2.5: Crystal multiplicity distribution for several incident gamma energies

hitting the neighbor crystals.

2.3.3. Results for proton beams

Geometrical observables and energy resolution

Let us now focus on the results for proton beams. For this simulation, a four-crystal prototype configuration was irradiated with protons at 90, 120, 180 and 220 MeV. This energy range was used to match that achieved at the proton test beam. The experimental results are presented in Chapter 4.

We performed simulations of two proton beams hitting two different points

in the setup. The first point was at the center of one of the four crystals (Case A), the second point was close to the boundary between two crystals (Case B). Both points are shown in Figure 2.15. By comparing these two cases, we were able to see the effect of protons hitting near the boundary between two crystals.
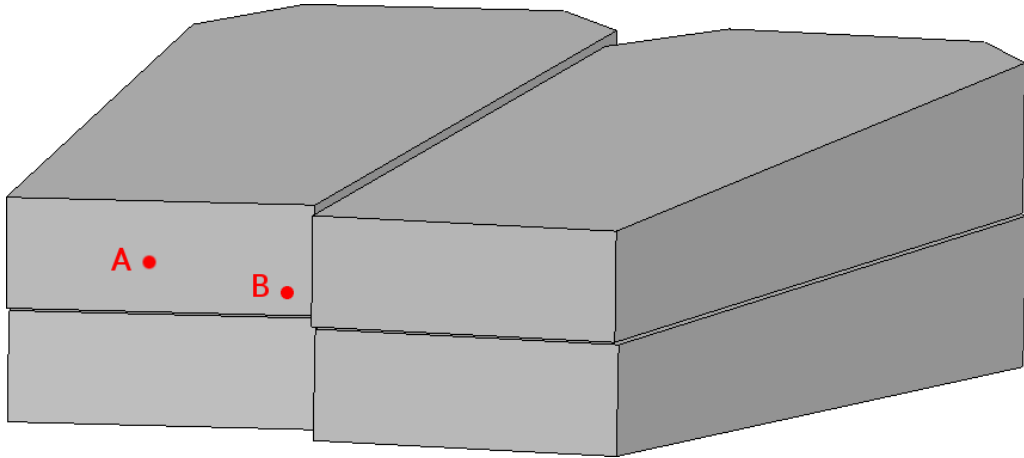
Figure 2.15: A schematic drawing of the four crystals setup including the two proton beam impinging positions defined in the text.

Case A involved proton beams of energies varying from 90 to 300 MeV. The reconstructed energy spectra are shown in Figure 2.16. For energies below 220 MeV, the reconstructed peak becomes more asymmetric as the energy increases. This asymmetry is due to energy losses in the wrapping material, which become very important at high proton energies, as we will see later in this chapter.

At energies higher than 220 MeV, protons pass through the setup and only a portion of their energy is deposited inside the prototype. Protons at 300 MeV leave less energy than those at 260 MeV, since the energy loss per unit length is lower as the proton energy increases, as predicted by the Bethe-Bloch formula (see [27], pp. 33-34).

The same spectra are shown in Fig. 2.17 for protons hitting near the boundary between two crystals. In this case, a clear secondary peak appears below the total energy peak, due to energy losses in the crystal wrapping. The size of this secondary peak becomes comparable to the total energy peak for energies above 180 MeV, making the distinction between them almost impossible.

The origin of this energy loss was studied for incident protons with an energy of 180 MeV. Figure 2.18 shows the energy spectrum obtained for these protons using different crystal wrapping thicknesses.

Since the (ESR [24]) commercial wrapping for the crystals has a thickness of 65 μm, we considered values between 0 (vacuum) and four times 65 μm. Note that for
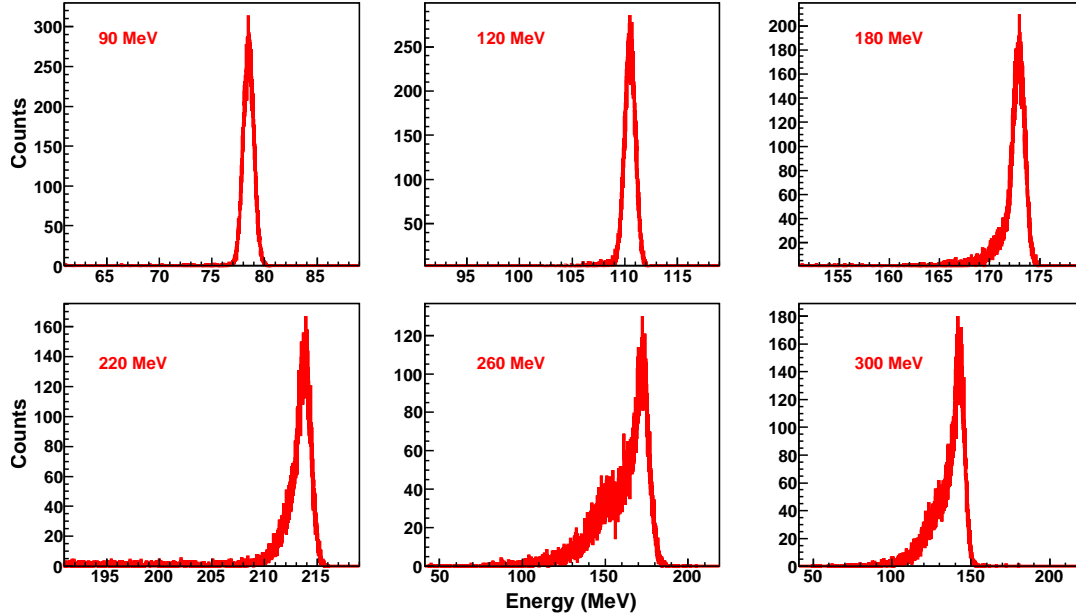
Figure 2.16: Spectra of the reconstructed energy for initial energies varying from 90 to 300 MeV in Case A, when protons hit the center of a ProtoZero crystal. An energy resolution of 7.5% FWHM at 1 MeV was used as smearing factor.

a single layer of this material per crystal, the total thickness between two crystals would be 130 μm. A double layer would increase this value to 260 μm.

Figure 2.18 indicates that the energy resolution was found to be around 1% FWHM for wrapping thicknesses up to 130 μm, a value that fulfills the initial CALIFA requirements. However, a double wrapping layer causes the secondary peak to appear and degrades the energy resolution.

Using the relative peak efficiency[2], we can estimate the percentage of protons that are lost due to energy losses in the wrapping material. The obtained values are depicted in Figure 2.18.

Figure 2.19 shows the energy resolution, the detection efficiency, the full energy peak efficiency, and crystal multiplicity under proton beam irradiation for the prototype configuration used in Cases A and B.

The energy resolution (top-left panel) is better in Case B than in Case A, because the energy resolution in Case B was obtained after fitting the resulting spectra to a double Gaussian function. This can be seen in Figure 2.17, where the right peak corresponds to the reconstructed proton energy. These peaks are wider

---

[2]Number of counts under each peak by counting entries within 1.8 sigmas of a Gaussian fit around the peak centroid and dividing them by the counts under the peak without wrapping taken as reference.
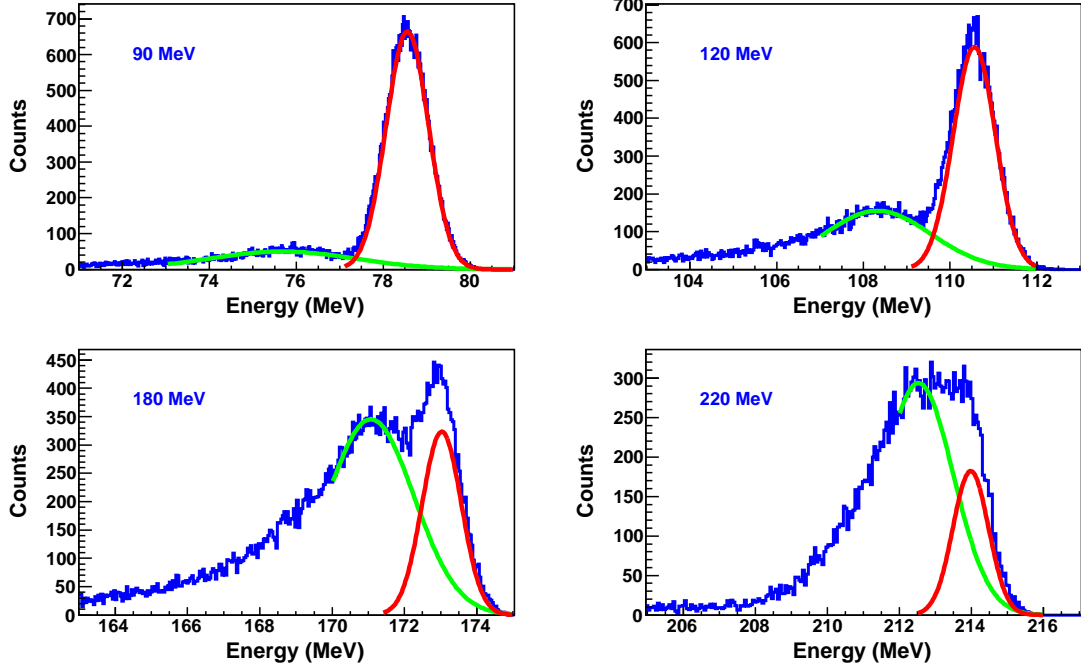
Figure 2.17: Spectra of the reconstructed energy for initial energies varying from 90 to 220 MeV in Case B, when protons hit near the boundary between crystals. An energy resolution of 7.5% FWHM at 1 MeV was used as smearing factor.
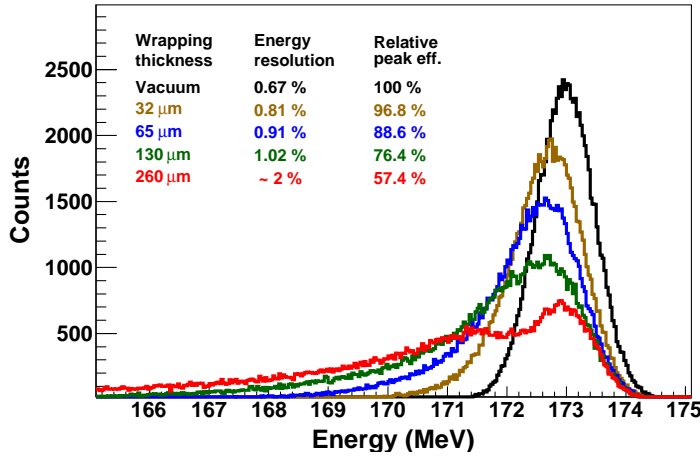
Figure 2.18: The ProtoZero reconstructed energy spectrum of a 180 MeV proton beam for crystals with wrapping thicknesses varying from 0 to 260 μm.

for Case A (indicating worse energy resolution) (see Figure 2.16) because the minor contribution of energy losses in the crystal wrapping cannot be disentangled from the reconstructed peak.
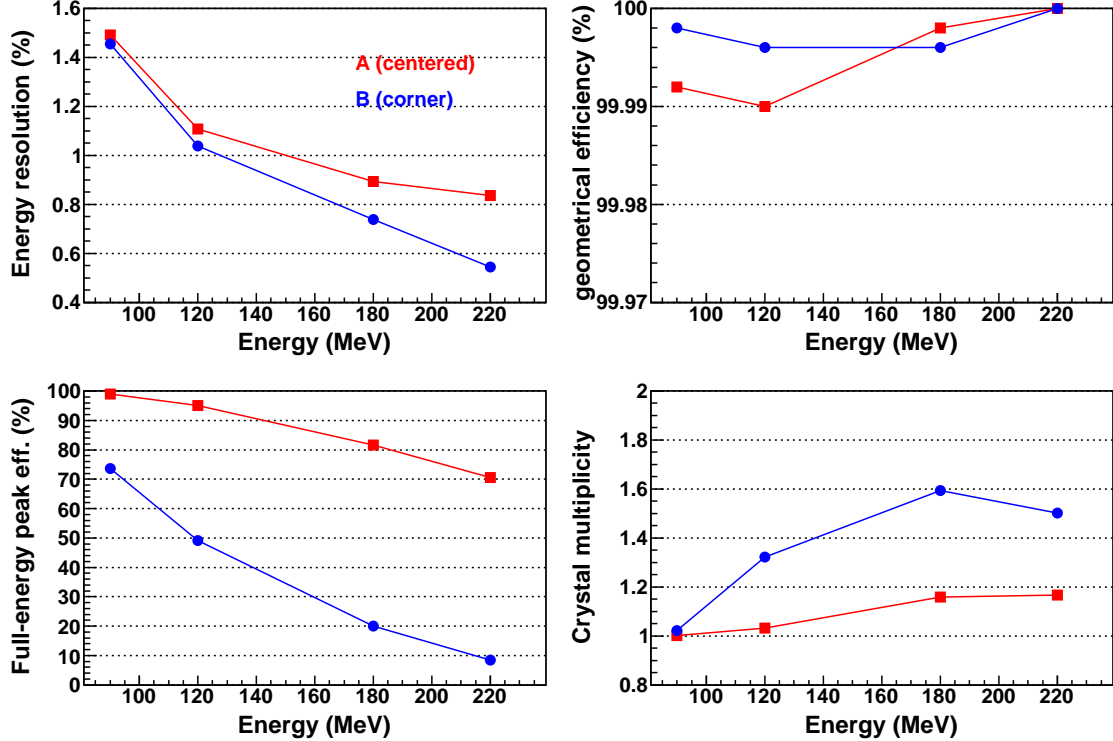
Figure 2.19: Dependence of the simulated observables in ProtoZero with the incident proton energy for Case A (red squares) and Case B (blue circles): energy resolution (top-left), geometrical efficiency (top-right), full-energy peak efficiency (bottom-left) and the crystal multiplicity (bottom-right).

In the entire energy range studied, geometrical efficiencies (Fig. 2.19 top-right panel) were higher than 99.99% in both cases, indicating that only a negligible part of the incident protons passed through the ProtoZero volume without experiencing any interaction in the crystals.

Full-energy peak efficiency (bottom-left panel) decreased as the energy increased, due to a rise in the energy losses. In Case B, the full-energy peak efficiency dropped drastically compared to Case A because the counts that are not in the main peak (see Figure 2.17) do not contribute to this observable. Note that the method here used to define the full-energy peak efficiency is quite restrictive.

In both cases, crystal multiplicity (bottom-right panel) increased as the energy increased, up to 180 MeV. For Case B this increment was more significant, since protons hitting near the boundary between crystals have a higher probability of reaching surrounding crystals. For protons with an energy of 220 MeV, the highest energy loss happens almost at the end of the crystal, and therefore the possibility of the protons escaping before hitting neighbor crystals is higher. The outcome is a lower multiplicity for this energy.

It should be pointed out that a multiplicity of one, means that only a single crystal was fired. However, if we look at the full-energy peak efficiency at 90 MeV (bottom-left panel), all the protons left their total energy inside the same crystal for Case A, but this happened for only 75% of the protons in Case B. Differences are accounted for energy losses in the crystal wrapping, and can be corroborated in Figure 2.17 (top-left).

ProtoZero energy calibration

In Figure 2.16, the peak centroid of the reconstructed proton energies reflects the energy losses in the interposed materials between the crystals and the proton source. According to the Bethe-Bloch formula [26], which allows us to calculate the energy losses in the interposed materials, the proton energy losses in the silicon sheet and the aluminum box are higher for lower energies. It means that protons with a real energy of 90 MeV, for example, were measured by the ProtoZero with a mean energy of 84 MeV, while protons with a real energy of 180 MeV were measured with a mean energy of 173 MeV.

In a real experiment, the proton energies are unknown and the detected proton energies must be corrected. We can use the simulation to calculate the calibration curve in order to correct the detected energies, allowing us to determine the real energy of the incident protons.

Figure 2.20 represents the detected energies in the ProtoZero vs. the real energy of the incident protons.

$$E_{meas} = E_p - 395.9/E_p \ln(0.15E_p)$$
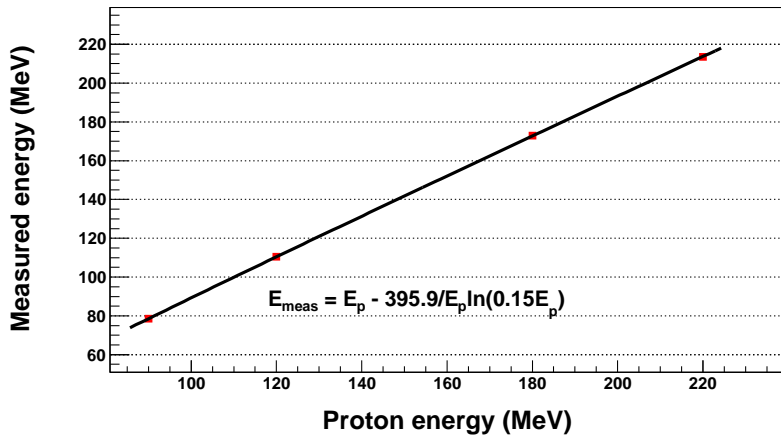
Figure 2.20: Energy calibration curve for ProtoZero under proton beam irradiation in the energy range between 90 and 220 MeV.

For this proton energy range (from 90 to 220 MeV), a simplification of the Bethe-

Bloch formula can be applied

$$\frac{\delta E}{\delta x} = -\frac{A}{\beta^2}ln(B\beta^2) \qquad (2.1)$$

where A and B are two parameters that depend on the material properties and $\beta = v/c$ is the relativistic velocity of the incident protons. The experimental values shown in Figure 2.20 were fitted to this expression and the values obtained for A and B are shown in the same figure.

Chapter conclusions

In this chapter, three different crystal lengths (*short*, *medium* and *long*) were introduced into the simulation code for this calorimeter geometry, in order to study the variations in efficiency and energy resolution. The geometrical contribution to the energy resolution was found to be below 3% for all tested energies in the Source Reference Frame (SRF). The energy resolution was quite independent of the crystal size. The geometrical efficiency at 700 AMeV was above 85% for the *long* crystals, above 82% for *medium* crystals and above 77% for *short* crystals. The Barrel covers more than 30% and the Endcap covers approximately 47% of the geometrical efficiency. The simulation values obtained for the geometrical efficiency meet the requirements described in the CALIFA specifications. The full-energy peak efficiency for *medium* size crystals decreased from 70% at low energies to around 50% at high energies (10 MeV in SRF). The crystal multiplicity (mean number of crystals with energy deposition over a threshold) increases with the γ-ray energy, from almost two at 0.5 MeV up to eight crystals at 10 MeV for the Forward Endcap. The multiplicities in the Barrel region are limited to a maximum of four fired crystals (mean values in all cases), since the gammas arriving at the Barrel section have less energy due to the Lorentz boost.

This section included a detailed comparison between of values obtained after the prototype and calorimeter simulations. The detector and full-energy peak efficiencies for gammas at high energies were lower than those of the calorimeter. This result confirms that they could be higher for a prototype with a higher number of crystals, since the escape probability of the scattered gamma decreases as the number of crystals increases. The mean multiplicity was between 1.7 and 3.3 in the studied energy range, and was in total agreement with the values obtained in the calorimeter simulation.

In the simulations using protons as impinging particles, it was demonstrated that the appearance of a secondary peak in the energy spectrum for protons hitting near the boundary between crystals was due to energy losses in the crystal wrapping. The simulation showed that for wrapping thickness up to a 130 μm, the energy resolution was around 1%, a value that fulfills the CALIFA energy resolution requirement for high-energy light-charged particles.

Chapter 3

Characterization of CsI(Tl) crystals and photosensors

THIS chapter describes the motivation behind the use of CsI(Tl) crystals for at least part of the CALIFA calorimeter. Studies performed with several samples of CsI(Tl) crystals coupled to avalanche photodiodes and to photomultipliers are discussed here.

The first part of this chapter provides an explanation of the scintillation principles and the justification of the use of CsI(Tl) as the optimal crystal for our applications (Section 3.1). This is followed by a description of the photodetectors used with the CsI(Tl) crystals, and the characterization of avalanche photodiodes in particular (Section 3.2) follows.

The results of the energy resolution study for crystals of lengths varying from 1 to 10 cm and with a 1 cm^2 square section are shown, with attention to different optimization parameters, such as crystal wrapping, the optical coupling to the avalanche photodiode and the electronic chain (Section 3.3). Finally, in Section 3.4, the details of the tests performed with bi-frustum shaped crystals are given. These crystals were sized according to the Conceptual Design described in Section 1.2.3.

3.1. Scintillation principles

Nuclear radiation absorbed by certain dielectric materials produces light twinkles called scintillations. A scintillator is a material able to convert ionizing radiation energy losses into light pulses. This can apply to X- or gamma-rays and charged particles with an energy range from several keV to hundreds of MeV or beyond. Scintillation is the method most commonly used for detecting particles and performing spectroscopy in a wide radiation spectrum.

An ideal scintillator should convert the energy of the incoming particles into light with the highest possible efficiency. The light produced by the incident radiation inside the crystal should be proportional to the deposited energy in the widest possible energy range. To allow sufficient light collection, the bulk material should be transparent to its own wavelength emission [27]. Moreover the crystal

bulk should be easily machinable. It is difficult to find a single material that fulfills all these properties, and the final choice must necessarily involve a bit of compromise.

In recent years, CsI(Tl) crystals have been widely used in a number of experiments, such as that of Babar [28], and Belle [29], and with different photosensors: PMTs, PIN diodes and APDs (see [30] and [31] and references therein). Large CsI(Tl) crystals are relatively cheap to make, easy to handle, and only slightly hygroscopic. Their density is relatively high (4.51 g/cm^3) and they produce a high light yield ($\sim$60000 photons/MeV) [30]. On the other hand, their long scintillation decay time of few μm require long integration times at the shaper amplifiers (see Section 3.3.3). According to Ref. [32], the intrinsic energy resolution of CsI(Tl) crystals is around 3.8% at 662 keV, which establishes a lower limit well suited to our purpose.

3.1.1. CsI(Tl) emission spectrum

Each crystal has a specific characteristic emission spectrum. The CsI(Tl) gamma-ray excited emission spectrum at room temperature was found to has two primary decay components with decay time constants of $\tau_1 = 679\pm10$ ns (63.7%) and $\tau_2 = 3.34\pm0.14$ μs (36.1%), and main emission bands at about 400 and 560 nm. The CsI(Tl) scintillation yield was observed to be only slightly temperature dependent between -30 and +50 °C, peaking at about -30 °C (about 6% above the room temperature yield) and monotonically decreasing above and below this temperature [33].

The CsI(Tl) emission spectrum depends on the thallium concentration used as dopant (see Ref. [34] and [35]). The shape of this spectrum depends also on the nature of the incident particles producing the scintillation in the crystal (gammas, alphas, betas, protons, etc.). For the small samples used in this work, the thallium concentration was around 0.2 mol% which produces the emission spectrum seen in Figure 3.1 (source: Saint Gobain Crystals [36]).

This emission spectrum has a significant yield at longer wavelengths (maximum yield at 550 nm) compared to the standard NaI(Tl) scintillation crystals. Since its spectral response covers this wavelength region, this crystal is ideal for coupling with silicon photodiodes, as we will see in the next section.

3.2. Photosensors

This section contains the description of the photodetectors used with CsI(Tl) crystals. It also includes a detailed description of the avalanche photodiodes, a comparison between different models and the results of the tests performed to ascertain their optimal working point.

Photomultiplier tubes (PMTs) and photodiodes (PDs) are the most widely used devices for detecting scintillation light. PMTs are vacuum tubes that use
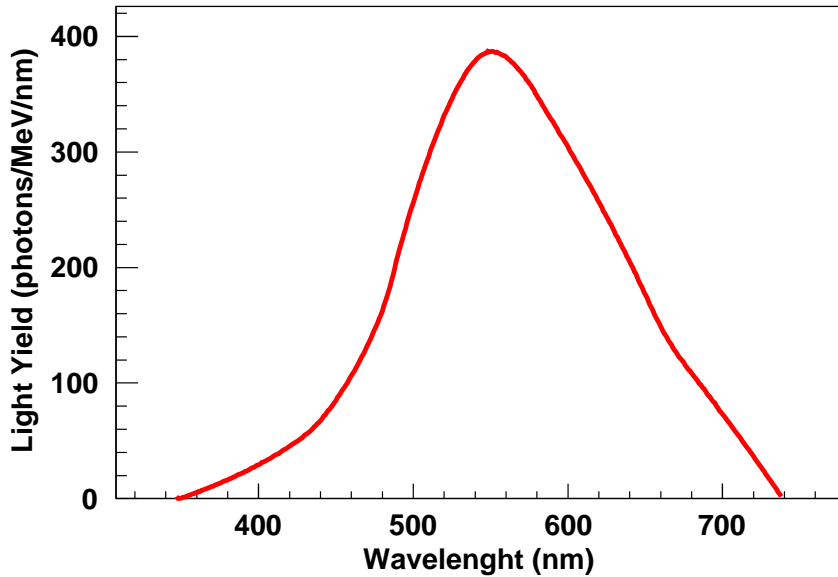
Figure 3.1: Estimated CsI(Tl) emission spectrum for the small samples used in this work (thallium concentration around 0.2 mol%).

the electron secondary emission effect to multiply the number of photoelectrons produced at the photocathode[1]. Not all the photons impinging the PMT window will produce an electron.

Quantum efficiency (QE) is a quantity defined as the percentage of photons hitting the entrance window that will cause an electron to be accelerated to the first dynode. The quantum efficiency of a PMT depends on the incident light wavelength; its maximum value is around 40% for the better ones. In the amplification process, a single photoelectron produces three or four secondary electrons per dynode. Eventually a high gain typically around 10^6 is obtained.

These extremely sensitive photodetectors can respond to very low illumination conditions while maintaining an acceptable noise level [37, 38]. Moreover, PMTs usually do not need further anode signal amplification, producing an excellent signal to noise ratio. However, PMTs have a few handicaps: they are very sensitive to magnetic fields and expensive compared to solid state electronics because the complicated mechanical structure inside the vacuum container is mostly hand-made [39].

PDs are made of a thin silicon layer which, upon illumination, creates free-charge carriers (holes and electrons). After optically coupling the photodiodes with the

---

[1]The photocathode is a negatively charged electrode coated with a photosensitive compound that, when struck by photons emits electrons due to the photoelectric effect.

crystals, the light pulse produced in the scintillator is collected in the photodiode. It creates a very small charge pulse that can be amplified with a charge preamplifier. The quantum efficiency for PDs can reach 70% between 500 nm and 900 nm, but decreases rapidly below 500 nm.

Many photodiodes are available: PIN, PN, Schottky, Silicon Photomultipliers (SiPM) and avalanche photodiodes (APDs). Three of them are of special interest for replacing the traditional photomultiplier tubes: PIN Diodes, SiPM and APDs.

The PIN[2] photodiode has been used in several high-energy physics experiments (CLEO, L3, BELLE, BABAR, GLAST) [39]. PIN photodiodes operate by converting optical photons into electron-hole pairs that are simply collected and require a high-gain charge-sensitive-preamplifier because they have no internal gain. APDs, on the other hand, incorporate an internal gain increasing the collected number of charge carriers. They can be produced with a large active area ranging from a few mm^2 to a few cm^2. This devices will be described in the next section.

Silicon photomultipliers (SiPMs) are silicon single-photon-sensitive devices built from an array of single APDs on a common silicon substrate. The idea behind them is to detect single-photon events in sequentially connected silicon APDs. The dimension of each single APD can vary from 20 to 100 μm, with a density up to 1000 per mm^2.

Every single APD in an SiPM operates in Geiger mode and is coupled to the others by a polysilicon quenching resistor. Although the device works in digital/switching mode, the SiPM is an analog device because all its microcells are read in parallel. This makes it possible to generate signals within a dynamic range from 1 to 1000 photons in a single square mm of device area.

The SiPM output signal is the sum of the signals from the number of pixels fired by photons. The supply voltage (Vb) depends on the APD technology used, and typically varies between 25 V and 70 V. This is 30 to 50 times lower than the voltage required for traditional photomultiplier tubes [40].

The best energy resolution obtained with avalanche photodiodes coupled to CsI(Tl) crystals are around 4.5% (FWHM) at 662 keV (see Ref. [41]). Results with SiPMs, Ref. [42], demonstrated an energy resolution of around 7% (FWHM) at 662 keV in the best case. The best results obtained with PMTs were around 6% for the same energy, as we will see later in this work. References [43–45] have reported values ranging from 5.5 to 7.9% for PIN Diodes coupled to CsI(Tl) crystals.

The energy resolution values obtained with Large Area Avalanche Photo-Diodes (LAAPDs) improve those reported with SiPMs, PMTs and PIN diodes, and this was one of the main reasons for choosing APDs as the ideal photosensors for the CALIFA Barrel scintillation crystals.

---

[2]PIN is an acronym that describes the structure, standing for p-, intrinsic and n-silicon.

3.2.1. Avalanche Photodiodes

Operational principles

When the light produced inside a scintillator crystal makes contact with the semiconductor, many electron-hole pairs are created. Photons corresponding to this scintillating light have a typical energy of 3-4 eV, which is enough to create an electron-hole pair in the semiconductor, which has an energy gap of 1-2 eV. This small amount of charge is multiplied through an *avalanche process*[3], pulling the signal up above the noise level.

The spectral response of a typical silicon photodiode extends much farther into the long wavelength region than that of typical photocathodes. This extended spectral response is particularly well suited for scintillators with emission spectra that have a significant yield at longer wavelengths [27].

APDs are ideal for scintillation detection because of their high quantum efficiency ($\geq$ 60% between 390 and 930 nm) and high internal gain [46, 47], and because their spectral response fits the CsI(Tl) emission spectra [48, 49].

Table 3.1 shows the parameters for the different APDs from Hamamatsu Photonics K. K. [50] that were tested in this work. Figure 3.2 provides a picture of these devices.
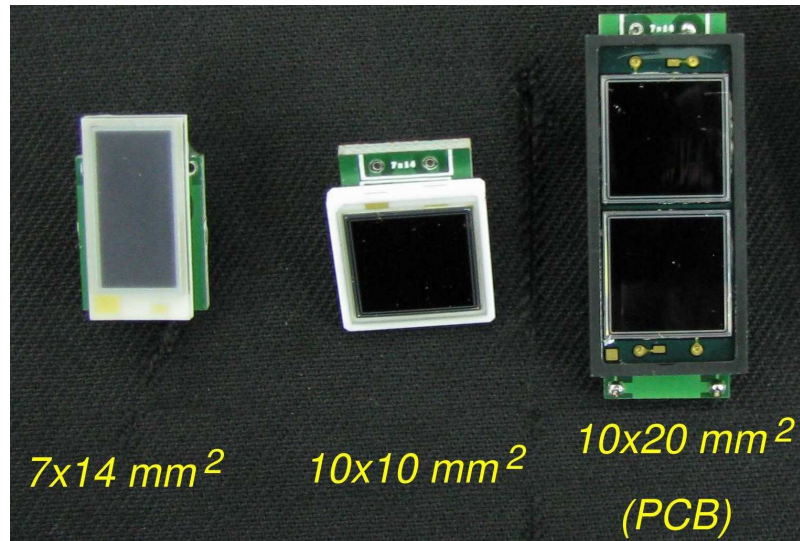

Figure 3.2: Different APDs tested in this work (see Table 3.1).

---

[3]Charge carriers are accelerated sufficiently between collisions to create additional electron-hole pairs along the collection path.

Model	S8664-1010	6817[a]	SPL 7210[b]	SPL 7209[b]
Active area (mm^2)	10x10	2 ch. 10x10	7x14	7x14
Number of Units	20	5	4	4
Window	Epoxy resin	Epoxy resin	Epoxy resin	Epoxy resin
Backing	Ceramic	PCB[c]	Ceramic[d]	Ceramic[d]
Dark current I_D[e]	10 - 31 nA	29-61 nA	41-67 nA	41-82 nA
Break-down voltage V_{brk} [f]	455 - 670 V	467 - 480 V	556 - 577 V	379 - 383 V
Bias Voltage V_G[e,f]	400 - 420 V	420 - 440	490 - 510	330-340 V
Capacitance: C_{det}[f]	270 pF	255 - 264 pF[g]	158-166 pF	284-288 pF

[a] Two-channel S8664-1010, specifically developed for this project. For further details see Ref. [52].
[b] This non-commercial 7x14 mm^2 APDs were provided by the PANDA collaboration.
[c] PCB stands for Printed Circuit Board.
[d] Instead of a standard encapsulation, this APD backing is a cutted ceramic sheet.
[e] Measured at a gain of 50.
[f] Measured at 25 ^oC.
[g] Per channel.

Table 3.1: Hamamatsu APD parameters tested in this work.

Advance Photonix provided another type of APD, model SD-630-70-73-500 [51], with a circular active area 16 mm in diameter. This APD offered similar results to the Hamamatsu Model S8664-1010 APD, but its encapsulation makes the coupling with large square crystals difficult.

3.2.2.   APD Characterization

This summarizes the work done to characterize the APDs by developing a procedure for identifying the APD contribution to the energy resolution (for additional details see Ref. [53]). We were looking for a simple way to obtain a light pulse with a stable number of optical photons, that is, within a narrow dispersion in energy. We started by measuring the APD response after excitation by a light emitting diode (LED).

Figure 3.3 shows the experimental setup used to compare the different APDs series. We used a green LED (producing light signals of around 550 nm) to imitate the scintillation light from a CsI(Tl) crystal. The APD gain could be not constant along its active area (see Ref. [49]), therefore, we used a light diffusing material placed between the APD and the LED to achieve a quite uniform light profile that would illuminate the entire active area of the APD.

A pulse generator was used to feed the LED through a load resistor. The pulse

width was 8 μs with a frequency of 1.8 kHz and variable amplitude for adjusting the amount of light produced by the LED. We also set a ^{55}Fe radioactive source in the same setup in order to establish a reference peak for quantifying the number of electron-hole pairs (hereafter Ne-h) produced in the APD (following the procedure of References [54] and [55]).
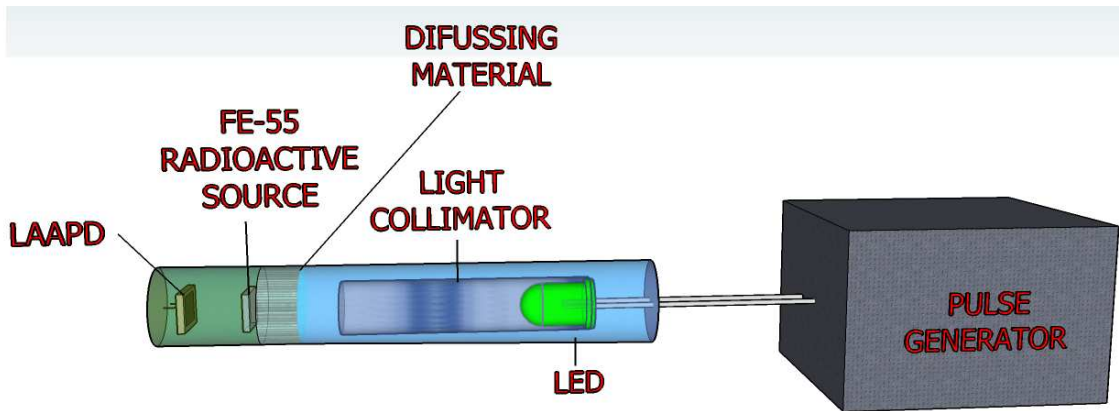

Figure 3.3: Experimental setup for comparing the different APD series.

The setup described in Figure 3.3 was placed inside a shielding box that served as a Faraday-cage, then covered by thermal insulating material to avoid temperature oscillations. APDs were readout by a charge-sensitive preamplifier[4]. The signal was sent to a spectroscopy amplifier[5]. The output signal of the spectroscopy amplifier was sent to an Amptek multichannel analyzer (MCA) and stored for off-line analysis.

Number of electron-hole pairs

Figure 3.4 (left) shows the amplitude spectrum produced in the APD by a ^{55}Fe radioactive source (main X-ray peak at 5.9 keV) along with the LED pulse spectrum. We were unable to measure the number of photons arriving at the APD active area, but we did actually define a new magnitude called *LED light yield* in arbitrary units.

When we increase the amplitude of the LED feed pulse, its photon light yield also increases and the position of the LED peak is displaced to the right in the energy spectrum. We know that ^{55}Fe X-rays produce an average of 1638 electron-hole pairs [56] in the depletion layer of the APD, creating a peak in the

---

[4]Different preamplifier models were tested: Ortec IH 142, Canberra 2001A, Cremat CR-110 and Mesytec MPR-1 (See Appendix D).

[5]Two spectroscopy amplifiers models were used: Canberra 2022 and Ortec 671. The Canberra 2022 gives a choice of 0.5, 1, 2, 4, 8 or 12 μs, while the Ortec offers 0.5, 1, 2, 3, 6 or 10 μs shaping times.

MCA that is proportional to this number. This can be used to convert the centroid of the LED pulse into a mean number of electron-hole pairs created in the APD by the LED pulses.

Figure 3.4 (right) shows the relationship of the number of electron-hole pairs created in the APD with the LED light yield (determined by the relation to the amplitude of the LED feed pulse).
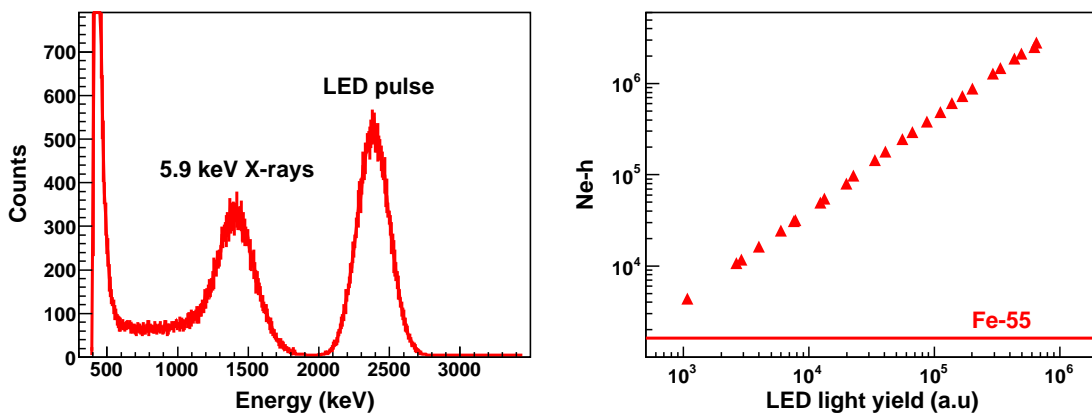

Figure 3.4: Left: Amplitude spectrum of the 5.9 keV X-rays from the ^{55}Fe radioactive source and the LED pulses. Right: Number of electron-hole pairs vs. LED light yield (a.u.) for the 10x10 mm^2 APD.

Optimal bias voltage determination and light pulse resolution

The light-pulse resolution is defined as the FWHM of the LED pulse (in ADC channel units) divided by the channel number of the peak centroid. The aim of this test was to find the optimal APD bias voltage, which is achieved when the light-pulse resolution is minimal.

The setup shown in Figure 3.3 was used to measure the dependence of the light-pulse resolution on the APD bias voltage. We also measured the APD dark current at the bias voltage that optimizes the light-pulse resolution. The APD bias voltage was obtained from the power supply value corrected by the voltage drop in the bias resistor network. The APD dark current was read out from the power supply (Iseg NHQ 225M) with a precision of 1 nA.

Table B.1 and figures in Appendix B summarizes the results for 10x10 and 7x14 mm^2 APDs (standard and low capacitances). As can be seen, the dark current values range from 7 to 39 nA.

Figure 3.5 (left) shows the light-pulse resolution as a function of the number of electron-hole pairs for the 10x10 mm^2 APD. From this plot, the APD contri-

bution to the energy resolution can be deduced. The behavior of the light-pulse resolution seems to be mainly due to the Ne-h statistics with an asymptotic value below 0.12% attributed to the electronic noise generated in the whole electronic chain[6].
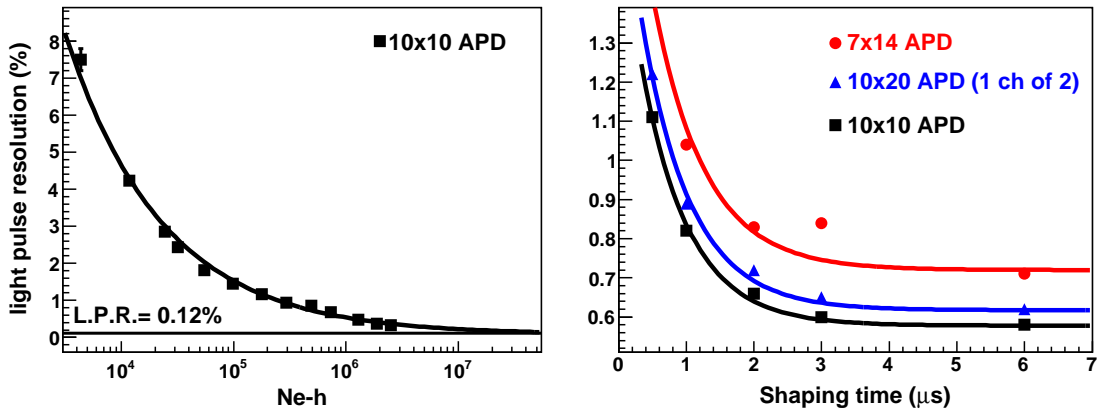

Figure 3.5: Left: Light-pulse resolution vs. Ne-h for a 10x10 mm^2 APD. Right: Light-pulse resolution vs. shaping time for different APD sizes

Figure 3.5 (right) shows a comparison of the light-pulse resolution as a function of the shaping time in the spectroscopy amplifier for three different APD sizes. This figure compares the 10x10, 7x14 and a single channel of the 10x20 mm^2 APDs. For a 6 μs shaping time in the spectroscopy amplifier, the 10x10 mm^2 APDs had a light-pulse resolution of around 0.6%, the 7x14 mm^2 APDs resolution was well above 0.7%, and the single-channel resolution for the 10x20 mm^2 APDs was around 0.65%. These values were obtained for light yields corresponding to around 7.10^5 Ne-h in Figure 3.5 (left), where the statistical fluctuations in the APD are small. From these data, we can conclude that the 10x10 mm^2 APDs series performs best.

3.2.3. Photomultipliers vs. APDs

Photodiodes offer higher quantum efficiency than photomultipliers, which constitutes a potential improvement, as long as their spectral response fits the scintillator emission spectrum [27]. Other advantages of photodiodes over photomultipliers include lower power consumption, compactness and insensitivity to magnetic fields.

In this test, a set of Photonis photomultipliers (XP1901, XP1918, XP3102) with different spectral responses (see Table 3.2) were selected with attention to the emission spectra of the CsI(Tl) scintillator. For comparison, the same crystals were coupled to APDs and PMTs and a set of measurements was performed to ascertain

---

[6]The whole electronic chain stands here for: APD + bias network + preamplifier.

optimal working conditions. Results are presented together with APD results in Section 3.3.5.

Model	diameter	Photocathode	Window	Ref. index[1]	spectral range
XP1901	19 mm	Bialkali GE[2]	lime glass	1.54	290-690 nm
XP1918	19 mm	Bialkali	fused silica	1.47	160-650 nm
XP3102	25 mm	Bialkali	borosilicate glass	1.48	270-650 nm

[1]: Refraction index measured at 420 nm
[2]: Green Extended

Table 3.2: List and main characteristics of different photomultipliers used in this work.

3.3. Test with small samples

In this section, we will present the results obtained with small CsI(Tl) samples coupled to both PMTs and APDs, and discuss about the main factors involved in achieving good energy resolution with these detectors.

Apart from the quality of the crystals, which we will discuss in Section 3.4, the energy resolution depends mainly on a set of parameters that includes the crystal wrapping (Section 3.3.1) and the optical coupling to the readout device (Section 3.3.2), along with the spectroscopy amplifier gain, shaping-time (Section 3.3.3) and APD bias-voltage (Section 3.3.4).

We started by looking for the combination of these parameters that provided the best energy resolution for three CsI(Tl) parallelepipedic samples (delivered by Saint-Gobain Crystals). Their sizes were 10x10x10 mm^3, 10x10x50 mm^3 and 10x10x100 mm^3, and they were coupled to an APD (Avalanche Photo-Diode) with an area of 10x10 mm^2.

All crystal surfaces were polished and the crystals had a Tl concentration of 0.2 mol%. All crystal surfaces except the one coupled to the APD were then wrapped with commercial Teflon tape and then covered with an aluminized-Mylar foil, to ensure uniform light collection along their length. Two types of optical grease were used as optical coupling between the crystal and the APD (see Section 3.3.2).

The APDs (S8664-1010 from Hamamatsu Photonics K. K.) were readout by an Ortec IH 142 preamplifier and a Canberra 2022 spectroscopic amplifier. The tests were done using a ^{137}Cs radioactive source with an activity of 10 μC, always placed in the same position, to ensure an approximately constant counting rate of about 1000 cps. This counting rate provides an spectrum with enough statistic in 60-120 s,

thus neither the bias voltage nor the temperature required monitoring for accuracy. Each measurement was performed at least two times in order to check stability.

All measurements were performed at room temperature. The humidity level was kept below 30%, due to the moderate hygroscopicity of these crystals.

3.3.1. Crystal wrapping for small samples

The crystal wrapping is probably the most critical parameter for obtaining maximum light collection, and thus for improving energy resolution. The highest Light Output (LO) for our crystal samples was achieved by optimizing the shape, quality and thickness of the crystal wrapping. Optical grease was used as the coupling between the crystal and the APD. Different diffusive and reflective wrappings were tested (see Table 3.3). The full width at half maximum (FWHM) divided by the photopeak channel for a 662 keV γ-ray from a ^{137}Cs radioactive source was taken as our reference estimation of the energy resolution. In this test, the temperature was monitored throughout the acquisition period in order to avoid gain variations.

The best energy resolution was achieved using four 75 μm-thick layers of Teflon tape covered by a 5 μm-thick layer of aluminized Mylar. Measurements done using only Teflon tape as the wrapping material revealed important losses in light collection. Note that the energy resolution values recorded in this test were obtained before the optimization of other parameters, and are consequently not the best values reported in this study.

Ref. [57] demonstrated that an optimal 5 μm thick aluminum foil over three layers of 38 μm-thick Teflon tape results in the same total light yield as the use of a fourth layer of Teflon. In this article they also claim that a multi-layer configuration results in better light collection than a monolayer configuration with the same thickness.

For our experiment, we used a multi-layer configuration, and our results confirmed the previous conclusions. In our case, the aluminized Mylar not only offered better light collection, but also provided an electric shielding for the crystal that reduced the electronic noise at the APD level.

3.3.2. Optical coupling

The optical coupling between crystal and the APD also has an important effect on the energy resolution. We tested several materials for coupling the crystals to the APDs. For some tests, temporary bonds were required to compare different crystals using the same photosensor under the same conditions. Some could be coupled with optical grease, for others we used optical pads, which provided more stable results in spite of their lower light transmission.

Crystal wrapping	Energy resolution (%)
Teflon tape (300 μm)	25.95±0.34
Teflon + Aluminum foil	10.00±0.09
Teflon + Metallic adhesive tape	8.68±0.09
Teflon + Copper tape	8.41±0.08
Teflon + Aluminized Mylar	7.48±0.08

Table 3.3: Energy resolution (FWHM) at 662 keV obtained with several crystal wrappings. These results were obtained prior to the optimization of other parameters.

Two optical greases were tested to discover which offered better optical contact for comparing different crystals coupled to the same APD: the Rhodosil Pâte 7 and the Bicron BC630. We performed a set of independent measurements for each under the same conditions. Those done with Pâte 7 had an energy resolution of around 8% (FWHM) (for the 662 keV γ-ray of a ^{137}Cs radioactive source), while the tests performed with the BC630 had an energy resolution of around 6.5% for the same energy.

For permanent bonds, we glued the crystals and APDs with Scionix RTV 681 optical cement [61], an epoxy adhesive mixture in a 10:1 mass ratio. The results obtained with this adhesive were slightly better than those obtained with the Bicron BC630 optical grease.

3.3.3.　Spectroscopic amplifier settings

This section will address the influence of the amplifier settings. The best results were generally achieved when the amplifier gain was set to cover the full dynamic range of the multichannel analyzer (Figure 3.6 - left). All along this work, the best energy resolutions among different crystals were compared by setting the APD bias voltage and the amplifier gain to ensure the presence of the ^{137}Cs peak in the upper quarter of the MCA channels, in order to guarantee that all measurements are performed under the same conditions.

Another factor with a significant influence on the energy resolution is the spectroscopy amplifier shaping time. To determine its effects, we measured the energy resolution obtained for the 662 keV γ-ray of a ^{137}Cs radioactive source as a function of the shaping time. These measurements are shown in Figure 3.6 (right), where the energy resolution is clearly seen to decrease as the shaping time increases. Shaping times between 4 and 8 μs seemed to be a good compromise: they provided good energy resolution without incurring pile-up effects.
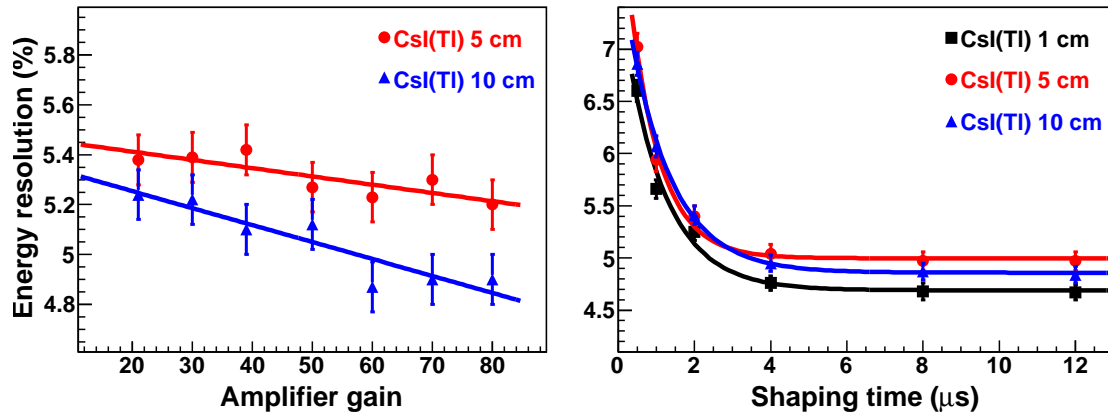
Figure 3.6: Left: Energy resolution vs. amplifier gain for 4 μs shaping time. The behavior was similar for 1 cm long crystals. Right: Energy resolution vs. shaping time for 1, 5, and 10 cm long crystals coupled to a S8664-1010 APD (4 μs shaping time and 380 V bias voltage).

3.3.4. Bias Voltage optimization

The best energy resolution achieved for a given crystal was found to depend on the level of voltage applied to the APD. The bias voltage supply required 30-60 minutes to stabilize. During this warm-up time, the stabilization of both the power supply and the electric field in the APD creates a gain change in the APD.

The bias voltage was optimized to keep the position of the photopeak constant around channel 6000 by adjusting the spectroscopy-amplifier gain. For this test, other factors such as shaping time were kept constant. The results for the 5 cm long CsI(Tl) crystal are shown in Figure 3.7 (left).

Measurements performed in the 370-420 V range (using a gain of around 50-70) showed the best energy resolutions. Once we established the optimal bias voltage, we tried to measure the effect of voltage drifts on the APD gain. Prior to this, we had to obtain the APD gain curve; recording the position of the photopeak channel for six bias voltage values (in this case, between 350 V and 400 V), for every crystal. The results are shown in Figure 3.7 (right).

From the fit of these experimental values, the slope of the curves around 380 V provided the relative gain variation due to bias voltage variation shown in Table 3.4. From these results, we can conclude that only a bias voltage variation below 0.35 V can guarantee a gain variation smaller than 1%.
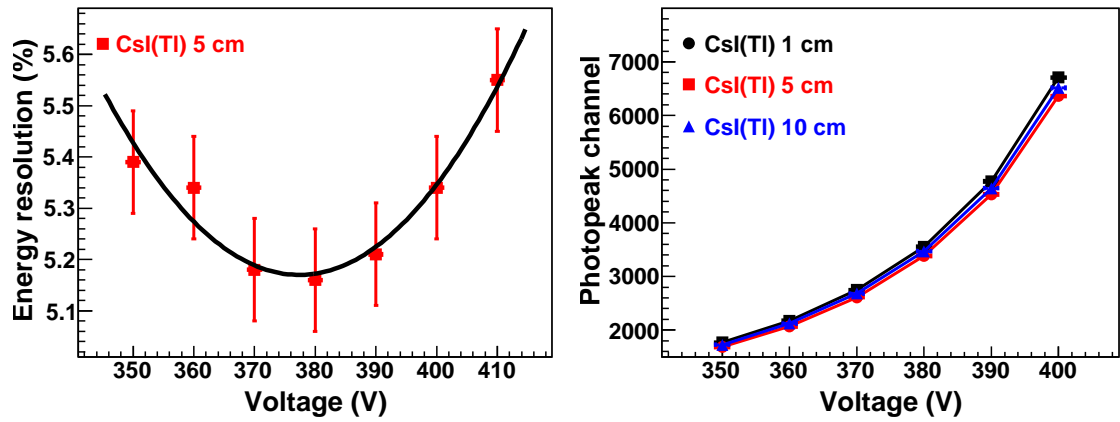
Figure 3.7: Left: Energy resolution vs. bias voltage, keeping the photopeak at a constant channel, for a 5 cm long crystal coupled to a S8664-1010 APD. Similar behavior occurred for 1 and 10 cm long crystals. Right: Typical gain curves of the S8664-1010 APD, using small CsI(Tl) crystals.

Crystal length	Gain variation (%/V)
1 cm	2.84±0.01
5 cm	2.83±0.01
10 cm	2.83±0.01

Table 3.4: Relative gain variation due to bias voltage variation for all crystals.

3.3.5. Energy resolution

APDs

Once the relevant energy resolution parameters had been optimized, a set of measurements were performed for 4 and 8 μs shaping times, keeping other conditions constant. The results for CsI(Tl) crystals coupled to APDs, shown in Table 3.5 and Figure 3.8, are an important improvement on those previously reported in [48], [55], [58], and are comparable to those obtained with Silicon Drift Chambers [59]. In this Table the mean energy resolution values from ten spectra are also shown.

PMTs

Table 3.6 shows the energy resolutions obtained with photomultipliers (XP1918, XP1901 y XP3102) coupled to CsI(Tl) crystals. All the results were obtained with a 4 μs shaping time and were performed after optimization of all the parameters mentioned in Section 3.3. The best energy resolution (6.07±0.10)% was obtained

Shaping	Crystal length (best values)			Crystal length (mean values)		
time	1 cm	5 cm	10 cm	1 cm	5 cm	10 cm
4 μs	4.68±0.12	5.11±0.12	4.74±0.12	4.98±0.12	5.22±0.09	5.17± 0.09
8 μs	4.42±0.12	4.87±0.09	4.72±0.08	4.68±0.12	5.02±0.09	4.90± 0.09

Table 3.5: Best and mean energy resolution values in % (FWHM) (at 662 keV), obtained for different crystal sizes using a Hamamatsu S8664-1010 APD.
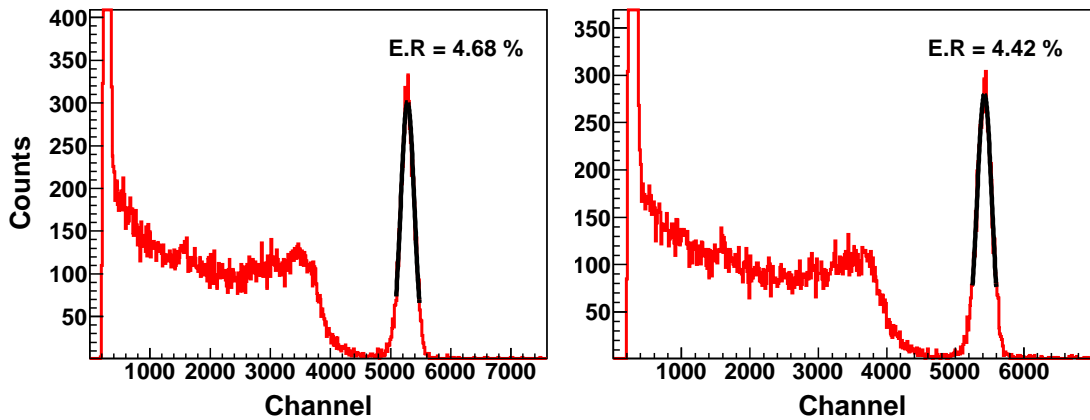

Figure 3.8: Energy resolution for 1 cm^3 CsI(Tl) coupled to a S8664-1010 APD for 4 μs and 8 μs shaping times.

using the XP1918 photomultiplier coupled to a 1 cm^3 CsI(Tl) crystal.

Crystal length		1 cm	5 cm	10 cm
	XP1901	7.0±0.1	8.4±0.1	12.8±0.1
PMTs	**XP1918**	6.1±0.1	7.4±0.1	10.7±0.1
	XP3102	9.1±0.1	9.9±0.1	16.5±0.2

Table 3.6: Energy resolutions in % (FWHM) (at 662 keV) obtained for different photomultipliers and different crystal lengths for 4 μs shaping time.

3.4.   Test with prototype crystals

This section contains the results of tests performed on a set of crystals with geometries very similar to those that correspond to the CALIFA Barrel section

located at 90° polar angle (see Section 1.2.3). The tests included optimization of the wrapping for these crystals (Section 3.4.2), a *light output* comparison of samples from several providers (Section 3.4.3), determination of the optimal working conditions (Section 3.4.4), measurements to determine the *non-uniformity in light collection* (Section 3.4.5), and finally a comparative study of the energy resolution (Section 3.4.6).

3.4.1. Crystal quality

Based on their technical drawings (see Figure 1.7), ten CsI(Tl) crystal samples with a 10x20 mm² exit face were ordered from five different providers for comparison. Each was adapted to the 6817 APD model (2 channels of 10x10 mm² APDs).

Each crystal was labeled with two identification codes (P1 to P5, and S1 or S2) to identify the different providers (P) and the different samples (S) from the same provider, respectively. After all the tests had been performed, two manufacturers were selected: Amcrys and IMP-Lanzhou. From these providers, crystals were ordered (see Figure 3.9) with different exit faces (10x10 and 7x14 mm²) adapted to the different APD active areas, like those presented in Figure 3.2.

Figure 3.9: Tested crystals with 10x10 and 7x14 mm² exit faces.

At our laboratory, each crystal was visually inspected to ensure quality criteria of transparency, surface treatment, polishing, and cutting edges. This qualitative inspection was not quantified, but helped to establish or discard any relevant correlations with the final energy resolution achieved.

Figure 3.10 shows the different appearance of the crystal samples from each provider. The samples found to have the best quality in the visual inspection did not necessarily provide the best values for energy resolution and light-collection non-uniformity, but there was one case where poor results were due to the poor surface quality. P1 samples had very rough surfaces, and the energy resolution improved substantially after they were re-polished. Both P3 samples came with a good finish, but P3-S1 performed poorly. It is not clear whether the wrapping or the optical coupling was responsible for this. P5 samples gave the worst results, in

spite of their surface treatment and excellent transparency.
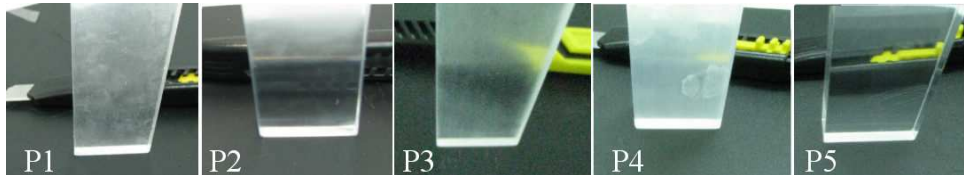
Figure 3.10: Photograph of raw crystal samples from all five providers.

3.4.2.   Optimal wrapping for prototype crystals

The ideal wrapping has not only to reflect the incident light but also to break up internal reflections between parallel surfaces and preferentially direct reflected light towards the photosensor.

We saw in Section 3.3.1, that the optimal wrapping for small samples was achieved using four 75 μm-thick layers of Teflon tape covered by a 5 μm-thick layer of aluminized Mylar. For the prototype crystals, we tested a new wrapping material called Enhanced Specular Reflector (ESR) [24] which supposedly increases the light output collection. The aim of this test was to determine the optimal wrapping configuration for prototype crystals.

This test was performed using prototype crystals with 10x10 mm^2 exit faces coupled to an XP 2A508 Photonis photomultiplier. Several wrapping configuration were tested:

- two layers of ESR (130 μm)

- a single layer of ESR (65 μm)

- a single layer of Teflon tape (75 μm), and a single layer of ESR

- two layers of Teflon tape and a single layer of ESR

- three layers of Teflon tape and a single layer of ESR

- six layers of Teflon tape and a single layer of ESR

Figure 3.11 shows the setup used to determine the optimal wrapping configuration. Crystals were coupled to an XP5A08 Photonis photomultiplier, using a silicon rubber disc as the contact material. The LED light entered the crystal through a small hole in the wrapping. A ^{137}Cs radioactive source was used as the reference peak, and can be used to check the previous results obtained with the LED pulse.
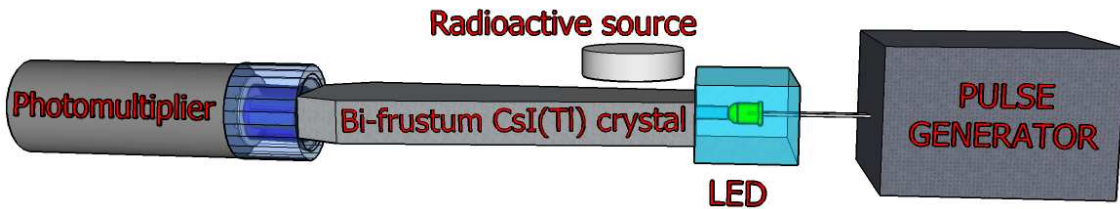
Figure 3.11: Setup for determining the optimal wrapping configuration.

The results are presented in Tables C.2 and C.3 (Appendix C). The best energy resolution was generally obtained using 2 layers of ESR, except with the Am08 crystal, where the best resolution was achieved using 1 layer of Teflon tape. This was confirmed using the energy resolution obtained with the ^{137}Cs radioactive source and two layers of Teflon tape.

We have concluded that the small differences in light-pulse resolution for one or two layers of ESR are insufficient to justify the use of a second layer of ESR in light of the energy losses in the wrapping when using proton beams. This was demonstrated in the prototype simulation described in Chapter 2.

3.4.3.   Crystal Light Output

Figure 3.12 shows the setup used to compare the light output of all the crystals tested in this work. For this test, we used an XP 2A508 Photonis photomultiplier and a ^{137}Cs radioactive source to irradiate the crystals. The idea was to compare the light output for all the samples under the same conditions[7].

This test was only reproducible without optical grease between the crystal and the photomultiplier. Even though the light output was higher with optical grease, the result was found to be strongly dependent on details of the contact, such as the amount of optical grease used, homogeneity or air bubbles (even for the same amount of optical grease). The crystal samples were covered with ESR wrapping [24] that was tailored to fit the crystal faces, and then wrapped with standard Teflon tape to keep the ESR tight.

Figure 3.13 shows the energy resolution of Amcrys and IMP Lanzhou crystals with different exit faces as a function of the photopeak channel, which is proportional to the light output. This plot indicates that crystals with the largest exit face ($10x20$ mm^2) have the largest light output, and in consequence the best energy resolution.

Table C.1 (Appendix C) compares the light output for the same crystals, using the light output of a $10x10x10$ mm^3 CsI(Tl) crystal from Saint Gobain

---

[7]Using the same high voltage in the PMT (1050 V), and the same gain (85) and shaping time (4 μs) in the spectroscopy amplifier.

Figure 3.12: Setup used to compare the light output of all the crystals tested in this work.
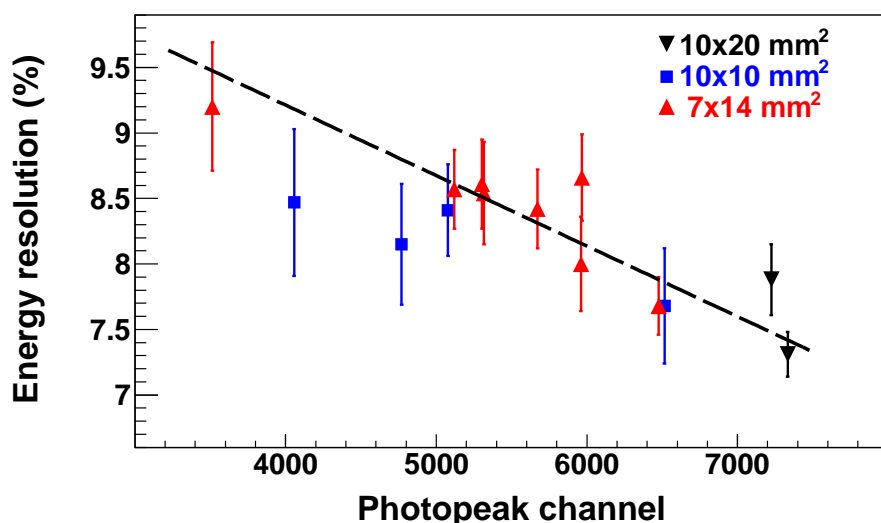

Figure 3.13: Energy resolution (FWHM) vs. photopeak channel for all the measured samples, without optical grease between the crystal and the photomultiplier. The dashed line is included to guide the eye.

as a reference. From this Table, we can see that crystals with a 2 cm^2 exit face have a light output of around 72 to 76%, while the light output for crystals with a 1 cm^2 exit face ranges from 46 to 62% with regard to the reference crystal.

The Amcrys and IMP Lanzhou samples exhibited a large spread in the crystal light output characterization. The significant differences in all the samples tested may exceed the required calorimeter tolerances in a future crystal production stage.

3.4.4. Optimal working conditions

The tests to determine the optimal working conditions for each sample were performed using a 10 μC ^{137}Cs radioactive source (662 keV), positioned to ensure an approximately constant counting rate ($\sim$ 1000 cps). A 1 mm thick piece of aluminum foil was interposed to absorb electrons emitted by the source. The acquisition time was chosen to obtain about 8000 counts under the photopeak.

The multichannel analyzer files obtained were histogrammed using ROOT [23]. The photopeak was fitted to a Gaussian function after subtracting a linear background. The energy resolution was established using 2.35 σ as the full width at half maximum. The error bars in all figures concerning the energy resolution were determined as 2.35 times the σ uncertainty given by the ROOT fitting algorithm.

LAAPD for prototype crystals

In order to collect the maximum light produced by the crystals, two units of the S8664-1010 APDs (Model 6817) [60] (characteristics shown in Table 3.1) were mounted in a common frame leaving a 2 mm dead (non-reflecting) zone between the two channels as shown in Figure 3.2 (right model).

The Hamamatsu APD units for this part of the work were chosen for their very similar gain curves. The APDs were glued to the crystals with optical cement [61].

Gain curve, optimal bias voltage and shaping time determination

An Ortec 671 spectroscopy amplifier was used for some samples (3 μs shaping time) and a Canberra 2022 was used for the rest (using 4 μs shaping time). The measurement of the photopeak position as a function of bias voltage revealed an exponential behavior, see in Figure 3.14 (left).
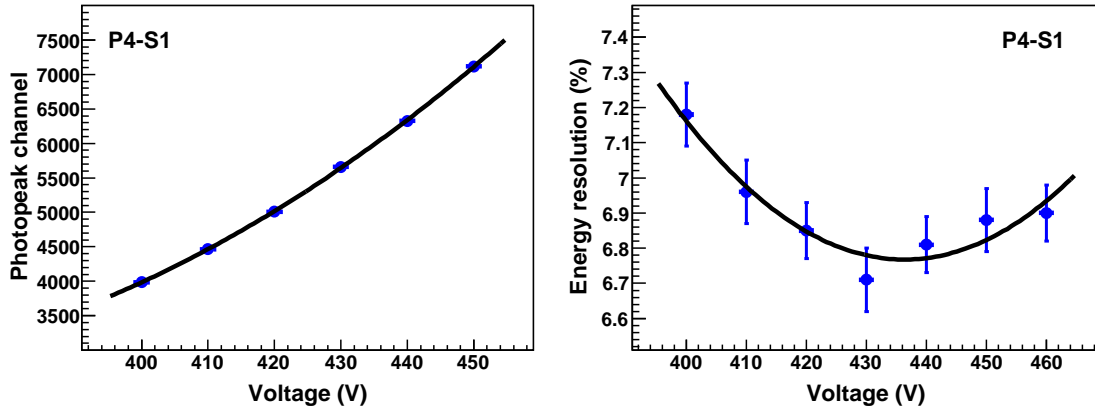

Figure 3.14: Left: Photopeak position vs. bias voltage, for a CsI(Tl) crystal coupled to a S8664-1010 2CH LAAPD (error bars are smaller than the symbol size). Right: Energy resolution as a function of the bias voltage for a CsI(Tl) crystal, coupled to a S8664-1010 2CH. The minimum value defines the working voltage.

The voltage that provided the best energy resolution was established as the working voltage of each crystal coupled to its corresponding APD, see in Figure 3.14

(right). The high voltage was thoroughly filtered and its stability was controlled in our measurements.
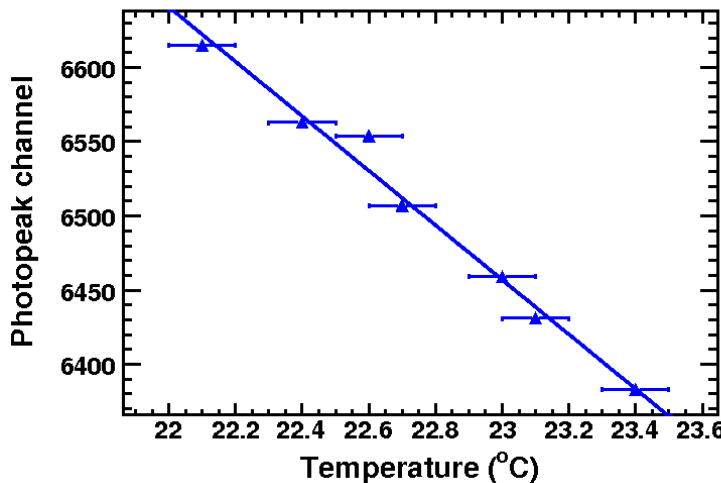
Figure 3.15: LAAPD gain vs. temperature

Figure 3.15 shows the dependence of the gain on the temperature. The experimental data at room temperature fit well in a linear function with a slope of 184 ch./°C. At a gain around 50 ($\sim$ channel 6500), we found a $(dM/dT)M^{-1}$ = -2.8 %/°C, which compares well with the of -2.5 %/°C Hamamatsu value [55], allowing us to correct the photopeak displacement by monitoring the temperature-drift. During our tests, the temperature was monitored and kept stable enough to avoid the need for such correction.

We used the shaping time to analyze the behavior of the energy resolution (Figure 3.16-left), in order to determine its best value in the spectroscopy amplifier. Minimum values ranged from 3-6 μs.

LAAPD readout configurations

We compared the performances of two different configurations for reading the output current from the APDs. In the first one, we added the currents from both APDs at the input of a Cremat CR-110 preamplifier. In the second one, we used individual preamplifiers for each APD, and the signals were summed with an analog adder after preamplification. In the second setup, two high-voltage supplies were used, and the optimal bias voltage was set independently for each APD.

In Figure 3.16 (right), we can see the dependence of the energy resolution on the bias voltage applied for the two different readout configurations. The second has an individual readout system for each LAAPD unit, using two bias voltage
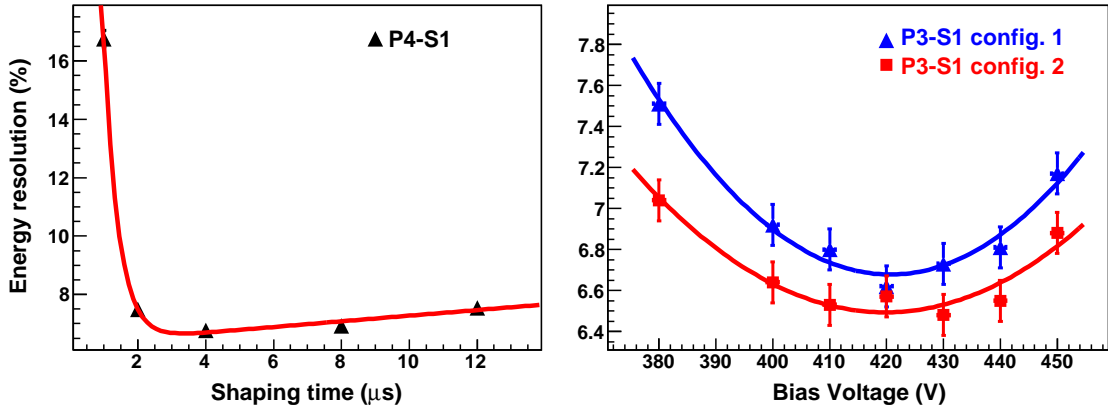
Figure 3.16: Left: Energy resolution as a function of the shaping time for a CsI(Tl) crystal coupled to a S8664-1010 2CH APD. The optimum value for all our measurements was established around 3-4 μs (Error bars are smaller than the symbol size). Right: Energy resolution as a function of the bias voltage. Config. 1 used a single power supply and a preamplifier; config. 2 used two independent voltage supplies and the currents were added in.

supplies and two Cremat preamplifiers. Their signal was added in a Fan In/ Fan Out module before being sent to the spectroscopy amplifier. Each of the LAAPD units was set at its optimal bias voltage for the final energy resolution measurement[8].

This configuration, when compared with the first one, provided a modest improvement in the energy resolution (from 6.7% to 6.5%). Note that both setups were influenced by different levels of electronic noise, which might have influenced the energy resolution obtained. Consequently, all the results presented below are based on the first configuration: both LAAPD units were fed by the same bias voltage with a single amplification chain, where the currents coming from the two LAAPD units were added in parallel at the preamplifier input.

3.4.5.   Non-uniformity in light collection

Non-uniformity in light collection (N.U.) is the variation in the amount of light collected by the photosensor and is one of the factors affecting energy resolution. This variation depends on the longitudinal position at which most of the energy deposition occurs in the scintillator. Several factors contribute to this process.

Light collected by the photosensor depends mainly on the crystal shape (focusing), wrapping, surface finish, transparency (light attenuation) and dopant concentration. We have seen that these factors are different for each crystal or

---

[8]In Figure 3.16 (right) the bias voltage for config. 1 was set as the mean value of the two APD units.

affect each crystal differently (mainly for large sizes).

For a fixed-energy ionizing particle, the photopeak position in the ADC is a direct measurement of the Light Output (L.O.) of the scintillation crystal. Therefore, by measuring the photopeak position produced by a radioactive source as a function of the longitudinal distance from the photosensor, we were able to obtain the variation produced in the light yield of the scintillation crystal.
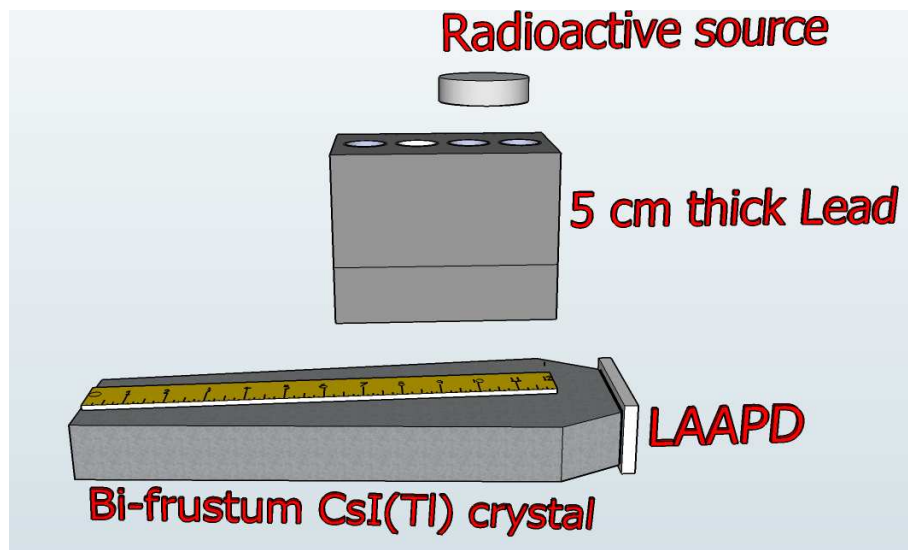

Figure 3.17: Schematic view of the experimental setup used for the light-collection non-uniformity measurements.

A collimated radioactive source (^{137}Cs) moving along the longitudinal crystal dimension (see Figure 3.17) was used to measure N.U. at six different positions from the crystal exit face, to which an LAAPD was glued. The N.U. parameter can be quantified by two different methods [62, 63]. It is defined in Ref. [62] as

$$G = \frac{LO_{max} - LO_{min}}{LO_{ave}} \tag{3.1}$$

where LO_{max} and LO_{min} stand, respectively, for the maximum and minimum ADC photopeak positions, and LO_{ave} is the average of all the recorded LO values.

Figure 3.18 shows the two extreme N.U. values, obtained for manufacturers P1 and P5. A summary of all the samples studied is shown in Table 3.7.

We observed important differences in light-collection non-uniformity for each crystal, even for two samples coming from the same provider. The crystal geometry and the surface treatment are the relevant parameter affecting the light transmission from the scintillation point up to the APD active area [64]. Ref. [34] indicates that light output is strongly dependent on thallium concentrations, and
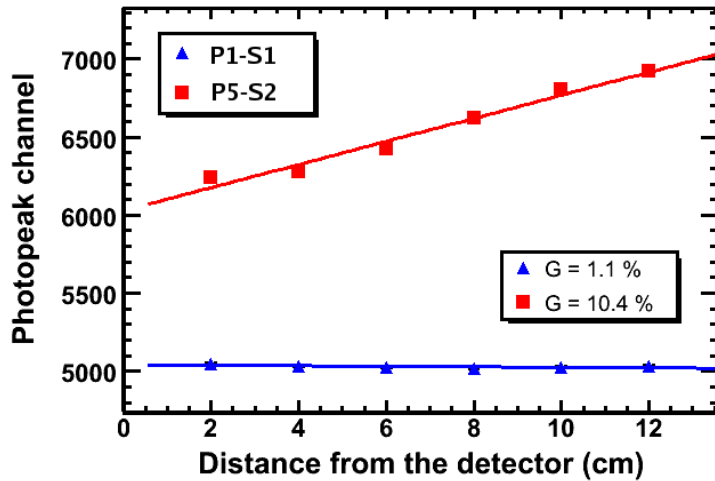
Figure 3.18: Light collection non-uniformity determination for P1-S1 (best) and P5-S2 (worst) samples. The G parameter is shown in the inset.

Sample	P1-S1	P1-S2	P2-S1	P2-S2	P3-S1	P3-S2	P4-S1	P4-S2	P5-S1	P5-S2
N.U.(%)	1.1	4.5	2.2	—	—	2.3	1.8	4.3	—	10.4
E.R. (%)	9.3[a]	6.4[b]	5.9[a]	6.1[a]	7.4[a]	6.6[b]	6.5[b]	7.3[b]	6.6[b]	7.4[b]

[a] Amplifier Ortec 671 set at 3 μs shaping time
[b] Amplifier Canberra 2022 set at 4 μs shaping time

Table 3.7: Summary of light collection non-uniformity and energy resolution $\Delta E/E$ (662 keV) (as explained in text)

at least 0.1 mol% is required for an optimal value using photodiodes. The thallium concentration is usually not constant along the ingot [63], and the non-uniformity of tapered crystals depends on the end from which the crystal was grown. Neither the thallium concentration nor the cutting direction were specified by the providers, except for P4, which states a Tl concentration of 0.2 mol%.

3.4.6.   Comparative study of the energy resolution

The second column in Table 3.7 shows the energy resolution average of eight measurements achieved under optimal working conditions. In this case, the radioactive source (^{137}Cs) was located at the entrance window of the crystal (opposite the LAAPD). The bias voltage of the LAAPDs was set for a gain of around 50 (ranging from 430-445 V).

Figure 3.19 provides the spectra for the best and worst cases (P2-S1 and P1-S1). They show a reasonably good peak-to-valley ratio.
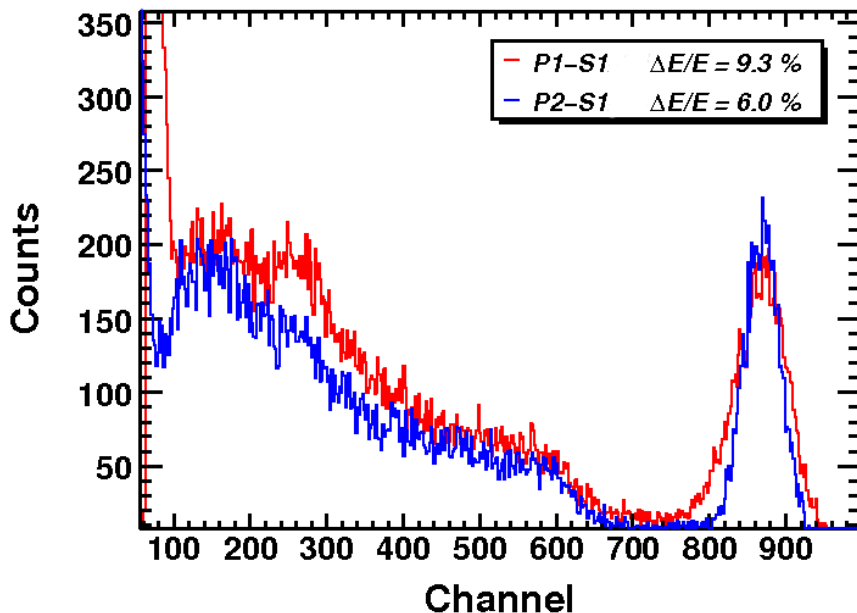

Figure 3.19: Experimental spectra of the two detection systems P1-S1 (red curve), and P2-S1 (blue curve), in response to a 662 keV γ-ray. The energy resolution values obtained for the P2-S1 sample are significantly better than P1-S1.

The best energy resolution values obtained in this case were around 6% at 662 keV. Compared to what was achieved for 10x1x1 cm^3 parallelepiped crystals (4.7% at 662 keV), we can conclude that the observed difference in energy resolution was mainly due to the different length/area ratios for the crystals used in both cases, as well as differences in the APDs used for prototype crystals.

For instance, in Section 3.2.2 we mentioned that each single channel of the 10x20 mm^2 APDs used for these crystals gave worse energy resolutions than the 10x10 mm^2 APDs. These results pointed to lower performances for APDs with PCB backing compared with those with ceramic backing. Moreover, since a 10% dead zone reduces the light collection proportionally, the 2 mm dead (non-reflecting) zone between each single channel (see Figure 3.2 - right model) results in certain light losses.

Energy resolution vs. photon energy

In order to investigate the evolution of the energy resolution for different incident energies, we performed a set of measurements with ^{60}Co (1170 keV and 1332 keV)
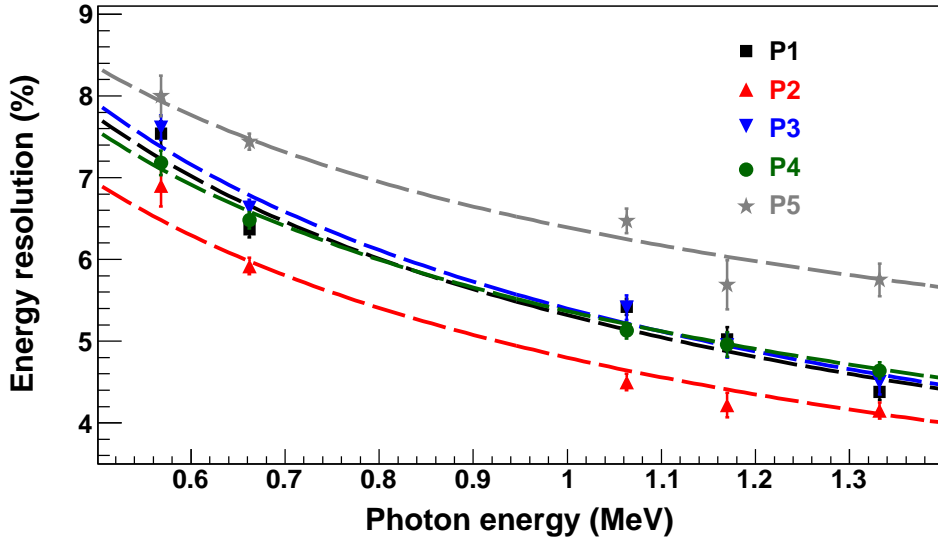
Figure 3.20: Experimental energy resolution as a function of the incident gamma energy. The dashed lines show the fitted function $A + B/\sqrt{E}$

and ^{207}Bi (569 keV and 1063 keV) radioactive sources. Figure 3.20 summarizes the results obtained. The dashed lines show the fitted function $A + B/\sqrt{E}$.

The best energy resolution with a radioactive source located at the entrance window of the crystal is not necessarily obtained for the crystal with the best light-collection non-uniformity (N.U.). The providers often depolish the surface of the crystal, improving the N.U. at the expense of energy resolution (P1-S1, for example). The best energy resolution, 5.1% at 1 MeV, was achieved for the P2-S1, and is close enough to the initial requirements of 5% to be suitable for use in the CALIFA Barrel [16].

Chapter conclusions

Characterization of CsI(Tl) crystals and photosensors revealed that the energy resolution depends on the crystal wrapping and a few other parameters related to the electronic chain used. Energy resolution was found to be approximately constant with crystal size for small samples (1-10 cm long and 1 cm^2 section). The result obtained with a 10x10x10 mm^3 CsI(Tl) crystal coupled to a 10x10 mm^2 APD (4.4% at 662 keV) were better than previously reported in the literature.

A four-layers wrapping of 75 μm-thick Teflon tape covered by a 5 μm-thick-layer of aluminized Mylar was optimal for small samples, while a 130 μm-thick ESR wrapping performed best on prototype crystals. The total wrapping thickness fulfils the requirement for a minimum dead space between crystals in the calorimeter. The energy resolution achieved for a given crystal was found to depend on the bias

voltage being applied to the APD, as well as on the spectroscopy-amplifier gain and the shaping time.

In the APD characterization, different APD models were compared and the contribution to the energy resolution was determined for these devices. Different APD series were compared for light-pulse resolution at the nominal bias voltage. The best light-pulse resolution was obtained for the 10x10 mm^2 APD series. The contribution of the APD to the energy resolution has an asymptotic limit below 0.12% that is associated with the noise contribution of the electronic chain. The APD encapsulation was also found to influence the energy resolution. APDs with PCB backing performed worse than those with ceramic backing. Use of an individual readout system for each unit of the 2 channel APD improved energy resolution to a certain degree, at the expense of greater complexity in both the electronics and the data analysis.

Chapter 4

In-Beam tests of the prototype

IN previous chapters, we presented the test results for single crystals irradiated with low-energy photons emitted from radioactive sources. These standard laboratory sources emit gammas with energies ranging from a few keV to 4 MeV. A CALIFA Barrel prototype with a small number CsI(Tl) crystals was built to explore crystal performances under high-energy proton and gamma beams. Two different prototype configurations[1] were evaluated.

This chapter contains the details of the prototype construction and the results of the tests performed in several beam facilities. These results are also compared with simulations for the different gamma and proton beam energies achieved in the experiments mentioned.

Other objectives of the beam tests include comparing the results obtained under optimal laboratory conditions with the results for several crystals working in a completely different setup, testing the electronic chain and the noise in configurations involving multiple channels and developing addback procedures to sum signals for several crystals, etc.

The tests were performed in three different facilities:

- The Svedberg-laboratoriet (TSL) in Uppsala (Sweden), where there is a proton accelerator with energies up to 200 MeV. In this experiment, the prototype was placed directly in the beam line. The results are discussed in Section 4.3.5).

- Centro de Microanálisis de Materiales (CMAM) in Madrid (Spain), consisting of a 5 MV Cockroft-Walton accelerator where protons at 1 MeV were used to produce the reactions ^{19}F(p,$\alpha\gamma$)^{16}O and ^{7}Li(p,γ)^{8}Be, using a Teflon target (containing LiF). In these reactions, 6.1 and 17.6 MeV gammas (the first excited states of ^{16}O and ^{8}Be) were produced. The results are in Section 4.3.5.

- Technische Universität Darmstadt (TUD) in Darmstadt (Germany) has an electron accelerator that serve for several experiments. One of these experiments is the NEPTUN facility, where the electrons collide against a thin

---

[1]Configurations depend on the number of crystals used for each test beam.

target called a 'radiator', producing gammas by bremsstrahlung radiation. In this facility, electrons passing through the target are deflected by a constant magnetic field and identified using 128 fibers in a focal plane, allowing us to determine the electron energy. The gamma-ray energy is deduced from a time coincidence between the electrons hitting the focal plane and the gammas hitting the prototype. The setup produced gammas from 3 to 20 MeV, with an energy resolution below 25 keV. The results are in Section 4.3.5.

In Section 2.3.2, we saw that the full energy peak efficiency decreases for high-energy gammas due to a rise in the number of secondary interactions as the energy of the incident gammas increases. Consequently, the prototype configuration for gamma beams had at least fifteen crystals for measuring the full gamma energy.

Moreover, the crystal multiplicity is higher for high energies because the multiple Compton scattering and the pair production increases with the energy. This means that more scattered gammas (or 511 keV photons) reach neighbor crystals. For example, the multiplicity for 7 MeV gammas is around 4 indicating that at least four crystals are needed to contain the full shower produced by these gammas.

For a proton beam, most of the protons hitting a single crystal leave their full energy in that crystal, and only those protons hitting near the boundary between crystals can scatter and end up in a neighbor crystal. Therefore, a prototype configuration with 4 crystals was used for the proton test beam.

4.1.   Beam test with 180 MeV protons

4.1.1.   Experimental setup

For the experiment performed at The Svedberg Laboratory (Uppsala, Sweden), a prototype configuration was built with four 10x20 mm^2 exit face bi-frustum shaped CsI(Tl) crystals, coupled to Hamamatsu 6867-10x20 APDs (2 channels), and wrapped with two layers of Teflon tape and two layers of ESR (see Figure 4.1). An aluminum box was used to electrically isolate the setup and to avoid external light contamination. Inside the box, the crystals and APDs were placed together with four Cremat CR-110[2] preamplifiers mounted on a common card.

The preamplifier outputs were connected to Mesytec MSCF-16[3] amplifiers, and APD bias voltage was provided using a CAEN N472 4-channel HV power supply. The amplifiers readout was done with a 32-channel VME Multi-event Peak Sensing ADC (CAEN V785) with 12-bit resolution and fast conversion time. The data acquisition system (DAQ) was based on the GSI Multi-Branch System

---

[2]Specifications in Appendix D.
[3]Specifications in Appendix D.

Figure 4.1: Prototype used for the detection of protons at 180 MeV.

(MBS) [65]. The VME crate readout was controlled by a CES RIO3 VME processor.

The APD bias voltage had to be set low (half of the optimal APD bias voltage) due to the huge amount of light produced by the protons in the crystals to avoid the preamplifiers saturation. Figure 4.2 shows the experimental setup used for this experiment. Double Sided Silicon Strip Detectors (2 mm thick), or DSSSDs, consisting of 32x32 perpendicular strips with a pitch of 1.86 mm were placed in front of the ProtoZero to determine the position and dimensions of the beam. The DSSSDs covered a total active area of 60x60 mm^2, and the total crystal entrance face was 58x19.6 mm^2.

The proton beam energy was 179.3 MeV after extraction, and was reduced to 179 MeV after passing through a stainless steel window. The beam energy was further reduced to approximately 177.2 MeV after traversing the DSSSDs located in front of the prototype. The beam was de-focused up to 40 mm in diameter in order to increase the impact area [25]. The proton energy uncertainty (σ_{beam}) following extraction was around 0.34 MeV. The energy straggling in the 100 μm thick stainless steel window ($\sigma_{steel-window}$) was as low as 0.06 MeV, but amounted to 0.21 MeV in the 2 mm thick silicon detectors (σ_{DSSSDs}), giving a final uncertainty of 0.4 MeV after traversing the DSSSDs.

The individual detectors were calibrated with 25 mm thick copper and iron degraders placed in front of the DSSSDs. The residual energies of the beam after passing though these degraders were 92.7 and 120 MeV respectively.
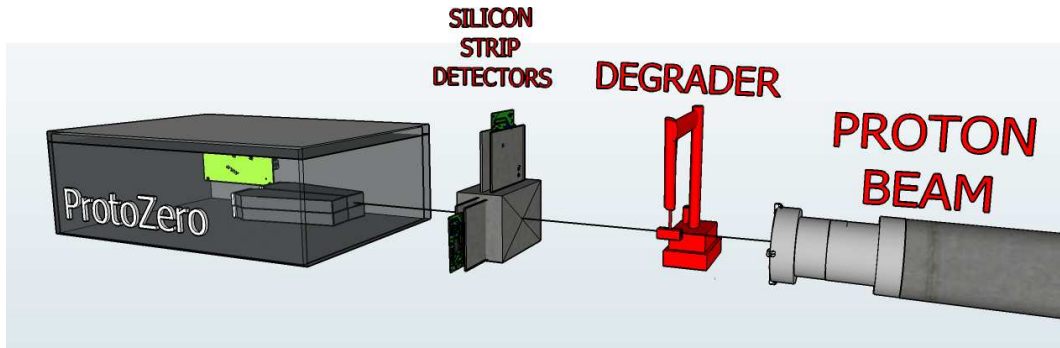
Figure 4.2: Setup used for the proton beam experiment.

4.1.2.   Results

Figure 4.3 shows the spectrum of incident 180 MeV protons obtained for each crystal in this prototype configuration.
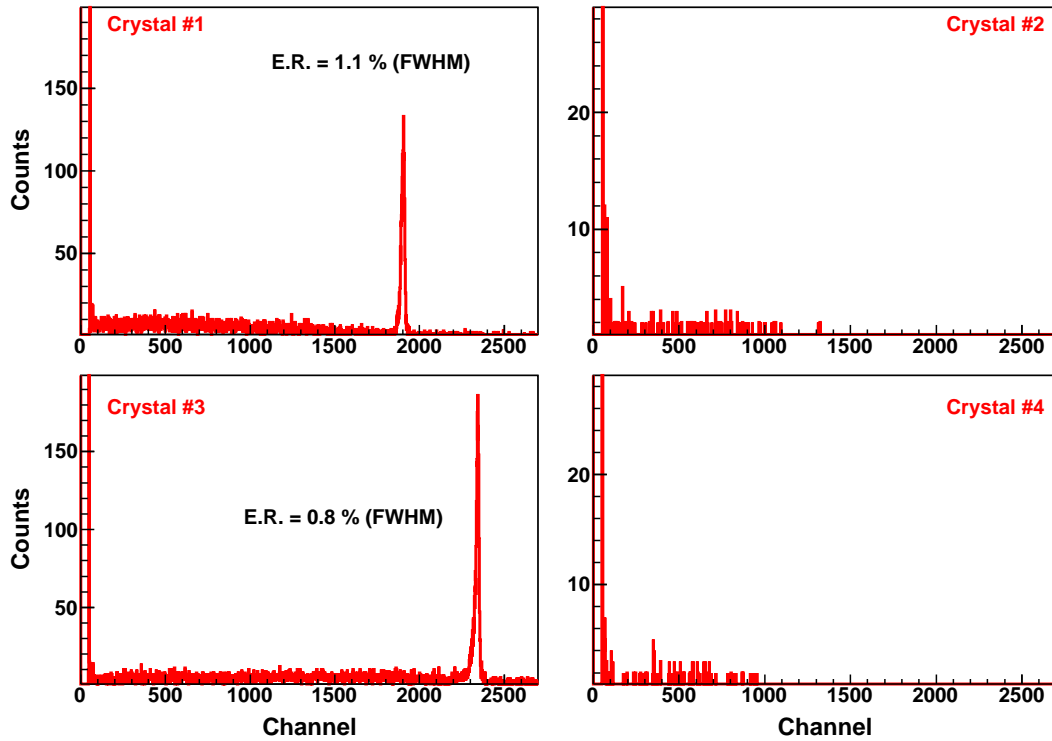

Figure 4.3: Spectrum of incident 180 MeV protons obtained for each crystal of this prototype configuration.

In spite of the APD bias voltage reduction, the energy resolutions obtained for these peaks are around 1% FWHM, corresponding to 0.74 σ, which is within the

calorimeter requirements. By accounting the energy straggling in the interposed materials, the energy resolution corresponding just to the crystals APDs can be estimated from the following expression where $\sigma_{Al-Box} = 0.35$ MeV is the straggling of the proton beam after passing through the 5 mm Aluminum wall of the ProtoZero box

$$\sigma_{Total}^2 = \sigma_{beam}^2 + \sigma_{steel-window}^2 + \sigma_{DSSSDs}^2 + \sigma_{Al-Box}^2 + \sigma_{crystal+APD}^2 \qquad (4.1)$$

Using the above calculated values in Equation 4.1, we obtain $\sigma_{crystal+APD} = 0.35$ MeV which corresponds to around 0.47% FWHM for protons at 173 MeV.

We can observe in these plots that the proton beam was impinging in the boundary between the Crystals #1 and #3, since both crystals produced a single peak with approximately the same number of counts. The absence of these peaks in the right spectra, shows that Crystals #2 and #4 were off the beam. This makes the energy calibration difficult. In order to reconstruct the events hitting more than one crystal is essential to obtain a calibration curve for all the detectors.
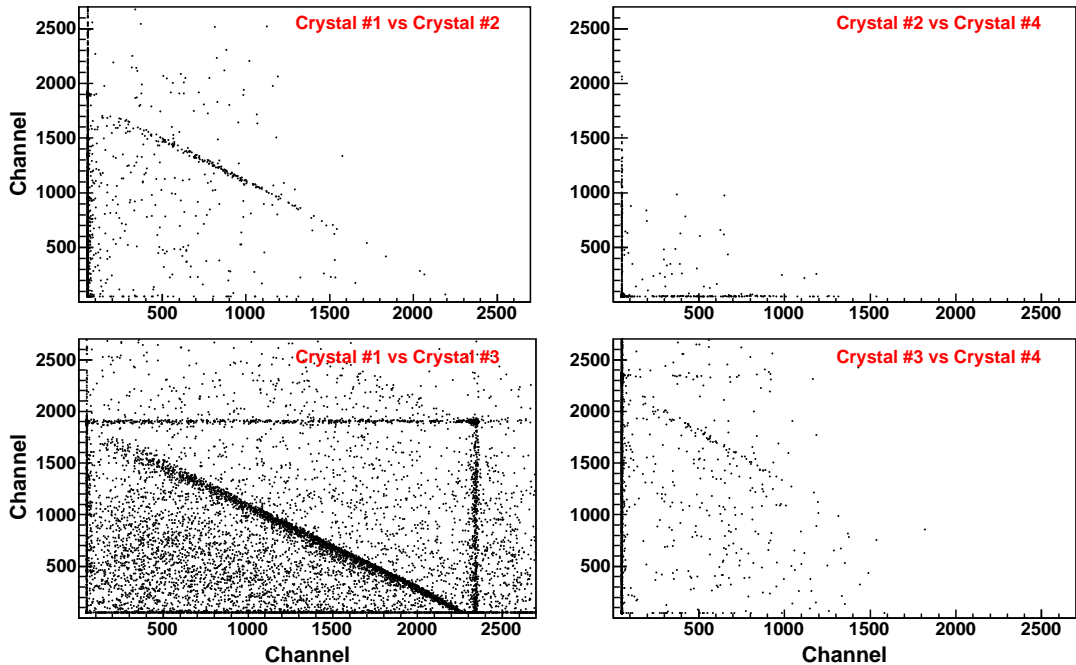

Figure 4.4: Correlation spectra obtained for neighbor crystals

To address this issue, we used the correlation between neighbor crystals (#1 vs. #2, and #3 vs. #4, see Figure 4.4), to obtain the gain relations. Once Crystals #1 and #3 had been calibrated, we used these gain relations to calibrate Crystals #2 and #4, which made it possible to reconstruct the energy protons hitting two or more crystals.

The energy calibration was performed using proton runs at 92, 120 and 180 MeV (corresponding, respectively, to 84, 117 and 173 MeV proton energies after energy losses in the DSSSD and the ProtoZero aluminum box). Figure 4.5 shows the calibration curves for all detectors of this prototype configuration. From this plot, we can conclude that CsI(Tl) crystals coupled to APDs have quite a linear response for protons in the energy range between 90 and 180 MeV.
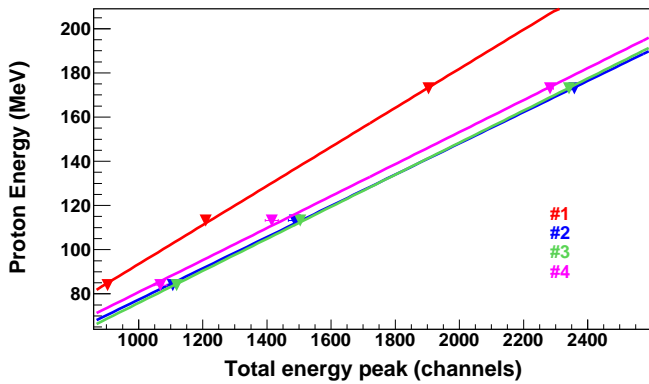

Figure 4.5: Energy calibration curves obtained using runs with protons at 92, 120 and 180 MeV for all detectors of this prototype configuration.

Using the correlation between Crystals #1 and #3, events leaving energy in both crystals could be selected, as seen in the diagonal cut in Figure 4.6 (left). When these events are added after an energy calibration, the result is the reconstructed peak in Figure 4.6 (right). In this plot, we can clearly see degradation at the left part of the peak. This degradation translates into an energy resolution of ∼3%, which is quite a bit worse than the resolutions obtained for Crystals #1 and #3 individually (see Figure 4.3).

We could also use the information provided by the DSSSD to identify protons hitting near the boundary between Crystals #1 and #3. Figure 4.7 (left) shows the beam profile obtained with the DSSSDs and the relative position of all the detectors (#1 to #4). In this plot, events in two different regions were selected. In Region A, events detected in the DSSSD correspond to protons hitting near the interface between Crystals #1 and #3, while in Region B the events detected correspond to protons that were deposited in Crystal #3.

Figure 4.7 (right) shows the reconstructed peaks for both regions, along with the reconstructed peak using all events. Here, we can see that events sharing the proton energy between Crystals #1 and #3 produce a wide peak located more than 1 MeV below the main peak. This peak shows the energy loss for protons passing from one crystal to another. These energy losses are produced because the electrons generated in the proton path are stopped and absorbed by the wrapping
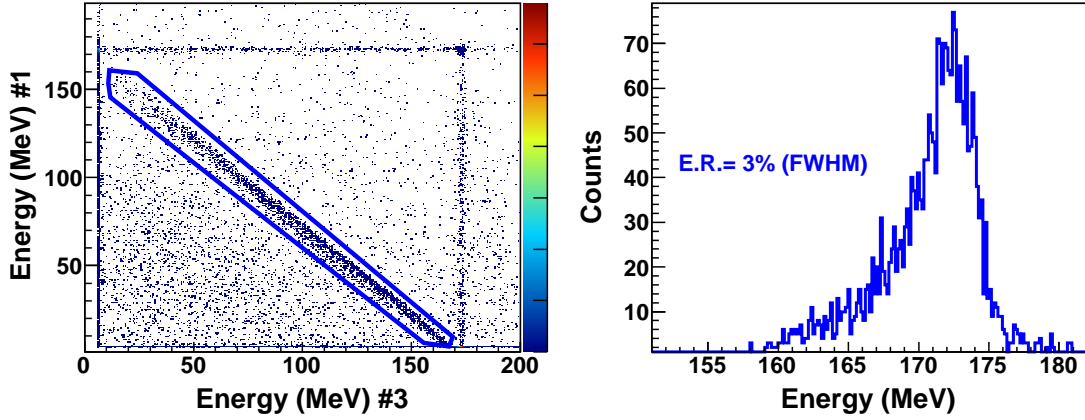
Figure 4.6: Left: Correlation between Crystals #1 and #3. Right: Addback between Crystals #1 and #3.

material. This was identified in the proton simulation presented in Chapter 2.
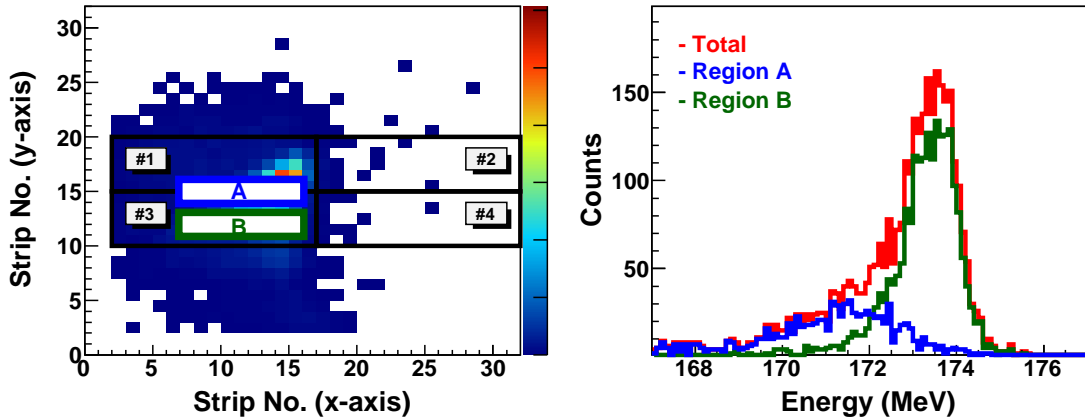
Figure 4.7: Left: Beam profile obtained with the DSSSDs, relative positions of all the detectors (#1 to #4), and selection of protons hitting A) the region between crystals B) region inside Crystal #3. Right: Spectra obtained for protons hitting in regions A, B and Total.

This problem was also addressed by Di Julio *et al.* (see [25]), who participated in this experiment with the irradiation of another CsI(Tl) prototype. Di Julio *et al.* performed a GEANT4 simulation to describe the problem and to calculate the minimum thickness producing this effect. The result of their simulation confirms the one presented in Chapter 2, which shows that the thicker the wrapping, the higher the energy loss (peak degradation). This degradation could be a problem in experiments where protons with slightly different energies have to be identified, but can be minimized using thinner crystal wrappings.

Another problem we encountered was that proton identification at the DSSSDs introduces a certain amount of beam straggling. Figure 4.8 shows for each axis the percentage of protons detected in each DSSSD strip when the full energy was deposited in crystals #1 and #3. Square boxes indicate the position occupied by each crystal (see labels in the upper part of the boxes).

For example, in Figure 4.8 (right), we can see that 3% of the protons leaving their full energy in Crystal #3 were detected in Strip 8, which is 4 mm away from this crystal. The same problem can be observed for protons that left their full energy in Crystal #1 and were detected beyond Strip 20 in the DSSSDs. A more complete analysis cannot be realized, due to the complex shape of the crystals and the lack of a complete proton tracking (angles) before the detection.
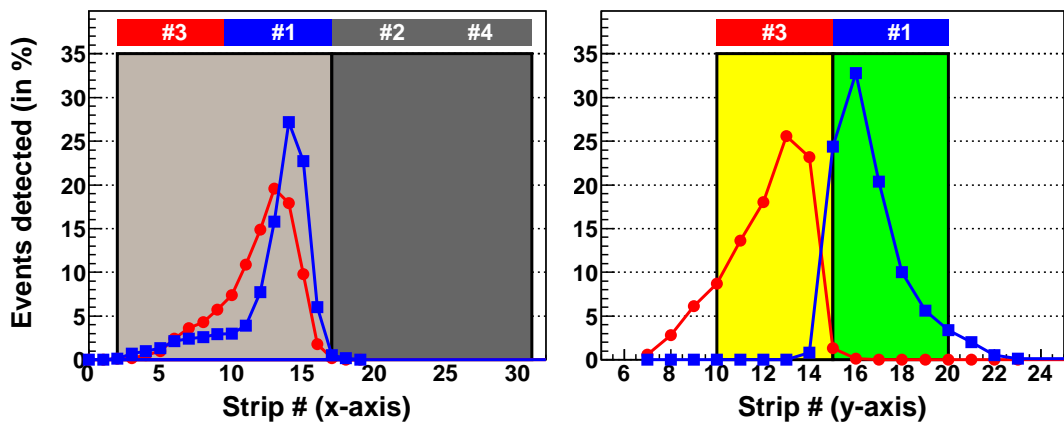

Figure 4.8: Number of events (in %) detected in Crystals #1 and #3, as a function of the strip number for the x and y axes in the Silicon Strip Detectors (DSSSD).

4.2. Beam test with 6.1 MeV gammas

4.2.1. Experimental setup

In this experiment, a Teflon target was bombarded using protons at 1 MeV extracted from the 5 MV Tandem accelerator at the Spanish facility 'Centro de Microanálisis de Materiales' (CMAM). The resulting reaction ($^{19}F(p,\alpha\gamma)^{16}O$) produced 6.1 gammas (the first excited state of ^{16}O) that were used to irradiate the prototype. The proton beam at 1 MeV had an approximately constant intensity of 1.5 μA. The Teflon target used was 30 mm in diameter, 5 mm thick, and covered with a Copper grid in order to discharge the current produced by the proton beam.

For this experiment, a prototype was built consisting of sixteen bi-frustum shaped CsI(Tl) crystals with different exit faces (10x10, 7x14 and 10x20 mm^2) to

match different APD models (Figure 3.2). These crystals were wrapped with two layers of Teflon tape and a single layer of ESR. An aluminum box was used to electrically isolate the system (see Figure 4.9).
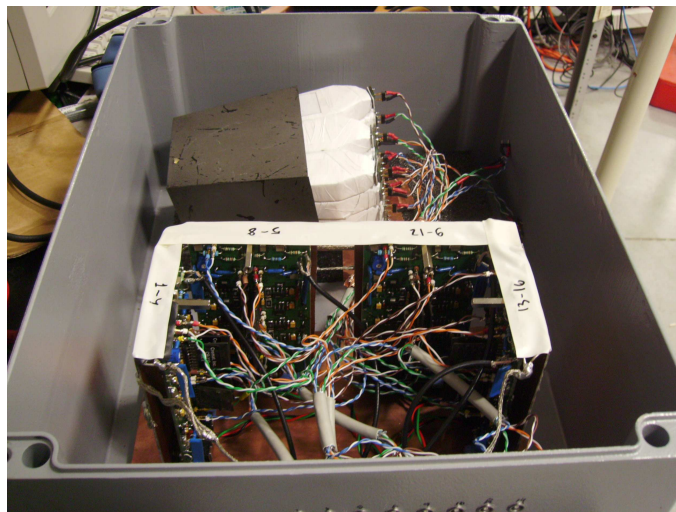
Figure 4.9: Detector used for the CMAM experiment

The crystals and APDs were placed inside the box, together with the Cremat CR-110[4]) 4-channel preamplifiers.

Mesytec MSCF-16[5] amplifiers were used in this prototype configuration along with a CAEN N472 4-channel power supply. The data acquisition was performed using Midas [66].

4.2.2. Results

In this section we will present the results obtained with this prototype configuration under 6.1 keV gammas irradiation. This part is focussed on the several relevant parameters that should be taken into account in the final CALIFA performances, for instance, the energy calibration, the crystal multiplicity, the system stability, etc.

In this particular case, noise problems prevented us from connecting more than 6 crystals to the data acquisition system. In order to collect as much information as possible, the central crystal and those surrounding it were chosen. Figure 4.10 shows the calibrated energy spectra obtained for these six crystals under irradiation. The Crystal #01, shown in the last position for convenience, was placed over Crystal #03 (central crystal). In this plot, we can distinguish peaks at energies of 511, 1275, 5107, 5618 and 6129 keV. The first two peaks correspond to

---

[4]Specifications in Appendix D.
[5]Specifications in Appendix D.

gamma photons produced in a ^{22}Na radioactive source placed near the crystals and taken as reference, and the third, fourth and fifth peaks are the single escape, the double escape, and the actual 6.1 MeV gamma peak from the ^{16}O produced at the target after proton irradiation (^{19}F(p,$\alpha\gamma$)^{16}O).
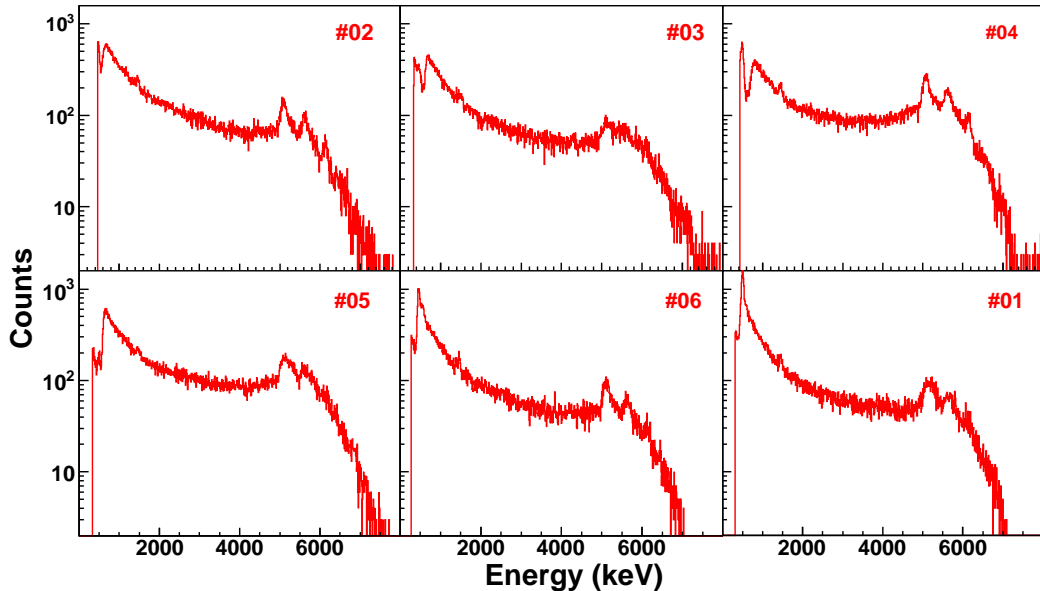

Figure 4.10: Spectra obtained with six prototype crystals

Since channel number is proportional to energy, the channel scale can be converted to an energy scale. The gamma energies mentioned above and their corresponding peak positions in the spectra were used to calibrate these detectors in energy.

Figure 4.11 shows the energy calibrations for all detectors in this prototype configuration. These experimental data fit well using a linear function, indicating that the detectors (CsI(Tl) crystals + APDs) have quite a linear response for gammas in the range between 511 keV and 6.1 MeV.

Once all the detectors had been calibrated, an add-back procedure to sum signals coming from different crystals was performed. Results are shown in Figure 4.12, along with the energies of the reconstructed peaks. Table 4.1 shows the calculated energy resolution for all the peaks. The resolution was obtained by fitting the peaks to a Gaussian function with an exponential background.

Crystal multiplicity

Crystal multiplicity is defined as the number of crystal hits in each event. A multiplicity of one indicates that the incident gamma or proton hit only one crystal;
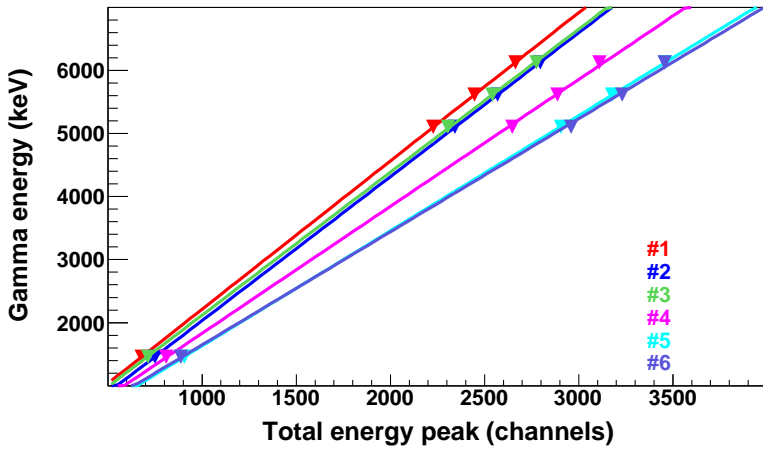
Figure 4.11: Energy calibration curves for six crystals of this prototype configuration.
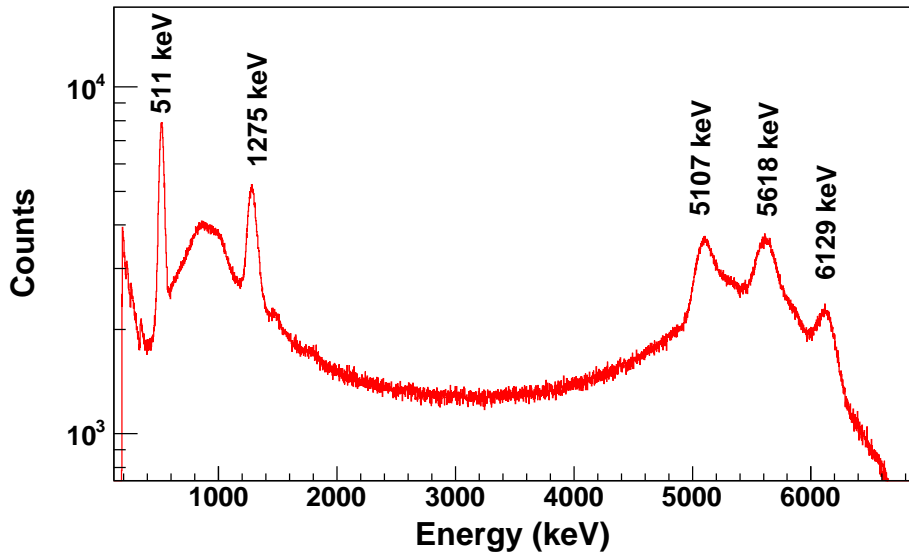
Figure 4.12: Spectrum obtained after adding the energy of all the crystals

Energy peak (keV)	511	1275	5107	5618	6129
Energy resolution (%)	9.0	7.0	3.4	3.1	2.8

Table 4.1: Energy resolution obtained after addback.

multiplicity two means that two crystals were hit, and so on. Figure 4.13 shows the multiplicity comparisons for runs with five and six crystals.

A closer look at the multiplicity reveals that the proportion among the three peaks depends on multiplicity in the addback spectrum (Figure 4.14). If a multi-
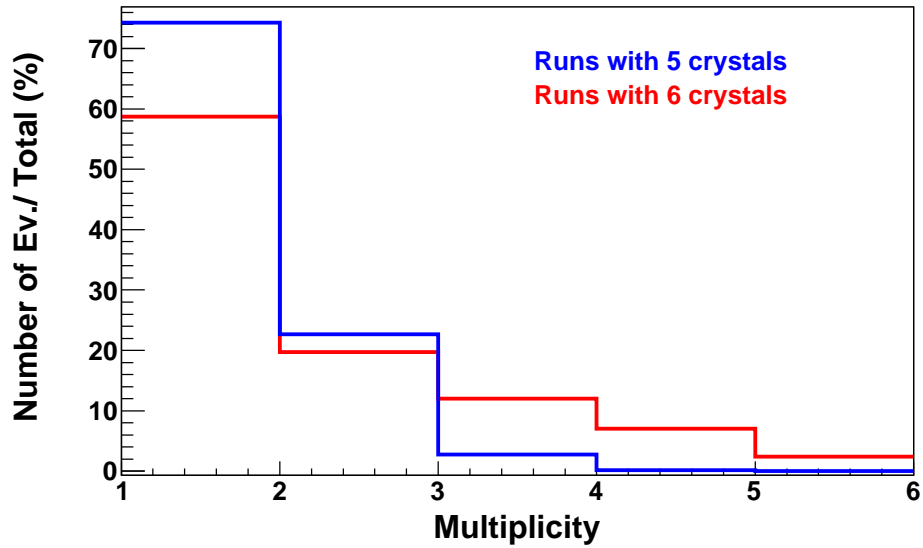
Figure 4.13: Multiplicity comparison for runs with five and six crystals
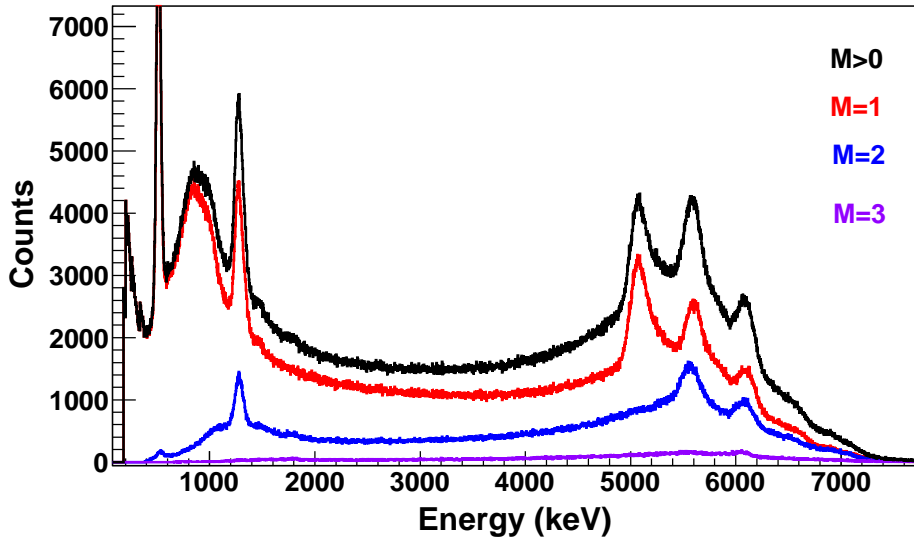
*Figure 4.14: Addback spectrum with different multiplicities*

plicity 2 is forced, at least one of the 511 keV gammas produced in the annihilation process is with larger probability recovered, resulting in the reduction of the double escape peak. If a multiplicity 3 is forced, the two 511 keV gammas are recovered, but the efficiency with only six crystals is very low.

System stability

For this beam test, neither voltage nor temperature required monitoring. However, a possible gain drift due to temperature or voltage variations during the measurements could be investigated by plotting, for each calibrated event, the ADC energy vs. the event number.
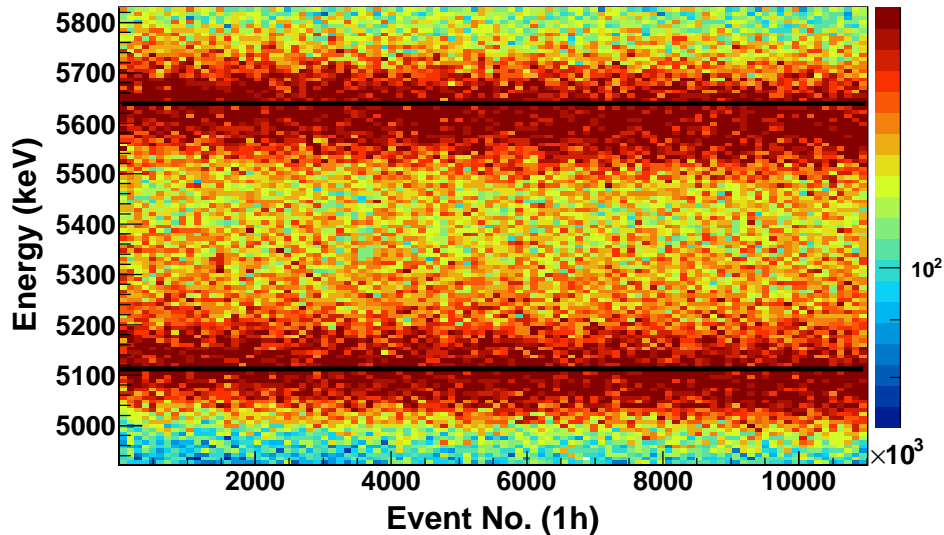

Figure 4.15: Representation of the energy in keV of each calibrated event vs. event number (∼1h run).

Figure 4.15 is obtained after compiling a histogram of the calibrated energy for each event as a function of the event number, which is proportional to time, for a 1-hour run. In this bi-dimensional histogram, the x-axis shows the accumulation of events and the y-axis represents the spectrum of the detected gammas. There are two regions (top and bottom) where the event density is high. These regions correspond to the 5107 and 5618 keV peaks in Figure 4.12.

The black lines indicate the initial energy for these two peaks during the entire acquisition time. We can observe how the event density is displaced from the black lines as the event number increases. The displacements indicate certain gain drifts for two peaks as a function of time, and allow us to correct each event using a function that depends on the event number.

In order to perform this procedure, the mean value of a selected region in these histograms was calculated. For instance, in Figure 4.16, the mean peak position vs. the event number for the 5107 keV peak is represented with black points. These points were obtained using a binning in the x-axis corresponding to a time window of 100 seconds, and the error bars indicate the dispersions of both the peak centroid

for the y-axis and time for the x-axis.
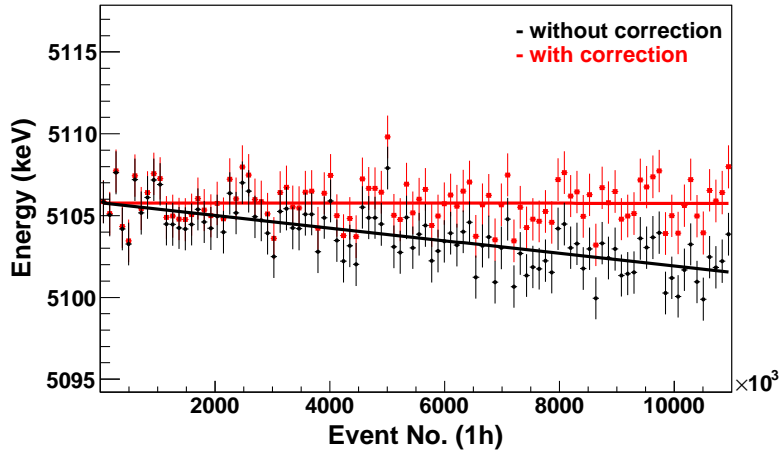
Figure 4.16: Mean peak position vs. event number. These points represent the gain variations and the error bars indicate the dispersions in peak determination (for y-axis) and in time (for x-axis).

If we fit these points using a linear function, the parameters obtained can be used to correct each event, giving as a result the red curve shown in the same plot.

We applied this correction to the energy spectrum for this gamma, which resulted in a slight improvement in the energy resolution (from 3.4% to 3.3%) that can be seen in Figure 4.17.
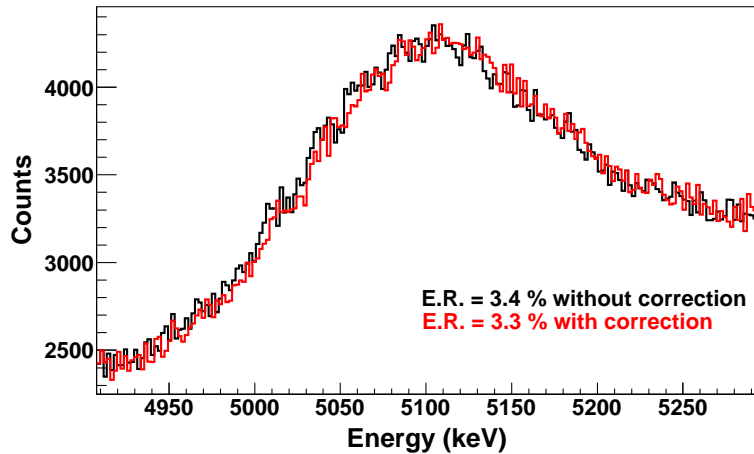
Figure 4.17: Energy spectrum of the 5107 keV peak with and without gain correction.

4.3. Beam test with tagged gammas at 4-10 MeV

This experiment was performed at the Technische Universität Darmstadt (TUD) in Darmstadt (Germany). This university has an electron accelerator (S-DALINAC) that serve the NEPTUN facility, where the electrons collide against a thin target called a 'radiator', producing gammas by bremsstrahlung radiation.

4.3.1. The NEPTUN tagger setup

The basic idea of a photon tagger is to select photons of a certain energy out of a continuous energy bremsstrahlung spectrum. This principle is shown in Figure 4.18. A continuous monoenergetic electron beam (E_0), typically 20-30 MeV, is used to produce bremsstrahlung photons on a radiator target made of 10 μm-thick gold.

When dealing with electrons or photons at high energies, it is convenient to define the so-called *radiation length* as the mean distance over which a high-energy electron loses all but $1/e$ of its energy by bremsstrahlung. With gold, this *radiation length* is 6.46 g cm^{-2} or 3.3 mm [67].

An electron may produce more than one photon on its way through the target; these are known as higher-order photons. Only first-order photon production is of interest in a tagging facility. The ratio of higher order photons must be kept lower than 1% in order to increase the tagging efficiency. This can be achieved with a 10 μm thick gold target [68].

By using a homogeneous magnetic field to deflect the inelastically scattered electrons onto a focal plane detector, the momentum of the electron (p_e) and therefore, the energy of the scattered electron (E_e) can be found by determining its position in the focal plane. The energy of the corresponding photon (E_γ) is simply calculated as the difference between the energy of the scattered electron and the incident beam energy (E_0)

$$E_\gamma = E_0 - E_e \tag{4.2}$$

The focal plane detector consists of 128 Bicron BCF-12 scintillating fibres with a 1 mm^2 square profile. To increase the light output without losing spatial resolution, two scintillating fibers are combined to form a single 1 x 2 mm^2 detector cell. Each pair of fibers is coupled to a pair of light guides (Bicron BCF-98), and then read by a single photomultiplier tube (Type 9108SB) (see [69]).

The energy resolution that can be achieved by such a tagging system corresponds directly to both the energy resolution of the electron beam and the granularity of the focal plane. Photons are assigned to electrons by a time-delayed coincidence between the electron hits in the focal plane and the gammas detected in the ProtoZero.

The event rate in the focal plane detector is around several MHz per fiber, indicating that the data acquisition cannot be triggered by the focal plane itself.

The hits in the focal plane detector cells were, therefore, continuously recorded in the hit buffer of a multihit TDC (CAEN V1190). This allowed us to read out the timestamps of each hit within a certain time window relative to a trigger signal, which was provided by the detectors at the ProtoZero.
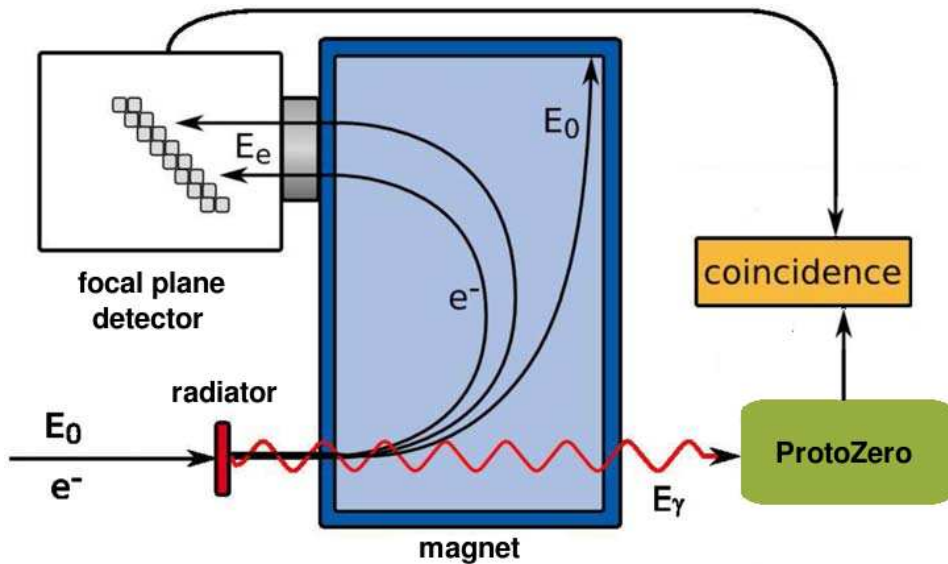

Figure 4.18: Principle of a photon tagger. A monoenergetic electron beam produces single photon events on a very thin radiator target. The scattered electrons are detected in a focal plane detector (fibers). If the photon undergoes a reaction at the experimental target and an appropriate coincidence has occurred, its energy is determined by Eq. 3 [70].

4.3.2.   Experimental setup

For this experiment at TUD Darmstadt, we used the same prototype configuration as that which was used for the CMAM test beam. Figure 4.19 shows the prototype configuration for this test beam.

The crystals and APDs were placed inside the box, along with two 8-channel Mesytec preamplifiers (MSI-8[6]). This box also contained two small plastic containers with Silica gel to keep the humidity level below 30%. Additionally, a PT-1000 temperature probe was placed near the APDs being monitored using one channel of the VME acquisition.

Signals from the preamplifiers were sent to Mesytec MSCF-16[7] amplifiers. The HV power was supplied by two I-SEG 2-channel high precision modules, which

---

[6]Specifications in Appendix D.
[7]Specifications in Appendix D.
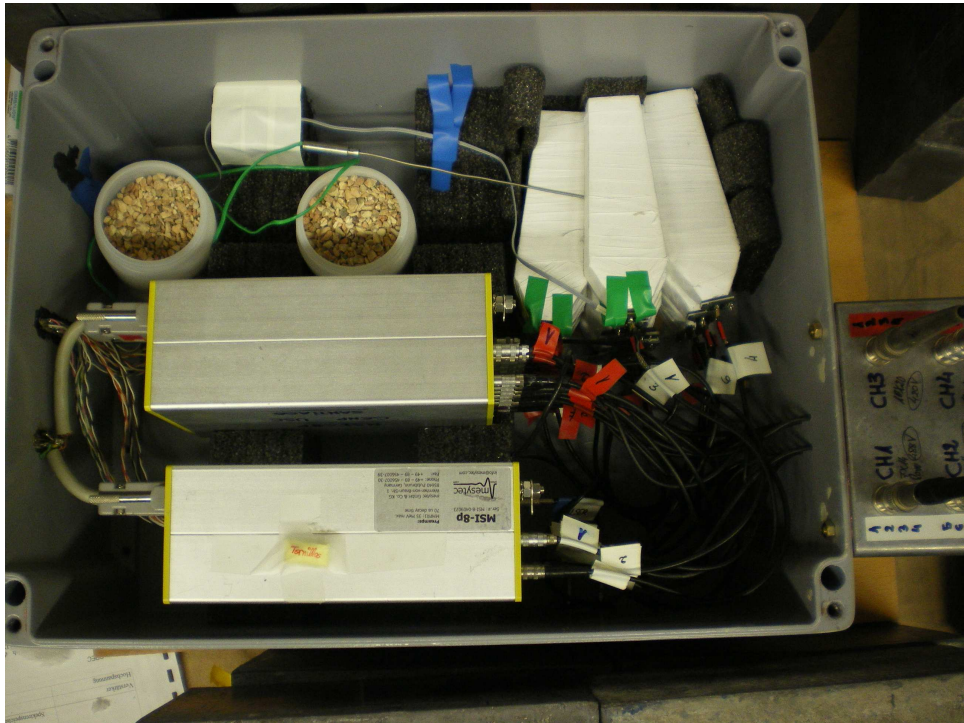
Figure 4.19: Configuration of the prototype for the TUD experiment

allowed us to monitor the bias voltage drift. The amplifiers readout was sent to a CAEN V785 32-channel VME multi-event peak-sensing ADC with 12-bit resolution and fast conversion time. The acquisition was performed using the CATCH module (for further details see Ref. [71].

4.3.3.   Results with calibration sources

Calibration sources

Several radioactive sources (^{137}Cs, ^{60}Co, ^{22}Na and ^{56}Co) were used to calibrate the prototype. Figure 4.20 shows the spectra obtained for the fifteen crystals used in this prototype configuration, using the ^{137}Cs and ^{60}Co radioactive sources. These sources were placed 2 cm away from the ProtoZero Box, and the ^{137}Cs source was placed just in front of detector 07, while the ^{60}Co source was placed in front of detector 09.

The information from these figures was used to determine pedestals and thresholds. Thresholds were established at three sigmas to the left of the pedestal's Gaussian fit. These thresholds allow us to discriminate if the detectors were hit by the incident gamma-ray. Once the detectors had been calibrated, the energy of the gammas emitted from the sources were reconstructed adding the signals of each crystal to obtain what is known as the *addback spectrum*.
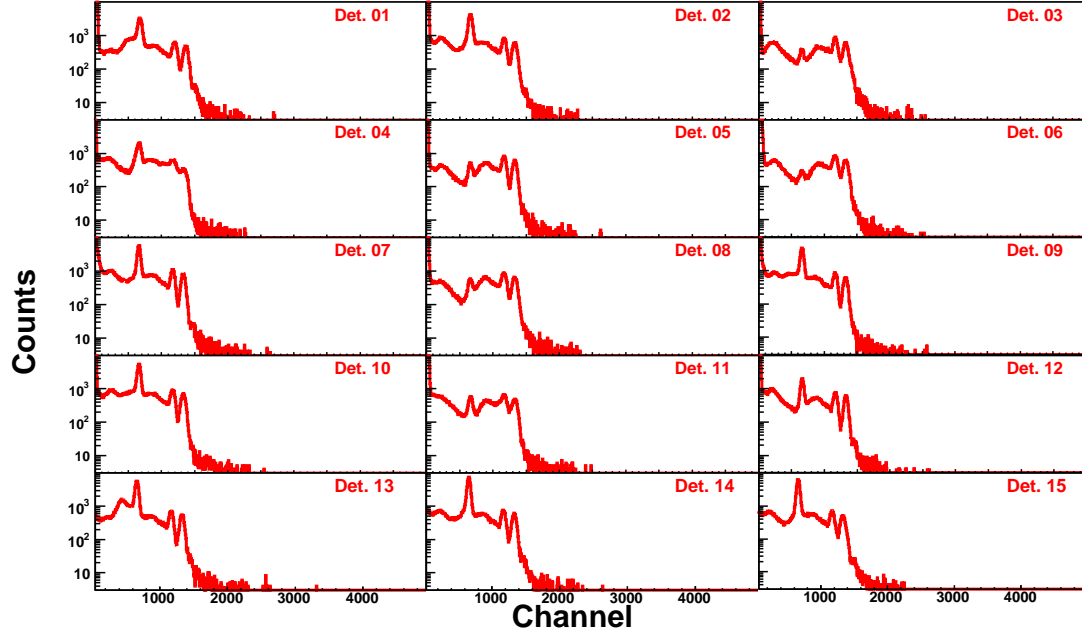
Figure 4.20: Spectra obtained for a prototype configuration with 15 crystals using
^{137}Cs *and* ^{60}Co *radioactive sources.*

Figure 4.21 shows the reconstructed spectra for ^{60}Co, ^{137}Cs and ^{56}Co. These
plots include the energies corresponding to each peak. Reconstruction of ^{137}Cs and
^{60}Co sources shows a small background below 662 keV, because all the scattered
gammas were fully recovered and thus contributed to the photopeak.
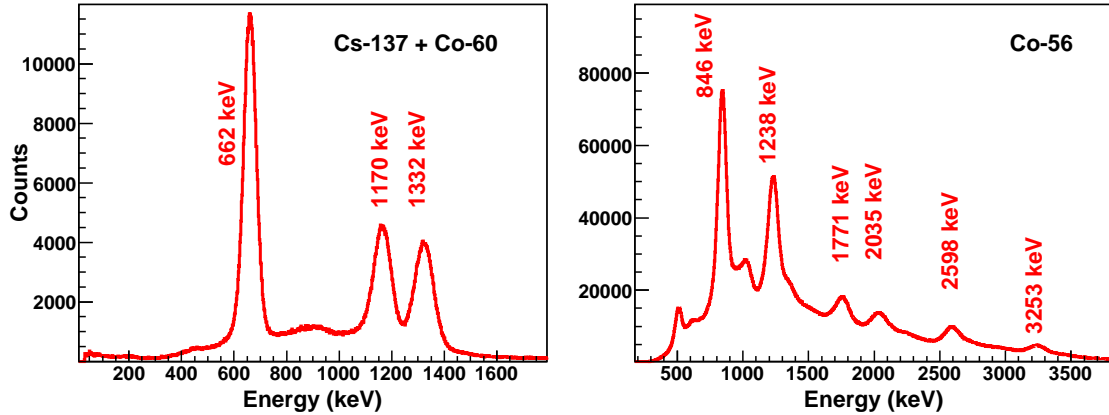
Figure 4.21: Left: addback spectrum for ^{60}Co *and* ^{137}Cs *radioactive sources. Right:*
addback spectrum for the ^{56}Co *radioactive source.*

Table 4.2 shows the energy resolution achieved after addback for a ^{56}Co

radioactive source. Note that these values are quite a bit worse than those obtained with single crystals in Chapter 3. This is due to the fact that the reconstructed peak has the average energy resolution (weighted mean) of all crystals. The values could be much better if all the crystals had the same exit face and the same type of APD.

| Energy peak (keV)	846	1238	1771	2035	2598	3253
Energy resolution (%)	6.9	5.8	5.5	5.7	4.0	3.9

Table 4.2: Energy resolution obtained after addback for ^{56}Co.

Background

In order to see the background contribution, a 4-hour background spectrum was recorded (Figure 4.22). In this spectrum, the 1460 keV peak from ^{40}K, the 1764 keV peak from ^{214}Bi and the 2614 keV peak from ^{208}Tl can be clearly distinguished. The first peak corresponds to ^{40}K, which is widely distributed throughout the natural world. It can be found in soil and in all plant and animal tissues. The second peak corresponds to ^{214}Bi, which belongs to the ^{238}U decay chain. The third peak corresponds to ^{208}Tl due to the ^{232}Th decay chain; both substances are present in the concrete walls of the experimental hall. As these isotopes (^{214}Bi and ^{208}Tl) decay, they emit several gamma rays with energies below 1460 keV, which cannot clearly be identified in the addback spectrum.

Temperature calibration

In Section 3.4.4, we explained how temperature drifts affect the APD gain. These variations affect the position of the peaks in the energy spectrum, resulting in energy resolution degradation. The temperature should be monitored in order to correct the APD gain, especially in experiments where low counting rate leads to long periods of data taking.

An experiment was performed to determine the gain drift due to temperature variations and to correct the peak position using the temperature information. For this purpose, a PT-1000 temperature probe was placed near the APD being monitored using one channel of the acquisition system.

The ProtoZero was cooled down using liquid nitrogen vapor, and warmed up using a heater (radiator). The radioactive reference source used was ^{137}Cs with an activity of 1.6 GBq, from which a peak with enough statistics can be obtained even when the temperature drift is pronounced and the acquisition time is very short.
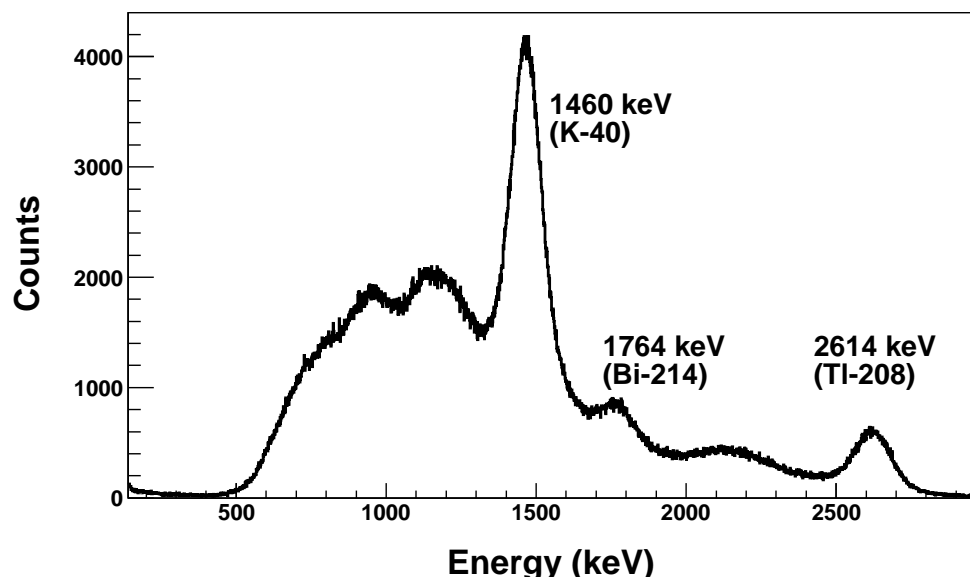
Figure 4.22: Reconstructed 4-hour background spectrum for the prototype.

Six 5 cm thick lead bricks with a 1 cm diameter hole were used as collimation.
Figure 4.23 shows the mean peak position and temperature vs. time recorded for
this experiment.
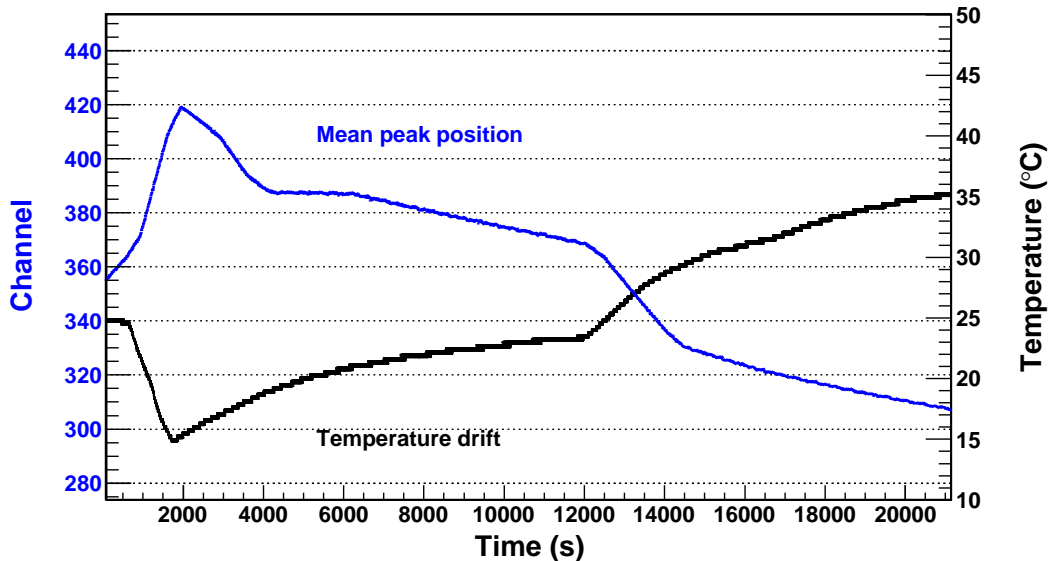
Figure 4.23: Mean Peak position and Temperature vs. time. See explanation in the
text.

We can observe a clear correlation showing that, if the temperature decreases, the peak position increases, as it was shown in Section 3.4.4. The plot also shows a 70 second time displacement between the minimum temperature value and the maximum peak position value, which indicates that the APDs were affected by temperature changes 70 seconds before the temperature probe was affected. This displacement will be much lower in the case of the CALIFA calorimeter, where the temperature drifts are expected to be of few degrees in several hours. The huge background present in the spectrum shown in Figure 4.24 is due to the pile-up produced by the high activity of this source. In addition, the backscattered gammas on the walls, the ground and the lead shielding of the radioactive source, together with the characteristic X-rays (produced in the lead bricks) also contributed to the background in the low energy region.
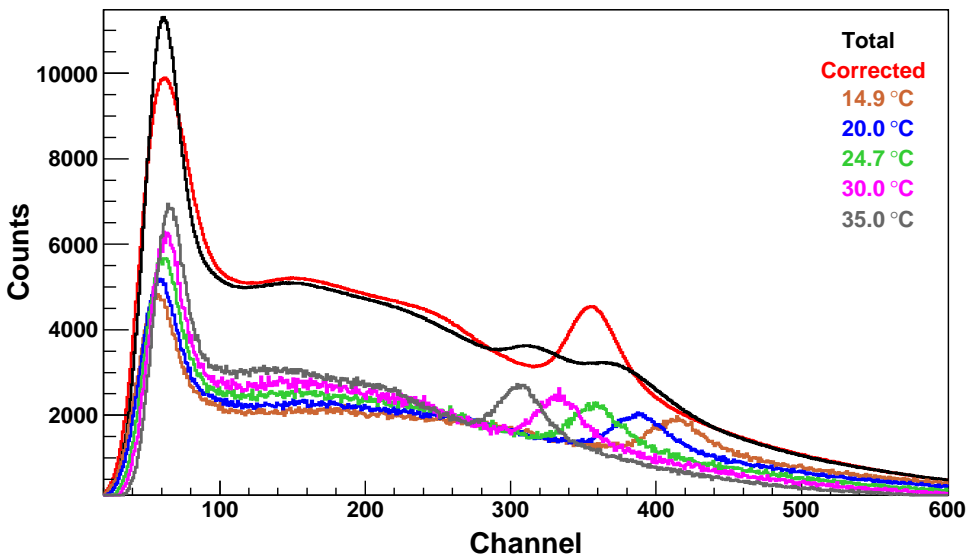
Figure 4.24: Total and gain drift corrected spectra for a ^{137}Cs radioactive source.

Using this information, the final spectrum was corrected and is shown in Figure 4.24. This plot also presents spectra for temperatures from 14.9 to 35 degrees, in order to see the constant displacement of the photopeak.

4.3.4. Results with tagged gamma beams

The energetic range of tagged gammas is around 1 MeV, for a given electron beam energy and magnetic field setting, and is determined by the size of the focal plane. Several runs centered at three tagged energies (4, 7, and 10 MeV) were performed. An additional run with 4 MeV tagged gammas using a lead collimator

was performed to see how the prototype would respond when the incident gamma impinged on the central crystal.

Time window

We discussed in Section 4.3.1, how photons of a certain energy have to be selected out of a continuous bremsstrahlung spectrum. In our case, the acquisition system recorded all the photons impinging on any crystal. A coincidence system was then used to select the desired photons.

The tagger setup has 64 fiber pairs (designated as fiber 00 up to fiber 63) that give a signal after each electron hit. These signals are in time coincidence with the master trigger (MA) signal, which can be given by any prototype crystal. Figure 4.25 shows the time correlation for different selected fibers in a run with a tagged energy of 10 MeV. The plot shows that all the correlated events between crystals and fibers are concentrated within a time window of around 100 ns.
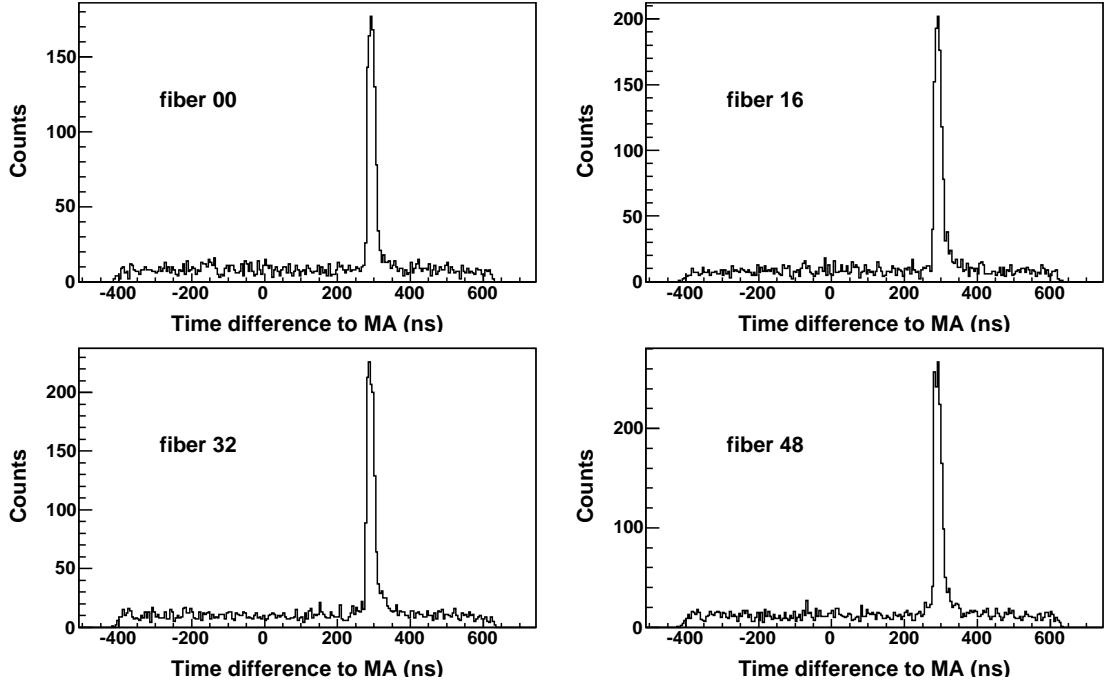
Figure 4.25: Histograms representing the time difference between the trigger given by the ProtoZero (MA) and the electrons hitting the fibers.

The flat background of these plots is due to non-correlated coincidences between electrons hitting in fibers and gammas hitting the ProtoZero crystals.

Figure 4.26 shows the same histograms for a selected fiber (fiber 00) at four different tagged energies. For runs without collimation, we can deduce that the

proportion between valid gammas (subtracting background) and non-correlated coincidences are of the order of 5-7%. For the run with collimation this proportion was very low, because most of the valid gammas were stopped by the lead block used for collimation.
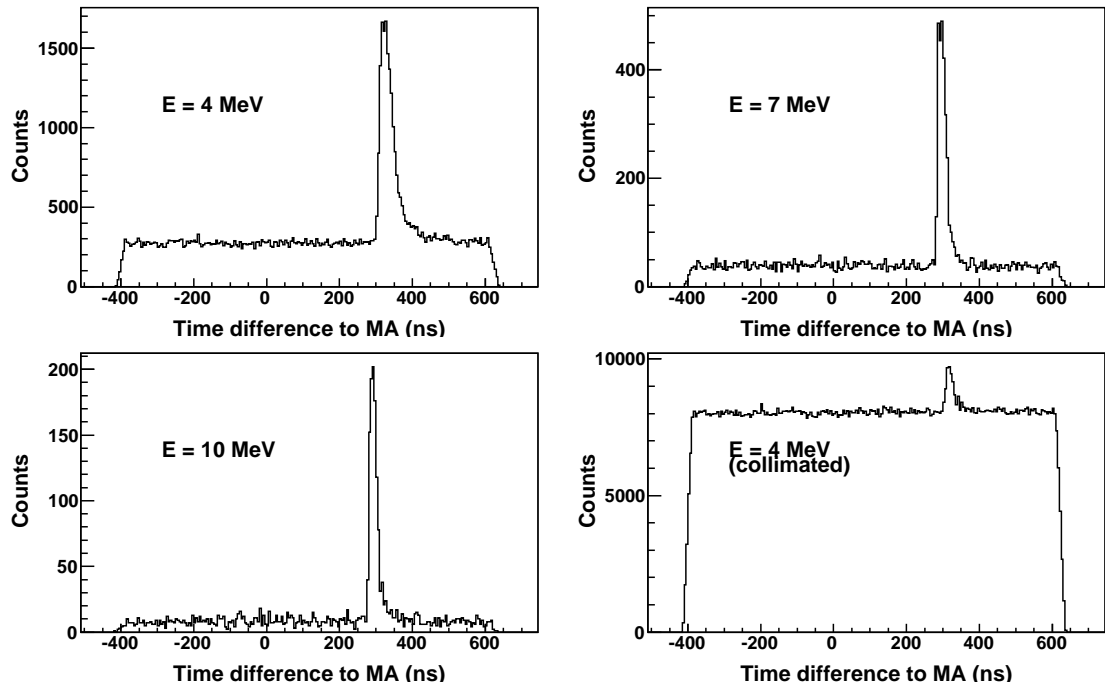
Figure 4.26: Histograms for addback at different energies, representing the time difference between the master trigger (MA) and the electrons hitting the selected fibers.

The time windows also depend on the fiber, as can be seen in Figure 4.27. Here, the higher the fiber number, the wider the selected window should be in order to get the correlated coincidences.

Fiber selection

Each fiber determines the electron energy and so the energy of the tagged photon (see Equation 3). Once the time windows had been chosen for each histogram, we represent those correlated events corresponding to a given energy. Figure 4.28 shows the spectra of the reconstructed gammas for different tagged energies.

The higher the tagged energy, the lower the statistics, due to a lower gamma yield at the radiator. In these plots, the proportion between the reconstructed peak and escape peaks (single and double) can be seen.
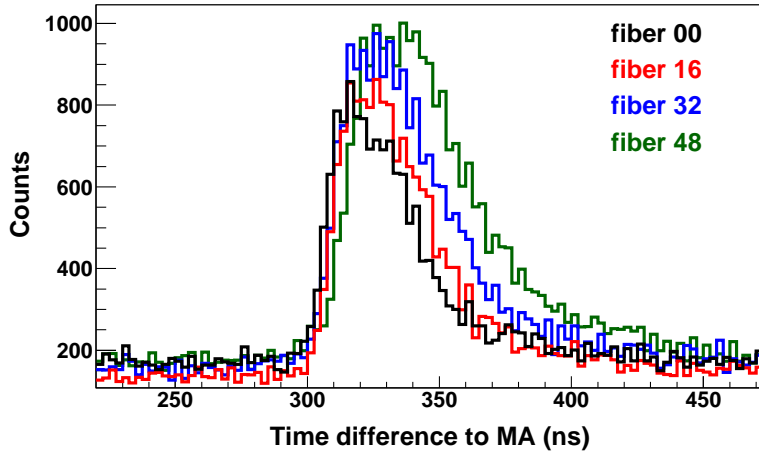
Figure 4.27: Histograms representing the time difference between the master trigger (MA) and the electron hitting the fibers for the same run (4 MeV tagged gamma energy).
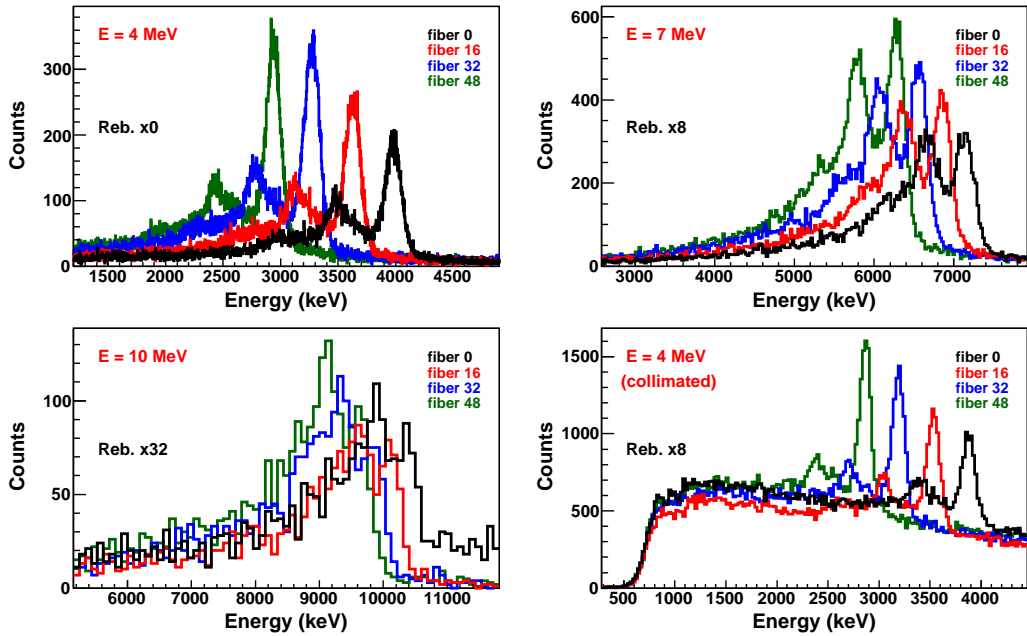
Figure 4.28: Energy spectra of the reconstructed gammas after selection of several fibers at different tagged energies.

Figure 4.29 shows the reconstructed energy spectra obtained after selection of fiber 48 at the three tagged energies (4, 7, and 10 MeV). The energy resolution of these peaks will be determined and compared with the simulated values in the next section.
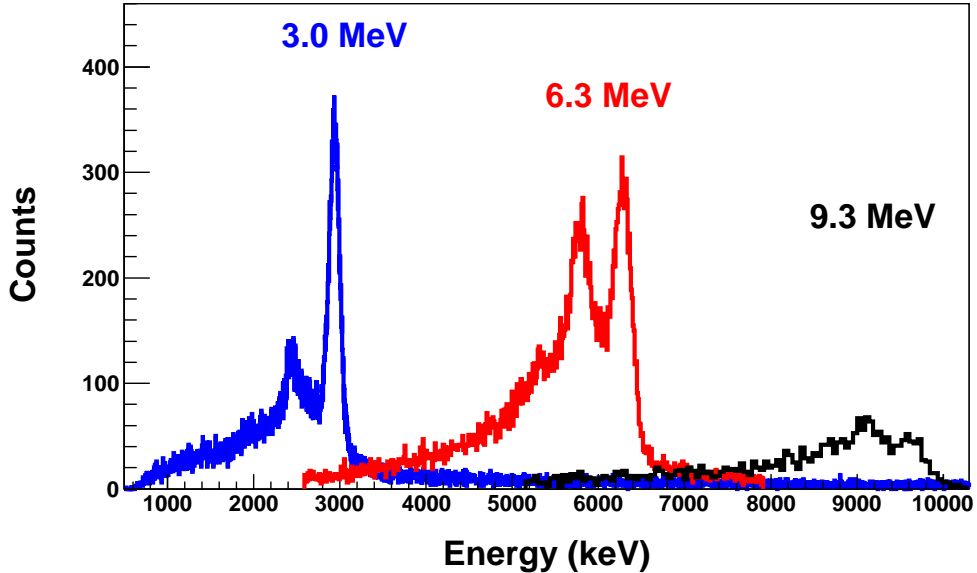
Figure 4.29: Reconstructed energy spectra obtained from the same fiber (48) at different tagged energies.

4.3.5. Comparison with simulations

The aim of the tagged gamma simulation was to compare the observables (energy resolution, full energy peak efficiency and crystal multiplicity) with the data obtained from the experiment performed at TUD Darmstadt. This simulation (based on GEANT4 and ROOT) allows to reproduce and guarantees a better understanding of the incident gamma interactions with the detector material. The simulation also allowed us to define several beam characteristics: shape, center, width, etc.

For a fixed gamma energy, we tried to reproduce the experimental mean energy deposition and multiplicity distribution for each crystal of this prototype configuration. In a first step, we allowed a variation of the beam properties (beam width, center and shape) and once the simulated results fit the experimental spectra, we adopted the beam description as correct and used it for all the tagged energies in the experiment.

The beam profile selected for this comparison is shown in Figure 4.30 (left). This profile was obtained using 10^6 emitted gammas from the source. Figure 4.30 (right) shows the frontal view (in the R3BSim Simulation code) of this prototype configuration, along with the entrance position in the prototype for 10^3 emitted gammas (depicted as red dots). The prototype frontal view shows the area covered by this profile, and the plot confirms that most of the emitted gammas impinge upon the three central crystals.
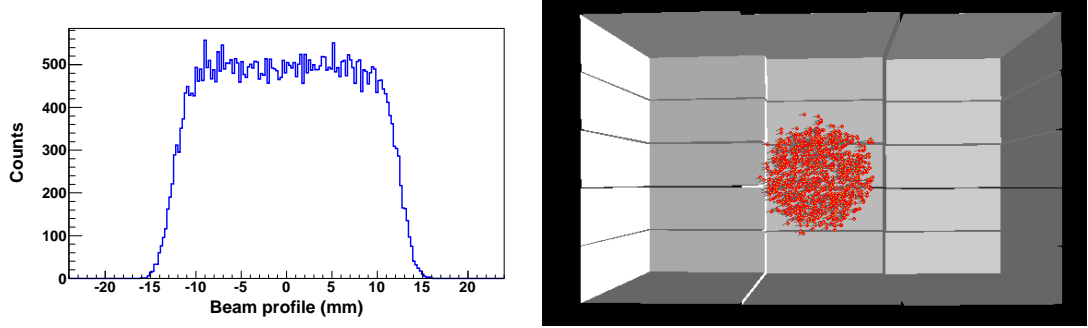
Figure 4.30: Left: Beam Profile used in the R3BSim program. Right: frontal view of the beam profile in the R3BSim program, together with the entrance position in the prototype for 10^3 emitted gammas (depicted as red dots).
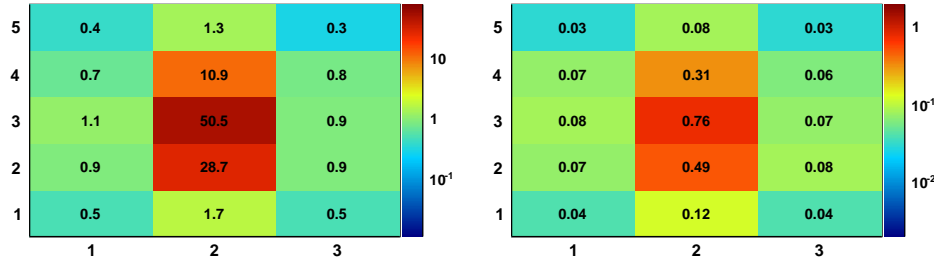
Figure 4.31: Experimental mean energy deposition in % (left) and crystal multiplicity distribution (right) for 4 MeV tagged gammas.
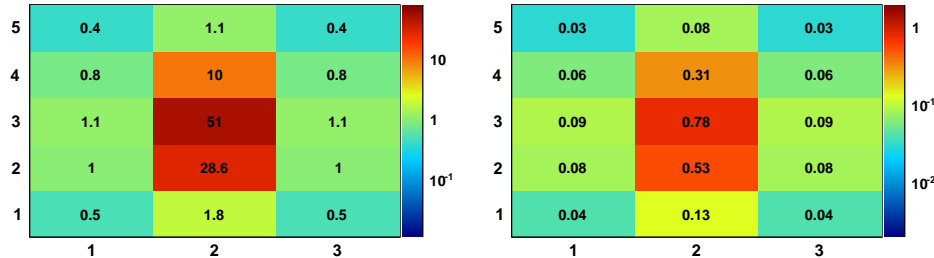
Figure 4.32: Simulated mean energy deposition in % (left) and crystal multiplicity distribution (right) for 4 MeV gammas.

Figure 4.31 gives a frontal view of the prototype with the experimental mean energy deposition (in %) (left) and crystal multiplicity distribution (right), measured for 4 MeV tagged gammas. The same observables can be obtained in

the simulation using the beam profile obtained from the simulation. Figure 4.32 shows the simulated mean energy deposition in % (left) and crystal multiplicity distribution (right) for the same energy of 4 MeV. The statistical uncertainty in these plots is not indicated, but the energy was below 0.1 keV and the multiplicity was below 0.01 for the simulated values, since they were obtained using very high statistics. However, the experimental values were obtained for around 1600 tagged gammas in the whole run, which produced uncertainties of about 0.3-0.5 keV in energy, and 0.02-0.05 in multiplicity. The simulated values are seen to be in good agreement with the experimental values, indicating that both the beam profile that was used and the interactions of the high-energy gammas with CsI(Tl) described the experimental situation rather well.

From these plots, the energy deposition and multiplicity distribution can be calculated for the different 'onion layers' around the central crystal, which we described in Chapter 2. These values, together with the experimental results for all the tagged energies, are compared in Figure 4.33.
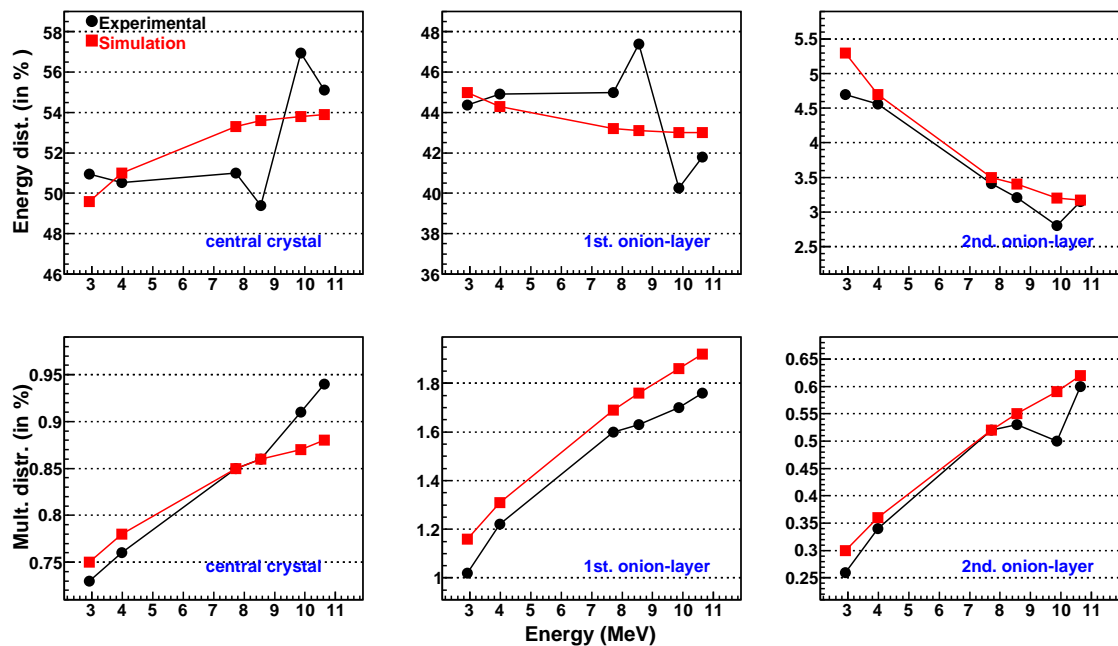

Figure 4.33: Experimental and simulated mean energy deposition (in % of the total energy), and multiplicity distribution, as a function of the tagged gamma energies.

These plots show the energy distribution (in % of the total energy) and multiplicity distribution for the central crystal, the nearest crystal neighbors (first onion layer) and for those crystals located in the outer part of the prototype (second onion layer).

A careful look at Figure 4.33, leads us to conclude that, despite the large statistical errors at high energies due to the low number of events recorded in the experiment, the simulation trends observed correspond rather well with the experimental data for energy and crystal multiplicity distributions.

Figure 4.34 provides a comparison between simulated and experimental values, for energy resolution (left), full energy peak efficiency (middle), and crystal multiplicity (right), as a function of the incident gamma energy. These observables were obtained after addback of all the crystals in this prototype configuration.
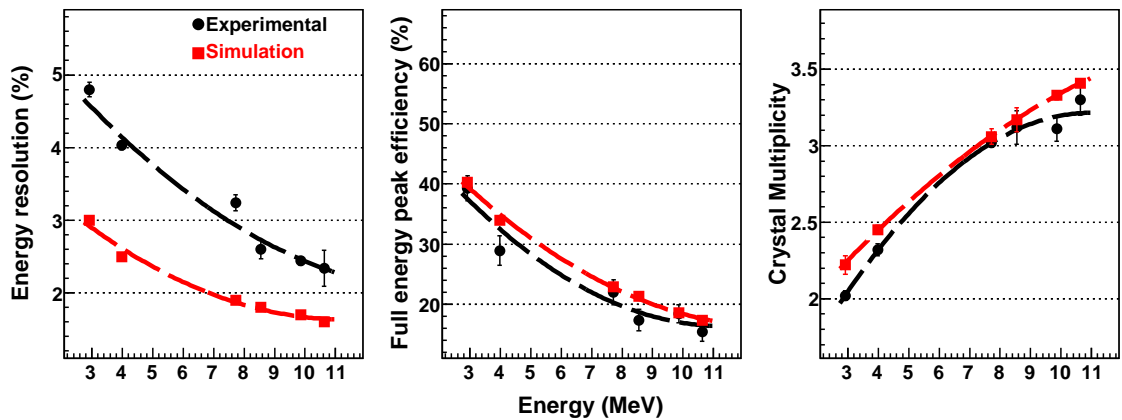
Figure 4.34: Experimental and simulated values in terms of energy resolution (left), full energy peak efficiency (middle), and crystal multiplicity (right), as a function of the tagged gamma energies.

Experimental energy resolutions were worse than simulated resolutions for two possibly reasons. Different types of crystals and APDs were used in this prototype, and they performed in different ways, resulting in worse energy resolution for some of them. This implies a energy resolution worsening when the final energy is calculated adding back the signal from all the crystals. In this experiments we have to deal with accidental coincidences coming from the bremsstrahlung process. These events cannot be properly separated from tagged gammas, which leads to a wider FWHM of the reconstructed peaks, as we can see in Figure 4.35.

The full energy peak efficiency was calculated as the ratio between the number of counts in the full energy peak and the total number of counts in the energy spectrum. This observable was corrected by a factor that takes into account the background contribution below the peak in the time correlation spectra (see Figure 4.26). The procedure consisted of counting the number of entries below these peaks and subtracting them from the total counts in the energy spectrum. Since these entries are non-correlated events and can have any energy, they can contribute equally to any channel in the energy spectrum. Once this procedure was applied, the experimental results fit well with the simulated values for this observable (see Figure 4.34).

Experimental and simulation values for crystal multiplicities were very close to each other. Small differences at low energies can be explained by differences in the noise level for each APD. If this noise level is higher than the signal produced by a scattered gamma, its corresponding energy is lost and the hit does not contribute to the multiplicity. In our simulation a 50 keV noise level for every detector was established, but the experimental levels ranged from 30 to 80 keV depending on the APD performance. This could explain the differences in multiplicity for low energies, though the effect seems to be smaller for high energies.
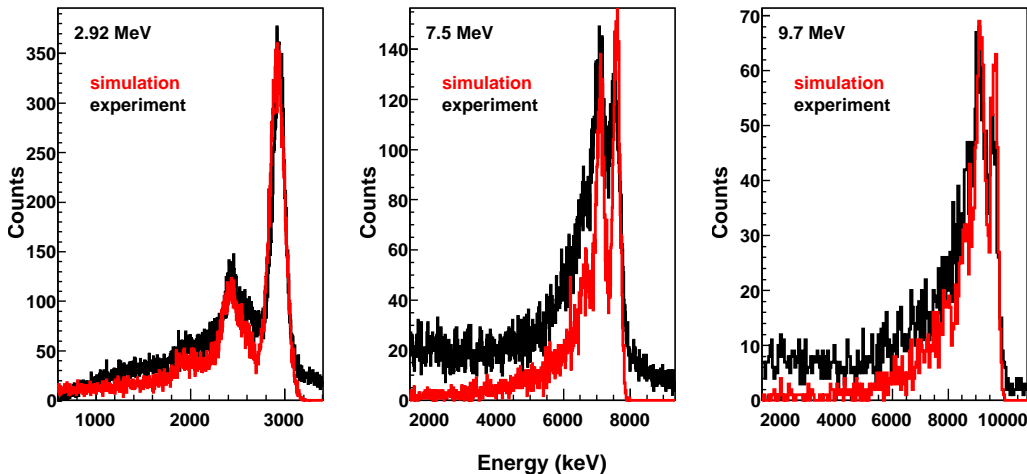
Figure 4.35: Comparison of simulation and experimental values for three different tagged gamma energies.

Figure 4.35 provides a the comparison for reconstructed peaks obtained in simulation and experimentally for three different gamma energies. Simulation peaks used a reference energy resolution of 7.5% at 1 MeV, a value which is close to the ones obtained for single crystals in the laboratory tests. The 2.92 MeV reconstructed peak in the simulation fits well with the experimental peak, but small differences can be seen at higher energies. This could be due to the non-correlated coincidences that can not be properly separated from the valid gammas during the bremsstrahlung process.

Chapter conclusions

In this chapter we presented the results of several test beams. In the proton beam test, the energy calibration curves showed that CsI(Tl) crystals coupled to APDs have quite a linear response for protons in the energy range between 90 and 180 MeV. The energy resolution obtained for 180 MeV protons is around 1%, which fulfills one of the main calorimeter requirements. In the experiment with 6.1 MeV

gammas, the linear crystal response was confirmed in the range between 511 keV and 6.1 MeV. The reconstructed peak for 6.1 MeV gammas showed an energy resolution of 2.8%, which is fairly close to the 2.2% required by CALIFA.

In the experiment with tagged gammas, the addback procedure was applied in each case and gave worse energy resolutions than those obtained for single crystals, due to the varied performance of the different detectors in this prototype configuration. The simulation results at the selected energies reproduced the experimental results for energy and crystal multiplicity distribution, which made it possible to obtain a hypothetical beam profile.

Conclusions

This thesis presents the main findings of the studies of CsI(Tl) crystals coupled to different photosensors, which was carried out as a part of the R&D program for the CALIFA R^{3}B/FAIR calorimeter. Several preliminary CALIFA calorimeter and ProtoZero prototype simulations, along with a detailed study of the energy resolution parameters that define CsI(Tl) and APD systems are also included. Chapter 3 deals with the characterization of small CsI(Tl) crystals coupled to different photosensors, and provides a comparison of different Large Area Avalanche Photo-Diodes (LAAPDs) coupled to several ad-hoc bi-frustum shaped CsI(Tl) crystals with adapted exit faces. Finally, the results of ProtoZero prototype testing in several facilities are given.

CALIFA will be constituted by an Endcap for the forward polar angles, where the highest gamma-ray energies are expected, and a Barrel to cover just up to 130 degrees for the backward polar angles. In the CALIFA simulation, three different crystal lengths (*short*, *medium* and *long*) were introduced into the simulation code for this first attempt of the calorimeter geometry, in order to study their influence on efficiency and energy resolution. The geometrical contribution to the energy resolution for perfect crystals was found to be below 3% for all tested energies in the Source Reference Frame (SRF) and the energy resolution was quite independent of crystal size. The geometrical efficiency at 700 AMeV was above 80% for *long* and *medium* crystal specifications. The Barrel accounts for more than 30% and the Endcap for around 47% of the geometrical efficiency. The simulation values obtained for the geometrical efficiency meet CALIFA specifications. The full-energy peak efficiency for *medium* size crystals decreases from 70% at low energies to around 45% at high energies (10 MeV in SRF).The crystal multiplicity (mean number of crystals with energy deposition over a threshold) increases with the γ-ray energy, from almost two at 0.5 MeV up to eight crystals at 10 MeV for the Forward Endcap. The multiplicities in the Barrel region are limited to a maximum of four fired crystals (mean values in all cases), since the gammas arriving at the Barrel section have less energy due to the Lorentz boost.

The values obtained in the prototype simulation at high energies for geometrical and full-energy peak efficiencies were lower than those obtained in the CALIFA simulation. They could be higher for a prototype with a greater number of crystals, since the escape probability of the scattered gamma decreases as the number of crystals increases. The mean multiplicity (between 1.7 and 3.3) in the studied en-

ergy range is in good agreement with the values obtained in the CALIFA simulation.

In simulations using protons as impinging particles, the appearance of a secondary peak in the energy spectrum corresponds to protons hitting near the boundary between crystals and was found to be the result of energy losses in the crystal wrapping. The simulation also revealed that the energy resolution is around 1% for up to a 130 μm wrapping thickness, which fulfils the CALIFA energy resolution requirements for high-energy light-charged particles. We used the simulation to calculate a calibration curve that would account for the energy losses in the materials placed between the ProtoZero and the proton source. Using this curve we could then calibrate the detected energy of incident protons with unknown kinetic energy.

The characterization of the CsI(Tl) crystals and the photosensors showed that the energy resolution depends on the crystal wrapping and other parameters related to the electronic chain used. From small samples (from 1 to 10 cm long with 1 cm^2 square section), the energy resolution was found to be approximately constant with the crystal size. The result obtained with a 1x1x1 cm^3 CsI(Tl) crystal coupled to a 1x1 cm^2 APD (4.4% at 662 keV) was better than what has been reported in prior literature.

For the test performed with small samples, a four-layer wrapping of 75 μm thick Teflon tape covered by 5 μm thick aluminized mylar was found to be optimal. For prototype crystals, a new wrapping material (ESR) was introduced. A thickness of 130 μm of this material gave the best performance. We have concluded that the small differences in light-pulse resolution for one or two layers of ESR are insufficient to justify the use of a second layer of ESR in light of the energy losses in the wrapping when using proton beams. This was demonstrated in the prototype simulation described in Chapter 2. The total wrapping thickness satisfies the calorimeter requirement of a minimum dead space between crystals.

A thoroughly study of the energy resolution achieved for a given crystal as a function of parameters as bias voltage applied to the APD, the spectroscopic-amplifier gain and the shaping time was performed. The results are discussed in detail in Chapter 3.

In the APD characterization, different APD models were compared and their contribution to the energy resolution was determined. A test-bench was developed to compare the light-pulse resolution at the nominal bias voltage. The best light-pulse resolution was obtained for the Hamamatsu 1x1 cm^2 APD series. The APD contribution to the energy resolution has an asymptotic limit below 0.12% that is associated with the noise contribution of the electronic chain. The APD encapsulation also influenced the energy resolution; APDs with ceramic backing performed better than those with PCB backing.

The innovative two-channel LAAPD (Hamamatsu S8664-1010) was specifically

developed for this project. The individual readout system for each of the two channels improved energy resolution, at the expense of greater complexity in both the electronics and the data analysis.

In the prototype crystal comparison, providers whose crystals offered the best results were identified. In these tests, a technical procedure was applied to measure the relative light output of CsI(Tl) crystals. Those with the largest exit face gave the largest light output. When compared to a 1x1x1 cm^3 CsI(Tl) reference crystal, light output was around 75% for crystals with a 2 cm^2 exit face and around 50% for those with a 1 cm^2 exit face. We observed important differences between light-collection non-uniformity and energy resolution for each crystal, even for two samples from the same provider. The best light-collection non-uniformity (N.U.) did not necessarily correspond to the best energy resolution with a radioactive source located at the entrance window of the crystal. The results obtained with some of the APD-crystal assemblies were close to 5% energy resolution for 1 MeV photons, indicating that they are a suitable solution for the CALIFA Barrel.

Prototypes were built to check crystal performances with proton and high-energy gamma beams. For the experiment using 180 MeV protons, a prototype configuration was built with four crystals coupled to Hamamatsu 10x10 2 channel APDs. In this test, the APD bias voltage had to be decreased because the huge amount of light produced by the protons in the crystals was saturating the preamplifiers. However, after reducing the APD bias voltage, the energy calibration curves indicated a rather linear response for protons in the energy range between 90 and 180 MeV. The energy resolution obtained for 180 MeV was around 1%, and this kind resolution for high-energy light-charged particles fulfils one of the most important calorimeter requirements.

The reconstructed peak in the experiment with 6.1 MeV gamma beam, showed an energy resolution of 2.8%, which is close to the 2.2% found in the simulation presented in Chapter 2. The selection of events with multiplicity equal two in the reconstruction process showed that at least one of the 511 keV gammas produced in the annihilation process is recovered, resulting in the disappearance of the double escape peak. Neither the voltage nor the temperature was monitored for this test, but it was possible to correct certain gain drifts using the mean position of one of the reconstructed peaks. This correction improved the energy resolution from 3.4% to 3.3% (FWHM) for the 5107 keV gammas.

The test with tagged gammas was performed with a prototype configuration of 16 crystals. In this experiment, the temperature was recorded in the acquisition system, which allowed us to correct the spectra obtained in the off-line analysis. The results obtained using calibration sources revealed the effectiveness of the addback procedure, but the energy resolution achieved was worse than resolutions obtained for single crystals. This can be explained by the fact that the prototype configuration incorporated detectors with quite different performances, and the

final energy resolution is a weighted mean value of them all. In this test, several runs with three tagged gamma energies (4, 7, and 10 MeV) were performed. In order to select photons of a certain energy out of a continuous bremsstrahlung spectrum, 64 pairs of fibers were used to identify the deflected electrons (using a constant magnetic field), from which the gamma-ray energy was then deduced. Time spectra were obtained by means of a time coincidence between the electrons hitting each fiber and the gammas hitting a prototype crystal. These spectra presented a flat background due to non-correlated coincidences between electrons in the fibers and gammas hitting the crystals. The background decreased as the energy of the tagged gamma increased, except for the trial with collimation, where the proportion of valid gammas to non-correlated coincidences was very low. Once the time windows had been chosen for each fiber, the reconstructed gammas for different tagged energies could be obtained.

A simulation was performed to compare the observables with the experimental data obtained in this test. The simulation reproduced the experimental results in terms of energy and crystal multiplicity distribution, giving a hypothetical beam profile. Experimental energy resolutions were worse than simulated resolutions for two possibly reasons. Different types of crystals and APDs were used in this prototype, and they performed in different ways, resulting in worse energy resolution for some of them. This implies a energy resolution worsening when the final energy is calculated adding back the signal from all the crystals. In this experiments we have to deal with accidental coincidences coming from the bremsstrahlung process. These events cannot be properly separated from tagged gammas, which leads to a wider FWHM of the reconstructed peaks. Experimental and simulated values for crystal multiplicities were very similar. Small differences at low energies can be explained by differences in noise levels for each crystal. The experimental mean energy deposition and the multiplicity distribution in the simulated results are in good agreement with the experimental values. The reconstructed peaks in the simulation were obtained using a 7.5% energy resolution at 1 MeV as reference, a value which is close to the ones obtained for single crystals in the laboratory tests.

In this work are shown the main contributions to the development of a very challenging detector like CALIFA. This contributions to the research and development stage of CALIFA became useful as input for the simulations to define the geometry of this detector. Data obtained in this work have helped to find the optimal characteristics required to the crystals and APDs, leading to the new and innovative APD developed specifically for this project by Hamamatsu.

Resumen en castellano

FAIR y el experimento R3B

FAIR (de sus siglas en inglés: Instalación para la Investigación con Iones y Antiprotones [1]) es un nuevo acelerador internacional que se va a construir próximo a la instalación de iones pesados (GSI) en Darmstadt, Alemania (Fig. 1). El objetivo de este proyecto es ofrecer a la comunidad científica internacional un acelerador técnicamente innovador y único en el mundo, para realizar investigación puntera en ciencias relacionadas con la estructura básica de la materia.
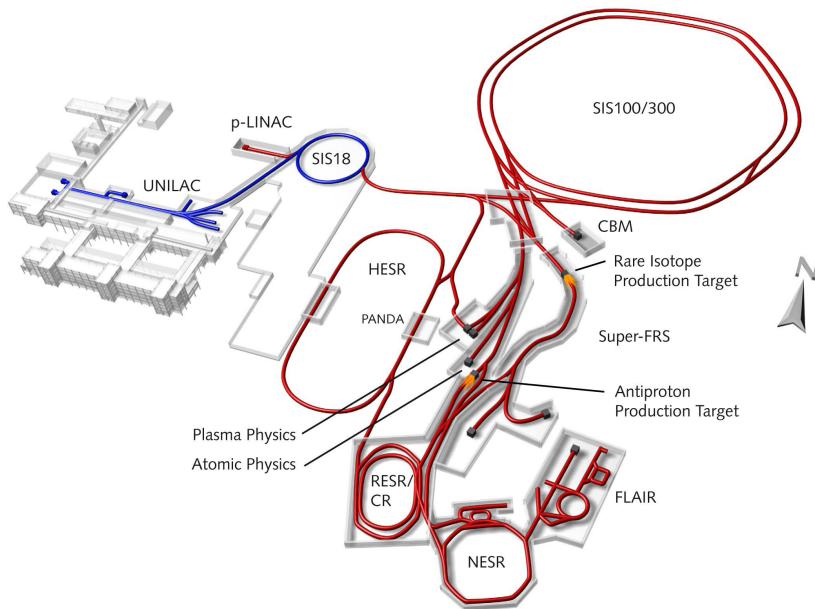
Figura 1: Instalación actual en el GSI (azul) e instalación planificada (rojo).

Esta instalación ofrecerá un extenso rango de haces de partículas (desde protones o antiprotones hasta haces de iones de todos los elementos químicos) con intensidades record en muchos aspectos y estará formado por un sincrotrón de doble anillo con un perímetro de 1,1 km. que contará con imanes superconductores y un sistema de anillos asociados para la colección, enfriamiento, optimización en el espacio de fases y experimentación de los haces. La intensidad de los haces de iones

se va a incrementar por un factor de 10^2 a 10^3, y en el caso de haces radiactivos secundarios por un factor de 10^5 con respecto a lo que ofrece actualmente el GSI. Finalmente este nuevo acelerador ofrecerá un incremento en la energía del haz por un factor 15 para haces de iones tan pesados como Uranio.

Uno de los programas específicos de investigación de esta futura instalación serán las reacciones de haces radiactivos a energías relativistas R^{3}B [4]. Este programa va a responder a cuestiones relativas a los núcleos exóticos, areas de astrofísica como la nucleosíntesis que se producen en supernovas y otros procesos estelares. R^{3}B es un montaje con alta eficiencia, aceptancia y resolución para obtener una medida cinemática completa de las reacciones inducidas por haces radiactivos de altas energías. Este montaje estará ubicado en el plano focal de la rama de altas energías del separador de fragmentos (Super-FRS) y está basado en un montaje que se encuentra en el GSI llamado LAND, pero introduciendo sustanciales mejoras en cuanto a resolución y un mejorado esquema de detección, incluyendo la detección de las partículas ligeras de retroceso y un espectrómetro de fragmentos de alta resolución (Fig. 2).
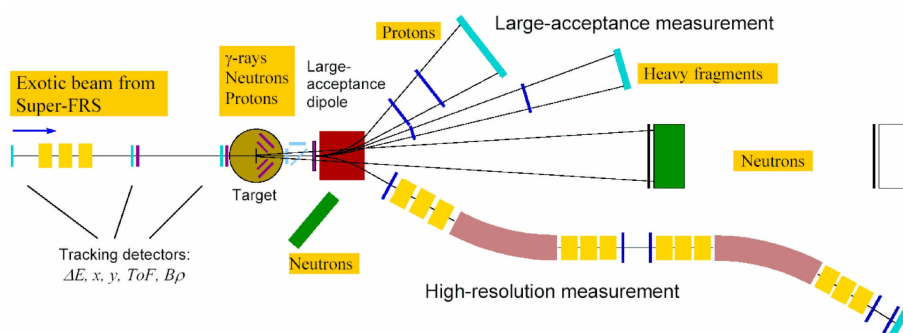
Figura 2: Representación esquemática del montaje experimental R^{3}B. Explicación en el texto.

CALIFA: El calorímetro de R^{3}B

CALIFA es un calorímetro para la detección de rayos gamma y partículas cargadas ligeras originadas en reacciones nucleares con haces exóticos a energías relativistas. Este calorímetro va a rodear el blanco de reacción del experimento R^{3}B y estará constituido por miles de cristales centelladores inorgánicos, que van a identificar rayos gamma y partículas cargadas emitidas por el blanco de reacción cuando se trabaje en coincidencia con el detector de partículas de retroceso del blanco (TRD).

Uno de los requisitos más complejos de los cristales que forman CALIFA, es el amplio rango dinámico que tiene que ser medido: desde gammas de bajas energías

hasta protones de 300 MeV. Un experimento típico de R^{3}B investigará reacciones en cinemática inversa inducidas por proyectiles con energías de hasta 1 A GeV, lo cual introduce un "boost de Lorentz"[8] no despreciable y una dispersión mayor en energía por efecto Doppler para los gammas emitidos desde el blanco. En ciertos casos se requiere medir la energía total de los gammas, mientras que en otros, este detector necesita medir las energías individuales o multiplicidades de los gammas con una resolución menor del 5 % (FWHM) a 1 MeV para realizar espectroscopía.

Para corregir el efecto Doppler, la granularidad en ángulo polar de CALIFA tiene que estar por debajo de 1,2 grados en ciertas partes, lo cual limita el espesor de los cristales (véase Ref. [16]). Este detector tiene que actuar como un calorímetro de absorción total cubriendo una región desde 7° hasta 130° en ángulo polar y con una eficiencia cercana al 80 %. Además, este calorímetro estará altamente segmentado (aproximadamente 5000 cristales individuales) y tendrá diferente forma y apertura angular para las diferentes regiones en ángulo polar.

La elección de cristales de CsI(Tl) para el Barril de este calorímetro se basa en la buena resolución, alta probabilidad para la interacción con gammas, facilidad de manejo y bajo coste de estos cristales. Para el Cierre (Endcap) del calorímetro hay dos versiones en consideración: una formada por cristales de LaBr$_3$(Ce) + LaCl$_3$(Ce) en modo phoswich, lo cual da una excelente resolución pero con el inconveniente de que estos cristales son altamente higroscópicos, y una segunda versión con cristales de CsI(Tl) con una longitud mayor de 20 cm, los cuales son más baratos pero tienen una resolución algo peor que los anteriores.

Simulación del Calorímetro

La cinemática de las reacciones con mayor velocidad de los iones incidentes (y por consiguiente mayor boost de Lorentz de los gammas emitidos) impone restricciones particulares en la geometría del calorímetro. La energía depositada en los cristales es mayor para aquellos gammas emitidos a bajo ángulo polar con respecto al haz y el boost de Lorentz incrementa la cantidad de gammas emitidos hacia adelante. Finalmente, para reconstruir la energía en el Sistema de Referencia en reposo respecto al Proyectil (SRP), se necesita una buena resolución en ángulo polar, siendo ésta diferente para diferentes ángulos. El diseño del calorímetro está basado en cristales bi-piramidales que cubren, cada uno, una región en ángulo polar compatible con la resolución en ángulo polar impuesta por la cinemática de la reacción. La longitud de los cristales que forman el calorímetro fue elegida para contener dentro del bloque de cristales la mayor parte de la energía de los gammas emitidos, siendo esta longitud dependiente del ángulo polar.

La simulación del calorímetro CALIFA se realizó usando el programa

---

[8]Se denomina boost de Lorentz al "empuje" que reciben las partículas relativitistas en la dirección de desplazamiento al aplicarle la transformación de Lorentz.

R3BSim [21], basado en GEANT4 [22] y ROOT [23]. El programa contiene la geometría del calorímetro. Cada cristal de CsI es definido individualmente incluyendo una separación de 1 mm entre cristales (medio mm para el recubrimiento de cada cristal). En esta simulación se incluyeron un blanco de parafina y el detector de silicio pero no se tuvieron en cuenta recubrimientos ni estructuras de soporte. Los gammas producidos dentro del blanco tienen un perfil de haz gaussiano con una anchura de 10 mm (FWHM). La energía de los gammas elegidos es 0,5; 1; 2; 5 y 10 MeV en SRP. A los gammas se le aplica un boost de Lorentz de acuerdo a la velocidad de la partícula incidente.

El objetivo de esta simulación es determinar los efectos del corrimiento Doppler y el ensanchamiento del pico producido en la energía reconstruida para esta geometría particular. Los resultados que se presentan aquí fueron obtenidos utilizando cristales de CsI(Tl) y los espacios entre cristales fueron simulados con vacío. La Fig. 3 muestra dos vistas diferentes del calorímetro CALIFA.
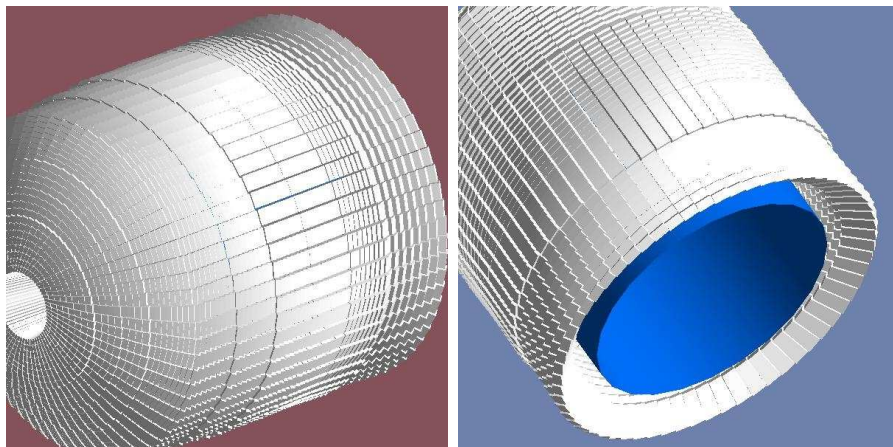
Figura 3: Dos vistas diferentes del Calorímetro CALIFA

Este calorímetro (versión 4.0b) fue producido en cooperación con IPN Orsay y presenta un Barril que cubre un ángulo polar entre 40 y 130 grados y un Cierre (Endcap) para ángulos entre 7 y 40 grados, donde se esperan gammas con las mayores energías. El Barril está compuesto por sólo 5 tipos de cristales diferentes, cada uno repetido 512 veces (uno de los tipos repetido 1024 veces), haciendo un total de 3584 cristales. El Cierre está formado por 24 tipos de cristales, repetidos cada uno 64 veces haciendo un total de 1536 cristales. El número total de cristales sería de 5120.

Para comprobar el efecto de la longitud del cristal sobre la eficiencia y la resolución se evaluaron tres tamaños de cristal en esta simulación: los llamados *corto*, *medio* y *largo* que corresponden a la misma geometría pero con diferentes longitudes en cada posición para cubrir aproximadamente el 60 %, 70 % y 80 % en

Energía del gamma (SRP)	0,5 MeV	1 MeV	2 MeV	5 MeV	10 MeV
Eficiencia de detección	90,0 %	88,9 %	87,7 %	87,1 %	87,8 %
Eficiencia de absorción total	83,1 %	80,5 %	76,8 %	72,3 %	65,2 %
Multiplicidad	2,1	2,7	3,5	5,8	9,3

Cuadro 3: Observables obtenidos en la simulación para diferentes energías.

eficiencia geométrica respectivamente para gammas de 5 MeV en SRP. El tipo *corto* incluye cristales desde 9 a 12 cm de longitud en la región del Barril aumentando en longitud a medida que aumentamos en ángulo polar. El tipo *medio* eran 3 cm más largos que el *corto* (11-15 cm) y el tipo *largo* 3 cm más largos que el tipo *medio* (14-18 cm).

La resolución de los cristales fue tenida en cuenta introduciendo una dispersión gaussiana en la energía detectada dependiente de la energía y que escala con $\sqrt{E}$. En nuestra simulación se usó una resolución de 3 %, 4 % y 5 % a 1 MeV (equivalente a 3,7 %, 4,9 % y 6,1 % a 662 keV tomados generalmente como referencia) y el caso sin dispersión (llamado resolución perfecta). Se seleccionaron gammas en el rango de interés (0,5; 1; 2; 5 y 10 MeV en SRP) para energía del haz de 700 AMeV ($\beta \sim$0,82). Los materiales interpuestos son un blanco de parafina, el detector de silicio y una capa de fibra de carbono (200 μm de espesor).

Resultados de la simulación

Como resultado de la simulación se reconstruyen varios observables: el número de cristales en los que hubo una energía depositada, la energía (de laboratorio) depositada en los cristales del calorímetro, el ángulo polar incidente del gamma emitido, la energía del gamma en SRP, etc. Independientemente de la resolución de los cristales hay ciertos observables que dependen sólo de propiedades geométricas del calorímetro, como son la eficiencia de detección o eficiencia geométrica (definida como el porcentaje de eventos que depositan toda o parte de su energía en los cristales), la eficiencia de absorción total o eficiencia de pico (porcentaje de todos aquellos eventos que depositan toda su energía sobre el total de emitidos por la fuente), y la multiplicidad (definida como el número de cristales promedio con deposición de energía por encima de un cierto umbral). Todos estos observables se muestran en el Cuadro 3 para diferentes energías consideradas en este estudio.

La razón de gammas detectados con toda su energía (y por lo tanto, la eficiencia de absorción total o eficiencia de pico) depende también del material elegido para los cristales. Para materiales con mayor densidad y Z efectivo, se espera tener una mayor eficiencia de pico. La resolución en energía se calcula del histograma de la energía reconstruida en SRP obtenida después de la suma y corrección por despla-

zamiento Lorentz. Utilizando este diseño de calorímetro, la contribución geométrica a la resolución en energía en SRP es comparable o menor que la contribución de la resolución de los cristales. Como se puede ver en la Fig. 4, el efecto de la longitud del cristal en función de la resolución en energía elegida solo es debida a pequeñas diferencias en eficiencia.
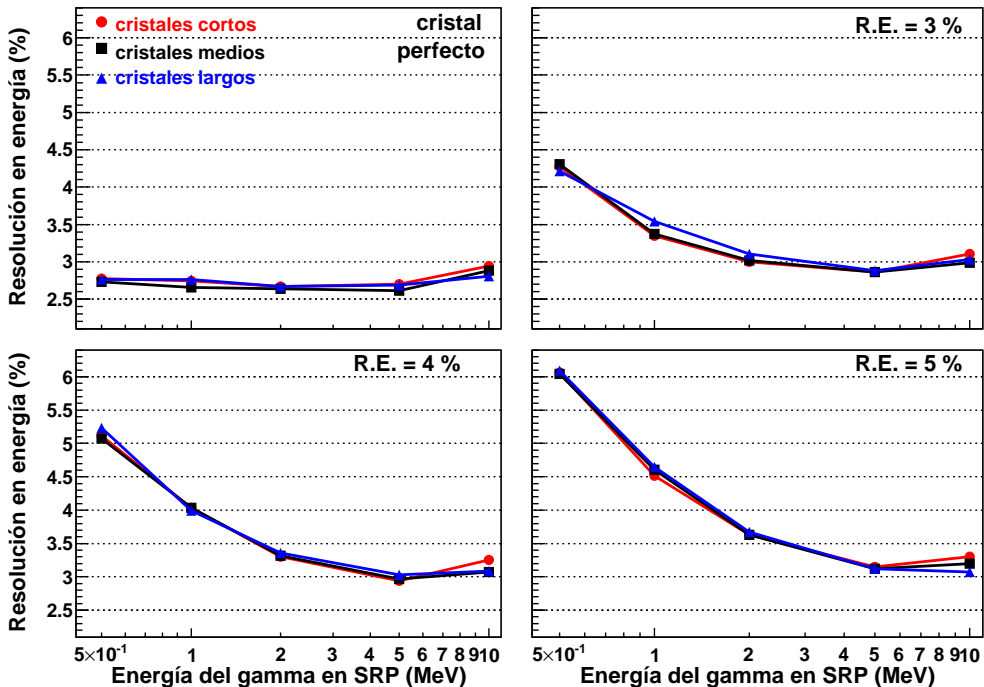

Figura 4: Resolución en energía para cristales medios, cortos y largos en función de la resoluciones elegidas: resolución perfecta (cristal perfecto), 3 %,4 % y 5 %.
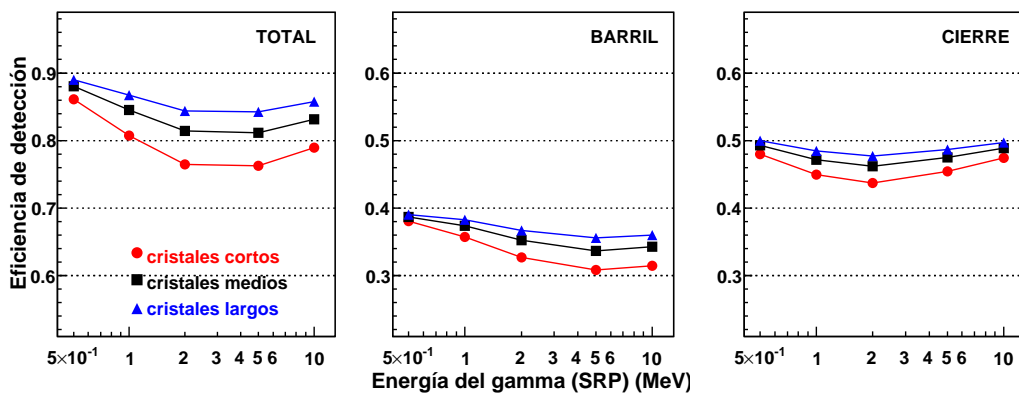

Figura 5: Eficiencia geométrica vs. energía para el a) total b) Barril c) Cierre

La eficiencia geométrica es mayor de 85 % para cristales grandes, mayor de 82 % para cristales medios y mayor de 77 % para cristales cortos. Tiene valores alrededor del 30 % para el Barril y del 47 % para el Cierre, disminuyendo ligeramente a medida que se aumenta la energía (Fig. 5). La eficiencia de pico se puede calcular multiplicando la eficiencia geométrica por la razón de eventos que depositan toda su energía o realizando un ajuste gaussiano del pico y contando las entradas dentro de 3 sigmas alrededor del centroide. La eficiencia de pico disminuye desde el 70 % para las energías más bajas hasta 45 % para las más altas (Fig. 6). La eficiencia de pico introduce una variación importante para altas energías de ~14 % para cristales largos (mayor eficiencia de pico) respecto a cristales cortos (menor eficiencia de pico).
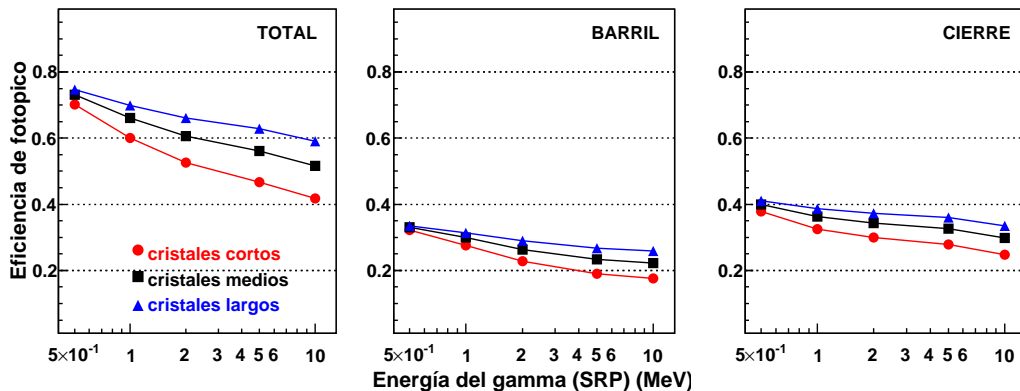

Figura 6: Eficiencia de pico vs. energía para cristales cortos, medios y largos.

La multiplicidad aumenta con la energía de los gammas, desde 2 cristales para 0,5 MeV hasta 7 cristales para 10 MeV. La multiplicidad en el Barril está limitada a un número máximo de 4 cristales debido a que los gammas que llegan al Barril tienen menor energía debido al boost de Lorentz (Fig. 7).

Simulación del ProtoZero

Se simuló un prototipo llamado ProtoZero y formado por 15 cristales bipiramidales truncados (para gammas) (Fig. 8) y 4 cristales para protones. El objetivo de esta simulación es comparar los resultados con los obtenidos en los experimentos del ProtoZero y validar la simulación. Los cristales se corresponden con el tamaño medio para CALIFA. En el caso de protones se implementó un recubrimiento reflector especular (ESR) para los cristales y se interpusieron un bloque de silicio 2 mm de espesor que simulaba los detectores de silicio del experimento y un bloque de aluminio de 5 mm de espesor que simulaba la caja del prototipo. Las energías consideradas para gammas fueron 1, 2, 4, 7 y 10 MeV y en el caso de protones fueron de 90, 120, 180, 220, 260 y 300 MeV para poder compararlas luego con los valores obtenidos en los experimentos. Tanto la fuente de protones como gammas estaban
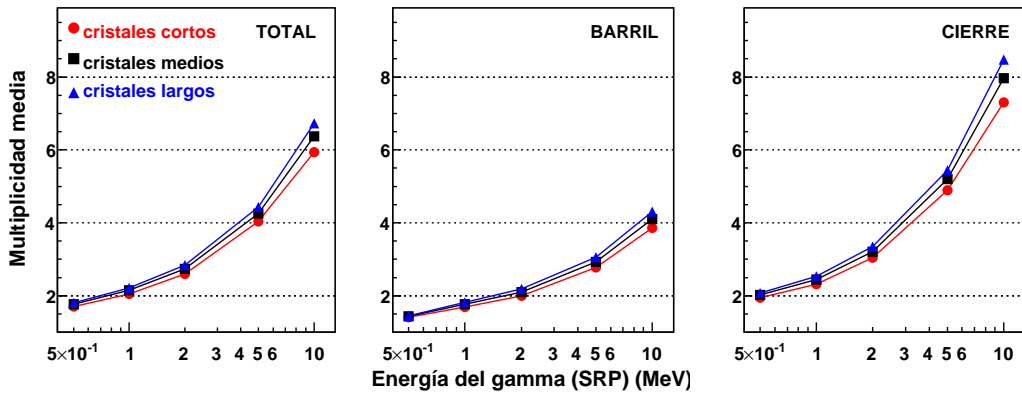
Figura 7: Multiplicidad vs. energía para cristales cortos, medios y largos.

colocadas a 25 cm del ProtoZero y la emisión fue isótropa desde una fuente circular de 1 mm de diámetro y paralela al eje del cristal central del protoZero.

Figura 8: Diferentes vistas del ProtoZero como se ve en el programa de simulación R3BSim.

Resultados para un haz de gammas

La Fig. 9 muestra las eficiencias, resolución en energía y multiplicidad para varias energías incidentes. La resolución disminuye proporcional a la raíz cuadrada de la energía porque así fue implementado en la simulación. Tomando como referencia un 5 % para 1 MeV se puede obtener una resolución por debajo del 2 % para gammas de 10 MeV. La eficiencia de detección tiene una tendencia decreciente hasta 4 MeV y creciente para mayores energías de acuerdo con el comportamiento que presenta la sección eficaz total de interacción para estos cristales. La eficiencia de pico disminuye con la energía a la par que disminuye la sección eficaz fotoeléctrica, pero sería mayor aumentando el número de cristales. La multiplicidad aumenta con la energía ya que la sección eficaz Compton también lo hace, permitiendo que los gammas dispersados manchen más cristales.
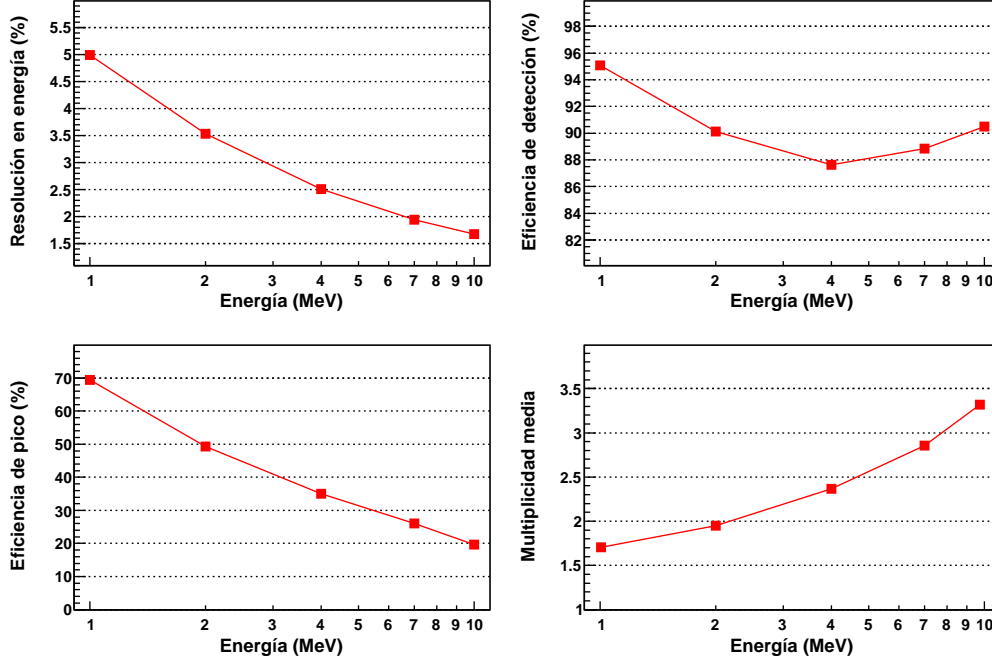
Figura 9: Observables simulados: resolución en energía (superior-izda.), eficiencia de detección (superior-dcha.), eficiencia de pico (inferior-izda.), y multiplicidad (inferior-dcha.) para cristales del ProtoZero en función de la energía de los gammas incidentes.

Resultados para un haz de protones

La simulación para protones se realizó de la misma forma que para gammas, pero teniendo en cuenta dos posiciones diferentes de entrada de los protones en el cristal. En el caso A, los protones entraban por el centro de uno de los cristales y en el caso B cerca de la superficie de contacto entre los 4 cristales. El motivo de utilizar estos dos casos es explicar mejor las perdidas de energía de los protones en el recubrimiento de los cristales. Para ello se realizó una simulación con diferentes espesores de recubrimiento. La Fig. 10 muestra el pico reconstruído para protones de 180 MeV y como se puede observar un espesor no mayor de 130 μm da como resultado una resolución por debajo del 1 %, que cumple los requisitos del calorímetro.

La Fig. 11 muestra los observables para los casos A y B. A partir de 220 MeV, los protones atraviesan los cristales dejando sólo parte de su energía dentro del cristal y por eso no están reflejados en los observables mostrados. Para el caso A, los picos tienen peor resolución debido a que las pérdidas en el recubrimiento de los cristales son una pequeña contribución que no puede ser separada del pico principal, mientras que para el caso B, se puede hacer un ajuste a dos gaussianas y tomando como resolución la de la segunda gaussiana que se corresponde con el pico principal. Las eficiencias de detección están próximas al 100 % en ambos casos. La
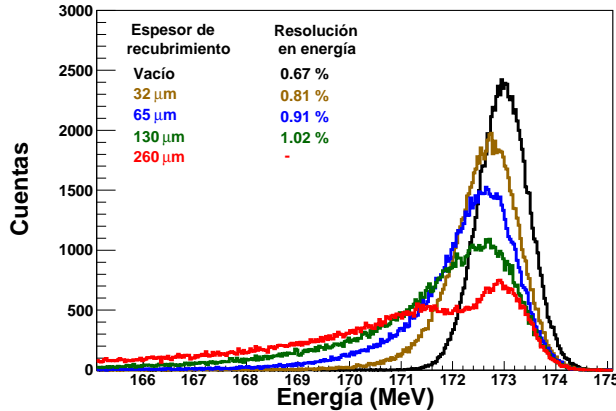
Figura 10: Simulación del pico reconstruido de un haz de protones de 180 MeV para el ProtoZero con diferentes espesores de recubrimiento.

eficiencia de pico cae drásticamente en el caso B debido a las pérdidas producidas en el recubrimiento, ya que estos eventos no son tenidos en cuenta para este cálculo. Respecto a la multiplicidad, el caso B tiene valores más altos hasta 180 MeV, ya que estos protones tienen mayor probabilidad de ser dispersados hacia cristales vecinos, mientras que para 220 MeV la cascada electromagnética se produce tan hacia el final del cristal que la probabilidad de alcanzar cristales vecinos es menor.
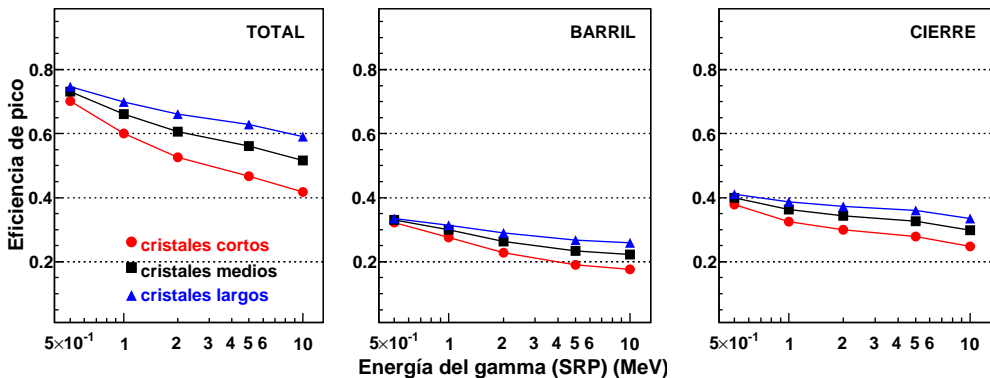
Figura 11: Observables simulados: Resolución en energía (superior-dcha.), eficiencia de detección (superior-izda.), eficiencia de pico (inferior-dcha.), y multiplicidad (inferior-izda.) para cristales del ProtoZero en función de la energía incidente.

Caracterización de cristales de CsI(Tl) y fotosensores

En los últimos años, los cristales de CsI(Tl) han sido ampliamente utilizados en numerosos experimentos tales como BABAR [28], y BELLE [29], y con diferentes

fotosensores tales como fotomultiplicadores, diodos de tipo PIN y fotodiodos de avalancha (APDs) (Véase [30] y [31] y referencias). Los cristales grandes de CsI(Tl) son relativamente baratos de fabricar, fáciles de manejar y ligeramente higroscópicos. Su densidad es relativamente alta (4.51 g/cm³) y tienen una alta producción de luz ($\sim$ 60.000 fotones/MeV) [30] pero tienen un tiempo de desexcitación de centelleo de unos pocos μs. La resolución intrínseca de estos cristales es aproximadamente 3.8 % de acuerdo con la Ref. [32] lo cual establece un límite inferior adecuado para nuestros requisitos.

Los APDs son ideales para la detección de centelleo debido a su alta eficiencia cuántica (≥ 60 % entre 390 y 930 nm) y su alta ganancia interna [46, 47]. Los APDs desarrollados por Hamamatsu [50] tienen una respuesta espectral que se adapta muy bien al espectro de emisión del CsI(Tl) [48, 49]. En un trabajo anterior (Véase Ref. [41]), se obtuvo una resolución en energía de 4,5 % (FWHM) para el pico de 662 keV de una fuente radioactiva de ^{137}Cs utilizando un cristal de 10x10x10 mm³ CsI(Tl) mientras que este valor está próximo al 6 % para fotomultiplicadores en el mejor de los casos.

El Cuadro 4 muestra los parámetros y la Fig. 12 la imagen de los APDs probados en este trabajo.

Modelo	S8664-1010	6817 [a]	SPL 7210[b]	SPL 7209[b]
Área activa (mm²)	10x10	2 ch. 10x10	7x14	7x14
Unidades	20	5	4	4
Ventana	resina epoxi	resina epoxi	resina epoxi	resina epoxi
Encapsulado	cerámica	PCB	cerámica[c]	cerámica[c]
Corriente de oscuridad I_D[e]	10 - 31 nA	29-61 nA	41-67 nA	41-82 nA
Voltaje de ruptura V_{brk} [e]	455 - 670 V	467 - 480 V	556 - 577 V	379 - 383 V
Voltaje de trabajo V_G[d],e	400 - 420 V	420 - 440	490 - 510	330-340 V
Capacitancia: C_{det}[e]	270 pF	255 - 264 pF[f]	158-166 pF	284-288 pF

[a] dos canales de 10x10 S8664, desarrollados específicamente para este proyecto. Para más detalles véase Ref. [52]
[b] los APDs de 7x14 mm² no comerciales fueron cedidos por la colaboración PANDA
[c] en vez de ser un encapsulado normal, se utilizó una cerámica cortada
[d] medido a ganancia 50
[e] medido a 25 °C
[f] por canal

*Cuadro 4: Párametros de los APDs probados en este trabajo.*
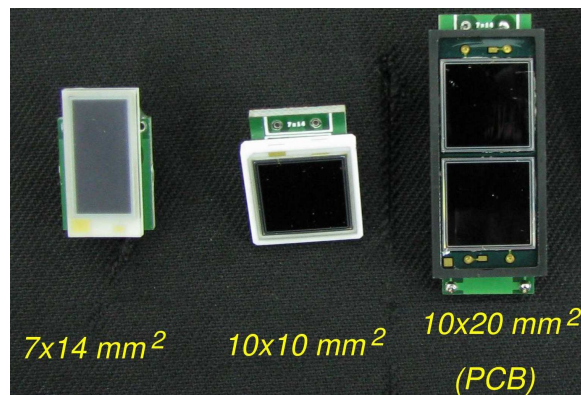
Figura 12: Diferentes APDs probados en este trabajo (Véase Cuadro 4).

Caracterización de APDs

En esta parte nos centramos en la caracterización de los APDs, desarrollando un procedimiento para identificar la contribución del APD a la resolución en energía. Para ello medimos la respuesta de los APDs cuando son excitados por un diodo LED que ilumina toda el área activa del APD a través de un material difusor. (Fig. 13). Se utilizó un generador de pulsos para alimentar el LED a través de una resistencia de carga. La anchura del pulso era de 8 μs con una frecuencia de 1.8 kHz. La amplitud era ajustable para variar la cantidad de luz producida por el LED. También se colocó en paralelo una fuente radiactiva de ^{55}Fe para establecer un pico de referencia y así cuantificar el número de pares electrón-hueco producidos en el APD (siguiendo referencias [54] y [55]).
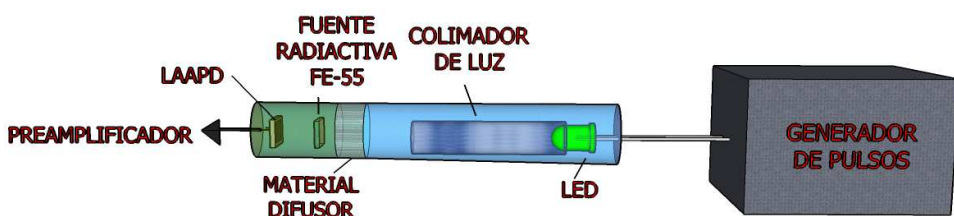
Figura 13: Montaje experimental utilizado para medir las diferentes series de APDs.

El montaje descripto en la Fig. 13 fue colocado dentro de una caja de Faraday cubierta por material aislante para evitar oscilaciones de temperatura. Los APDs fueron leídos por un amplificador de carga[9] y la señal fue enviada a un amplificador espectroscópico[10]. La señal de salida del amplificador espectroscópico fue enviada a

---

[9]se probaron diferentes modelos: Ortec IH 142, Canberra 2001A, Cremat CR-110 (Apéndice C), Mesytec MPR-1.

[10]se usaron dos modelos: Canberra 2022 y Ortec 671. El Canberra 2022 nos permite seleccionar

un analizador multicanal AMPTEK (AMC) y almacenada para su posterior análisis.

Número de pares electrón-hueco

La Fig. 14 (izda.) nos muestra el espectro de amplitudes de una fuente radiactiva de ^{55}Fe (pico principal de rayos X a 5.9 keV) y el pulso del LED. Cuanto mayor es la amplitud del pulso que alimenta el LED, mayor es su producción de luz. Los rayos X producen en promedio 1616 pares electrón-hueco en la capa de vaciamiento del APD, siendo el pico de la AMC correspondiente (en canales de ADC) proporcional a este número. El centroide del pulso del LED se puede traducir en número medio de pares electrón-hueco creados en el APD. La Fig. 14 (dcha.) muestra la relación que hay entre el número de pares electrón-hueco creados en el APD y la producción de luz del LED (determinada por la amplitud del pulso que alimenta el LED).
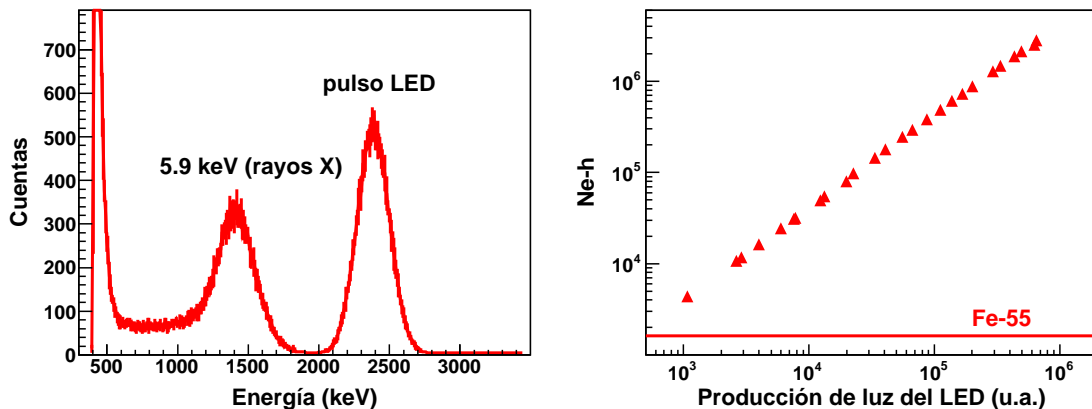
Figura 14: Izda.: Espectro de amplitudes de los rayos X de 5,9 keV y pulsos del LED para el APD de 10x10 mm². Dcha.: Número de pares electrón-hueco vs. producción de luz del LED (u. a.) para el APD de 10x10 mm².

Determinación del voltaje óptimo y resolución de un pulso de luz

El montaje de la Fig. 13 se utilizó para medir la dependencia de la resolución de un pulso de luz con el voltaje de trabajo del APD. Medimos además la corriente de oscuridad del APD para el voltaje de trabajo que optimiza la resolución de un pulso de luz. El voltaje de trabajo del APD se obtiene de la fuente de alimentación después de haber sido corregido por la caída en voltaje en la red de resistencias de la alimentación. La corriente del APD se obtiene de la fuente de alimentación

tiempos de integración entre 0,5, 1, 2, 4, 8 y 12 μs mientras que el Ortec entre 0,5, 1, 2, 3, 6 y 10 μs.

(ISEG NHQ 225M) con una presición de 1 nA.

La resolución de un pulso de luz se define como la anchura (FWHM) de un pulso LED (en unidades de canales de ADC) dividido por el canal del centroide. De la Fig. 15 (izda.) se puede deducir la contribución del APD a la resolución en energía. El comportamiento de la resolución de un pulso de luz parece ser debido fundamentalmente a la estadística de pares electrón-hueco con un valor asintótico de alrededor de 0,12 % atribuído al ruido electrónico debido a toda la cadena electrónica[11].
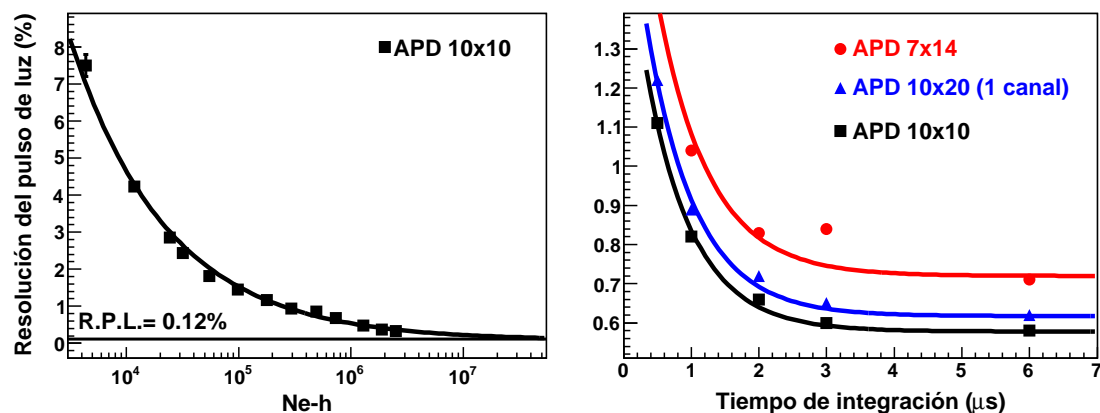

Figura 15: Izda.: Resolución de un pulso de luz vs. Ne-h para un APD de 10x10 mm². Dcha.: Resolución de un pulso de luz vs. tiempo de integración para diferentes tamaños de APD.

La Fig. 15 (dcha.) muestra la resolución de un pulso de luz como función del tiempo de integración en el amplificador espectroscópico. Estos valores fueron obtenidos para producciones de luz correspondientes a alrededor de 10^5 Ne-h, donde las fluctuaciones estadísticas en el APD eran más bajas (véase Fig. 15 - izda.). La Tabla B.1 en el Apéndice B resume los resultados para APDs de 10x10 y 7x14 mm² (de capacidades estándar y baja). Los valores de corriente de oscuridad varían entre 7 a 39 nA.

Comparamos el APD de 10x10 con el de 7x14 y un canal individual del APD de 10x20 mm². Podemos observar que para 6 μs de tiempo de integración en el amplificador espectroscópico, el APD de 10x10 mm² tiene una resolución de un pulso de luz de alrededor de 0,6 %, mientras que el de 7x14 mm² es alrededor de 0,7 % y para un canal individual del APD de 10x20 mm² es de alrededor de 0,65 %. De estos datos podemos concluir que el APD de 10x10 mm² es el que mejor resultados ofrece.

---

[11]La cadena electrónica se compone de: APD + red de resistencias de alimentación + preamplificador

Test con cristales pequeños

Además de la calidad de los cristales, la resolución en energía depende de un conjunto de parámetros como el recubrimiento del cristal, el acoplamiento óptico al dispositivo de lectura, tiempo de integración en el amplificador espectroscópico, y voltaje de alimentación del APD. Se buscaron la combinación de esos parámetros que ofrecen la mejor resolución en energía para tres cristales de CsI(Tl) (de la empresa Saint-Gobain Crystals) con tamaños que van desde 1 cm^3 hasta 10 cm^3, acoplados a APDs con una área de 10x10 mm^2.

Los APDs (S8664-1010 de Hamamatsu Photonics K. K.) fueron leídos por un preamplificador ORTEC IH 142 y un amplificador espectroscópico CANBERRA 2022. Para estas pruebas no se monitorizó ni la temperatura ni la el voltaje de alimentación. Todas las pruebas fueron hechas utilizando una fuente radiactiva de ^{137}Cs con una actividad de 10 μC, siempre colocada en la misma posición, lo que aseguraba una tasa de conteo aproximadamente constante ($\sim$1000 cps).

Los cristales estaban pulidos en todas sus superficies y tenían una concentración de Tl de 0,2 mol %. Estaban recubiertos en todas sus superficies, excepto la que va acoplada al APD, con 300 μm de Teflón comercial y una hoja de Mylar aluminizado de 5 μm de espesor que aseguraba una colección de luz uniforme a lo largo de toda longitud del cristal. Todas las medidas se realizaron a temperatura ambiente, manteniendo el nivel de humedad por debajo del 30 %, debido a que estos cristales son ligeramente higroscópicos. En todas las figuras, los puntos fueron medidos al menos dos veces para comprobar la estabilidad del sistema.

Recubrimiento de los cristales

El recubrimiento del cristal es probablemente el parámetro más crítico para mejorar la resolución en energía. Para esta prueba, el acoplamiento entre el cristal y el APD se realizó con grasa óptica. Se probaron diferentes recubrimientos difusores y reflectantes. La mejor resolución se obtuvo utilizando 4 capas de Teflón de 75 μm de espesor y una capa exterior de Mylar aluminizado de 5 μm de espesor.

Acoplamiento óptico

Se realizaron un grupo de medidas independientes en las mismas condiciones para dos tipos de grasa óptica: Pâte 7 de Rhodosil y BC630 de Bicron. Mientras que para el Pâte 7 tenía una resolución en energía de alrededor del 8 % (FWHM) (a 662 keV), para la grasa BC630 este valor bajaba hasta el 6,5 % para la misma energía.

Optimización del voltaje de alimentación

El voltaje de alimentación precisa entre 30 minutos y una hora para estabilizarse, de lo contrario, el APD sufre variaciones de ganancia debido al calentamiento de la fuente de alimentación. Se encontró que la resolución final obtenida para un cristal dado, depende del voltaje de alimentación aplicado al APD y también de la ganancia del amplificador espectroscópico. Por este motivo, se optimizó el voltaje de alimentación manteniendo la posición del fotopico alrededor del canal 6000 para lo cual se tuvo que modificar la ganancia del amplificador espectroscópico. Este test fue realizado manteniendo constante otros factores como el tiempo de integración. Los resultados para el cristal de 5 cm se muestran en la Fig. 16 (izda.).
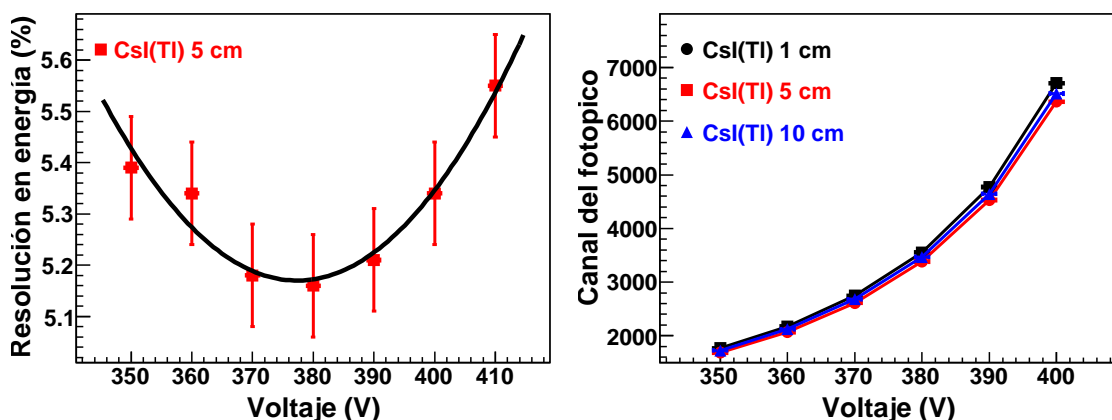

Figura 16: Izda.: Resolución en energía vs. voltaje de alimentación manteniendo la posición del fotopico en canal constante, para el cristal de 5 cm acoplado al APD S8664-1010. Un comportamiento similar fue encontrado para los cristales de 1 y 10 cm. Dcha.: Curva de ganancia del APD S8664-1010, utilizando cristales de CsI(Tl).

Se observó que las medidas realizadas a 380 V arrojaron la mejor resolución en energía para este APD. Una vez conseguido el voltaje óptimo de trabajo, tratamos de medir el efecto en la ganancia causado por una variación de voltaje. Para ello fue necesario obtener la curva de ganancia del APD, almacenando la posición del canal del fotopico para seis valores de voltaje y para cada cristal. Los resultados se muestran en la Fig. 16 (dcha.). Del ajuste de los datos experimentales, la pendiente de las curvas alrededor de 380 V da la variación de ganancia relativa debido a variaciones en el voltaje de alimentción que son mostrados en el Cuadro 5. De estos resultados se puede concluir que una variación de voltaje mejor de 0,35 V garantiza una variación en ganancia menor del 1 %.

Longitud del cristal	Variación de ganancia (%/V)
1 cm	2,84±0.01
5 cm	2,83±0.01
10 cm	2,83±0.01

Cuadro 5: Variación relativa de ganancia debida a variaciones en el voltaje de trabajo para todos los cristales.

Parámetros del Amplificador Espectroscópico

Los mejores resultados se consiguen cuando el APD está trabajando en su voltaje óptimo de trabajo usando la máxima ganancia del amplificador que permite el rángo dinámico del analizador multicanal. Otro factor que tiene una influencia importante en la resolución, es el tiempo de integración del amplificador. A medida que se aumenta el tiempo de integración tenemos mejores resultados pero aumentamos el apilamiento de los pulsos. Por lo tanto, tiempos de integración de entre 4 y 8 μs parecen ser un buen compromiso.

Resolución en energía para APDs

Una vez que fueron optimizados todos los parámetros que intervienen en la resolución en energía (R.E.), realizamos un conjunto de medidas utilizando 4 y 8 μs de constantes de integración. Los resultados para CsI(Tl) acoplado a APDs se muestran en el Cuadro 6 y en la Fig. 17. Los resultados aquí mostrados mejoran los publicados previamente en [48], [55], [58], y son comparables a los obtenidos con cámaras de deriva de Silicio [59].

Constante de integración	Longitud de cristal (mejores val.)			Longitud de cristal (val. promedios)		
	1 cm	5 cm	10 cm	1 cm	5 cm	10 cm
4 μs	4,68±0,12	5,11±0,12	4,74±0,12	4,98±0,12	5,22±0,09	5,17± 0,09
8 μs	4,42±0,12	4,87±0,09	4,72±0,08	4,68±0,12	5,02±0,09	4,90± 0,09

Cuadro 6: Mejores valores y valores promedios de la resolución en energía en % (FWHM) (a 662 keV), obtenidos para diferentes tamaños de cristal acoplados a un APD S8664-1010 de Hamamatsu.
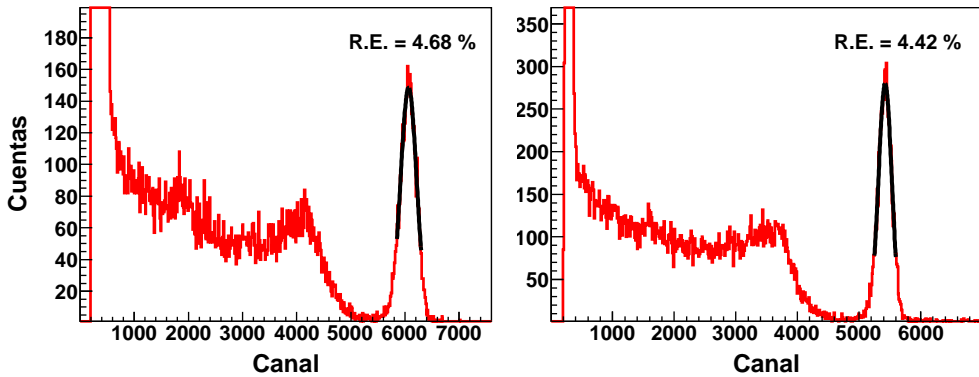
Figura 17: Resolución en energía para 1 cm³ de CsI(Tl) acoplado a un APD S8664-1010 usando 4 µs y 8 µs de constantes de integración.

Pruebas con cristales prototipos

En este punto de nuestro trabajo, podemos presentar los resultados de nuestro objetivo original, que era probar cristales con geometrías correspondientes a una sección localizada a 90° en ángulo polar del CALIFA. Para ello se compraron cristales, con cara de salida de 10x20 mm² adaptadas al APD modelo 6817 (formado por 2 canales del APD de 10x10 mm²), a cinco proveedores para compararlos entre ellos. Cada cristal fue etiquetado con dos códigos (de P1 a P5, y S1 o S2) que identifican a los diferentes proovedores (P) y a los diferentes cristales (S) de un mismo proveedor. Una vez que se realizaron todas la pruebas, se eligieron dos proveedores (Amcrys y IMP-Lanzhou) y se compraron nuevos cristales con caras de salida (10x10 y 7x14 mm²) adaptadas a las diferentes áreas activas de los APDs. En nuestro laboratorio, cada cristal fue visualmente inspeccionado siguiendo criterios en transparencia, tratamiento de superficie, pulido, y calidad de los cortes. Incluso, a pesar de ser una inspección cualitativa, esto ayudó a establecer o descartar correlaciones con la resolución final obtenida. La Fig. 18 muestra una foto con los cristales de los cinco proveedores mostrando las diferencias en transparencia.
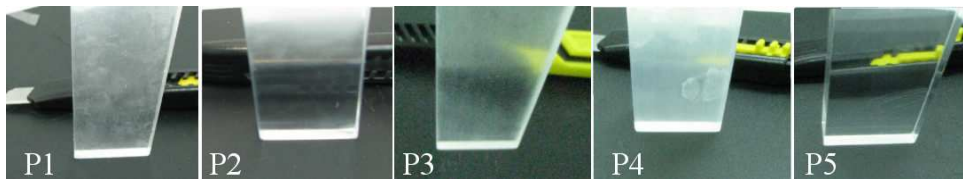

*Figura 18: Fotografía de los cristales de los cinco proovedores.*

Recubrimiento óptimo para cristales del prototipo

En una sección previa se vio que, para cristales pequeños, el recubrimiento óptimo se consigue usando cuatro capas de 75 μm de espesor de Teflón cubierta por una capa de 5 μm de Mylar aluminizado. Para cristales del prototipo se probó un nuevo material llamado Enhanced Specular Reflector (ESR) que incrementa la colección de luz. Para ello, el objetivo de esta prueba era determinar la configuración de recubrimiento óptimo para estos cristales. Esta prueba se realizó utilizando cristales del prototipo con una cara de salida de 10x10 mm^2 acoplados a un fotomultiplicador XP 2A508 de Photonis. Los resultados se presentan en el Apéndice C, y como se puede comprobar, la mejor resolución se obtiene generalmente utilizando dos capas de ESR, excepto para el cristal Am08, donde la mejor resolución se obtuvo cuando se utilizaba una capa de Teflón. Se puede concluir que las pequeñas diferencias en resolución de un pulso de luz entre una y dos capas, no justifica el uso de una segunda capa, ya que existen perdidas de energía importantes para protones.

Colección de luz de los cristales

La Fig. 19 muestra el montaje utilizado para comparar la colección de luz de los cristales utilizados en este trabajo. Para esta prueba se utilizó un fotomultiplicador XP 2A508 de Photonis y una fuente radiactiva de ^{137}Cs para irradiar los cristales. El objetivo es comparar la colección de luz para todos los cristales en las mismas condiciones[12].
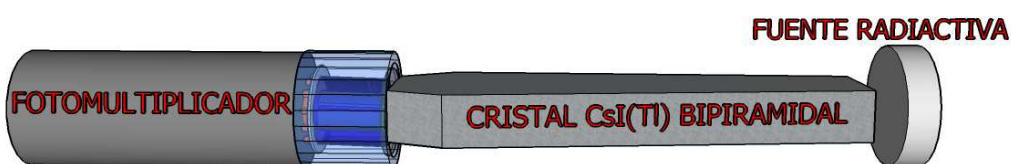
Figura 19: Montaje utilizado para comparar la colección de luz entre los cristales probados en este trabajo.

La Fig. 20 muestra la resolución en energía para los cristales de Amcrys y IMP Lanzhou con diferentes caras de salida en función del canal del fotopico, siendo este proporcional a la colección de luz. Esta gráfica revela que los cristales con caras de salida mayores tienen la mayor colección de luz y también demuestra que una mayor colección de luz mejora la resolución en energía.

---

[12]utilizando el mismo voltaje en el fotomultiplicador (1050 V), la misma ganancia (85) y tiempo de integración (4 μs) en el amplificador espectroscópico.
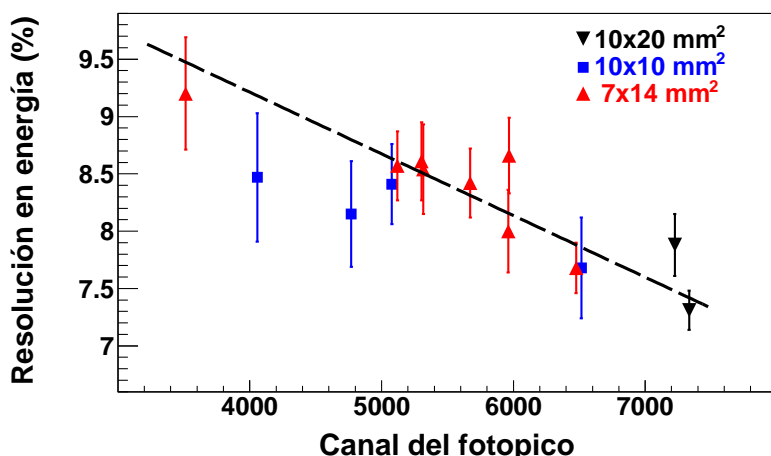
Figura 20: Resolución en energía (FWHM) vs. canal del fotopico para todas los cristales.

No uniformidad en la colección de luz
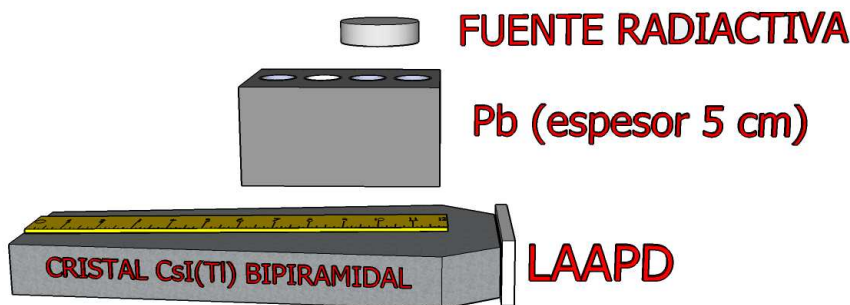
Figura 21: Vista esquemática del montaje utilizado para las medidas de la no uniformidad en la colección de luz.

Moviendo longitudinalmente una fuente radiactiva (^{137}Cs) a lo largo del cristal (véase Fig. 21) se midió la no uniformidad para seis posiciones diferentes desde la cara de salida del cristal. Los resultados de no uniformidad (N.U.) y resolución en energía (R.E.) se resumen en el Cuadro 7.

Estudio comparativo de resolución en energía

La segunda columna de el Cuadro 7 muestra la resolución en energía promediada de ocho medidas en las condiciones óptimas de funcionamiento de los APDs. En este caso, la fuente radiactiva se colocó frente a la ventana de entrada del cristal (opuesto al APD). La Figura 22 muestra los espectros para el mejor y el peor caso (P2-S1 y P1-S1). El mejor valor de resolución en energía obtenido en este caso, es

| Cristal	P1-S1	P1-S2	P2-S1	P2-S2	P3-S1	P3-S2	P4-S1	P4-S2	P5-S1	P5-S2
N.U.(%)	1,1	4,5	2,2	—	—	2,3	1,8	4,3	—	10,4
R.E. (%)	$9,3^a$	$6,4^b$	$5,9^a$	$6,1^a$	$7,4^a$	$6,6^b$	$6,5^b$	$7,3^b$	$6,6^b$	$7,4^b$

[a] Amplificador Ortec 671 usando 3 μs de tiempo de integración
[b] Amplificador Canberra 2022 usando 4 μs de tiempo de integración

Cuadro 7: Resumen de los resultados para no uniformidad y resolución en energía $\Delta E/E$ (662 keV) (explicación en el texto).

6 % a 662 keV. Si la comparamos con la obtenida para cristales pequeños (4.7 % a 662 keV) podemos concluir que la diferencia se debe a la relación longitud/área de los cristales utilizados como también a la zona no activa de los APDs que se utilizaron para los cristales del prototipo.
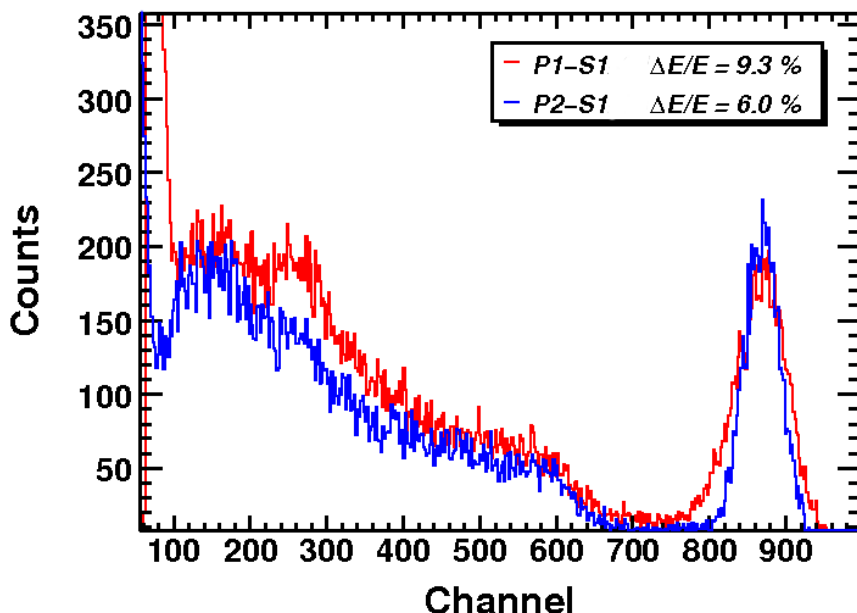
Figura 22: Espectros experimental para los cristales P1-S1 (rojo), y P2-S1 (azul), como respuesta a un gamma de 662 keV.

Resolución en energía vs. energía del fotón.

Para investigar la evolución de la resolución en energía para diferentes energías de fotones incidentes, se realizó un conjunto de pruebas utilizando fuentes radiac-
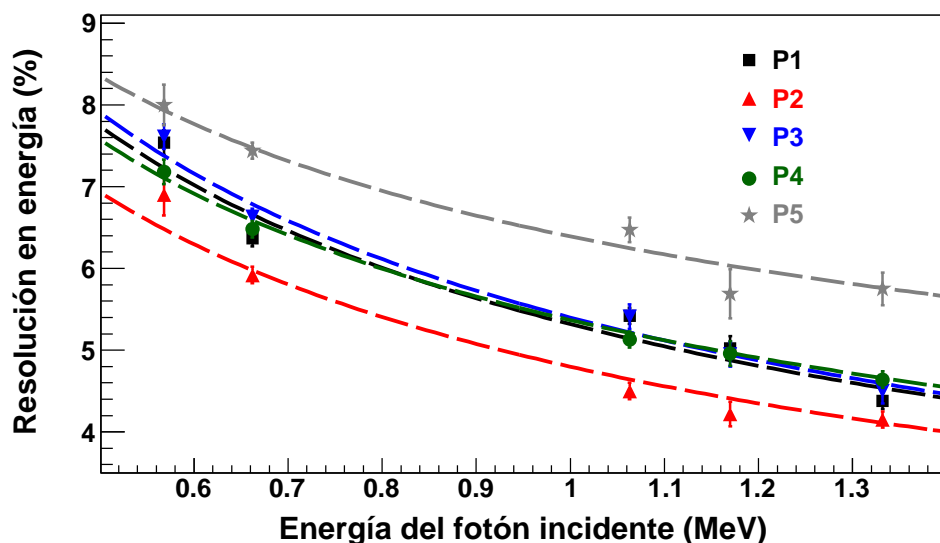
Figura 23: Resolución en energía experimental en función de la energía del gamma incidente. La línea entrecortada muestra la función ajustada $A + B/\sqrt{E}$

tivas de ^{60}Co (1170 keV y 1332 keV) y ^{207}Bi (569 keV y 1063 keV). La Fig. 23 resume los resultados obtenidos. La línea entrecortada muestra la función ajustada $A + B/\sqrt{E}$.

Pruebas en haz del prototipo.

Para poder comprobar el rendimiento de estos cristales en haces de protones y gammas de altas energías se utilizaron dos configuraciones diferentes para un prototipo del calorímetro CALIFA, formado por unos pocos cristales de CsI(Tl). El objetivo de éstas pruebas en haz es comparar los resultados obtenidos en el laboratorio, en donde las condiciones son óptimas, con los resultados obtenidos para varios cristales funcionando en un montaje completamente diferente.

Se utilizaron tres instalaciones para realizar las pruebas en haces de protones y gammas:

- The Svedberg-laboratoriet (TSL) en Uppsala (Suecia), que cuenta con un acelerador de protones hasta energías de 200 MeV. En este experimento el prototipo fue colocado directamente sobre la línea de haz.

- Centro de Microanálisis de Materiales (CMAM) en Madrid (España), que cuenta con un acelerador Cockroft-Walton de 5 MV, donde los protones acelerados a 1 MeV que son utilizados para producir la reacción ^{19}F(p,$\alpha\gamma$)^{16}O, utilizando un blanco de Teflón en la cual se producen gammas de 6,1 MeV (primer estado excitado de ^{16}O).

- Technische Universität Darmstadt (TUD) en Darmstadt (Alemania) tiene un acelerador de electrones que se utiliza para varios experimentos. Uno de estos experimentos es la instalación NEPTUN, donde los electrones colisionan contra un blanco fino llamado 'radiador' produciendo gammas por radiación de frenado. En ésta instalación los electrones pasan por el blanco y son deflectados por un campo magnético constante e identificados utilizando 64 pares de fibras centelladoras que se encuentran en el plano focal, y permitiendo de esa manera conocer la energía de los gammas que inciden en el prototipo. En este experimento se producen gammas desde 3 a 20 MeV, con una resolución en energía menor de 25 keV.

La eficiencia de fotopico disminuye para gammas de altas energías debido a la disminución en la sección eficaz fotoeléctrica. Por este motivo, la configuración del prototipo contaba con, al menos, 15 cristales para poder medir la energía total de dichos gammas. Además la multiplicidad es mayor para gammas de altas energías ya que la sección eficaz Compton aumenta con la energía, haciendo que los gammas dispersados alcancen mayor número de cristales. En el caso de un haz de protones, la mayoría de los protones que inciden en un cristal dejan toda su energía dentro de ese cristal, y por lo tanto para esta prueba se utilizó una configuración del prototipo con 4 cristales.

Resultados con un haz de protones de 180 MeV

Para este experimento, llevado a cabo en TSL (Uppsala), se construyó un prototipo con cuatro cristales bipiramidales de CsI(Tl) con caras de salida de 10x20 mm^2 acoplados a APDs de 2 canales S8664-1010 de Hamamatsu y recubiertos con dos capas de Teflón y dos capas de ESR. Se utilizó una caja de aluminio para aislar eléctricamente el montaje y así evitar la contaminación lumínica exterior. Dentro de esta caja se colocaron los cristales y APDs, junto con los preamplificadores (cuatro Cremat CR-110[13] montados en una única tarjeta en nuestro laboratorio). Los amplificadores utilizados en este experimento fueron Mesytec MSCF-16[14] y la fuente de alta tensión era CAEN N472 de cuatro canales. La lectura de los amplificadores se realizó con un módulo de 32 canales de ADC (Caen V785) y el sistema de adquisición estaba basado en un sistema MBS [65].

El voltaje de los APDs tuvo que ser reducido a alrededor de 200 V debido a que la cantidad de luz producida por los protones en los cristales saturaba los preamplificadores. La Fig. 24 muestra el montaje utilizado para este experimento. Se colocaron detectores segmentados de silicio (DSSSDs) de 32x32 segmentos en frente de los cristales para identificar los protones antes de ser detectados por los cristales. Además, se utilizaron bloques de hierro y cobre para disminuir la energía

---

[13]Especificaciones en el Apéndice D.
[14]Especificaciones en el Apéndice D

de los protones hasta 92 y 120 MeV respectivamente.
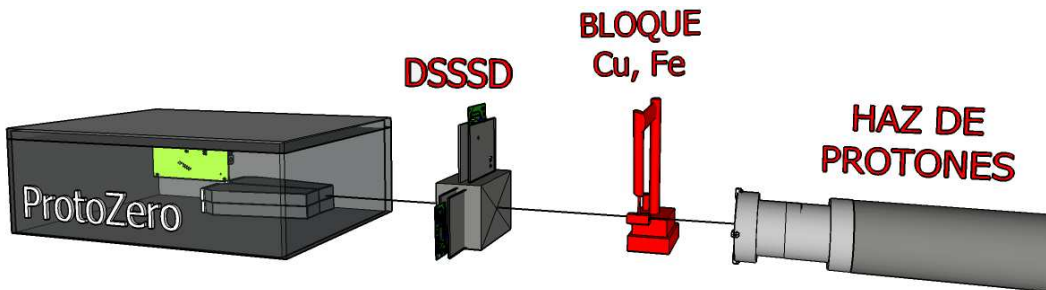
Figura 24: Montaje utilizado para el experimento con protones.

La Fig. 25 muestra los espectros de protones incidentes a 180 MeV para cada cristal de esta configuración del prototipo. En esta gráfica se puede observar que el haz de protones estaba incidiendo entre los cristales etiquetados con #1 y #3, ya que estos cristales presentan un pico con un número similar de cuentas. La ausencia de estos picos en los espectros de la derecha, indica que los cristales #2 y #4 estaban fuera del haz. Este hecho complica la calibración en energía, ya que para reconstruir los eventos que involucran estos cristales se requiere que estén todos los cristales calibrados. La resolución en energía para estos picos es de aproximadamente 1 %, lo cual satisface uno de los principales requisitos del calorímetro, que es tener dicha resolución para partículas cargadas de altas energías.

Utilizando la correlación entre cristales vecinos se pudo obtener una calibración en ganancia entre los cristales y de esa manera, los detectores #2 y #4 pudieron ser calibrados como se puede ver en la Fig. 26. La calibración en energía se hizo utilizando protones de 92, 120 y 180 MeV (que se corresponden con 84, 117 y 173 MeV después de las pérdidas producidas en los detectores de silicio y la caja del prototipo. En esta gráfica se puede observar que el cristal de CsI(Tl) acoplado a APDs tiene una respuesta lineal para protones en un rango de energías entre 90 y 180 MeV.

Utilizando la correlación entre los cristales #1 y #3, se pueden seleccionar aquellos eventos que dejan energía en ambos cristales, como se muestra en el corte diagonal de la Fig. 27 (izda.). Estos eventos se pueden sumar después de la calibración en energía, dando como resultado el pico reconstruido de la Fig. 27 (dcha.). En esta gráfica, se puede ver claramente una degradación en la parte izda. del pico que lleva a tener una resolución energía de ∼3 %, la cual es bastante peor si la comparamos con la obtenida en los cristales #1 y #3 (véase Fig. 25).

Además, podemos utilizar la información ofrecida por los DSSSDs para identificar aquellos protones que inciden cerca de la superficie de contacto entre los cristales #1 y #3. La Fig. 28 (Izda.) muestra el perfil del haz obtenido con los DSSSDs y la posición relativa de todos los detectores (desde #1 hasta #4). En esta gráfica se seleccionaron dos regiones diferentes. Eventos detectados en la región
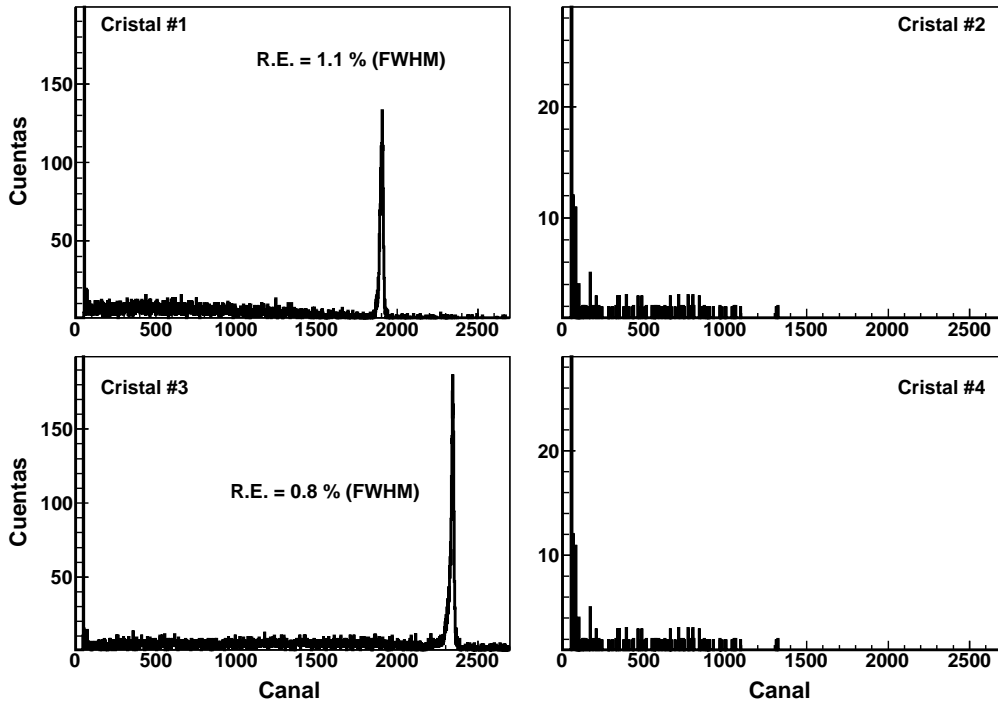
Figura 25: Espectros obtenidos para cada cristal de esta configuración del prototipo usando protones de 180 MeV de energía.
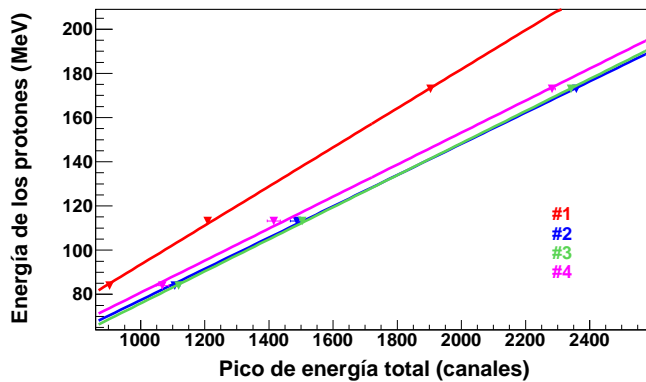
Figura 26: Curvas de calibración en energía obtenidas con protones a 92, 120 y 180 MeV para todos los detectores de esta configuración del prototipo.

A, se corresponden con protones incidiendo entre cristales #1 y #3 y la región B corresponde a aquellos protones que entraron por el cristal #3. La Fig. 28 (dcha.) muestra el pico reconstruído para ambas regiones junto con el pico reconstruído utilizando todos los eventos. En esta figura podemos ver que, aquellos protones que comparten energía entre los dos cristales, producen un pico que está 1 MeV por debajo del pico principal. Esto demuestra las perdidas de energía producidas en
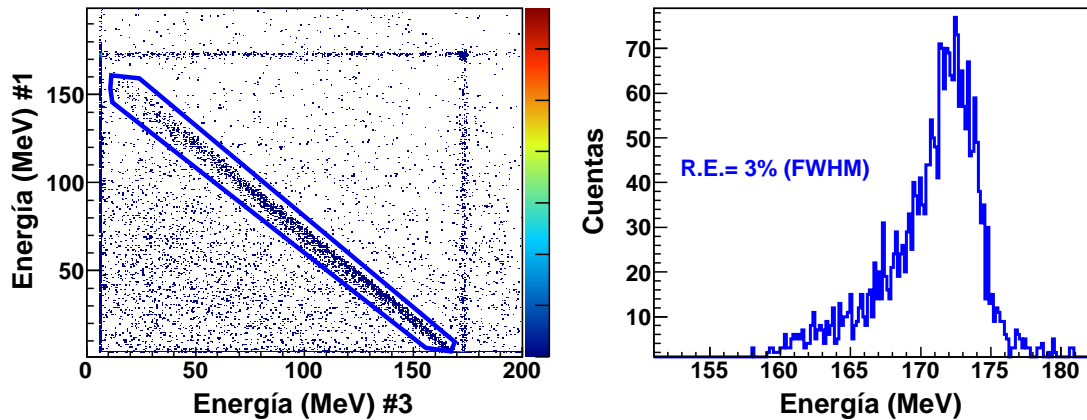
Figura 27: Izda.: Correlación entre cristales #1 y #3. Dcha.: Pico reconstruido para cristales #1 y #3.

aquellos protones que pasan de un cristal a otro. Esta pérdida de energía se produce debido a que los electrones generados en el recorrido de los protones son detenidos y absorbidos por el recubrimiento como se demostró en la simulación para protones.

Resultados en haz de gammas de 6,1 MeV

Para este experimento se construyó un prototipo con 16 cristales bipiramidales de CsI(Tl) con diferentes caras de salida (10x10, 7x14 y 10x20 mm^2) adaptados para los diferentes modelos de APD (Fig. 12). Estos cristales estaban recubiertos con dos capas de Teflón y una capa de ESR. También se utilizó una caja de aluminio para aislar el sistema (Fig. 29). Dentro de la caja se colocaron los APDs junto con los preamplificadores (4 canales Cremat CR-110[15]). Los amplificadores utilizados fueron Mesytec MSCF-16[16] y la fuente de alimentación era CAEN N472 de cuatro canales. La adquisición se realizó utilizando el programa Midas [66]. En este experimento, el haz de protones de 1 MeV tenía una intensidad constante de 1.5 μA y se utilizó un blanco de Teflón de 30 mm de diámetro y 5 mm de espesor recubierto con una malla de cobre para descargar la corriente producida por el haz de protones.

Problemas de ruido nos impidieron colocar más de 6 cristales al sistema de adquisición, por lo tanto, para obtener la máxima información posible se eligieron cristales que rodeaban al cristal central. La Fig. 30 muestra los espectros obtenidos para seis cristales de este prototipo. En esta figura, se pueden distinguir picos a 511, 1275, 5107, 5618 y 6129 keV. Los dos primeros se corresponden con una fuente radiactiva de ^{22}Na colocada cerca de los cristales como referencia, y los últimos tres son el pico de escape simple, escape doble y el propio pico del gamma de 6,1 MeV producido por el ^{16}O generado en el blanco tras la irradiación con protones. El

---

[15]especificaciones en el Apéndice C

[16]Especificaciones en el Apéndice D
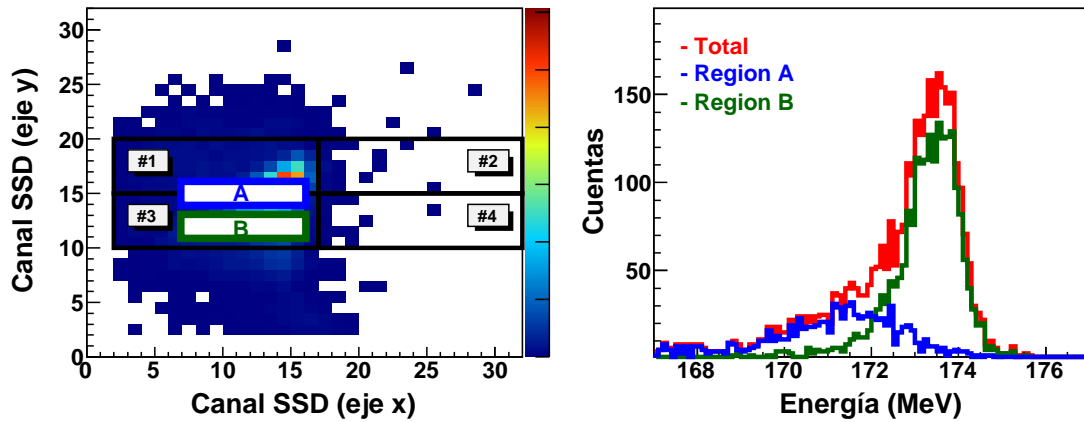
Figura 28: Izda.: Selección de protones incidiendo en A) región entre cristales B) región dentro de cristal #3. Dcha.: Espectro obtenido para protones incidiendo en regiones A, B y total.
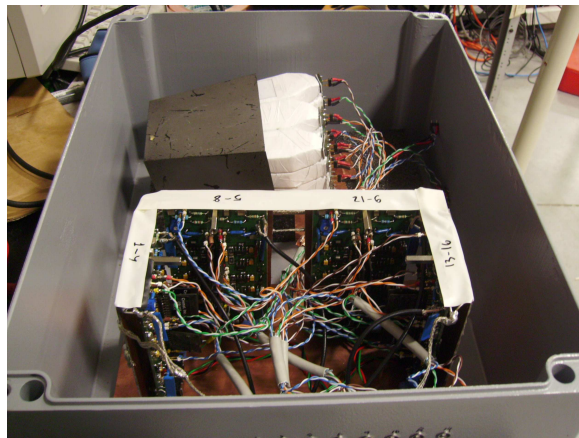
Figura 29: Detector utilizado para el experimento en CMAM.

cristal etiquetado con #01 y mostrado en la última posición por conveniencia, estaba ubicado sobre el cristal #03 (cristal central).

Utilizando la posición de estos picos, se realizó una calibración en energía como se puede observar en la Fig. 31. De esta gráfica se puede concluir que estos detectores (cristales CsI(Tl) + APDs) ofrecen una respuesta lineal para gammas en el rango entre 511 keV y 6,1 MeV.

Una vez que los detectores fueron calibrados, se realizó el procedimiento de recontrucción. Los resultados se muestran en la Fig. 32, en donde se indican las energías de cada pico. El Cuadro 8 muestra la resolución en energía obtenida para todos estos picos.
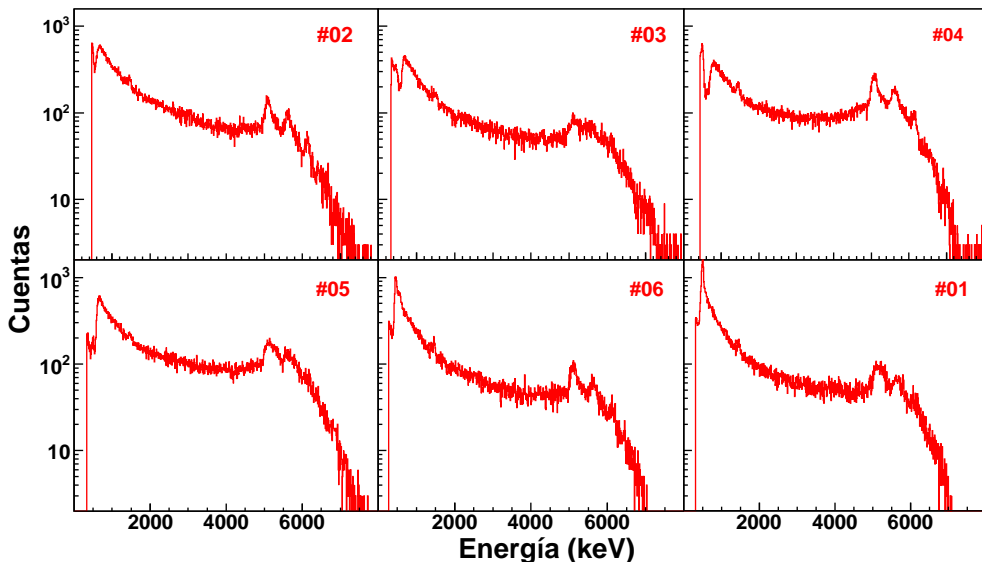
Figura 30: Espectros obtenidos para seis cristales de este prototipo.
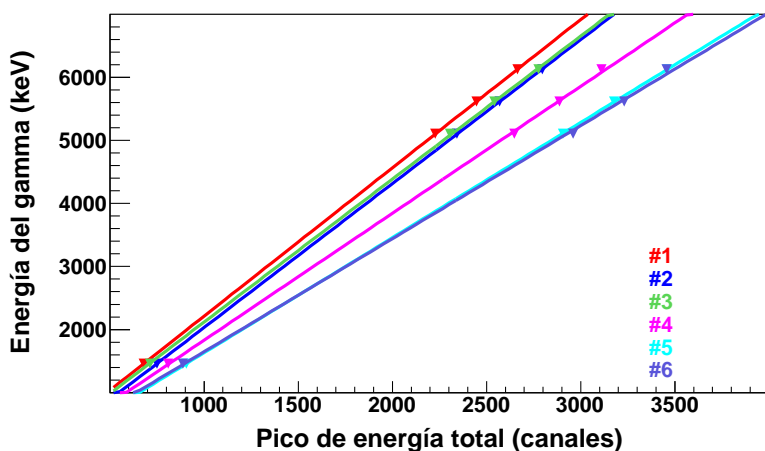
Figura 31: Curvas de calibración para los seis cristales de este prototipo.

Energía del pico (keV)	511	1275	5107	5618	6129
Resolución en energía (%)	9,0	7,0	3,4	3,1	2,8

Cuadro 8: Resolución obtenida después de la reconstrucción.

Resultados de un haz con gammas a 4-10 MeV en la instalación Neptun

La idea básica de este experimento es seleccionar gammas de una cierta energía que vienen mezclados sobre un espectro continuo de radiación de frenado.
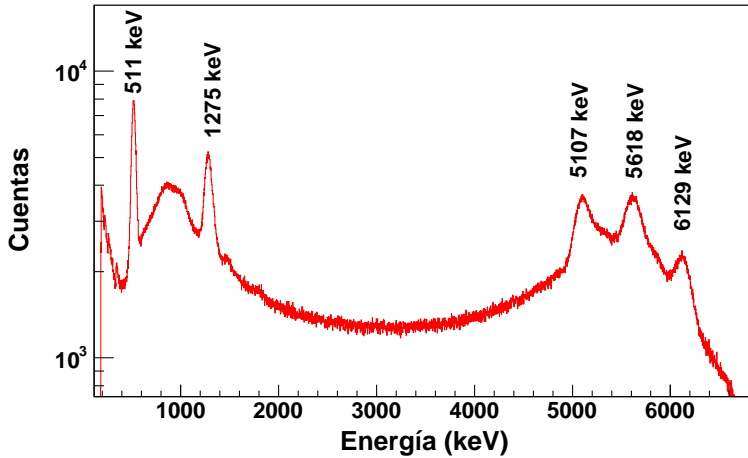
Figura 32: Espectro resultante de la reconstrución de los seis detectores de esta configuración.

El funcionamiento de este experimento se muestra en la Fig. 33. Un haz de electrones monoenergéticos (E_0) se utilizan para producir la radiación de frenado sobre un blanco 'radiador', en el cual, cada electrón produce como máximo un fotón. Deflectando los electrones dispersados con un campo magnético homogéneo hacia un detector colocado en el plano focal, se determina el momento de estos electrones p_e, y por tanto, su energía E_e. El imán convierte la información del momento de los electrones a posición en el plano focal. Por lo tanto, la determinación de energía del electrón se consigue determinando su posición en el plano focal.

La energía del gamma correspondiente E_γ se calcula como la diferencia entre la energía del electrón dispersado E_e y la energía del haz incidente (E_0)

$$E_\gamma = E_0 - E_e \tag{3}$$

El plano focal del imán está cubierto por 64 pares de fibras centelladores (Bicron BCF-12) con un perfil cuadrado de 1 mm^2. Cada par de fibras está acoplado a una guía de luz que lleva la luz hacia un fotomultiplicador. La asignación de los fotones y electrones se realiza por una coincidencia temporal entre el plano focal y el experimento [69].

Para este experimento se utilizó el mismo prototipo utilizado en el experimento realizado en el CMAM. La Fig. 34 muestra una foto del prototipo utilizado. Dentro de la caja se colocaron los cristales y APDs, junto con dos preamplificadores Mesytec MSI-8[17] de ocho canales. Esta caja también contenía, dos recipientes con silica gel para mantener la humedad por debajo del 30 %, y una sonda de temperatura PT-1000 que monitorizaba la temperatura enviándola al sistema de acquisición. Se utilizaron preamplificadores Mesytec MSCF-16[18] y fuentes de

---

[17]Especificaciones en el Apéndice D

[18]Especificaciones en el Apéndice D
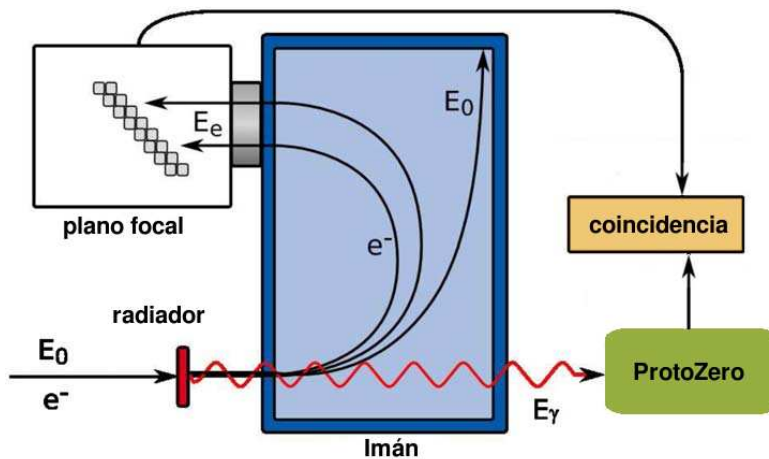
Figura 33: Principios de funcionamiento para seleccionar gammas de un continuo de radiación de frenado [71].

voltaje Iseg de 2 canales que permitían monitorizar las variaciónes de voltaje. La lectura de los amplificadores se realizó con un módulo VME de ADC (Caen V785) y la acquisición se realizó con el sistema MBS [65].
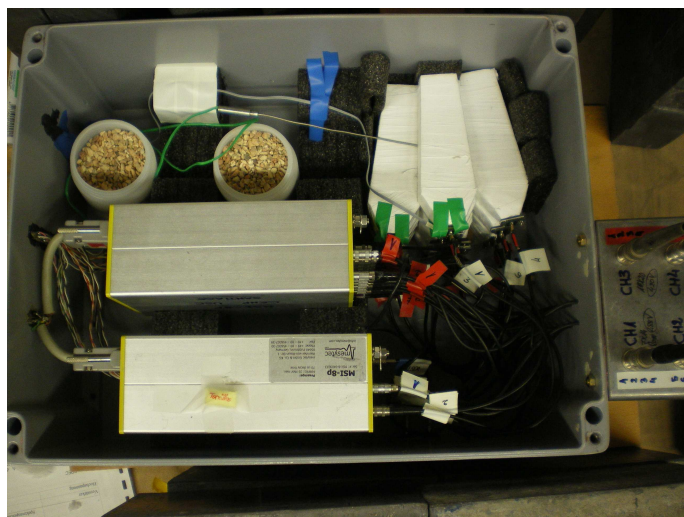
Figura 34: Configuración del prototipo utilizado en TUD.

Se utilizaron varias fuentes radiactivas para calibrar el prototipo (^{137}Cs, ^{60}Co, ^{22}Na y ^{56}Co). La Fig. 35 muestra los espectros obtenidos para los 15 cristales de este prototipo.

Utilizando la información de estas figuras, se realizó una calibración en energía y se obtuvieron los espectros de reconstrucción como los que se muestran en la Fig.
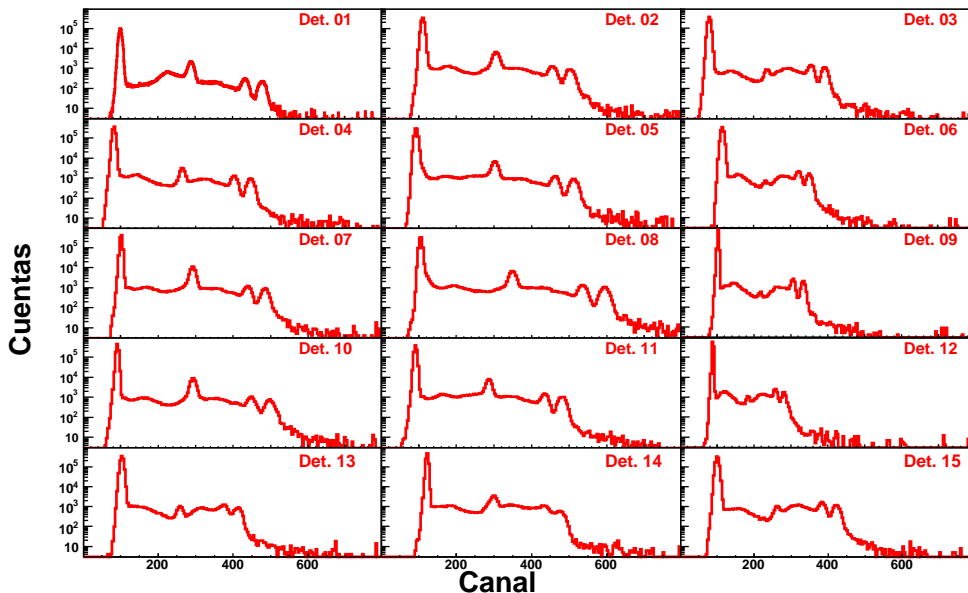
Figura 35: Espectros obtenidos para esta configuración de 15 cristales usando fuentes radiactivas de ^{137}Cs y ^{60}Co.

36. En esta gráfica, se observa los espectros reconstruídos para una fuente de ^{60}Co, ^{137}Cs (izda.) y ^{56}Co (dcha.).
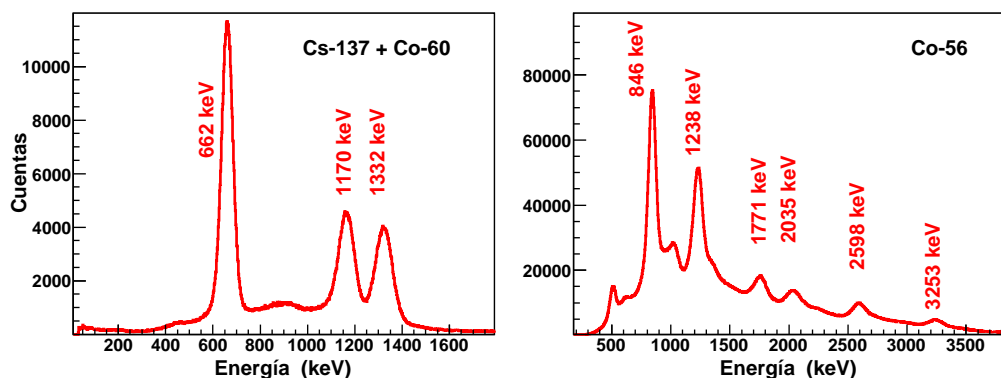
Figura 36: Izda.: Espectro de reconstrucción para las fuentes radiactivas de ^{60}Co y ^{137}Cs. Dcha.: Espectro de reconstrucción para una fuente radiactiva de ^{56}Co.

Para el haz de gammas, se seleccionaron gammas de tres energías (4, 7, y 10 MeV). Se realizó además una prueba para un haz de gammas de 4 MeV utilizando un colimador de plomo para ver la respuesta del prototipo cuando los gammas inciden sobre el cristal central. Para un gamma válido, las señales producidas por los electrones en el plano focal están en coincidencia temporal con

las señal dada por uno de los cristales del prototipo.

La Fig. 37 muestra la correlación temporal para una de las fibras selec-
cionadas y para un haz de gammas con cuatro energías diferentes. Como se
puede ver en esta figura, todos los eventos correlacionados están concentrados
en una ventana temporal de 100 ns. El fondo plano de estas gráficas se debe
a coincidencias no correlacionadas entre electrones que dan señal en la fibras
y gammas incidiendo en los cristales. Como se puede observar en esta figura,
cuanto mayor es la energía del gamma seleccionado, mayor es el fondo, excepto
para prueba con colimación que tiene un fondo mayor debido a que la mayoría de
los gammas válidos son absorbidos por el bloque de plomo utilizado para colimación.
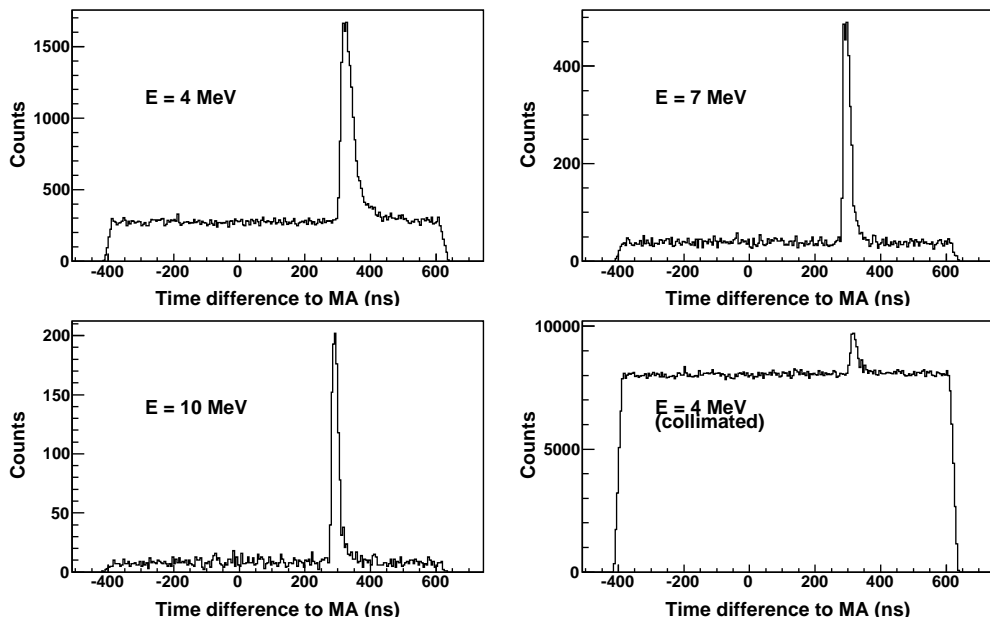
*Figura 37: Fibras seleccionadas para la reconstrucción de los gammas a diferentes
energías.*

Una vez elegidas las ventanas temporales para cada fibra, podemos representar
aquellos eventos que tienen la energía seleccionada. La Fig. 38 muestra el espectro
de los gammas reconstruídos para diferentes energías. A medida que aumentamos
la energía, la estadística es menor debido a que la producción de gammas en el
'radiadorés menor. En estas gráficas se puede observar también como cambia la
proporción entre los picos reconstruídos y los picos de escape simple y doble.

Se realizó también una simulación para comparar los observables (resolución en
energía, eficiencia de pico y multiplicidad) con los datos experimentales obtenidos
en este experimento. La simulación nos permite definir características del haz (p.e.,
forma del haz, posición del centro, anchura, etc.). El objetivo es conocer detalles
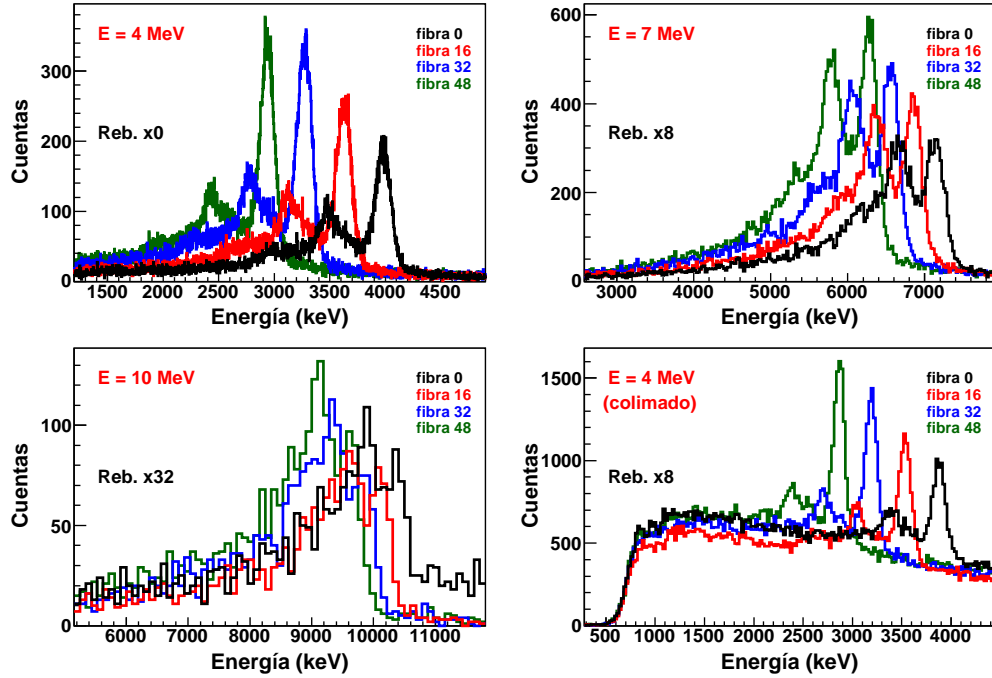
Figura 38: Espectro de energía reconstruído para varias fibras y varias energías seleccionadas.

del haz que produjo en el prototipo los espectros obtenidos. Para ello, tratamos de reproducir los resultados experimentales en términos de distribución de energía y multiplicidad en los cristales para una energía fija, variando la característica del haz. Una vez que los resultados simulados coinciden con los experimentales, usamos el mismo haz para todas las energías seleccionadas en este experimento.

La Fig. 39 muestra la comparación entre los valores experimentales y simulados para resolución en energía (izda.), eficiencia de pico (medio) y multiplicidad (dcha.) en función de la energía de los gammas seleccionados.

Los valores experimentales de resolución en energía son peores que los simulados debido posiblemente a varias razones. Por un lado, los cristales y APDs utilizados en este prototipo son distintos y con rendimientos muy dispares, lo cual produce una resolución peor para algunos de ellos. Por esto, obtenemos una resolución final en el pico reconstruído que es peor que la ideal. Por otro lado, en este tipo de experimentos, tenemos coincidencias accidentales producidas en la radiación de frenado que no pueden ser separadas de los gammas seleccionados, dando lugar a un pico reconstruído de peor resolución en energía.

La eficiencia de pico fue calculada como la razón entre el número de cuentas en el pico de energía total y el número total de cuentas en el espectro de energía. Este observable fue corregido por un factor que tiene en cuenta la contribución de
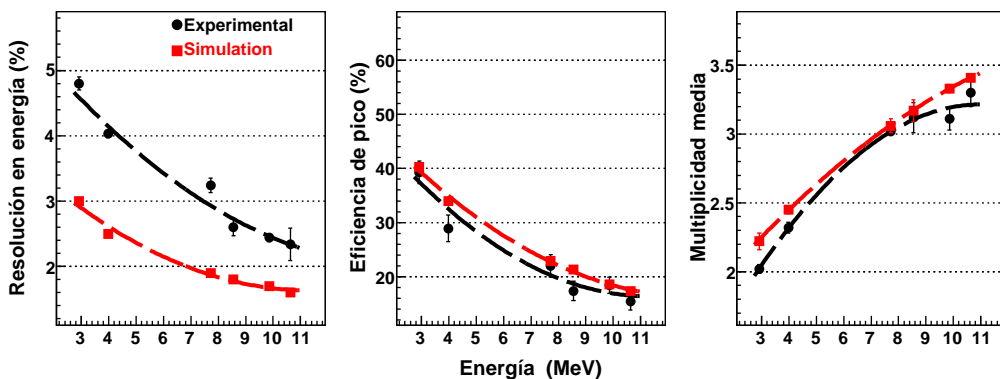
Figura 39: Comparación entre los valores experimentales y simulados para resolución en energía (izda.), eficiencia de pico (medio) y multiplicidad (dcha.) en función de la energía de los gammas seleccionados.

fondo bajo el pico en los espectros de correlación temporal (véase Fig. 37). El procedimiento consiste en contar el número de entradas bajo estos picos, y sustraerlos al número total de cuentas en el espectro de energía, ya que estas entradas son eventos no correlacionados y tienen cualquier energía, contribuyendo igualmente a cualquier canal del espectro de energía. Una vez aplicado este procedimiento, los resultados experimentales obtenidos se ajustan bien a los valores simulados para este observable.

Los valores de multiplicidad experimentales y simulados son similares. Las pequeñas diferencias encontradas a bajas energías se explican teniendo en cuenta las diferencias en el nivel de ruido de cada APD. Si el nivel de ruido es mayor que la señal producida por gamma dispersado, su energía correspondiente se pierde y por tanto, este gamma no contribuye a la multiplicidad. A altas energías este efecto parece ser menor.

La Fig. 40 muestra la comparación de los picos recontruídos obtenidos en la simulación y el experimento para tres energías de gammas seleccionados. Los picos simulados fueron obtenidos tomando como referencia una resolución en energía de 7,5 % a 1 MeV, valor que se aproxima al obtenido con cristales individuales del prototipo. El pico de 2,92 MeV es el que más se aproxima al experimental, pero a altas energías vemos pequeñas diferencias debidas posiblemente a que las coicidencias accidentales no pueden ser separadas de las verdaderas en el proceso de radiación de frenado.

Conclusiones

En este trabajo se presentan los estudios realizados con cristales de CsI(Tl) acoplados a diferentes fotosensores, llevado a cabo como parte del programa de I+D para el calorímetro CALIFA de R^3B/FAIR. Esta tesis incluyó simulaciones
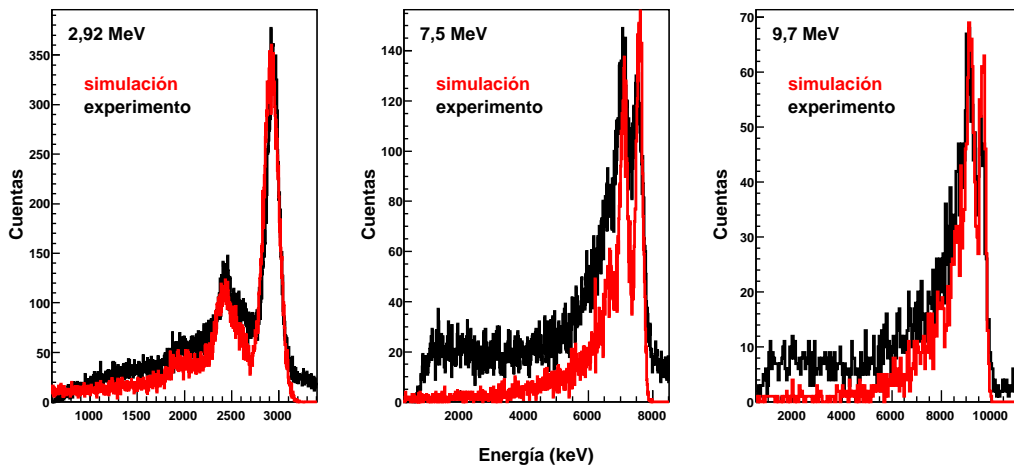
Figura 40: Comparación entre simulación y experimento de los picos reconstruídos para tres energías seleccionadas.

del calorímetro y el prototipo ProtoZero. Se realizó un estudio detallado de los diferentes parámetros que definen la resolución en energía del detector de CsI(Tl) y APD. Se presentó la caracterización de pequeños cristales de CsI(Tl) acoplados a diferentes fotosensores, y se compararon diferentes fotodiodos de avalancha acoplados a cristales bipiramidales de CsI(Tl) con caras de salida adaptadas para estos APDs. Finalmente se detallaron la construcción y resultados obtenidos con el prototipo ProtoZero en distintas instalaciones.

En la simulación del calorímetro se introdujeron tres longitudes de cristales diferentes para estudiar la variación en eficiencia y resolución en energía. Se comprobó que la contribución geométrica a la resolución en energía está por debajo del 3 %, para todas las energías probadas en sistema de referencia del proyectil en SRP. Se demostró que, para una geometría de cristales *medios*, la eficiencia de pico obtenida va del 70 % (para bajas energías) hasta el 45 % para 10 MeV en SRP. La multiplicidad va desde 2 cristales para 0,5 MeV hasta 7 para 10 MeV. La multiplicidad en la zona del Barril se reduce hasta 4 cristales, incluso para la energía más alta, debido a que los gammas que llegan a esta zona ven reducida su energía en el laboratorio debido al 'boost de Lorentz'.

En la simulación del prototipo se obtuvieron los mismos observables que en la simulación del calorímetro y se observó que la eficiencia de pico es más baja que para el calorímetro debido a que la probabilidad de escape de los gammas dispersados es mayor. La multiplicidad está entre 1,7 y 3,3 en todo el rango estudiado y concuerda con los datos obtenidos para el calorímetro. En la simulación con protones se comprobó que las perdidas de energía de aquellos protones que pasan de un cristal a otro son debidas al recubrimiento. La simulación demostró que un recubrimiento de ESR menor de 130 μm de espesor reduce las pérdidas de

energía en dicho material y cumple con los requisitos del calorímetro para partículas cargadas de altas energías. En esta simulación también se obtuvo una estimación de las pérdidas de energía en los materiales interpuestos entre la fuente de protones y los cristales que permite calibrar el prototipo cuando se miden protones con energías que no se conocen.

En la caracterización de los cristales y APDs se comprobó como la resolución en energía depende del recubrimiento del cristal y otros parámetros relacionados con la cadena electrónica utilizada. Para cristales pequeños, en el rango de 1-10 cm de longitud y sección cuadrada (1 cm²), se comprobó que esta resolución es aproximadamente constante. Los resultados obtenidos para el cristal de 1 cm³ son comparables o mejoran los encontrados en la literatura. Se encontró que un recubrimiento de 75 μm de espesor de Teflón y 5 μm de Mylar aluminizado es óptimo para cristales pequeños, mientras que para cristales del prototipo el recubrimiento ideal es de una capa de ESR. Se demostró que la resolución final obtenida para un determinado cristal, depende del voltaje aplicado al APD, como también de la ganancia y tiempo de integración utilizados en el amplificador espectroscópico. En la caracterización de APDs, se compararon los diferentes modelos y se encontró la contribución que estos dispositivos introducen en la resolución en energía. También se descubrió la influencia del encapsulado de los APD en la resolución en energía. En la comparación de cristales se identificaron aquellos proveedores cuyos cristales ofrecen los mejores resultados y se estableció un procedimiento para comparar dichos cristales en términos de resolución en energía y salida de luz. Se demostró también la importancia que tiene la superficie de la cara de salida de los cristales para obtener la mayor colección de luz y se comprobó que la resolución en energía obtenida para los mejores cristales (5 % a 1 MeV) satisface uno de los requisitos del calorímetro CALIFA y demuestra que la combinación de estos cristales con APDs es una posible solución que se puede utilizar para el Barril de este calorímetro.

En los experimentos realizados en diferentes instalaciones con aceleradores, se utilizó un prototipo de cristales de CsI(Tl) acoplados a APDs, que se corresponden a una zona ubicada a 90° en ángulo polar de la geometría presentada para el calorímetro CALIFA. Estos experimentos sirvieron para comprobar el rendimiento de estos cristales cuando son irradiados con haces de protones y gammas de altas energías. En el caso de un haz de protones, se comprobó la linealidad de estos detectores en un rango de 90 a 180 MeV. También se demostró que, a pesar de reducir el voltaje de alimentación de los APDs (para aumentar el rango dinámico), se midió la energía de estos protones con una resolución (1 % FWHM) que satisface otro de los requisitos principales de este calorímetro para partículas cargadas de altas energías. En el experimento con gammas de 6,1 MeV se obtuvo una resolución en energía de 2,8 % para este pico, que está próxima a la estimada por la simulación (2,2 %). Se demostró la linealidad de estos detectores en el rango entre 511 keV y 6,1 MeV, y se demostró que cuando hay derivas de la ganancia es posible mejorar la resolución en energía utilizando la posición media del pico reconstruído a pesar

de no monitorizar la temperatura. En el experimento con gammas de energías en el rango de 4 a 10 MeV se demostró la efectividad del procedimiento de reconstrucción y se observó que las resoluciones en energía obtenidas en este rango eran peores que las simuladas debido a la disparidad en rendimiento de los APDs utilizados para este prototipo, lo cual remarca la importancia de tener detectores individuales de similares características. Los observables simulados concuerdan con los datos experimentales y las pequeñas diferencias encontradas se deben fundamentalmente, a ciertas particularidades de este experimento y a la falta de estadística.

Appendix A

Uncertainty calculation of the gamma ray energy emitted by a moving source

Energy (E^S) in the Source Reference Frame (SRF) for γ-rays emitted by residual fragments moving at relativistic velocities can be expressed as

$$E^S = \frac{E^L}{DF} \tag{A.1}$$

where E^L is the energy of the emitted gamma measured in the Laboratory Reference Frame (LRF) and DF is the Doppler factor $[\gamma(1 - \beta\cos\theta)]^{-1}$, as defined in Section 1.2.3.

The uncertainties in this Equation can be described using the GUM[1] approach, which establishes general rules for evaluating and expressing uncertainty in measurement. The uncertainties are divided into two categories based on their method of evaluation: Type A, the evaluation of uncertainty by the statistical analysis of series of observations and Type B, the evaluation of uncertainty by means other than the statistical analysis of series of observations.

In Type A evaluations of measurement uncertainty, the assumption is often made that the expectation of an input quantity X is given by repeated, independently obtained, measured values of it. The distribution best describing the dispersion of these measured values is often a Gaussian distribution, in which the expectation equals the average measured value, with a standard deviation equal to the sigma parameter of the Gaussian function. Other considerations apply when

---

[1]The Guide to the Expression of Uncertainty in Measurement (GUM) was prepared by the Joint Committee for Guides in Metrology (http://www.bipm.org/en/committees/jc/jcgm/) following the Recommendation 1(C1-1981) of the Comit'e des Poids et Mesures (CIPM). The development of the GUM was supported by the Bureau International des Poids et Mesures (BIPM), the International Electrotechnical Commission (IEC), the International Federation of Clinical Chemistry (IFCC), the International Organization for Standardization (ISO), the International Union of Pure and Applied Chemistry (IUPAC), the International Union of Pure and Applied Physics (IUPAP), and the International Organization of Legal Metrology (OIML).

the measured values are not obtained independently. For a Type B evaluation of uncertainty, often the only available information is that the quantity X is found within a specified interval [a, b]. In a simple case, knowledge of its dispersion can be characterized by a rectangular probability distribution with limits a and b. In this distribution, the expectation is (b-a)/2 and its associated variance is (b-a)^2/12.

Figure A.1 shows the uncertainty in θ (FWHM) of the emitted gamma.

Here, $E^L(\omega)$ is a Type A measurement, since it comes from the statistical response of the scintillation process in the crystals, which can be assumed as a Gaussian distribution. We will denote the uncertainty in E^L as $\Delta E^L(\omega)$.

In contrast, the Doppler factor $[DF(\theta)]$ is a Type B measurement, since its dispersion comes from the polar angle θ uncertainty, which is determined using finite intervals defined by the crystal width. Taking into account the uncertainty in the Doppler factor expressed as $\Delta DF(\theta)$, the Equation A.1 can be rewritten as

$$E^S(\theta,\omega) \pm \Delta E^S = \frac{[E^L(\omega) \pm \Delta E^L]}{[DF(\theta) \pm \Delta DF]} \tag{A.2}$$

where ω and θ are considered uncorrelated, and therefore independent. The uncertainty in E^S is defined as 'combined standard uncertainty' and, following the GUM approach, can be expressed as

$$(\Delta E^S)^2 = \left[\frac{\partial E^S}{\partial \omega}\Delta_A \omega\right]^2 + \left[\frac{\partial E^S}{\partial \theta}\Delta_B \theta\right]^2 \tag{A.3}$$

by replacing A.1 in A.3 we obtain

$$(\Delta E^S)^2 = \left[\frac{1}{DF(\theta)}\left(\frac{\partial E^L(\omega)}{\partial \omega}\right)\Delta_A \omega\right]^2 + \left[E^L(\omega)\frac{\partial}{\partial \theta}\left(\frac{1}{DF(\theta)}\right)\Delta_B \theta\right]^2 \tag{A.4}$$

dividing twice by Eq. A.2 we obtain

$$\left(\frac{\Delta E^S}{E^S}\right)^2 = \left[\frac{\partial E^L(\omega)}{\partial \omega}\frac{\Delta_A \omega}{E^L(\omega)}\right]^2 + \left[\frac{\partial}{\partial \theta}\left(\frac{1}{DF(\theta)}\right)\frac{\Delta_B \theta}{DF(\theta)}\right]^2 \tag{A.5}$$

The relative uncertainty in E^S is the positive square root of the combined uncertainties of the E^L data dispersion measured from the scintillation process in the crystals, together with the uncertainty in the determination of the polar angle θ, which can be treated separately.

Strictly speaking, this is not so simple, since Eq. A.4 is only valid when both $\Delta_A \omega$ and $\Delta_B \theta$ are expressed with the same kind of uncertainty estimator; such as the square root of their variance. Usually the energy resolution is expressed in terms of the FWHM of the peak obtained in the MCA when measuring the amplitude of the signals produced by the shaping amplifier after the scintillator readout. This FWHM is easily related to the σ-parameter of a Gaussian function fitting the peaks, and σ^2 is the associated variance with the mean value of the
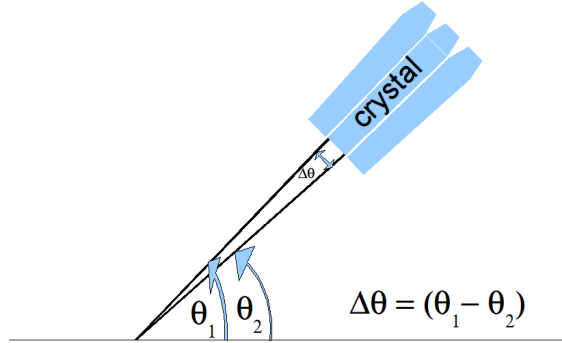
Figure A.1: Diagram of the uncertainty in θ (FWHM) of the emitted gamma.

Gaussian fit. However, $\Delta_B\theta$ (as defined by Figure A.1) is expressed in terms of its FWHM and so, to be strict, one must take $(\theta_1 - \theta_2)/\sqrt{12}$ as the value of $\Delta_B\theta$ in Eq. A.4, when $\Delta_A\omega$ is taken as a σ value. For the sake of simplicity, we chose to always use FWHM values to express the energy resolutions and so we can take $\Delta_B\theta = 2.35 \cdot [(\theta_1 - \theta_2)/\sqrt{12} \simeq 0.68(\theta_1 - \theta_2)$.

It is worth mentioning also that the function $E^L(\omega)$ is somewhat related to the variable θ, since the energy resolution that can be achieved with a scintillating crystal depends on its size. However, this value is not important to our work and can be disregarded.

For a 'perfect crystal' (as defined in Section 2.2.4), we can calculate the contribution to the E^S that is only due to the uncertainty in the polar angle θ, obtaining

$$\left(\frac{\Delta E^S}{E^S}\right)_\theta^2 = \left[\frac{\partial}{\partial\theta}\left(\frac{1}{DF(\theta)}\right)\frac{\Delta_B\theta}{DF(\theta)}\right]^2 \tag{A.6}$$

where

$$\frac{\partial}{\partial\theta}\left(\frac{1}{DF(\theta)}\right) = \frac{\partial[\gamma(1 - \beta\cos\theta)]}{\partial\theta} = \gamma\beta\sin\theta \tag{A.7}$$

replacing Eq. A.7 and $DF(\theta)$ in Eq. A.6, we obtain

$$\left(\frac{\Delta E^S}{E^S}\right)_\theta = \frac{\beta\sin\theta}{1 - \beta\cos\theta}\Delta(\theta) \tag{A.8}$$

This expression is used to estimate the contribution of the limited angular resolution to the energy resolution in the source reference frame.

For real crystals, a finite value must be introduced for the energy resolution scaling with $1/\sqrt{E}$ in the LRF in Eq. A.5. So the Eq. A.5 becomes

$$\left(\frac{\Delta E^S}{E^S}\right)^2 = \left[\frac{A}{\sqrt{E^L}} + B\right]^2 + \left[\frac{\beta\sin\theta}{1 - \beta\cos\theta}\Delta\theta\right]^2 \tag{A.9}$$

where A is the energy resolution at 1 MeV and B is an asymptotic value that includes the intrinsic energy resolution of the crystals and the contribution of the whole electronic chain.

Replacing A.1 in A.9, we obtain

$$\left(\frac{\Delta E^S}{E^S}\right)^2 = \left[\frac{A \cdot \sqrt{\gamma(1 - \beta\cos\theta)}}{\sqrt{E^S}} + B\right]^2 + \left[\frac{\beta\sin\theta}{1 - \beta\cos\theta}\Delta\theta\right]^2 \qquad (A.10)$$

For real crystals, this expression can be used to estimate the final energy resolution in the SRF due to both the crystal resolution and the contribution of the polar angle uncertainty .

Appendix B

APDs characterization

APD No.	Active area	Capacitance	Optimal bias voltage	Light-pulse resolution	$I_D(^c)$
1	10x10 mm^2	standard	406 V	5.2%	20 nA
2	10x10 mm^2	standard	404 V	5.4%	22 nA
3	10x10 mm^2	standard	410 V	5.3%	8 nA
4	10x10 mm^2	standard	411 V	5.5%	7 nA
5	7x14 mm^2	standard	332 V	7.2%	23 nA
6	7x14 mm^2	standard	322 V	8.1%	23 nA
7	7x14 mm^2	standard	332 V	8.7%	32 nA
8	7x14 mm^2	standard	333 V	9.2%	39 nA
9	7x14 mm^2	low	491 V	7.5%	24 nA
10	7x14 mm^2	low	484 V	8.2%	30 nA
11	7x14 mm^2	low	493 V	8.4%	31 nA
12	7x14 mm^2	low	492 V	9.8%	32 nA

^{c} I_D: dark current at the optimal bias voltage

Table B.1: APD characteristics for optimal performance.
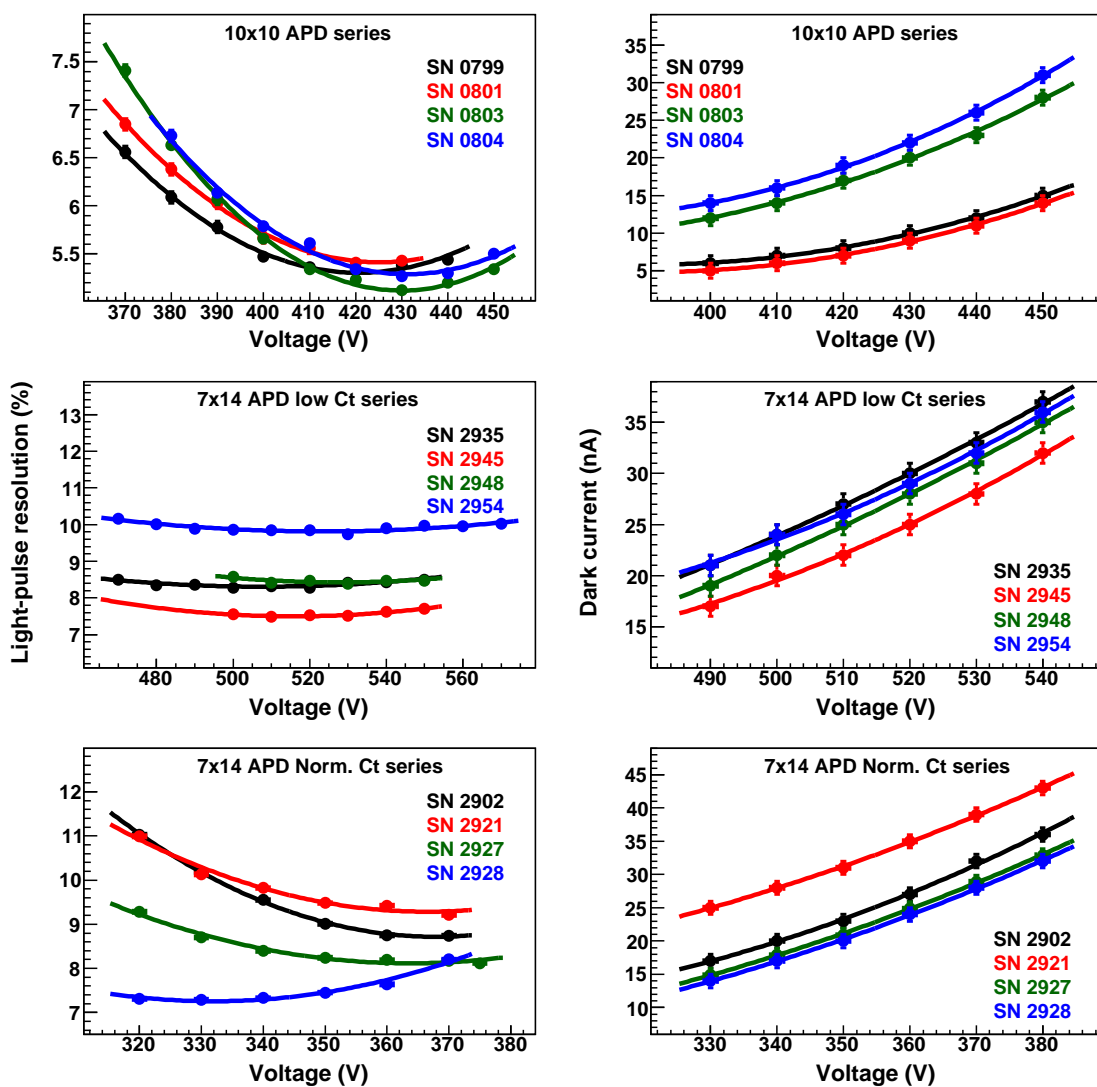
Figure B.1: Light-pulse Resolution (left) and Dark Current (right) vs. Bias Voltage for 7x14 and 10x10 mm² APD series

Appendix C

Crystals characterization

Provider	Exit face (mm^2)	Photopeak Ch.	Light output
Ref.(^{d})	10x10	5938	100 %
Amcrys-1	7x14	3343	56 %
Amcrys-2	7x14	2808	47 %
Amcrys-3	7x14	3499	59 %
Amcrys-4	7x14	2745	46 %
Lanzhou-1	7x14	3711	62 %
Lanzhou-2	7x14	2844	48 %
Lanzhou-3	7x14	3485	59 %
Lanzhou-4	7x14	2900	49 %
Amcrys-5	10x10	3393	57 %
Amcrys-6	10x10	2778	47 %
Amcrys-7	10x10	3429	59 %
Amcrys-8	10x10	2782	47 %
Lanzhou-5	10x20	4249	72 %
Lanzhou-6	10x20	4540	76 %

^{d} 10x10x10 mm^3 CsI(Tl) crystal from St. Gobain (reference)

Table C.1: Summary of light output comparison for a set of 7x14, 10x10 and 10x20 mm^2 exit face crystals.

Crystal->	Am005	Am006	Am007	Am008	Am009
Wrapping	L.P.R (%)	L.P.R. (%)	L.P.R. (%)	L.P.R. (%)	L.P.R. (%)
2x ESR	**5.49±0.06**	**5.92±0.05**	**6.04±0.04**	6.10±0.04	5.93±0.04
1x ESR	5.53±0.06	5.99±0.04	6.25±0.06	6.19±0.03	**5.91±0.04**
1x ESR + 1x TF	5.71±0.04	6.04±0.05	6.25±0.08	**6.08±0.04**	5.99±0.04
1x ESR + 2x TF	5.71±0.04	6.15±0.03	6.15±0.05	6.09±0.03	6.07±0.06
1x ESR + 3x TF	5.73±0.04	6.00±0.04	6.14±0.07	6.09±0.04	6.12±0.07
1x ESR + 6x TF	5.93±0.06	6.08±0.04	6.28±0.05	6.13±0.05	6.11±0.06

Table C.2: Light pulse resolutions (FWHM) obtained using a LED with different $10x10$ mm^2 exit face crystals and different wrapping configurations, coupled to an XP5A08 PMT without optical grease. 1x,2x,3x,6x is the number of layers, and TF is Teflon tape

Crystal->	Am005	Am006	Am007	Am008	Am009
Wrapping	E.R (%)	E.R (%)	E.R (%)	E.R (%)	E.R (%)
2x ESR	**14.6±0.7**	**14.8±0.7**	**15.4±1.1**	16.6±0.5	**15.8±1.2**
1x ESR	15.0±0.7	15.4±1.1	15.7±1.2	16.9±0.8	16.0±1.0
1x ESR + 1x TF	15.0±0.7	16.2±0.8	17.5±0.9	16.3±0.6	16.4±0.6
1x ESR + 2x TF	14.9±0.7	15.8±1.2	15.7±1.3	**15.7±3.7**	16.5±0.9
1x ESR + 3x TF	15.1±0.8	15.0±0.9	16.0±1.3	15.9±1.2	15.9±1.0
1x ESR + 6x TF	15.5±1.0	15.5±1.2	17.4±0.9	16.7±0.9	17.9±1.2

Table C.3: Energy resolutions (FWHM at 662 keV) obtained using a ^{137}Cs radioactive source, for different crystals with a $10x10$ mm^2 exit face and different wrapping configurations, coupled to an XP5A08 PMT without optical grease. 1x,2x,3x,6x is the number of layers, and TF is Teflon tape

Appendix D

Hardware specifications

Cremat CR-110 preamplifiers

During the R&D stage of the crystal and APD characterization, a compact Cremat preamplifier was used. The Cremat CR-110 is a single-channel, charge-sensitive preamplifier module intended for use with various types of radiation detectors including semiconductor detectors (e.g. CdTe and CZT), PIN photodiodes, avalanche photodiodes (APDs), and various gas-based detectors. The CR-110 model is small (25x22 mm^2) and allows for modular design and construction of compact multichannel detection systems.

Figure D.1 provides a picture and a simplified equivalent circuit diagram of the CR-110, which is a two-stage amplifier. The first stage is high gain and the second stage is low gain designed to supply sufficient output current to drive a terminated coaxial cable. Pin numbers corresponding to the CR-110 preamplifier are shown. Rf (100 MΩ) and Cf (1.4 pF) are the feedback resistor and capacitor respectively.
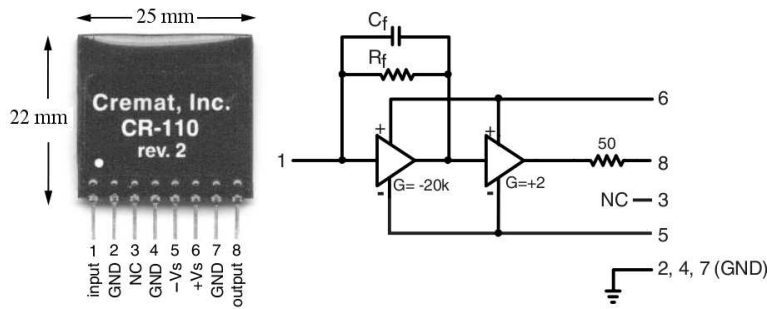
Figure D.1: Picture and simplified equivalent circuit diagram of the Cremat CR-110 preamplifier. For further details, see explanation in text.

The hardware specifications are shown in Table D.1.

MSCF-16 shaper amplifier with CFD

The Mesytec MSCF-16 is a shaping/timing filter amplifier with a constant fraction discriminator and multiplicity trigger. It provides active baseline restorers
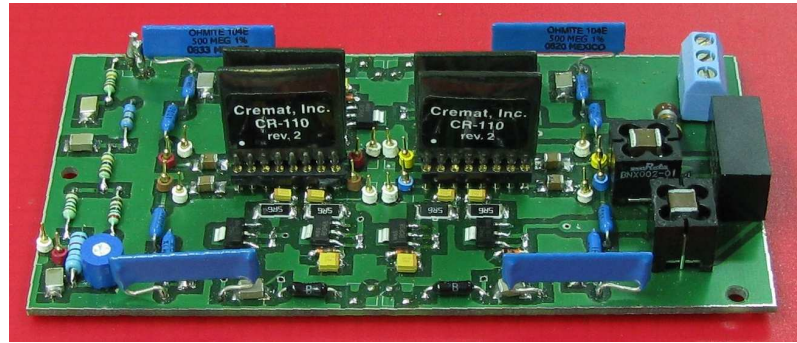
Figure D.2: Four Cremat CR-110 preamplifiers mounted on a board, ready for the ProtoZero setup.

and is well suited for high quality spectroscopy applications. This 16-channel NIM module can be locally or remote controlled using a USB port; 5th. order filter CR-RC; four shaping times can be selected for groups of 4 channels; active baseline restorer.
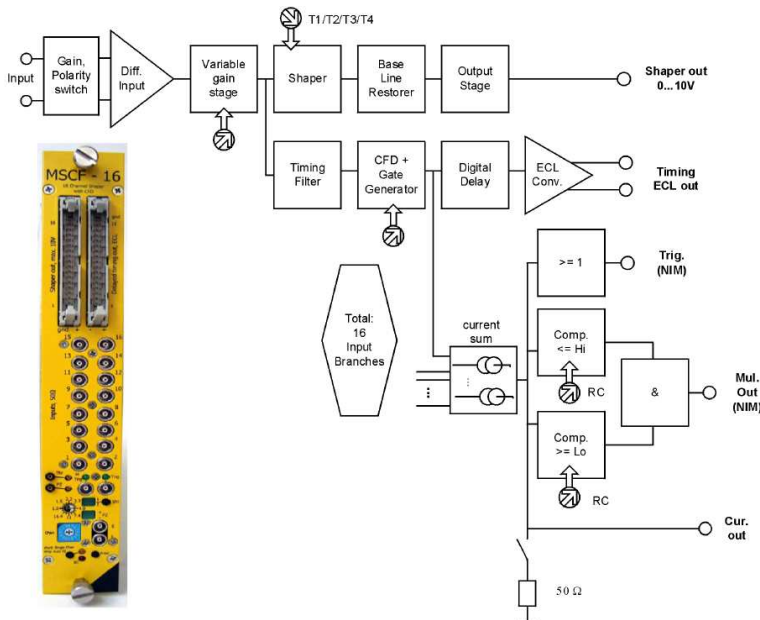
Figure D.3: Picture and a simplified circuit diagram of the Mesytec MSCF-16 amplifier. For further details, see explanation in text.

The hardware specifications are shown in Table D.2.

|	Cremat CR-110	units
Preamplification channels	1	
ENC[a] RMS	200	electrons
	0.03	femtoCoul
Equivalent noise in silicon	1.7	keV (FWHM)
Equivalent noise in CdZnTe	2.4	keV (FWHM)
ENC slope	4	elect. RMS/pF
Gain	1.4	volts/pC
Rise time[b]	7	ns
Decay time constant	140	μs
Unsaturated output swing	-3 to +3	volts
Maximum charge detectable per event	$1.3.10^7$	electrons
	2.1	pC
Power supply voltage		
maximum	$V_S = \pm 13$	volts
minimum	$V_S = \pm 6$	volts
Power supply current (pos)	7.5	mA
Power supply current (neg)	3.5	mA
Power disipation	70	mW
Operating temperature	-40 to + 85	°C
Output offset	+0.2 to -0.2	volts
Output impedance	50	ohms

[a] Equivalent noise charge, measured with the input disconnected using a Gaussian shaping amplifier with time constant = 1 μs. With a detector attached to the input, noise from the detector capacitance, leakage current, dielectric losses will add to this figure.

[b] The pulse rise time (defined as the time needed to attain 90% of the maximum value) has a linear relationship with input capacitance. The value cited in the table assumes zero added input capacitance. To calculate the pulse rise time for practical situations, use the equation: tr =0.4 Cd + 7 ns, where tr is the pulse rise time in ns, and Cd is the added capacitance (e.g. detector capacitance) in pF. Keep in mind that others factors within the detection system may further limit this value.

Table D.1: Summary of the Cremat CR-110 preamplifier specifications. Specifications assume temperature = 20 °C, Vs = 6.1 V, unloaded output

MSI-8 preamplifier

The Mesytec MSI-8 is a compact 8-channel preamplifier shaper box with integrated timing filter amplifiers. Due to its modular setup, preamplifier and shaper module types can be selected individually for each channel. MSI-8 is the ideal solution for setups with a mix of different detectors that require individual bias supplies and energy ranges. This is an easy to use and flexible lab system that is also well

	Mesytec MSCF-16	**units**
Amplification channels	16	
Input connector	34	pins
Output connector (male connector)	34	pins
Input resistance (terminated with)	100	ohms
Gain range	from 2 to 600	
Common mode suppression	> 50	dB
Input noise (G=100) (sh.time=2μs)	7	μVrms
Output amplitude (at 1 kV)	0 to 10	V
DC-Offset	± 5	mV
Integral nonlinearity	< 0.05	%
Gain drift	< 0.0075	%/C°
Offset drift	< 50	μV/C°
Power consumption (max)	9	W
+6V	350	mA
-6V	-700	mA
+12V	200	mA

Table D.2: Summary of Mesytec MSCF-16 specifications.

suited for moderately segmented strip detectors.
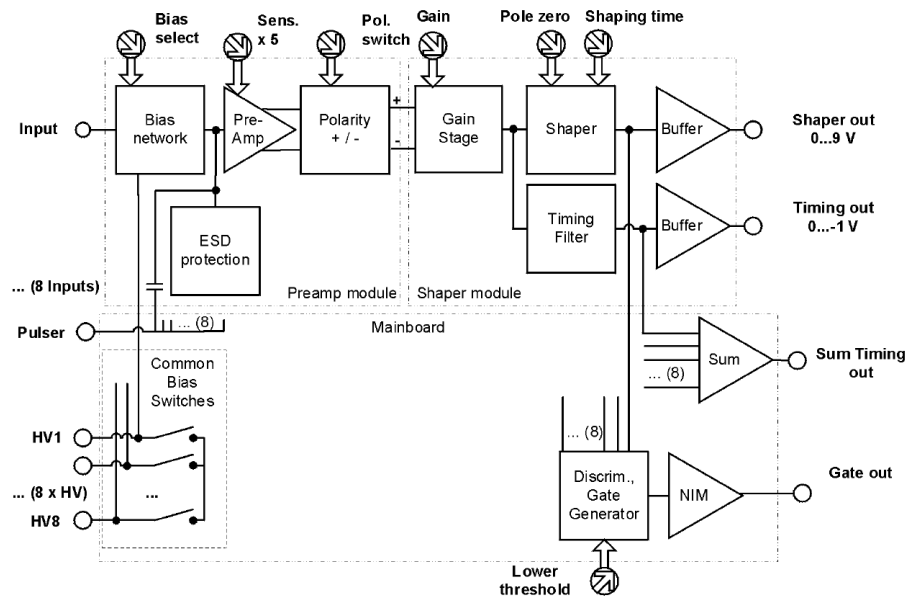
Figure D.4: Picture and a simplified circuit diagram of the Mesytec MSI-8 preamplifier. For further details, see explanation in text.

Bibliography

[1] FAIR. http://www.gsi.de/fair.

[2] Facility for Antiproton Ion Research. Conceptual Design Report. http://www.gsi.de/GSI-Future/cdr/

[3] J. Eschke, "International Facility for Antiproton and Ion Research (FAIR) at GSI, Darmstadt", *J. Phys. G: Nucl. Part. Phys., Vol. 31, pp. S967-S973, 2005.*

[4] Technical proposal for the Design, Construction, Commissioning and Operation of R3B. FAIR-PAC/NUSTAR/R3B, January 2005. http://www-land.gsi.de/r3b/

[5] GSI Scientific report 2006. http://www.gsi.de.

[6] T. Suzuki et al., "Neutron Skin of Na Isotopes Studied via Their Interaction Cross Sections", *Phys. Rev. Lett. 75, pp. 3241-3244 (1995).*

[7] P. Egelhof et al., "Nuclear-matter distributions of halo nuclei from elastic proton scattering in inverse kinematics", *Eur. Phys. J. A 15, pp. 27-33 (2002).*

[8] M. H. Smedberg et al., "New results on the halo structure of 8B", *Phys. Lett. B 452, pp. 1-7 (1999).*

[9] G. Krein, Th. A. J. Maris, B. B. Rodrigues, and E. A. Veit, "Medium effects on spin observables of proton knockout reactions", *Phys. Rev. C 51 pp. 2646-2655 (1995).*

[10] T. Aumann, P. F. Bortignon, and H. Emling, "Multiphonon Giant Resonances in Nuclei", *Ann. Rev. Nucl. Part. Sci. 48 pp. 351-399 (1998)*

[11] A. Kraznahorkay et al., " Excitation of Isovector Spin-Dipole Resonances and Neutron Skin of Nuclei", *Phys. Rev. Lett. 82 pp. 3216-3219 (1999).*

[12] K.-H. Schmidt et al., "Relativistic radioactive beams: A new access to nuclear-fission studies", *Nucl. Phys. A 665 pp. 221-267 (2000).*

[13] J. E. Ducret et al., SPALADIN experiment performed at GSI, proposal S248.

[14] H. Mueller and B. D. Serot., "Phase transitions in warm, asymmetric nuclear matter", *Phys. Rev. C 52 pp. 2072-2091 (1995).*

[15] http://www-land-gsi.de/r3b/docu/R3B-TP-Dec05.pdf

[16] H. Álvarez-Pol, J. Benlliure, E. Casarejos, D. Cortina-Gil, I. Durán, M. Gascón, "Design studies and first crystal tests for the R3B Calorimeter", *Nucl. Inst. and Meth. B 266 (2008) 4616-4620.*

[17] R^{3}B Calorimeter Internal Notes. R3B CAL 01-02/05, "A first proposal for the geometry of the Total Absorption Calorimeter design at R3B", available in http://www.usc.es/genp/r3b

[18] R^{3}B Calorimeter Internal Notes. R3B CAL 01/06, "First simulation results of the finger-like crystals calorimeter for R3B (CALIFA)", available in http://www.usc.es/genp/r3b

[19] R^{3}B Calorimeter Internal Notes. R3B CAL 02-03/06, "R3B Calorimeter Design Status Report", available in http://www.usc.es/genp/r3b

[20] R^{3}B Calorimeter Internal Notes. R3B CAL 01/07, "Simulation of the CALIFA detector: results for the geometry v4.0b", available in http://www.usc.es/genp/r3b

[21] Internal R^{3}B Simulation notes, "R3BSim description and results", available in http://www.usc.es/genp/r3b

[22] S. Agostinelli et al, "Geant4 - a simulation toolkit", *Nucl. Instr. & Meth. A 506 (2003) 250-303.*

[23] Rene Brun and Fons Rademakers, Proceedings AIHENP'96 Workshop, Lausanne, Sep. 1996, *Nucl. Instr. & Meth. in Phys. Res. A 389 (1997) 81-86.* See also http://root.cern.ch/

[24] Vikuiti ESR is a trademark of 3M

[25] D.D.DiJulio et al., "Proton in-beam tests of the Lund R3B calorimeter prototype", *Nucl. Instr. and Meth. A, vol. 612, pp. 127-132, 2009*

[26] http://en.wikipedia.org/wiki/Bethe_formula

[27] Knoll, G. F. *Radiation Detection and Measurements* (Wiley, New York, 1979).

[28] http://www.slac.stanford.edu/BFROOT/www/Detector/Calorimeter/index.html

[29] A. Abashiana et al., "The Belle detector", *Nucl. Inst. and Meth. A479 (2002) 117-232*

[30] R. Novotny, "Inorganic scintillators, a basic material for instrumentation in physics" *Nucl. Inst. and Meth. A537 (2005) 1-5.*

[31] V.P. Semynozhenko, B.V Grinyov, V.V. Nekrasov, Yu.A. Borodenko, "Recent progress in the development of CsI(Tl) crystal-Si-photodiode spectrometric detection assemblies" *Nucl. Inst. and Meth. A537(2005)383-388.*

[32] M. Moszyński, "Inorganic scintillation detectors in γ-ray spectrometry" *Nucl. Inst. and Meth. A505 (2003) 101-110.*

[33] J. Valentine, W. Moses, S. Derenzo, D. Wehe and G. Knoll, "Temperature dependence of CsI(Tl) gamma-ray excited scintillation characteristics", *Nucl. Inst. and Meth. A 321 vol. 1-2 (1993) 147-157*

[34] P. Schotanus, P. Kamermans and P. Dorenbos, "Scintillation characteristics of pure and T1-doped CsI crystals," *IEEE Trans. Nuc. Sci*, vol. 37 no. 2 pp. 177-182, 1990.

[35] V. Babin, A. Krasnikov, H. Wieczorek and S. Zazubovich, "Luminescence of complicated thallium centres in CsI:Tl", *Nucl. Inst. and Meth. A486 (2002) 486-489.*

[36] Saint-Gobain *Scintillation Products*, 2004.

[37] A. G. Wright Electron Tubes Ltd: *http://www.electrontubes.com/info/papers.html*

[38] Photonis. *Photomultiplier tubes basics*

[39] D. Renker. "Geiger-mode avalanche photodiodes, history, properties and problems", *Nucl. Inst. and Meth. A567 (2006) 48-56.*

[40] http://en.wikipedia.org/wiki/Silicon_photomultiplier

[41] M. Gascón, H. Álvarez-Pol, J. Benlliure, E. Casarejos, D. Cortina-Gil, I. Durán, "Optimization of energy resolution obtained with CsI(Tl) crystals for the R3B Calorimeter", *IEEE Trans. Nuc. Sci 55 (2008) 1259-1262.*

[42] A. Osovizky, U. Wengrowicz, M. Ghelman et al., "Sintillation Light Readout Using Silicon Photomultipliers - Review and Experimental Results," *2008 IEEE Nuclear Science Symposium Conference Record. N30-358.*

[43] A.J. Bird, T. Carter, A.J.Dean ,D. Ramsden, B.M.Swinyard, "The Optimization of Small CsI(Tl) crystals Gamma-ray Detectors", *IEEE Trans. Nuc. Sci 40 (1993) 395-399.*

[44] H.S.Kim et al., "Fabrication and performance characteristics of a CsI(Tl)/PIN diode radiation sensor for industrial applications", *Applied Radiation and Isotopes 67 (2009) 1463-1465*

[45] L.J. Meng et al., "The design and performance of a large-volume spherical CsI(Tl) scintillation counter for gamma-ray spectroscopy", *Nucl. Inst. and Meth. A485 (2002) 468-476.*

[46] M. Moszyński, M. Szawlowski, M. Kapusta, M. Balcerzyk, "Avalanche photodiodes in scintillation detection", *Nucl. Inst. and Meth. A497 (2003) 226-233.*

[47] D Renker, "Properties of avalanche photodiodes for applications in high energy physics, astrophysics and medical imaging", *Nucl. Inst. and Meth. A486 (2002) 164-169.*

[48] J. Kataoka, T. Saito, Y. Kuramoto, T. Ikagawa, Y. Yatsu, J. Kotoku, M. Arimoto, N. Kawai, Y. Ishikawa., N. Kawabata, "Recent progress of avalanche photodiodes in high-resolution X-rays and γ-rays detection", *Nucl. Inst. and Meth. A541 (2005) 398-404.*

[49] R Sato et al., "Development of 2 cm-square Hamamatsu avalanche photodiodes for high-resolution X-rays and g-rays detection", *Nucl. Inst. and Meth. A556 (2006) 535-542.*

[50] http://sales.hamamatsu.com/en/products/solid-state-division/si-photodiode-series/si-apd/part-s8664-1010.php

[51] http://www.advancedphotonix.com

[52] M. Gascón, H. Álvarez-Pol, S. Ancelin, J. Benlliure, E. Casarejos, D. Cortina-Gil, I. Durán, Michaël Josselin, Jean Antoine Scarpaci and Jean Peyré, "Characterization of Large Frustum CsI(Tl) crystals for the R3B Calorimeter", *IEEE Trans. Nuc. Sci 56 (2009) 962-967.*

[53] M. Gascón, H. Álvarez-Pol, J. Benlliure, E. Casarejos, D. Cortina-Gil, I. Durán, D. González and N. Montes, "Test of LAAPDs Coupled to CsI(Tl) Crystals for the CALIFA R3B/FAIR Calorimeter", *IEEE Trans. Nuc. Sci 57 No. 3 (2010) 1465-1469.*

[54] M. Moszyński, M. Szawlowski, M. Kapusta, M. Balcerzyk, "Large area avalanche photodiodes in scintillation and X-ray detection", *Nucl. Inst. and Meth. A485 (2002) 504-521.*

[55] T. Ikagawa, J. Kataoka, Y. Yatsu, T. Saito, Y. Kuramoto, N. Kawai, M. Kokubun, T.Kamae, Y. Ishikawa, N. Kawabata, "Study of large area Hamamatsu avalanche photodiode in a γ-rays scintillation detector", *Nucl. Inst. and Meth. A538 (2005) 640-650*

[56] S. Howard, G. Ritter, K. Singh , S. Wurzel, H. Wieman, E. Yamamoto, "A CMOS Active Pixel Sensor for Charged Particle Detection", *IEEE Nuclear Science Symposium Conference Record (2002) 10.1109/NSSMIC.2002.1239312.*

[57] J. Brose, G. Dahlinger and K.R. Schubert, "Properties of CsI(Tl) crystals and their optimization for calorimetry of high energy photons," *Nucl. Inst. and Meth. A417 (1998) 311-324.*

[58] J. Kataoka, R. Sato, T. Ikagawa, J. Kotoku, Y. Kuramoto, T. Saito, Y. Tsubukua, Y. Yatsu, N. Kawai, Y. Ishikawa., N. Kawabata, "An active gain-control system for Avalanche photo-diodes under moderate temperature variations" *Nucl. Inst. and Meth. A564 (2006) 300-307.*

[59] C. Fiorini, A. Longoni, F Perotti, C. Labanti, P. Lechner and L. Strueder, "Gamma ray Spectroscopy with CsI(Tl) Scintillator Coupled to Silicon Drift Chamber", *IEEE Trans. on Nucl. Sci. 44 (1997) 2553-2560.*

[60] S8664-1010 2CH specifically made by Hamamatsu Photonics K. K.

[61] RTV 681 from Scionix Netherlands.

[62] D. M. Beylin, et al, "Study of the radiation hardness of CsI(Tl) scintillation crystals," *Nucl. Inst. and Meth. A*, vol. 541, pp. 501-515, 2005.

[63] Guohao Ren et al, "Non-uniformity of light output in large-sized CsI(Tl) crystals grown by non-vacuum Bridgman method," *Nucl. Inst. and Meth. A, vol. 564, pp. 364-369, 2006.*

[64] A. Syntfeld-Kazuch et al., "Non-proportionality and Energy Resolution of CsI(Tl)," *IEEE Trans. Nuc. Sci., vol. 30, pp. 1144-1149, 2006.*

[65] http://www-win.gsi.de/daq/

[66] Multi Instance Data Acquisition System. http://npg.dl.ac.uk/MIDAS/

[67] Yung-Su TSai, "Pair production and Bremsstrahlung of charged leptons", *Review of Modern Physics, Vol. 46 No. 4 pp. 815-851*

[68] Kai Lindenberg, "Development and Construction of the Low-Energy Photon Tagger NEPTUN", *PhD Thesis work. Technischen Universität Darmstadt. Germany*

[69] D. Savran, K. Lindenberg, J. Glorius, B. Löher, S. Müller, N. Pietralla, L. Schnorrenberger et al., "The low-energy photon tagger NEPTUN", *Nucl. Inst. and Meth. A, vol. 613, pp. 232-239, 2010.*

[70] Bastian Löher, Master Thesis, Technischen Universität Darmstadt, "Gamma Ray Spectroscopy with a LaBr_3:Ce at ultra high count rates"

[71] M. Elvers, J. Hasper, S. Müller, D. Savran, L. Schnorrenberger, K. Sonnabend and A. Zilges,"Nuclear astrophysics with real photons: the data acquisition system of the NEPTUN tagger setup", *J. Phys. G: Nucl. Part. Phys. vol. 35. 014027 (7 pp.), 2008.*